EXPERIMENTAL INVESTIGATION AND CREEP CORRELATION OF Zr-2.5Nb ALLOY

A Thesis Submitted to

Indian Institute of Technology Guwahati

in Partial Fulfilment of the Requirements

for the award of the degree of

DOCTOR OF PHILOSOPHY

by

SAPTARSHI DUTTA

DEPARTMENT OF MECHANICAL ENGINEERING

INDIAN INSTITUTE OF TECHNOLOGY GUWAHATI

GUWAHATI – 781039, INDIA

NOVEMBER 2023

Dedicated to my parents

Ma (Smt. Archana Dutta)

&

Babai (Shri. Sudip Kumar Dutta)

Department of Mechanical Engineering

Indian Institute of Technology Guwahati

Guwahati-781039 India

CERTIFICATE

It is certified that the work contained in the thesis entitled **"Experimental Investigation and Creep Correlation of Zr-2.5Nb alloy"** submitted by **Mr. Saptarshi Dutta** to the **Indian Institute of Technology Guwahati** for the award of the degree of **Doctor of Philosophy** has been carried out under my supervision in the **Department of Mechanical Engineering**. This work has not been submitted elsewhere for the award of any other degree or diploma.

This thesis, in my opinion, has reached the standard fulfilling the requirements for the award of the degree of Doctor of Philosophy in accordance with the regulations of the Institute.

(Prof. P.S.Robi)

Professor,
Department of Mechanical Engineering,
Indian Institute of Technology Guwahati
Guwahati-781039
India

Department of Mechanical Engineering

Indian Institute of Technology Guwahati

Guwahati-781039, India

SELF DECLARATION

I declare that,

a. The work contained in this thesis is original and has been carried out by me under the supervision of **Prof. P.S.Robi**
b. To the best of my knowledge, the work has not been submitted to any other Institute for any degree or diploma.
c. I have followed all the guidelines provided by the Institute in preparing the thesis.
d. Whenever I have used any materials (data, theoretical analysis, figures) from any other sources, due credit has been given to all of them by properly citing the documents.

(Saptarshi Dutta)
Department of Mechanical Engineering,
Indian Institute of Technology Guwahati,
Guwahati-781039
India

ACKNOWLEDGMENT

The journey of doctoral study is always a difficult yet a spiritual one. I would have never successfully completed this thesis without the constant support of numerous people to whom I am indebted to.

At the foremost, I express my deepest gratitude to my supervisor, Prof. P.S.Robi, for his invaluable guidance and immense support throughout my Ph.D. work . His zeal and dedication to work for society have always inspired me. His approach, combined with critical thinking, professional ethics, and the presence of mind, will remain a great lesson for the rest of my life. His guidance on doing systematic and constructive research with utmost liberty and a focused mind is remarkable.

I am thankful to my Doctoral Committee members, Prof. R. Ganesh Narayanan, Prof. S. Kanagaraj, and Prof. A. Srinivasan, for their insightful comments and valuable suggestions during my progress of research work. My sincere gratefulness to Prof. K. S. R. Krishna Murthy, HOD, Mechanical Engineering Department for his support. I would like to thank Bhabha Atomic Research Centre, Mumbai, India, for providing the pressure tubes and much useful information regarding the tube.

Very special thanks to all the faculties and staff members of the Department of Mechanical Engineering and Central Instruments Facility center of IIT Guwahati for providing all the necessary facilities to carry out the research works. I thank Mr. N. K Das, Asst. Workshop Superintendent very much for providing appropriate solutions to any kind of experimental difficulty. I would like to acknowledge my sense of gratitude to all the staffs of the Central Workshop. A special mention goes to Mr. Mrinal Sarma, Mr. Dilip Chetri, and Mr. D Khaklary for helping me whenever I needed them

The company of my beloved friends, notably Avinish, Ashutosh, Ajit, Sudip, Sujit, Pranay, Samrat, Pritam ji, Amritava, Saibal, and Sujoy made my years of stay balanced, enjoyable and memorable at IIT Guwahati. Each of them deserves special appreciation. I am very much grateful to my juniors, Rockey, Rishabh, Gaurav, Amay, Srikant for their invaluable support and joyful life. I wish them all the best for their future.

I wish to express my deepest respects and gratitude to my beloved parents (Sudip Kumar Dutta and Archana Dutta)), my in-laws (Alak Kumar Chakraborty and Aparna Chakraborty), and my elder sister Ms. Sathi Das, for providing unconditional love and support. This Ph.D was a collective dream of all of us, especially my Late Grand Father, Mr. Jagadish Chandra Dey. I wish I could have presented my work to him in his presence. Finally, I extend my warm appreciation to my wife, Mrs. Ishita Chakraborty, and love to our daughter Ms. Shivangshi Dutta. Their constant support during this sinusoidal journey of research kept me sane and my peace index reasonably high.

Above all, I am thankful to God.

Saptarshi Dutta

ABSTRACT

Pressure tubes (PT) are a key component of Pressurized Heavy Water Reactors used in Nuclear Power Plants. They support the fuel bundles and offer structural stability. Pressure tubes operate at temperatures between 290 °C and 350 °C and with variable coolant pressures of up to 11 MPa, corresponding to hoop stresses of up to 130 MPa.Zr-2.5Nb alloys are widely employed as PT materials because of their excellent corrosion resistance, low neutron absorption cross-section, and good mechanical properties. Creep deformation has been identified as one of the main performance-degrading mechanisms in this alloy, which could compromise the structural integrity of reactors. The PTs may fail due to creep in both the longitudinal (longitudinal creep) and diametral (transverse creep) directions. A thorough understanding and prediction of the creep life of PTs along both the longitudinal and transverse directions becomes imperative for the proper functioning of reactors. Hence, this work was carried out to investigate the microstructure, high-temperature tensile behavior, and constant stress creep behavior of Zr-2.5Nb alloys.

High-temperature tensile tests reveal that Young's Modulus, yield Strength, and ultimate tensile strength of the material decrease with the increase in test temperature. At all conditions of temperatures, the longitudinal samples displayed lower strength and higher ductility than the transverse ones. The strain hardening exponent increases up to 400 °C, beyond which it starts decreasing. TEM studies on sample tensile tested at 800°C showed a network of Nb-enriched β-Zr phase around the α- phase, which led to grain boundary sliding. Zr-2.5Nb alloy exhibited superplasticity at elevated temperatures. Tensile properties obtained for both the specimen orientations were correlated with respect to temperature with high accuracy, having an R^2 value of 0.99.

Creep behaviour of the PT material was investigated by carrying out accelerated creep tests in the temperature range of 600-850°C and in the stress range of 2-5MPa and 22-58MPa for the longitudinal and transverse samples, respectively. The strains in the three creep regions were analyzed in terms of temperature, stress, and minimum creep rate. Analysis of minimum creep rate, strain to rupture, and rupture time by Monkman-Grant relation and modified Monkman-Grant relation indicate both methods are valid for the investigated alloy. The relationship between time to reach Monkman-Grant ductility and rupture life was established for the alloy in terms of creep damage tolerance factor.

The creep stress exponent showed a non-linear second-order polynomial relationship with temperature for the longitudinal and transverse creep tests. The expression for the minimum creep rate obtained by constitutive modeling follows the power law relation in the form $\dot{\varepsilon}_s = 8.02 \times 10^{-6}\sigma^{2.2}exp\left(-\frac{292480}{RT}\right)$ and $\dot{\varepsilon}_s = 4.08 \times 10^{-6}\sigma^{2.6}exp\left(-\frac{302680}{RT}\right)$ for the longitudinal and transverse creep tests, respectively.

Artificial Neural Network (ANN) and Multiple Linear Regression (MLR) modeling were used to predict the creep curves of Zr-2.5Nb alloy. It was found that although MLR could effectively predict the primary creep region, it over-predicted the secondary creep region. However, the ANN model could accurately predict all three creep regions very distinctively. In this model, 98 % of the creep strains could be successfully predicted within a deviation error of ± 5%. Two sets of additional experiments were also carried out for each of the longitudinal and transverse creep tests to check the authenticity of the creep curve simulation. The R^2-value and mean relative error (MRE) between experimental and predicted strain were found to be around ~0.998 and ~2.64% for all the cases, indicating a very good prediction capability of the ANN model.

Prediction of the creep life of Zr-2.5Nb alloy under various combinations of temperatures and stresses was carried out using Larson-Miller parametric technique. It was observed that under constant stress test conditions, the iso-stress lines in the $\log_{10}(t_r)$ vs. 1/T plot are not meeting at a single point. The $C_{L\text{-}M}$ value was stress-dependent. Creep life prediction was done by considering $C_{L\text{-}M}$ as a constant as well as a stress-dependent function. The result obtained from the analysis indicated lower creep life by considering $C_{L\text{-}M}$ as a function of stress rather than a constant, thus giving a more conservative prediction.

CONTENTS

CERTIFICATE……..…….…..**I**

SELF DECLARATION…….…….…..……**II**

ACKNOWLEDGEMENT……..……. **III**

ABSTRACT……...……...…….. **IV**

LIST OF NOMENCLATURE...…….……....**IX**

LIST OF ABBREVIATIONS .....**X**

LIST OF FIGURES .....**XII**

LIST OF TABLES ..... **XIV**

CHAPTER 1 INTRODUCTION **23**

CHAPTER 2 LITERATURE REVIEW.....**27**

2.1 Introduction 27

2.2 Zirconium alloys in Pressure Tubes 27

2.3 Creep deformation.....28

2.4 Creep curve models.....31

2.5 Constitutive equations for steady state creep 33

2.6 Activation energy for creep.....34

2.7 Creep deformation mechanisms 35

2.7.1 Nabarro-Herring creep 36

2.7.2 Coble creep 37

2.7.3 Harper-Dorn creep 38

2.7.4 Dislocation creep models.....38

2.7.5 Viscous-glide creep model.....39

2.7.6 Dislocation climb controlled creep 39

2.7.7 Glide of jogged screw dislocations 40

2.7.8 Cross-slip mechanism 41

2.8 Kocks-Mecking model 41

2.9 Creep deformation mechanism maps 42

2.10 Creep fracture mechanism.....43

2.11 Creep rupture models 45

2.11.1 Monkman-Grant relationships and Creep Damage Tolerance Factor 46

2.11.2 Larson–Miller parameter 47

2.12 Multiple Linear Regression modeling.....49

2.13 Artificial Neural Network modeling 50

2.14 Technical gaps 53
2.15 Research objectives 53
CHAPTER 3 RESEARCH METHODOLOGY 54
3.1 Introduction 54
3.2 Experimental procedures 54
3.2.1 Raw material 54
3.2.2 Scanning Electron Microscopy 55
3.2.3 X-ray Diffraction 55
3.2.4 Transmission Electron Microscopy 55
3.3 Mechanical property testing 56
3.3.1 Tensile test 56
3.3.2 Creep test 58
3.3.2.a Constant stress creep test set-up 58
3.3.2.b Calibration of load cell 63
3.3.2.c Calibration of strain measurement system 64
3.3.2.d Creep testing procedure 65
3.3.3 Creep test matrix 67
3.4 Analysis of creep test data 68
3.4.1 Constitutive modeling of creep behavior 68
3.4.2 Multiple Linear Regression modeling 70
3.4.3 Artificial Neural Network modeling 70
3.4.4 Larson-Miller parametric technique 74
3.4.5 Monkman-Grant relationships 75
CHAPTER 4 RESULTS AND DISCUSSIONS 77
4.1 Introduction 77
4.2 Microstructure of the as-received alloy 77
4.3 Mechanical properties 79
4.3.1 Stress-Strain curves 79
4.3.2 High-temperature tensile test 80
4.3.3 Empirical relationships of temperature dependent tensile properties 83
4.3.4 Effect of temperature and sample orientation on the σ–ε and φ–σ behavior 85
4.3.5 Variation of strain hardening parameters with temperature 86
4.3.6 Microstructure of Zr-2.5Nb alloy tensile tested at 800°C 89
4.3.7 Fractography 91

4.3.8 Strain rate jump test 92
4.4 Creep Test 95
4.4.1 Load-Displacement behavior 95
4.4.2 Creep curves 98
4.4.3 Creep strains and rupture time 109
4.4.3.a Longitudinal creep tests 110
4.4.3.b Transverse creep tests 113
4.4.4 Constitutive modeling 117
4.4.4.a Longitudinal creep tests 117
4.4.4.b Transverse creep tests 120
4.4.5 Monkman-Grant relationships 123
4.4.5.a Longitudinal creep tests 124
4.4.5.b Transverse creep tests 126
4.4.6 Creep Damage Tolerance Factor 128
4.5 Modeling of creep curve by Multiple Linear Regression and Artificial Neural Network 130
4.5.1 Multiple Linear Regression modeling 131
4.5.2 Artificial Neural Network Modeling 132
4.5.2.a Longitudinal Creep Curve 137
4.5.2.b Transverse Creep Curve 140
4.5.3 Comparison of minimum creep rate 144
4.6 Creep life prediction by Larson-Miller parametric technique 147
4.6.1 Longitudinal creep life by L-M parameter 148
4.6.2 Transverse creep life by L-M parameter 152
4.7 Summary 157
CHAPTER 5 CONCLUSION AND SCOPE FOR FUTURE WORK 159
5.1 Introduction 159
5.2 Scope for future work 161
REFERENCES 162
APPENDIX 183
LIST OF PUBLICATIONS 186

NOMENCLATURE

RMS_{err}^{f}	Root-mean-square functional error
$n_{v,K-M}$	Rate of decrease of work hardening
A_i	Instantaneous area of the gauge section
A_o	Initial gauge area
$C_{L\text{-}M}$	Larson-Miller constant
$C_{L\text{-}M}(\sigma)$	$C_{L\text{-}M}$ as a function of stress
C_{MG}	Monkman-Grant constant
C_{MMG}	Modified Monkman-Grant constant
E	Young's modulus
E_i	Experimental value
F_i	Instantaneous load
G	Modulus of rigidity
K	Strength coefficient
L_{gauge}	Initial gauge length
n	Strain-hardening exponent
n_c	Stress exponent
N_{obs}	Number of observations
P_i	Predicted value
$P_{L\text{-}M}$	Larson-Miller parameter
Q_{app}	Apparent activation energy for creep
R	Universal gas constant(=8.314 $JK^{-1}mol^{-1}$)
R^2	Coefficient of determination
t	Time
T	Test temperature
t_{MGD}	Time to reach MGD
t_o	Initial thickness of gauge section
t_{os}	Onset of secondary creep
t_r	Time to rupture or rupture life
W_o	Initial width of gauge section
Y	Net input to the neuron

$\dot{\varepsilon}_s$	Minimum creep rate
Δ	Change in gauge length
ε	Strain
ε_0	Initial strain or instantaneous strain on loading
ε_1	Primary creep strain
ε_2	Secondary creep strain
ε_3	Tertiary creep strain
ε_f	Fracture strain
ε_{total}	Total strain
λ	Creep damage tolerance factor
σ	Applied stress
$\sigma_{S,\ K\text{-}M}$	Saturation stress
φ	Strain hardening rate
$\varphi_{o,K\text{-}M}$	Initial strain hardening rate

ABBREVIATIONS

ANN	Artificial neural network
ASTM	American Society for Testing and Materials
BCC	Body Centred Cubic
BPNN	Back-propagation neural network
CDM	Continuum Creep Damage Mechanics
DAQ	Data acquisition
EDS	Energy Dispersive X-ray Spectrometer
FCC	Face Centered Cubic
FESEM	Field Emission Scanning Electron Microscope
HDBSD	High definition backscattered electron detector
MGD	Monkman-Grant ductility
MGR	Monkman-Grant relationship
MLR	Multiple Linear Regression
MMGR	Modified Monkman-Grant relationship
MRE	Mean Relative Error
PID	Proportional-integral-derivative
RMS	Average root mean square
SAD	Selective area diffraction
TEM	Transmission electron microscopy
UTM	Universal Testing Machine
UTS	Ultimate Tensile Strength
WEDM	Wire cut electrical discharge machining
XRD	X-ray Diffraction
YS	Yield Strength

LIST OF FIGURES

Figure 2.1 Photographs of (a) original and ballooned pressure tube[27] and (b) failure in power plant pipe due to creep[28]. 30

Figure 2.2 Typical creep curve with three stages marked as (I) primary creep, (II) secondary creep, and (III) tertiary creep. Curve A: constant–load test and Curve B: constant–stress test[29]. 30

Figure 2.3 Schematic representation of strain rate as a function of total strain [29]. 31

Figure 2.4 Andrade's analysis of the competing processes determines the creep curve [29].....32

Figure 2.5 Creep curves of (a) Ni-base super alloy DS CM 247 at constant temperature [43] and (b) 9Cr-1.5Mo-1Co-VNbBN steel at constant stress [44]. 33

Figure 2.6 Plot showing activation energy for creep of polycrystalline (a) Copper and (b) Nickel [64] 35

Figure 2.7 Schematic diagram depicting the process of N-H creep in single grain [21]. 36

Figure 2.8 Deformation mechanism map for (a) pure Aluminium [98] and (b) pure Silver [98].....43

Figure 2.9 Fracture paths showing (a) intergranular failure in superalloy (IN 100) [115] and (b) transgranular failure in IN 718 superalloy turbine disc [116].....44

Figure 2.10 The simplest classification of creep fracture mechanisms [117]. 45

Figure 2.11 (a) Schematic representation of constant stress lines for P_{L-M} and(b)plots of P_{L-M} vs. stress for Zr-4.5Sn- 1Mo alloy [158].....49

Figure 3.1 Photograph of the as-received Zr-2.5Nb Pressure tubes. 54

Figure 3.2(a) Schematic of (a) orientation of the test specimen (TD-Transverse direction and LD- Longitudinal direction) and (b) sample geometry. 56
Figure 3.3 Variations of φ with σ at 400° C in Zr-2.5Nb for a longitudinal sample. (The line of best fit is represented as a dashed line in stage-III hardening.) 58
Figure 3.4 Schematic diagram of creep setup..... 60
Figure 3.5 Schematic of the impedance heater assembly. 61
Figure 3.6 Photo of creep testing apparatus with a pyrometer, load cell, video camera, and inert gas chamber. 62
Figure 3.7 Plots of load vs. elongation required for constant stresses with straight line fit for (a) Longitudinal and (b) Transverse creep tests. 63
Figure 3.8 (a) S-type load cell and (b) plot of load on UTM vs. load on the load cell indicator for a 200kg load cell. 64
Figure 3.9 Plot of sample extension using image analysis vs. extensometer reading..... 65
Figure 3.10 Schematic of the specimen attachment. 66
Figure 3.11 Photographs of (a) impedance heating system and (b)non-contact IR pyrometer. 66
Figure 3.12 Schematic of the ANN architecture. 71
Figure 3.13 A typical creep curve demonstrating the various material parameters used for explaining creep behavior[194]. 76
Figure 4.1 (a) SEM micrographs (HDBSD mode) and (b) XRD plot of the Zr-2.5Nb alloy in as-received condition. 78
Figure 4.2 (a) TEM micrograph of the as-received sample, (b) corresponding SAED pattern, and (c) EDS spectrum of the precipitate shown in (a)..... 79
Figure 4.3 Stress-strain plots of the Zr-2.5Nb alloy tested at various temperatures for (a) longitudinal and (b) transverse specimens. The

inset shows the stress-strain graphs obtained from tests done at 700 and 800°C.....80
Figure 4.4 Variation of UTS, YS, and % elongation for (a,b,c) longitudinal and (d,e,f) transverse specimens. 81
Figure 4.5 Variation of Young's modulus(E) and strain hardening exponent(n) with temperature for (a,b)longitudinal specimens and (c,d) transverse specimens.....82
Figure 4.6 Plot of σ vs. ε for (a)longitudinal and (b) transverse samples.....86
Figure 4.7 Plot of φ vs. σ for (a) longitudinal and (b) transverse samples...86
Figure 4.8 Variation of (a) $\varphi_{o,\,K\text{-}M}/E$, (b) $\sigma_{s,\,K\text{-}M}/E$, (c) $n_{v,\,K\text{-}M}$, (d) σ_Y/E, (e) $(\sigma_{s,\,K\text{-}M} - \sigma_Y)/E$ with respect to temperature for Zr-2.5Nb for the longitudinal and transverse samples. 88
Figure 4.9 (a) Bright-field TEM micrographs of sample tensile tested at 800°C, (b) Magnified image of inset A showing the presence of grain boundaries and Niobium precipitates. (c) Point EDS of the precipitate.....89
Figure 4.10 EDS mapping of inset B of Fig 4.9 (a) shows Niobium, Zirconium, Chromium, and Iron distribution at grain boundaries. 90
Figure 4.11 Fractographs of samples tensile tested at (a&b)- 200°C, (c&d)- 600°C. a, c are of longitudinal specimens, and b,d of transverse specimens. 92
Figure 4.12 (a) Strain rate curves for Zr-2.5Nb alloy deformed at various temperatures and strain rates, (b)plot showing the variation of peak stress vs strain rate at various temperatures. L and T denote longitudinal and transverse specimens, respectively.....93
Figure 4.13 Plots of peak stress vs. 1/T for various strain rates. L and T denote longitudinal and transverse specimens, respectively. 94
Figure 4.14 Load vs. displacement plot for creep tests carried out at (a) 650 °C/3 MPa, (b) 750 °C/4 MPa, and 750 °C/5 MPa. 96

Figure 4.15 Load vs. displacement plot for creep tests carried out at (a) 750 °C/22 MPa, (b) 650 °C/38 MPa, and 700 °C/58 MPa. 97
Figure 4.16 Typical creep curves obtained from experiments conducted on longitudinal samples at stresses of 2 MPa for different temperatures... 99
Figure 4.17 Typical creep curves obtained from experiments conducted on longitudinal samples at stresses of 3 MPa at different temperatures... 100
Figure 4.18 Typical creep curves obtained from experiments conducted on longitudinal samples at stresses of 4 MPa at different temperatures... 101
Figure 4.19 Typical creep curves obtained from experiments conducted on longitudinal samples at stresses of 5 MPa at various test temperatures. 102
Figure 4.20 Typical creep curves obtained from experiments conducted on transverse samples at stresses of 22 MPa at different temperatures.... 103
Figure 4.21 Typical creep curves obtained from experiments conducted on transverse samples at stresses of 38 MPa at various test temperatures. 104
Figure 4.22 Typical creep curves obtained from experiments conducted on transverse samples at stresses of 58 MPa at various test temperatures. 105
Figure 4.23 Creep curves at constant (a) stress of 3 MPa and (b) temperature of 750 °C for longitudinal samples 106
Figure 4.24 Creep curves at constant (a) stress of 38 MPa and (b) temperature of 700 °C for transverse samples. 106
Figure 4.25 Plot of creep strain rate (ε) vs. creep strain at stresses (a) 2 MPa, (b) 3 MPa, (c) 4 MPa and (d) 5 MPa at different temperatures for longitudinal samples. 108
Figure 4.26 Plot of creep strain rate (ε) vs. creep strain at stresses (a) 22 MPa, (b) 38 MPa, and (c) 58 MPa at different temperatures for transverse samples. 109

Figure 4.27 Typical creep curve showing different terms[194]. 110
Figure 4.28 Plot of minimum creep rate vs. (a) stress and (b) temperature for the longitudinal creep tests.....111
Figure 4.29 Plot of (a) rupture strain(ε_f) and secondary creep strain (ε_2) and (b) relative creep strains of the three creep regions vs. minimum creep rate determined from longitudinal creep tests of the Zr-2.5Nb alloy. .111
Figure 4.30 Plot of (a) rupture strain(ε_f) and secondary creep strain (ε_2) and (b) relative secondary creep strain ($\varepsilon_2 / \varepsilon_f$) vs. stress at temperatures of 650°C and 750 ˚C for longitudinal creep tests.....112
Figure 4.31 Plot of (a) rupture strain(ε_f) and secondary creep strain (ε_2) and (b) relative secondary creep strain ($\varepsilon_2 / \varepsilon_f$) vs. temperature at stresses of 3 MPa and 4 MPa for longitudinal creep tests.....112
Figure 4.32 Plot of (a) ln(σ) vs. ln (t_r), (b) t_r vs. temperature for the longitudinal creep tests.....113
Figure 4.33 Plot of minimum creep rate(ε_s) vs. (a) stress and (b) temperature for the transverse creep tests. 114
Figure 4.34 Plot of (a) rupture strain(ε_f) and secondary creep strain (ε_2) and (b) relative creep strains of the three creep regions vs. minimum creep rate for the transverse creep tests of the alloy.....115
Figure 4.35 Plot of (a) rupture strain(ε_f) and secondary creep strain (ε_2) and (b) relative secondary creep strain ($\varepsilon_2 / \varepsilon_f$) vs. stress at temperatures of 700°C and 850 ˚C for the transverse creep tests. 115
Figure 4.36 Plot of (a) rupture strain(ε_f) and secondary strain (ε_2) and (b) relative secondary creep strain ($\varepsilon_2 / \varepsilon_f$) vs. temperature at stresses of 22 MPa and 58 MPa for transverse creep tests. 116
Figure 4.37 Plot of (a) ln(σ) vs. ln (t_r), (b) t_r vs. temperature for the transverse creep tests.....116
Figure 4.38 Plot of (a) log (ε_s) vs. log ($\boldsymbol{\sigma}$) and (b) n_c vs. T for longitudinal sample. 118

Figure 4.39 Plot of (a) log (ε_s) vs. 1/T and (b) Q_{app} vs. σ for longitudinal samples.....119
Figure 4.40 Variation of experimentally obtained ε_s and calculated ε_s using Eq. 4.9 with (a) 1/T and (b) σ for longitudinal creep tests.....120
Figure 4.41 Plot of (a) log (ε_s) vs. log ($\boldsymbol{\sigma}$) and (b) n_c vs. T for transverse samples.....121
Figure 4.42 Plot of (a) log (ε_s) vs. 1/T and (b) Q_{app} vs. σ for transverse samples.....122
Figure 4.43 Variation of experimental **εs** and calculated ε_s using Eq. 4.14 with (a) 1/T and (b) σ for transverse creep tests. 123
Figure 4.44 Plot of (a) rupture time vs. ε_s and (b) t_r / ε_f vs. ε_s for the longitudinal creep tests. 124
Figure 4.45 Plot of (a) t_{os}/ε_1 vs. ε_s and (b) t_t/ε_3 vs. ε_s for longitudinal creep tests.....125
Figure 4.46 Plot of (a) rupture time vs. ε_s and (b) t_r / ε_f vs. ε_s for transverse creep tests.....127
Figure 4.47 Plot of (a) t_{os}/ε_1 vs. ε_s and (b) t_t/ε_3 vs. ε_s for transverse creep tests.....127
Figure 4.48 Comparison between rupture time calculated using MMG equation and obtained experimentally for (a) longitudinal and (b) transverse creep tests.....128
Figure 4.49 Plot of average creep rate vs. minimum strain rate for (a) longitudinal and (b) transverse creep tests.....129
Figure 4.50 Plot of t_{MGD} vs. t_r for (a) longitudinal and (b) transverse creep tests.....130
Figure 4.51 Comparison of MLR predicted curve and experimental curve. Symbols indicate the experimental curves, whereas the solid lines represent the MLR simulated curves. 132
Figure 4.52 Correlation between neural network predicted and

experimentally obtained creep strain from longitudinal creep tests after (a) training and (b) testing.....134
Figure 4.53 Correlation between neural network predicted and experimental creep strain after (a) training and (b) testing for transverse creep.....134
Figure 4.54 Relative error between neural network predicted and experimentally obtained creep strain from longitudinal creep tests after (a) training and (b) testing.....135
Figure 4.55 Relative error between neural network predicted and experimental creep strain after (a) training and (b) testing for transverse creep. 136
Figure 4.56 The graph between residuals and neural network estimated creep strain after (a) training and (b) testing in case of longitudinal creep test.....137
Figure 4.57 The graph between residuals and neural network estimated creep strain after (a) training and (b) testing for transverse creep tests.....137
Figure 4.58 Plots of (a) ANN predicted strain vs. experimental strain, (b) frequency counts vs. relative error, and (c) residuals versus predicted strain values obtained during the validation phase for longitudinal creep curves. 138
Figure 4.59 Comparison of creep curves obtained from ANN simulation and longitudinal creep experiments. Symbols denote experimental curves; solid lines indicate the simulated curves.....139
Figure 4.60 Plots of (a) ANN predicted strain vs. experimental strain, (b) frequency counts vs. relative error, and (c) residuals versus predicted strain values obtained during the validation of transverse creep.....140
Figure 4.61 Comparison of creep curves obtained from ANN simulation and transverse creep experiments. Symbols denote experimental curves; solid lines indicate the simulated curves.....141

Figure 4.62 The relative importance of the three input parameters on the prediction of creep strain for (a) longitudinal and (b) transverse creep tests.....142
Figure 4.63 Comparison of graphs obtained from MLR and ANN model with that obtained from (a) longitudinal and (b) transverse creep tests. Symbols denote experimental curves. 143
Figure 4.64 Plot showing the comparison of experimentally obtained, calculated using power law(Eq. 4.9) and ANN predicted ε_s with (a) $1/T$ for constant stresses and (b) σ for constant T for the longitudinal creep tests.....145
Figure 4.65 Plot showing the comparison of experimentally obtained, calculated using power law(Eq. 4.14) and ANN predicted $\varepsilon_s$with (a) $1/T$ for constant stresses and (b) σ for constant T for the transverse creep tests.....146
Figure 4.66 Plot of (a) $\log_{10}(t_r)$ vs. 1000/T, (b) $\log_{10}(t_r)$ vs. 1000/T with extrapolated curves up to 1000/T = 0, and (b) $C_{L\text{-}M}$ vs. applied stress (σ) calculated from the longitudinal creep tests. 149
Figure 4.67 Plot of (a) σ vs. $P_{L\text{-}M}$ and (b) σ vs. average $P_{L\text{-}M}$ calculated from the longitudinal creep tests. 150
Figure 4.68 Creep life prediction using (a) $C_{L\text{-}M}$ =20 and (b) $C_{L\text{-}M}$ =$C_{L\text{-}M}$ (σ) at different stresses.....151
Figure 4.69 Creep life prediction using(a) $C_{L\text{-}M}$ =20 and (b) $C_{L\text{-}M}$ =$C_{L\text{-}M}$ (σ) at different temperatures. 151
Figure 4.70 Plot of comparison of creep life prediction by using $C_{L\text{-}M}$ =20 and $C_{L\text{-}M}$ =$C_{L\text{-}M}$ (σ) at (a) different stresses and (b) temperatures for longitudinal creep tests. 152
Figure 4.71 Plot of (a) $\log_{10}(t_r)$ vs. 1000/T, (b) $\log_{10}(t_r)$ vs. 1000/T with extrapolated curves up to 1000/T = 0 and (b) $C_{L\text{-}M}$ vs. applied stress (σ)

calculated from transverse creep tests.....153
Figure 4.72 Plot of (a) σ vs. $P_{L\text{-}M}$ and (b) σ vs. average $P_{L\text{-}M}$ calculated from the transverse creep tests.....154
Figure 4.73 Creep life prediction using(a) $C_{L\text{-}M}$ =20 and (b) $C_{L\text{-}M}$ =$C_{L\text{-}M}$ (σ) at different stresses.....155
Figure 4.74 Creep life prediction using(a) $C_{L\text{-}M}$ =20 and (b) $C_{L\text{-}M}$ =$C_{L\text{-}M}$ (σ) at different temperatures. 156
Figure 4.75 Plot of comparison of creep life prediction by using $C_{L\text{-}M}$ =20 and $C_{L\text{-}M}$ =$C_{L\text{-}M}$ (σ) at (a) different stresses and (b) temperatures for transverse creep tests.....157

LIST OF TABLES

Table 2.1 Nominal composition of Zirconium based alloys in weight %[21].....28
Table 2.2 Equations of primary, secondary, and tertiary creep regions put forward by various researchers.....32
Table 3.1 Experimental matrix for creep-rupture test for longitudinal specimens ("✓" indicates the experiments carried out).....67
Table 3.2 Experimental matrix for creep-rupture test for transverse specimens ("✓" indicates the experiments carried out).....67
Table 3.3 ANN architecture for the longitudinal creep tests.....73
Table 3.4 ANN architecture for the transverse creep tests.....73
Table 4.1 Empirical relations of variation of tensile properties with temperature for longitudinal specimens.....84
Table 4.2 Empirical relations of variation of tensile properties with temperature for transverse specimens.....85
Table 4.3 Maximum percentage deviation and RMS error for various true stresses and temperatures for longitudinal creep tests.....97
Table 4.4 Maximum percentage deviation and RMS error for various true stresses and temperatures for transverse creep tests.....98
Table 4.5 Creep constitutive parameters of Eq. 4.4, 4.5, and 4.6 and corresponding R^2- values.....119
Table 4.6 Creep constitutive parameters of Eq. 4.4, 4.5 and 4.6 and corresponding R^2- values.....122
Table 4.7 Values of R^2, MRE, and RMSE of the MLR predicted curve with respect to the experimental curves obtained from longitudinal and transverse creep tests.....132
Table 4.8 Values of R^2, MRE, and RMSE of the ANN predicted curve with

respect to the experimental curves obtained from longitudinal creep tests.....139
Table 4.9 Values of R^2, MRE, and RMSE of the ANN predicted curve with respect to the experimental curves obtained from transverse creep tests.....141
Table 4.10 Comparison of ANN and MLR model. 144
Table 4.11 Comparison of the minimum strain rate obtained experimentally, calculated using Eq. 4.9 and predicted by ANN technique for the longitudinal creep tests.....145
Table 4.12 Comparison of the minimum strain rate obtained experimentally, calculated using Eq. 4.14 and predicted by ANN technique for the transverse creep tests.....146
Table 4.13 $P_{L\text{-}M}$ and $C_{L\text{-}M}$ values at different stresses. 150
Table 4.14 Creep life of the Zr-2.5Nb alloy along the longitudinal axis for different stress and temperature combinations. 152
Table 4.15 $P_{L\text{-}M}$ and $C_{L\text{-}M}$ values at different stresses. 154
Table 4.16 Creep life of the Zr-2.5Nb alloy along the transverse axis for different stress and temperature combinations. 157

Chapter 1 Introduction

Demand for higher energy generation has been rising continuously during the last several decades over the globe as a consequence of factors like population growth, industrialization, and increased technological use. At present, the maximum amount of energy generation is met by burning fossil fuels. However, in recent times, policymakers worldwide have been concerned about the use of fossil fuel for energy generation due to factors like fossil fuel depletion and environmental impact, such as toxic emissions affecting the life of human beings and animals. In this respect, alternate energy sources are a viable alternative to meet the global energy crisis while simultaneously addressing the issues of a sustainable energy future. Nuclear power continues to be a significant energy source in several countries while emitting no greenhouse gases. Nuclear power plants (NPP) generate electricity by harnessing the energy released by nuclear reactions. Thermal reactors are one of the essential constituents of NPPs for power generation. The majority of the reactors used are either pressurized water reactors (PWRs) or pressurized heavy water reactors (PHWRs)[1]. Pressure tubes (PT) are an essential component of PHWRs, as they house the fuel bundles and provide structural stability.

Zr–Sn-based alloys, also called Zircaloys, were commonly used as pressure tube materials for older-generation PHWRs[2, 3]. For decades, Zircaloy-2 and Zircaloy-4 were utilized in light water reactors. Subsequently, Zirconium alloys with 2.5%wt Niobium (Zr-2.5Nb) were developed because they exhibited more excellent structural stability and lower hydrogen embrittlement in the reactor working conditions compared to Zircaloy-2 and Zircaloy-4[2–5]. Zr-2.5Nb alloys are now extensively used as PT materials because of their low neutron absorption cross-section, enhanced corrosion resistance, good mechanical strength, and less irradiation creep [6–9]. The processing steps of Zr–2.5Nb alloy PTs of Indian PHWRs followed at Nuclear Fuel Complex (NFC) Hyderabad, India, is in the order of 1) extrusion at 850°C; 2) pilgering in which 50-55% reduction takes place; 3) annealing at 550°C; 4)pilgering for achieving 20-25% reduction and finally 5) autoclaving at 400°C for stress relief[8]. The above fabrication process of cold-worked and stress-relieved Zr-2.5Nb PTs forms a dual-phase microstructure of highly textured and elongated α-grains along the tube axis bordered by thin, almost continuous β-phase along the grain boundaries[6].

During service, Zr-2.5Nb pressure tubes operate at temperatures between 290 °C and 350 °C and with variable coolant pressures of up to 11 MPa, corresponding to hoop stresses of up to 130 MPa[10]. In the scenario of a postulated design accident such as a loss-of-coolant accident (LOCA), the temperature of operation of the PTs could shoot up very rapidly to a temperature above 800 °C, which may be due to the inability of the primary coolant to remove the heat from the core [7]. Under such adverse conditions, the pressure tube will either elongate, sag, or balloon. This may lead to the pressure tubes coming into contact with the concentric calandria tube. Any failure of the PTs will eventually result in the release of radioactive radiation, severely impacting the environment. The PTs may fail due to creep in both the longitudinal (longitudinal creep) and diametral (transverse creep) directions[6]. Thus, a thorough understanding and prediction of the creep life of PTs along both the longitudinal and transverse directions are necessary for the proper functioning of reactors.

Conducting creep tests to determine its creep life is time-consuming. Therefore the procedure followed by practicing engineers is to perform accelerated creep tests and use the data from these tests to predict the creep life. Constitutive models have been developed to calculate the minimum creep rate as a function of stress, temperature, and time, which can be used for predicting the creep life of components [11]. In this method, the minimum creep rate is calculated using constitutive parameters, and the material's creep life is determined by the duration it takes to achieve a specific creep strain. However, the creep life prediction by constitutive modeling gives inaccurate results, especially when the process parameter regime is extensive. According to Monkman-Grant relationships, the prediction of rupture life is made on the basis of experimental values of creep rupture time and minimum creep rate. Several parametric approaches have also been proposed for predicting the long-term creep life of engineering components and are being used by industries[12–17]. Though each technique has its own advantages and disadvantages, the Larson-Miller parameter (LMP) technique is extensively used by industries.

In LMP technique, the creep life of a material is determined from σ vs. $P_{L\text{-}M}$ master curve. In this technique, the Larson-Miller constant $C_{L\text{-}M}$ in the equation of $P_{L\text{-}M}$ is considered to be a constant. A critical analysis revealed that $C_{L\text{-}M}$ is not a constant but is rather dependent on the applied stress. By using the $C_{L\text{-}M}$ value as a function of stress, the scatter in the master curve could be minimized substantially, thereby enabling the prediction of the creep life.

Creep curve of a material provides essential information regarding its structural integrity and effective life span, especially when exposed to elevated temperatures and stresses. As a result, predicting the creep curve of the material over a wide range of temperatures and stresses is essential. The data-driven modeling techniques such as artificial neural network (ANN) and multiple linear regression (MLR) approaches have gained importance due to their high accuracy and ease of modeling. In addition, ANN has the advantage of generating large amounts of data from limited short-time experimental data, which can be effectively used for the prediction of creep life by extrapolation techniques. ANN modeling was successful in predicting the creep curve of reformer tubes which exist as a single-phase austenitic structured alloy from room temperature to its melting point [18]. So far, the applicability of ANN for two-phase alloys, where the relative volume fraction of phases changes with temperature, has not been attempted. Zr-2.5Nb alloy exhibits a dual-phase microstructure. In the current study, an attempt has been made to predict the creep curves of Zr-2.5Nb alloy using the ANN and MLR techniques.

The present work was taken up with the main objective of investigating the creep behavior of Zr-2.5Nb dual-phase alloy by conducting accelerated creep tests at various temperatures and stresses on samples extracted from the longitudinal and transverse directions of the Zr-2.5Nb tube; use the obtained data to develop creep deformation models by constitutive equations; estimate the rupture life of the material by Monkman-Grant relationships; predict the creep life by Larson-Miller parametric technique and evaluate the efficacy in the prediction of creep curve of dual phase alloy by ANN and MLR modeling.

The present thesis is organized into five chapters:

- Chapter-1 introduces the significance of creep deformation in pressure tubes and highlights the objective and organization of the thesis work.
- Chapter-2 summarizes the literature available related to pressure tubes and creep deformation. The various creep deformation models for determining the creep life of materials have also been discussed. Finally, the technical gaps that need to be addressed in this area are highlighted. The chapter concludes by presenting the key objectives of the present work.
- Chapter-3 describes the methodology adopted for achieving the objectives of the work. These include the design, development & calibration of the creep testing setup,

the detailed experimental procedures, material characterization techniques, constitutive modeling, L-M parameter, and the ANN and MLR techniques used for predicting the creep curves using the data obtained from the limited experiments.

- Chapter-4 presents and discusses the results of the investigation carried out. In this chapter, the tensile properties of the material at various temperatures have been presented and correlated to the microstructure and fracture behavior. Empirical relationships were developed correlating the mechanical properties with temperature. The creep constitutive relations developed are presented. The creep life of the material is presented based on Larson-Miller parameter. The results of the data-driven models for predicting the creep curves are presented and discussed in detail.
- Chapter-5 presents the conclusions and scope for future work, followed by references and appendices.

Chapter 2 Literature Review

2.1 Introduction

Zirconium alloys have a long history of being used in pressurized heavy water reactors (PHWRs) as structural components such as fuel claddings and pressure tubes (PTs). This is because of their desirable qualities: low thermal neutron absorption cross sections, capacity to function in corrosive environments, good strength at high temperatures, and reduced irradiation creep[7, 19, 20]. Within the PHWR core, these materials are subjected to extreme circumstances such as high pressures, temperatures, and fast neutron fluxes. The reactor generally operates in the temperature region of 290 °C – 350 °C. In the scenario of a postulated loss-of-coolant accident (LOCA), the PTs' operation temperature could shoot up very rapidly to a temperature above 800 °C [7]. Under such unfavorable conditions, the pressure tubes may fail due to creep deformation.

2.2 Zirconium alloys in Pressure Tubes

Zirconium was not the material of choice for fuel claddings until Oak Ridge researchers discovered the presence of naturally occurring Hafnium (approximately 2.5%) in Zirconium, which has a high absorption coefficient for thermal neutrons. Low absorption characteristics for thermal neutrons for greater neutron economy rank highly among the attributes necessary for nuclear structural materials. When Zirconium was refined by removing Hafnium, its neutron absorption properties improved and made it ideal for nuclear uses [21].

Initially, researchers focused on developing Zirconium as pure as possible to increase the neutron economy until it was discovered that corrosion resistance degraded due to nitrogen in the absence of other metal impurities. As a result, Zircaloy-1 was developed with 2.5% tin as the main alloying element, which was mainly to balance out the effects of Nitrogen. Zircaloy-1, however, corroded at a constant rate rather than the preferred decreasing corrosion rate over time in high-temperature and long autoclave tests [21]. This was followed by the development of Zircaloy-2, which had 1.5% Tin, 0.15% Iron, 0.05% Nickel, 0.10% Chromium, and balance Zr, significantly improving the corrosion resistance while maintaining the tensile strength comparable to Zircaloy-1. The percentage of tin was reduced to 0.25% with a concurrent increase in the iron content to 0.25% in Zircaloy-3, which

reportedly has the highest corrosion resistance of all Zircaloys[21]. This was done because it was discovered that the presence of tin had a negative impact on the long-term corrosion resistance of Zircaloys in pressurized water reactors (PWR) conditions. However, the mechanical strength of Zirclaoy-3 was discovered to be insufficient, leading to its discontinuation as a cladding material [21].

Later studies showed that Hydrogen absorption, which was shown to be aided by Nickel, considerably decreased the fracture resistance of Zircaloys. In order to make up for the decrease in corrosion resistance caused by the removal of Nickel, Nickel-free Zircaloy-2 was made with a higher proportion of iron (0.24%) and given the name Zircaloy-4. Zircaloy-4 is primarily employed as cladding, spacer grids, and intermediate flow mixers in pressurized heavy water reactors (PWRs), channels in boiling water reactors (BWRs), and calandria tubes in PWRs (PHWR)[22].

Niobium has been discovered to be effective in the development of zirconium alloys for improving long-term corrosion resistance and mechanical qualities without significantly reducing the neutron absorption characteristics., This is attributed to the distribution of β-Nb precipitates in the microstructure[23, 24]. Zr-2.5Nb alloys were subsequently created. In comparison to Zircaloy-2 and Zircaloy-4, they demonstrated more excellent structural stability and less hydrogen embrittlement [2–5]. Zr-2.5Nb alloys are widely utilized as PT materials due to their good creep properties, increased corrosion resistance, and reduced neutron absorption cross-section [6–9]. The composition of the various zirconium alloys developed is shown in Table 2.1.

Table 2.1 Nominal composition of Zirconium based alloys in weight %[21]

Alloy	Sn	Nb	Fe	Cr	Others
Zircaloy-1	2.5	----	----	----	----
Zircaloy-2	1.5	----	0.12	0.10	Ni-0.05
Zircaloy-3	0.25	----	0.25	----	----
Zircaloy-4	1.5	----	0.21	0.10	----
Zirlo	1.5	1.0	0.21	0.10	----

2.3 Creep deformation

Creep is referred to as the time-dependent plastic deformation of materials under constant temperature and stress conditions. An experimentally generated creep curve at any

combination of stress and temperature can reveal the creep deformation of the particular material. A creep curve gives the time-dependent dimensional changes for the material till failure. Dislocation motion and diffusion of vacancies or atoms are two possible fundamental causes of creep. Since vacancies diffuse much more quickly at high temperatures, creep typically gets more pronounced. Some materials, however, can creep even at ambient temperature or sub-zero temperatures [21].

Although creep as a deformation phenomenon was recognized several centuries ago, it wasn't until the industrial revolution in the 20th century that it started to have technological significance. Heat-resistant materials with a long lifespan were needed to make the high-temperature operating components for steam engines, generators, and jet engine blades. Creep has been identified as one of the causes of mechanical property degradation of the components during reactor operation in the energy sector, particularly in nuclear power plants [25]. Pressure tubes (PT) in Pressurized Heavy Water Reactors (PHWR) house fuel bundles. As highlighted before, Zr-2.5Nb alloys are generally used as pressure tubes due to their ability to work in a corrosive environment, low neutron absorption cross-section, good mechanical strength, and less irradiation creep [7, 19]. These materials are subjected to harsh environments within the PHWR core, including high pressures and temperatures and fast neutron fluxes. In the scenario of a postulated loss-of-coolant accident (LOCA), the PTs' operation temperature could shoot up very rapidly to a temperature above 800 °C, which may be due to the inability of the primary coolant to remove the heat from the core [7]. Under such conditions, there will be axial elongation, sagging, and ballooning of the pressure tube, which in turn might come in contact with the concentric calendria tube. These adverse conditions might lead to failure by creep along the longitudinal direction (longitudinal creep) as well as in the diametral direction (transverse creep) of the pressure tubes [26]. Any form of failure of the PTs in these circumstances will eventually lead to the discharge of radioactive radiation causing adverse effects in the environment, which would be disastrous. Effective understanding and prediction of the creep life of PTs is a prerequisite for the proper functioning of reactors. Figure 2.1(a) and (b) show the failure of a tube and pipe due to creep deformation.

(a) (b)

Figure 2.1 Photographs of (a) original and ballooned pressure tube[27] and (b) failure in power plant pipe due to creep[28].

The creep curve, independent of the application, is a plot of creep strain vs. time at constant stress (or load) and temperature. Figure 2.2 shows a standard creep curve.

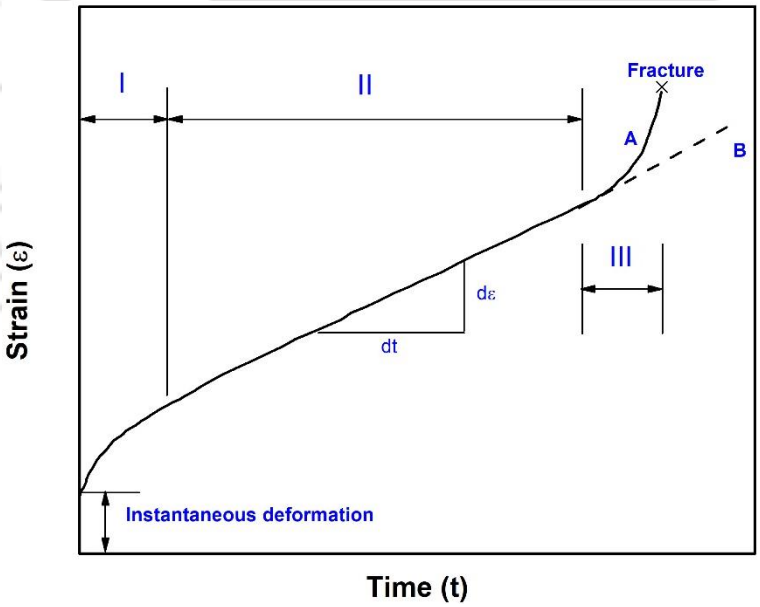

Figure 2.2 Typical creep curve with three stages marked as (I) primary creep, (II) secondary creep, and (III) tertiary creep. Curve A: constant–load test and Curve B: constant–stress test[29].

The instantaneous strain is purely elastic and can be obtained by $\varepsilon = \sigma/E$, where E is the Young's modulus, σ is the applied stress and ε is the elastic strain. The creep curve shown in Figure 2.2 has three regions which are discussed below:

1. Primary creep- During this stage, the strain increases continuously. This is also referred to as the primary creep, during which the creep resistance of the material rises with time but at a decreasing rate.
2. Secondary creep – In this region, the strain increases linearly with time and is a region of constant strain rate. This area, also known as the steady state creep region, balances the opposing processes of strain hardening and recovery.
3. Tertiary creep- Here, the strain increases exponentially with time, leading to final failure. Tertiary creep is characterized by a large reduction in the cross-sectional area due to the formation of voids or necking. The time taken to failure is often referred to as the time to rupture or rupture life (t_r).

Variation of creep rate with the total strain for the three creep regions is shown in Figure 2.3.

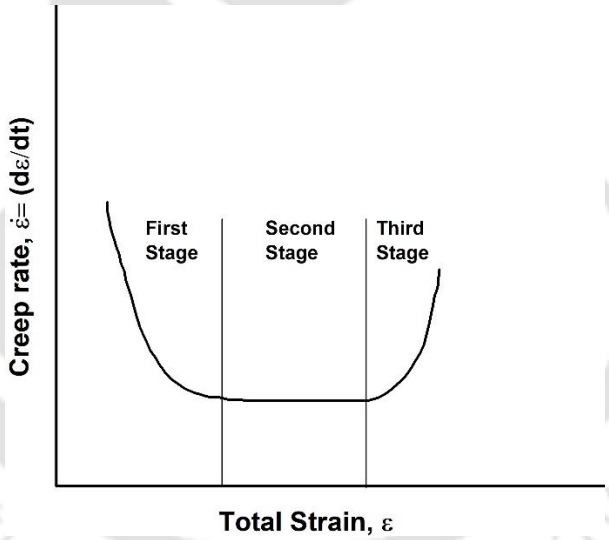

Figure 2.3 Schematic representation of strain rate as a function of total strain [29].

2.4 Creep curve models

Previous researchers have attempted to explain the behavior of the creep curve. Most people agree with Andrade's creep model. As shown in Figure 2.4, it is based on the superposition of a transient creep and a viscous creep after the initial sudden strain. The viscous creep increases over time while the rate of transient creep gradually diminishes.

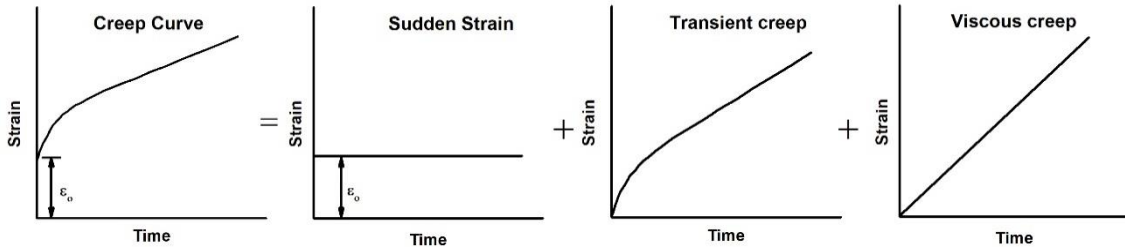

Figure 2.4 Andrade's analysis of the competing processes determines the creep curve [29]

The creep curve could be expressed by an empirical relation [29]

$$\varepsilon = \varepsilon_0 \left(1 + \beta t^{\frac{1}{3}}\right) e^{(\kappa t)} \tag{2.1}$$

where t is the time taken to reach strain ε. β and κ are constants. ε_o is the sudden strain achieved when the external load is applied. Table 2.2 gives the different mathematical equations given by investigators for the different creep regimes.

Table 2.2 Equations of primary, secondary, and tertiary creep regions put forward by various researchers

Equation	Reference
Primary creep	
Logarithmic: $\varepsilon_p = A_1 \log(1 + bt)$	[30]
Exponential: $\varepsilon_p = A_2(1 - \exp(-ct))$	[31]
Sinh law: $\varepsilon_p = A_3 \sinh\left(ct^{\frac{1}{3}}\right)$	[32]
Secondary creep	
Power law: $\dot{\varepsilon}_s = A_4 \sigma^n$	[33]
Sinh law: $\dot{\varepsilon}_s = \dot{\varepsilon}_o \sinh\left(\frac{\sigma}{\sigma_o}\right)$	[34] ,[35]
Tertiary creep	
Exponential: $\varepsilon_t = A_5 \left[\exp(-mt) - 1\right]$	[36] [37]
$\dot{\varepsilon}_t = \frac{a\sigma^n}{(1-\omega)^q}$, where $\dot{\omega} = \frac{c\sigma^k}{(1-\omega)^r}$	
Omega: $\dot{\varepsilon}_t = \dot{\varepsilon}_o \exp(\Omega\varepsilon)$	[38]

Stress and temperature significantly influence the nature of the creep curve[39–42]. Figure 2.5(a) and (b) show the creep curves under constant temperature and loads, respectively. These figures show that the secondary creep region is almost negligible at combinations of high stresses and temperatures. The creep rate accelerates almost immediately after the creep test begins. The primary and secondary creep regions are more evident at intermediate loads and temperatures. At low stress and temperature, the creep curves display a distinct secondary creep stage having a slow creep rate.

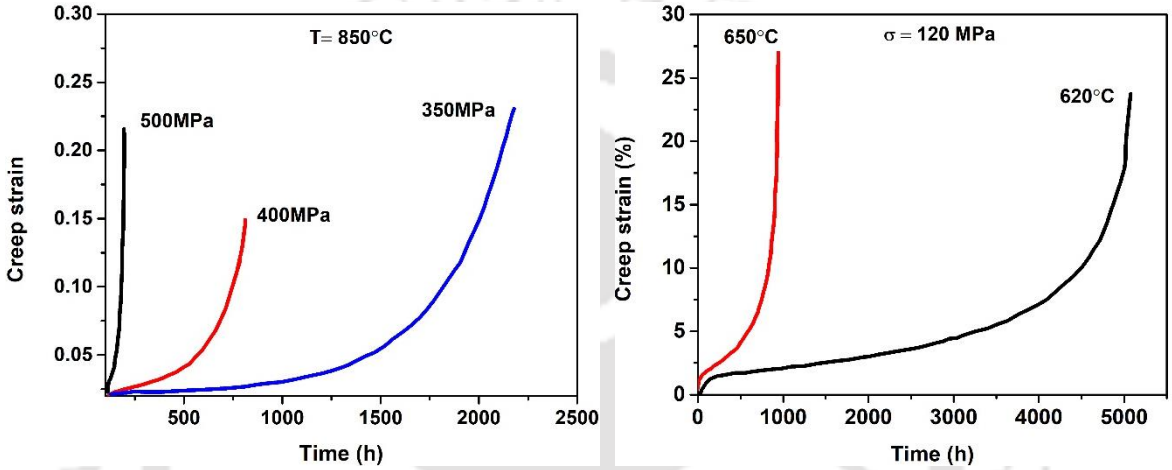

(a) (b)

Figure 2.5 Creep curves of (a) Ni-base super alloy DS CM 247 at constant temperature [43] and (b) 9Cr-1.5Mo-1Co-VNbBN steel at constant stress [44].

2.5 Constitutive equations for steady state creep

A creep curve generally consists of three zones. The effective creep life of the material is determined by the secondary creep region, where the creep rate remains constant. The minimum creep rate, also known as the steady-state creep rate($\dot{\varepsilon}_s$) is experienced in this regime. For all real-life purposes, the design of a material's creep life depends on the time it takes to enter the tertiary creep region or reach the end of the secondary creep zone. This is considered by determining the minimum creep rate and creep strain under operational circumstances.

Based on the physical and metallurgical characteristics of materials, constitutive creep equations are used to calculate the minimum creep rate [41]. Among the different models, the most extensively used are the power law approach[45], the Dorn approach [46], and the Prandtl approach [34]. The power law equation is written as [45],

$$\dot{\varepsilon}_s = A_1 \sigma^{n_c} \exp\left(-\frac{Q_{app}}{RT}\right) \quad (2.2)$$

At a combination of high stresses and temperatures, Dorn [46]derived an equation to calculate the minimum creep rate $\dot{\varepsilon}_s$, which is of the form:

$$\dot{\varepsilon}_s = A_2 \exp(\beta\sigma) \exp\left(-\frac{Q_{app}}{RT}\right) \quad (2.3)$$

Prandtl [34] proposed the hyperbolic sine function for calculating minimum creep rate at high stress, which is given by:

$$\dot{\varepsilon}_s = A_3 [\sinh(\alpha\sigma)] \exp\left(-\frac{Q_{app}}{RT}\right) \quad (2.4)$$

In Eq. 2.2, 2.3, and 2.4, A_1, A_2, A_3, n_c, β and α are material constants, σ is the applied stress, Q_{app} is the apparent activation energy for creep, R is the universal gas constant (= 8.314 J K^{-1} mol^{-1}), and T is the test temperature. n_c is also referred to as the stress exponent. Eq. 2.4 can be re-written as,

$$\dot{\varepsilon}_s = A_3 \left(\frac{e^{\alpha\sigma} - e^{-\alpha\sigma}}{2}\right) \exp\left(-\frac{Q_{app}}{RT}\right) \quad (2.5)$$

The value of $e^{-\alpha\sigma}/e^{\alpha\sigma}$ tends to zero when the value of $\alpha\sigma$ is greater than 1.5, which is generally taken into consideration[47]. Under such case, Eq. 2.5 can be re-written as:

$$\dot{\varepsilon}_s = A_3 \left(\frac{e^{\alpha\sigma}}{2}\right) \exp\left(-\frac{Q_{app}}{RT}\right) \quad (2.6)$$

2.6 Activation energy for creep

Based on studies conducted on a wide variety of materials, it has been seen that the activation energy for creep is nearly identical to the activation energy for self-diffusion Q_c. It has also been seen that Q_c depends on temperature [48, 49, 58, 50–57] and stress [51, 52, 55, 59–62]. The activation energy in the case of polycrystalline Copper and Nickel is illustrated in Figure 2.6. In Zircaloy-2, creep occurs due to dislocation interaction processes in the low-temperature range (range I) [52].In range II, creep occurs by cross–slip, while at a higher temperature range (range III), it occurs by dislocation climb[52]. At lower temperatures, apparent activation energy is comparable to the value for diffusion along grain boundaries. [63].

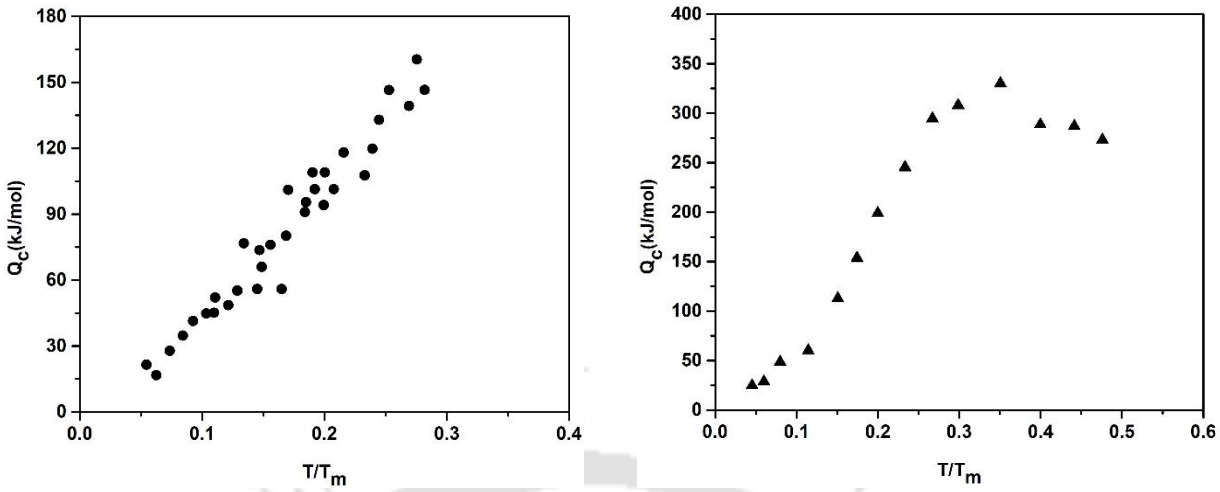

(a) (b)

Figure 2.6 Plot showing activation energy for creep of polycrystalline (a) Copper and (b) Nickel [64]

It has been reported in the literature that an increase in grain size results in an increase in activation energy for creep [65, 66]. The activation energy for lattice diffusion in Zr and Nb for β-Zr is around 212 and 243 kJ/mol, respectively[67]. The activation energy reported for Zr and Nb in α-Zr is 190 and 132 kJ/mol, respectively[68]. In case of Zr and Nb in β-Zr, the activation energy for grain boundary fusion is 127 and 145 kJ/mol, respectively[67].

2.7 Creep deformation mechanisms

Researchers studying the creep deformation of materials have identified a number of potential deformation mechanisms for various combinations of stress, temperature, and microstructure. Some of them are a) Coble creep, b) Nabarro-Herring creep, c) Harper-Dorn creep, d) grain boundary sliding, e) dislocation glide, and f) dislocation climb controlled creep. A general equation representing the steady state creep rate controlled by any of the creep mechanisms can be of the form:

$$\dot{\varepsilon} = A\left(\frac{DEb}{kT}\right)\left(\frac{b}{d}\right)^{p}\left(\frac{\sigma}{E}\right)^{n} \tag{2.7}$$

where $\dot{\varepsilon}$ is the steady state creep rate, D is the diffusion coefficient that characterizes a particular creep mechanism, E the elastic modulus, b the burger's vector, k the Boltzmann constant, T is the temperature, d the grain size, σ the applied shear stress, A the pre-factor, p the inverse grain size exponent and n the stress exponent [21]. The different creep

mechanisms are discussed in the following sections.

2.7.1 Nabarro-Herring creep

This model was proposed by Nabarro and Herring simultaneously[69, 70]. Atoms or vacancies are transported through the lattice as part of the Nabarro-Herring or N-H creep mechanism. The phenomenon of atomic diffusion in N-H creep mechanism can be described by considering a single grain experiencing a tensile load, as shown in Figure 2.7.

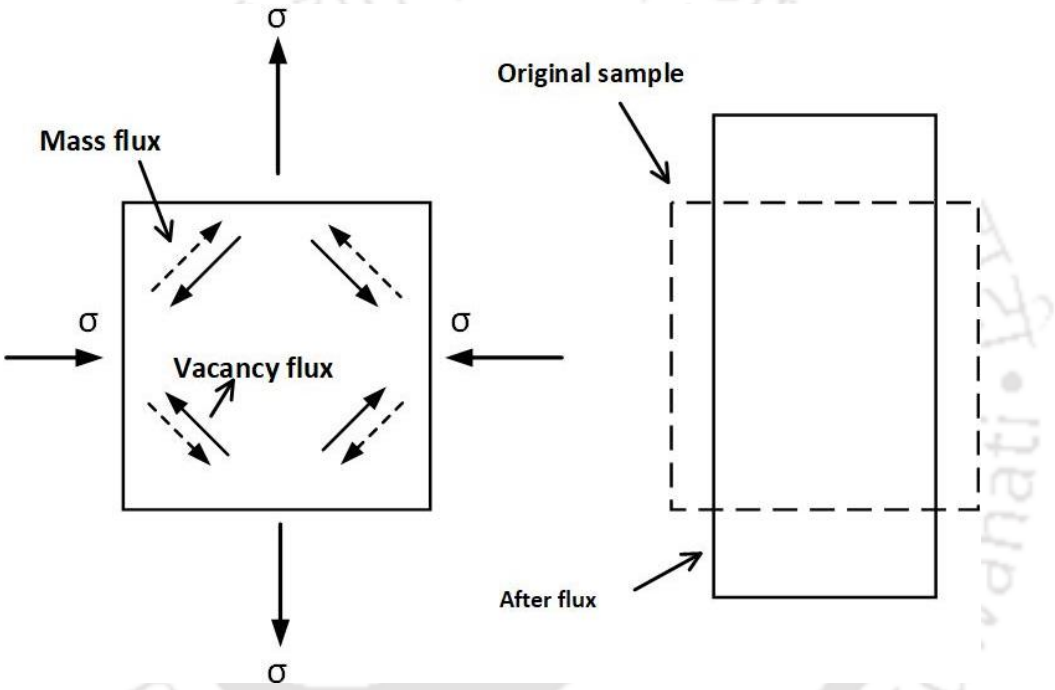

Figure 2.7 Schematic diagram depicting the process of N-H creep in single grain [21].

Here, the grain boundaries perpendicular to the tensile load axis experience tensile stresses, whereas those parallel to the tensile axis is subjected to compressive stress. Thus the activation energies for vacancy formation at the grain boundaries are changed by a value of ± $\sigma\Omega$, where σ is the applied stress, which takes a sign depending on the nature of stress (+ for tension and – for compression) and Ω is the atomic volume. The vacancy concentration (c_v) at the grain boundaries experiencing tensile and compressive stresses can then be written as[71],

$$c_v(tension) = exp\left(-\frac{Q_f}{kT}\right) exp\left(\frac{\sigma\Omega}{kT}\right) \quad (2.8)$$

$$c_v(compression) = exp\left(-\frac{Q_f}{kT}\right) exp\left(-\frac{\sigma\Omega}{kT}\right) \quad (2.9)$$

where Q_f is the vacancy formation energy, R is the universal gas constant, and T is the temperature. The vacancy concentration at tensile boundaries is always higher than that at the compressive boundaries, according to equations 2.8 and 2.9. The compositional gradient created by the difference in vacancy concentration between the tensile and compressive boundaries facilitates vacancies to move via the lattice diffusion, causing expansion along the tensile axis and contraction along the compressive axis. Based on this, Nabarro and Herring derived the equation for creep (N-H creep) as the dominant mechanism, which can be written as [69],

$$\dot{\varepsilon_{NH}} = 12\left(\frac{D_l Eb}{kT}\right)\left(\frac{b}{d}\right)^2\left(\frac{\sigma}{E}\right)^1 \quad (2.10)$$

where D_l is lattice diffusivity. According to the constitutive equation for N-H creep, the creep rate increases linearly with the applied stress leading to a stress exponent of 1. Hence this deformation is of Newtonian viscous flow. Additionally, the activation energy for N-H creep is identical to that for lattice self-diffusion because the deformation is governed by the diffusion of atoms or vacancies across the lattice. Since deformation mostly takes place around grain boundaries, there is negligible strain in the centers of the grains[72].

2.7.2 Coble creep

Coble modified the N-H creep theory to include the diffusion of vacancies or atoms through grain boundaries; therefore, they are closely related mechanisms[73]. The equation for Coble creep is derived by following a similar methodology as in N-H creep, which is given as,

$$\dot{\varepsilon_C} = A_c\left(\frac{D_g Eb}{kT}\right)\left(\frac{b}{d}\right)^3\left(\frac{\sigma}{E}\right)^1 \quad (2.11)$$

where D_g is grain boundary diffusivity. The value of A_c was determined to be 148 by Coble, which was later modified to ~50 by Dorn[74]. As seen from equation 2.11, Coble creep exhibits a stress exponent of 1 similar to that of N-H creep. Coble creep, however, has a similar activation energy to self-diffusion via grain boundaries. As a result, Coble creep takes on greater significance than N-H creep at lower temperatures. It has an inverse linear

relationship to the third power of grain size, showing that Coble creep is more sensitive to changes in the grain size of materials. By testing materials with various grain sizes under comparable test settings, this property can be used to differentiate Coble creep from N-H creep. When compared to N-H creep, Coble creep becomes more prevalent in materials with smaller grains.

2.7.3 Harper-Dorn creep

Harper and Dorn[72] reported that polycrystalline aluminum deformed similarly to the Newtonian viscous flow at high temperatures ($T = 0.99T_m$) and low stresses with the activation energy near to that of lattice diffusion. However, they determined that the experimental creep rates are three orders higher than the N-H creep predictions, indicating the presence of some other additional mechanism operating at the test conditions. Further, they observed distinct primary creep and recovery after stress drop, neither of which are the characteristics of N-H creep. Also, the creep rates measured in single-crystal Aluminum matched those obtained in polycrystalline Aluminum, confirming a mechanism other than N-H or Coble creep responsible for the deformation. The authors concluded that the creep could have resulted from the dislocation motion. H-D creep has been reported later in several materials [75–77]. Yavari et al. examined Al-5%Mg specimens deformed under H-D creep conditions by etch-pits and TEM and determined most of the dislocations had edge character[78, 79]. With a stress exponent of 1, H-D creep is comparable to diffusional creep mechanisms. In contrast to N-H creep and Coble creep, where the creep rate has an inverse linear connection with the grain size with powers 2 and 3, the creep rate in the case of H-D creep is independent of grain size.

2.7.4 Dislocation creep models

Dislocations-mediated creep processes become rate-governing as the applied stress rises moderately. In contrast to diffusional creep processes or grain boundary sliding, these creep mechanisms demonstrate a greater dependence of creep rate on applied stress, with stress exponents often falling in the range of 3–8. This type of creep is referred to as power-law creep. Some creep mechanisms, including the dislocation glide model, dislocation climb model, non-conservative motion of jogs in screw dislocations, and cross-slip of screw dislocations, have been proposed under the power law creep category[21].

2.7.5 Viscous-glide creep model

In dislocation-mediated plasticity, dislocations from various origins glide when stress is applied and are annihilated by meeting with dislocations from the opposite burgers vectors by climbing at high enough temperatures. Dislocation glides and climb are sequential processes, with the slower of the two controlling the rate of deformation. Nevertheless, regardless of what regulates the creep rate, the dislocation glide process contributes the majority of the overall strain. Due to the interaction of solutes with the dislocations in some solid solution alloys (class A), dislocation glide becomes slower than climb and serves as the rate-controlling mechanism.

Weertman first developed a model for viscous-glide creep in which the velocity of dislocations was presumed to be linearly proportional to the stress acting on them[80]. This process is known as the viscous-glide creep model because of its similarity to diffusional creep models, where the creep rate depends on the applied stress. In his model, Weertman considered a pile-up of dislocations for a length of L. When one dislocation gets annihilated by climb, another one is generated by the source resulting in a steady state creep rate. The average velocity of the dislocations, v, in the pile-up was shown to be proportional to σbn where n is the number of dislocations in the pile-up, which is given by $n\,\alpha\,\sigma bL$[79]. Therefore, the average dislocation velocity is,

$$v = A\sigma^2 b^2 L \tag{2.12}$$

where A is a constant decided by the type of viscous-glide mechanism. According to this model, the activation energy for solute atom diffusion in the alloy is the same as the activation energy for creep. This activation energy value is equivalent to that for lattice self-diffusion for practical purposes.

2.7.6 Dislocation climb controlled creep

In the case of pure metals or class II alloys, dislocation glide proceeds at a faster rate without any locking from solute atoms and with the only resistance being raised by the Peierls frictional stress. As a result, dislocation climb acts as the factor which governs the mechanism of rate control in these materials.

Weertman developed a model to obtain the constitutive equation to describe the creep

rates in materials deformed by the dislocation-climb controlled process [45, 81, 82]. This model is referred to as the pill-box model. In this model, *M* number of dislocation sources per unit volume is assumed to be operative. The dislocations generated from the sources glide for a distance of *L* before climbing up or down to get annihilated, with the dislocations approaching in parallel planes. The climbing height is assigned to be *h*. Once the leading dislocation gets annihilated, a dislocation will be released from the source. Based on these initial settings, Weertman obtained the following relation for the creep rate[81],

$$\dot{\varepsilon} = \alpha \left(\frac{D_l}{b^{3.5} M^{0.5}}\right) \left(\frac{\sigma}{G}\right)^{4.5} \left(\frac{G\Omega}{kT}\right) \tag{2.13}$$

where *G* is the shear modulus, Ω is the atomic volume, α is a constant whose values are in the range $0.015 < \alpha < 0.33$, and $D_l = D_0 exp\left(-\frac{Q_l}{RT}\right)$. A stress exponent of 4-7 is observed in the power law creep regime. The activation energy for creep and lattice self-diffusion match because the diffusion of vacancies governs the climb process. Although the Weertman model predicted a stress exponent of 4.5, larger stress exponents of up to 7 have also been reported associated with dislocation core diffusion by climb at low-temperature [83].

2.7.7 Glide of jogged screw dislocations

Non-conservative motion of jogs in screw dislocation as a rate-controlling mechanism was proposed by several researchers [84, 85]. Among them, the theory developed by Barrett and Nix was of interest to the research community since the steady state creep rate equation derived by them was based on experimentally measurable parameters [84]. In this proposal, screw dislocations were assumed to have both vacancy-absorbing jogs and vacancy-emitting jogs, all exhibiting edge character. As the screw dislocation glides along the slip plane, these jogs must move non-conservatively by absorbing and emitting vacancies, which causes a drag force on the jogs due to the change in vacancy concentration in the surroundings. This force (f_a) can be written as[86],

$$f_a = \pm \frac{kT}{b} ln \frac{c}{c_o} \tag{2.14}$$

where *c* is the concentration of vacancies in the surrounding of the jogs and c_o is the equilibrium concentration. Barrett and Nix applied the results of Rosenthal's analysis to derive the following steady-state creep rate equation for the jogged screw dislocations mechanism,

$$\dot{\gamma}_s = 4\pi D\beta \left(\frac{b}{a_o}\right)^3 \rho_s sinh\left(\frac{\tau b^2 \lambda}{kT}\right) \quad (2.15)$$

where β is the number of atoms in the unit cell, a_0 is the lattice parameter. On deriving the equation, it was assumed that the height of the jogs was on the order of the burgers vector.

2.7.8 Cross-slip mechanism

According to Poirier, cross-slip of screw dislocations is a rate-controlling mechanism for creep deformation[87, 88]. In his model, the climb of edge dislocations and the cross-slip of screw dislocations were both considered to be the controlling factors during deformation. The creep rate equation derived by him can be written as,

$$\dot{\varepsilon} = \dot{\varepsilon}_{O,SD} \exp\left(-\frac{Q_{SD}}{kT}\right) + \dot{\varepsilon}_{O,CS} \left(\frac{\sigma}{\mu}\right)^2 \exp\left(\frac{-Q_{CS}}{kT}\right) \quad (2.16)$$

where Q_{SD} and Q_{CS} is the activation energy for lattice self-diffusion and cross-slip, respectively.The first and second terms in the right-hand side of the equation are the creep rates resulting from climb-controlled and cross-slip-controlled creep, respectively. The creep activation energy is a function of the applied stress, as can be observed from the rate equation associated with the cross-slip process. In particular, Friedel's calculations show that the activation energy varies inversely proportional to the applied stress [89]. Poirier has also reported that cross-slip was an active creep mechanism in Copper, Aluminum, and some of the HCP crystals from their creep data [87].

2.8 Kocks-Mecking model

The Kocks-Mecking (K-M) model describes the deformation mechanism in metals when a material is subjected to stress exceeding its yield strength. The model states that plastic deformation results from the repeated breaking and formation of dislocation networks. The dislocations migrate and form tangles under stress, which later annihilate or reorganize in various configurations. This is being widely used to analyze and model the strain-hardening nature of metals and alloys [90, 91]. The Kocks-Mecking (K-M) curve is a good approach to describe the changes in the dislocation structures during different stages of strain hardening rate. The strain hardening rate can be generally divided into three regions. Stage I, or the Transient stage, is characterized by a rapidly decreasing strain-hardening rate with respect to stress. Stage II is defined by a gradually decreasing strain hardening rate. According to K-M theory, there is constant storage and annihilation of dislocations in stage II. The slope of the

strain hardening rate (φ) vs. true stress (σ) curve $\left(i.e.\frac{d\varphi}{d\sigma}\right)$ in this stage gives the rate of change of strain hardening rate with stress [90–92]. Subsequently, with the increase in stress, the strain hardening rate (φ) becomes almost asymptotic and is identified as stage III. This stage is sensitive to applied strain rate and temperature. Among these three stages, stage III is the most extensively studied part in terms of work-hardening behavior. The decrease in φ with an increase in σ is expressed as

$$\varphi = \varphi_o\,(1 - \frac{\sigma}{\sigma_s}) \tag{2.17}$$

where φ is the rate of strain hardening at stress σ, φ_o denotes the initial rate of strain hardening, and σ_s is the saturation stress when φ=0. The slope of the linear plot of instantaneous work hardening rate(φ) with that of true stress(σ) determines the rate at which strain hardening decreases with stress. Choudhary et al.[93] applied the K-M approach to illustrate the tensile flow and strain hardening characteristics of P9 steel in the range of 25-600°C. Three temperature zones were identified in the work-hardening behavior of this steel. A strain-hardening model for a Ti-Al alloy and 25CrMoS4 steel using the K-M method was proposed by Bambach et al. [94]. They reported that Stage–III hardening was not observed in the case of Ti-Al alloy. Angella et al.[95] analyzed the high-temperature flow stress behavior of austenitic stainless steel (AISI 316L) with the help of the K-M approach and Voce equation. They found that both these approaches predicted the flow curves at larger strains but failed at smaller strains. Kocks –Mecking approach satisfactorily described the behavior of strain hardening of 9Cr-1Mo ferritic steel within 25-600°C. [96, 97]. Two-stage work-hardening was observed in the variation of φ vs. σ at all test conditions for the alloy.

2.9 Creep deformation mechanism maps

Based on the various combinations of stress and temperature, the creep behavior of materials can change. Ashby (1972) [98] was the first person to propose a creep deformation mechanism map. As shown in Figure 2.8 (a) and (b), these maps graphically represent the different creep regions on a normalized stress-temperature plane. These maps are organized into different stress and temperature zones, each of which has a dominant deformation mechanism. These maps give a correlation between strain rate, temperature, and stress. If any pair of these variables is provided, any one of them can be found on the map. Multiple fields are created from the deformation mechanism maps depending on the predominant creep

mechanism. The constitutive equations of two adjacent creep processes are paired up to form the field boundaries. Deformation mechanism maps for a wide variety of metals and alloys such as pure Nickel, Tungsten, Cobalt, Silicon Carbide, Indium Antimonide (InSb), IN738LC superalloy, polycrystalline LiF and NaCl, high entropy alloys have been constructed by researchers [98, 99, 108–114, 100–107].

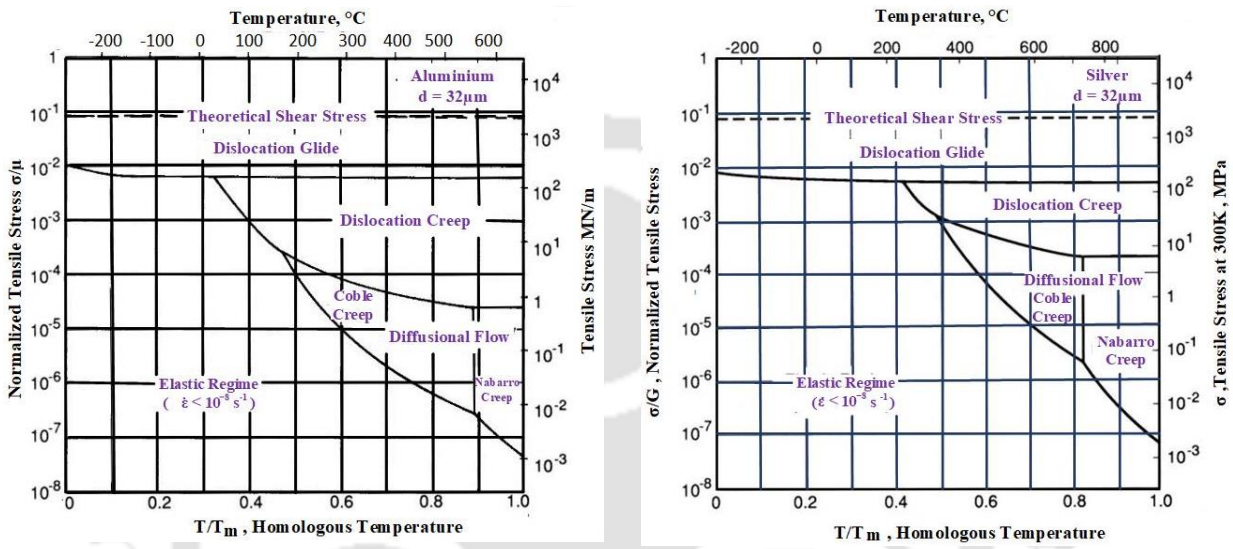

(a) (b)

Figure 2.8 Deformation mechanism map for (a) pure Aluminium [98] and (b) pure Silver [98].

2.10 Creep fracture mechanism

Creep rarely happens at low temperatures; however, as the temperature increases, creep starts, which ultimately results in fracture. The tertiary creep region begins when the constant creep rate deviates on a creep curve, eventually leading to failure. This region generally comes before the fracture in a constant stress test. Tertiary creep may be caused by

1. mechanical instability, such as necking, which causes a localized reduction in cross-sectional area,
2. microstructural instability, e.g., grain growth, recrystallization with single-phase materials, or sluggish decline in creep strength because of over-aging and/or
3. nucleation and growth of internal micro-cracks leading to an increase in the creep rate.

Materials may either fail by intergranular creep fracture (I.C.F.) or transgranular creep fracture (T.C.F.). Examples of I.C.F and T.C.F of different material is shown in Figure 2.9.

Many materials experience dynamic recrystallization at temperatures near their melting point, causing rupture or necking. At elevated temperatures, there is microcracks formation that propagates along the grain boundaries, resulting in "inter-granular" failure.

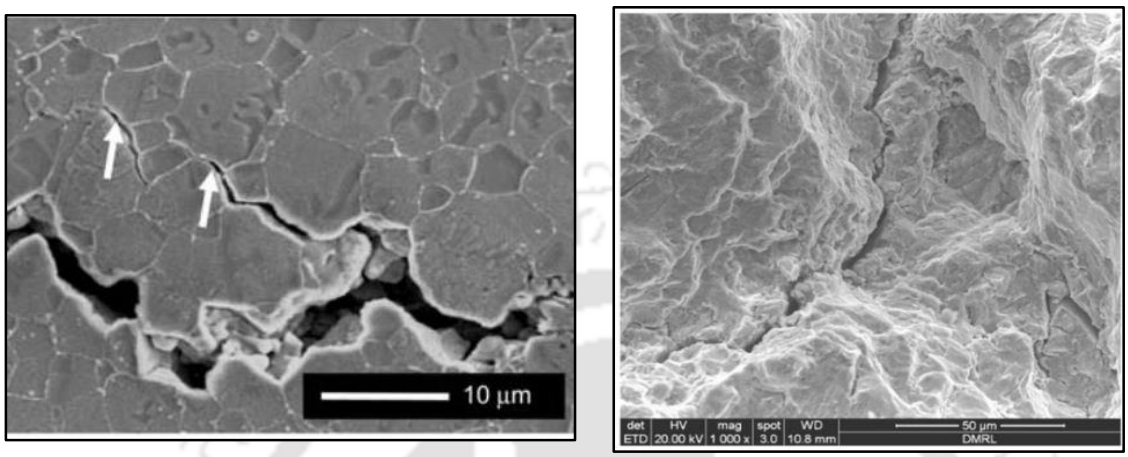

(a) (b)

Figure 2.9 Fracture paths showing (a) intergranular failure in superalloy (IN 100) [115] and (b) transgranular failure in IN 718 superalloy turbine disc [116]

Shear stress caused by grain boundary sliding leads to stress concentrations that are sufficient to initiate cracks at triple sites. The initial formation of the voids as well as their continued growth, are caused by grain boundary sliding. The grains within a polycrystalline material move relative to one another under high-temperature creep conditions, resulting in a wedge or triple point cracks, i.e., w–type cracking that is initiated by grain boundary sliding. When cavities are small, they expand via diffusion. As the size of the cavity grows, power-law creep mechanism dominates. The r-type cavitation is preferred over the w–type as the strain rate lowers or as the temperature rises. The total creep rate governs the rate of grain boundary sliding and, thus, the growth rate of wedge fracture.

Ashby et al. have discussed the fracture mechanism maps in polycrystalline materials. When a cylindrical bar of a crystalline solid is pulled under tension, it can fail in a number of different ways, as demonstrated in Figure 2.10[117]. The figure depicts seven modes by which fracture can occur in metals and alloys. These include cleavage fracture, transgranular creep fracture, intergranular fracture, and fracture due to pure diffusion.

Even though the mechanisms of creep fracture have been studied in a wide variety of materials, designing a reliable component depends on the relationship between the minimum

creep rate and time to rupture (in hours) at a constant temperature and stress. The Monkman-Grant relationships, explained in more detail in the subsequent section, can be used to achieve this correlation.

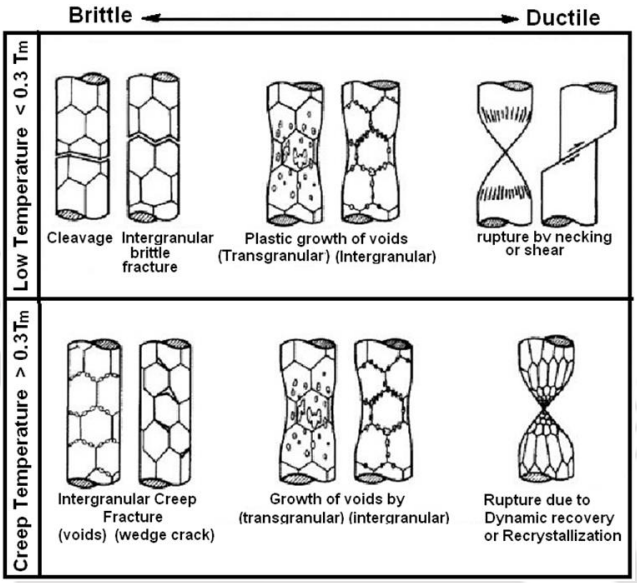

Figure 2.10 The simplest classification of creep fracture mechanisms [117].

2.11 Creep rupture models

Creep strength is a crucial factor in determining the life of structures subjected to high temperatures and stresses for long periods. At locations where creep is possible, strict restrictions on the allowed stress are put in place to keep the creep strain substantially lower than the creep rupture strain. In applications where weight is not crucial, this is typically achieved by overdesigning the structure to avoid creep.

A creep curve can be used to calculate the creep life of structural components. It would require almost a decade of uninterrupted creep testing to complete one test. Therefore, conducting creep tests for the entire service life of the component is impractical. The process of extrapolating creep data is well accepted. In order to keep the testing time reasonable, accelerated creep tests are performed-at temperatures and stress much greater than the service conditions. The design life of the component is then determined using these test data by extrapolation techniques.

Extrapolation techniques exist for establishing relationships between temperature T, time to rupture t_r, and stress σ using the data from accelerated tests. To predict the creep life

over longer durations, a number of time-temperature parameters need to be established. Due to the numerous uncertainties associated with using the data from the accelerated creep test, parametric models have been designed. In these methods, the region composed of experimental and extrapolated zones is assumed not to undergo any microstructural changes. The parametric model predictions are considered safe because the experimental conditions are considerably higher than the real-world conditions. Several techniques of creep life prediction exist, such as constitutive modeling, Monkman-grant relationship, and parametric approaches, each having its own advantages and disadvantages. Values of rupture time and minimum creep rate obtained from experiments serve as the foundation for Monkman-Grant relationships used to predict rupture life. Several parametric approaches have been in practice for predicting the long-term creep life of engineering components and are being used by industries[12–17]. Among them, the Larson-Miller parameter (LMP) technique is widely used by industries. Monkman- Grant reltionships and the LMP technique is explained in the following sub-sections.

2.11.1 Monkman-Grant relationships and Creep Damage Tolerance Factor

The Monkman-Grant relationship(MGR) gives a correlation between the minimum creep rate $\dot{\varepsilon}_s$ and the rupture time t_r in materials. It can be expressed as [16]:

$$\dot{\varepsilon}_s{}^m . t_r = C \tag{2.18}$$

where *m* and *C* are constants. Eq. 2.18 is used to predict the rupture time of a material using the data obtained from accelerated creep tests. The values of constants *m and C* generally lie in the domain of 0.6 - 0.95 and 3 – 20 [118–121]. Studies have shown that *C* is a function of temperature[86]. Toscano and Boček [122] have reported that the constants *m* and *C* are dependent on not only temperature but also stress. In order to reduce the scatter in the experimental data, Dobes and Milicka [17] modified the existing Monkman-Grant relation by introducing the failure strain ε_f term in Eq. 2.18. They proposed it as modified Monkman-Grant relation (MMGR), which is of the form:

$$\dot{\varepsilon}_s{}^{m'} . \frac{t_r}{\varepsilon_f} = C' \tag{2.19}$$

where *m'* and *C'* are constants. Researchers have validated MMGR for different materials [1, 119, 130, 131, 122–129]. In case of *m* = *m'* = 1, Eq. 2.17 and Eq. 2.18 can be expressed as:

$$\dot{\varepsilon}_s . t_r = C_{MG} \tag{2.20}$$

and

$$\dot{\varepsilon}_s . \frac{t_r}{\varepsilon_f} = C_{MMG} \tag{2.21}$$

Eq. 2.20 shows that an inverse relationship exists between the rupture time and the minimum creep rate. C_{MMG} was found to be more sensitive to the growth of cavity. So, the creep life could be predicted more appropriately using C_{MMG} compared to that by C_{MG} [132].

Monkman-Grant relationship follows first-order kinetics and is valid for all three creep regions[133–136]. Phaniraj et al. [137, 138] said that the product of $\dot{\varepsilon}_s$ and t_r gives Monkman-Grant Ductility (MGD). The time to reach MGD (t_{MGD}) can be taken as the time to reach a critical level of damage. Based on the concept of continuum creep damage mechanics (CDM), Kachanov[139] and later Rabotnov[140] took the creep damage as an internal state variable ω. The concept of CDM was applied further [141–144] by introducing a term known as the creep damage tolerance factor (λ). Mathematically, λ can be written as :

$$\lambda = \frac{\varepsilon_f}{\dot{\varepsilon}_s t_r} \tag{2.22}$$

where, $\dot{\varepsilon}_s t_r$ is the Monkman-Grant ductility and ε_f is the failure strain. From Eq. 2.21 and Eq. 2.22 it can be seen that λ is the reciprocal of C_{MMG} [137]. Based on the concept of the criterion of critical damage, Phaniraj et al. [138] proposed a relationship between t_r and t_{MGD} which can be written as:

$$\frac{t_{MGD}}{t_r} = 1 - \left(\frac{\lambda - 1}{\lambda}\right)^{\lambda} = constant = f_{CDM} \tag{2.23}$$

Eq. 2.23 is applicable to materials where the mechanism of creep failure is dominated by cavitation. As the time of creep starts reaching t_{MGD}, the cavity begins achieving a critical value, and the deformation enters the tertiary stage. During tertiary creep, the creep rate increases at a faster rate because of the growth of the voids, ultimately resulting in the failure of the component.

2.11.2 Larson–Miller parameter

Larson and Miller, considering Hollomon–Jaffee [145] expression for steel, introduced the correlations between the time to rupture and temperature. In the case of a

particular material, plot of stress with respect to Larson-miller parameter ($P_{L\text{-}M}$) resulted in a single plot with any combination of time and temperature. Larson–Miller parameter ($P_{L\text{-}M}$) is generally expressed as:

$$P_{L\text{-}M} = f(\sigma) = T(\log_{10} t_r + C_{L\text{-}M}) \tag{2.24}$$

where $C_{L\text{-}M}$ is a constant, and T is in Kelvin. The detailed derivation of Larson-Miller parameter is given in the Appendix.

A plot of $\log_{10} t_r$ vs. $1/T$ for constant stresses is shown in Figure 2.11(a). In the figure, the plot gives a straight line and it is assumed that these straight lines intersect at a single point which is given by $C_{L\text{-}M}$ as $1/T$ reaches zero. In the analysis, the value of $C_{L\text{-}M}$ in Eq. 2.23 is always assumed constant and is dependent on the material. The time can either be the time to rupture by creep or the time to attain a specific level of creep strain. A master curve between the stress vs. Larson-Miller parameter is obtained from where the life of the component can be calculated. A typical master curve obtained for Zr-4.5Sn- 1Mo alloy is shown in Figure 2.11(b).

As mentioned earlier, among all the parametric models, the prediction of creep life by the Larson–Miller parameter is extensively used in industries. The advantage of this technique is that it can be used by extrapolating accelerated creep test data and can predict the life of a material. Researchers generally assume the value of $C_{L\text{-}M}$ =20, as proposed by Larson and Miller [14], for the prediction of the creep life of a wide range of materials[146, 147, 156, 148–155]. Subsequent work carried out by various investigators revealed $C_{L\text{–}M}$ value lying in the range of 8 - 57[157].

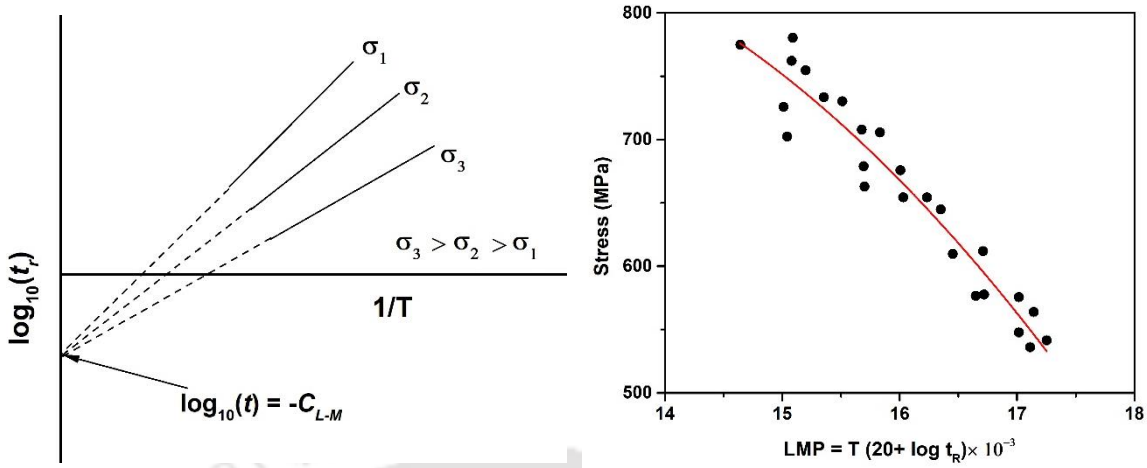

(a) (b)

Figure 2.11 (a) Schematic representation of constant stress lines for $P_{L–M}$ and(b)plots of $P_{L–M}$ vs. stress for Zr-4.5Sn- 1Mo alloy [158].

Larson–Miller parameter was used for calculating the creep life of in-service high-temperature components using aging temperature and aging time[159]. Shlyakman [160] proposed a method for calculating the constant C_{L-M} in the Hollomon temperature–time parameter [145]. Service condition-creep rupture property interference (SCRI) model based on the method of Z-parameter was used by different researchers to calculate the creep rupture life of a wide variety of materials [161–164].

2.12 Multiple Linear Regression modeling

The Multiple Linear Regression (MLR) modeling method is a soft computing technique that uses data from experiments to establish a relationship between the dependent parameter and a large number of independent parameters. The MLR approach has been shown to accurately predict the tensile characteristics of Sn-Ag-Cu and Ti-6Al-4V alloys [165, 166]. The effect of cutting parameters on the surface topography of Ti-6Al-4V alloy during peripheral milling was investigated using MLR as a surface analysis technique [167]. Milhomme et al. used MLR to predict the bead geometry made on Ti-6Al-4V alloy plates using the technique of laser metal powder deposition [168]. The model was developed by taking the bead geometry as a function of laser power, scanning speed, and powder feed rate. MLR analysis has been used to develop models to study the effects of the variations in the lattice parameters of γ and γ' phases of nickel based super alloys. The model was developed by taking the chemical composition and temperature as the input parameter [169]. It appears

that MLR technique can be effectively used for predicting creep curves using experimental data.

2.13 Artificial Neural Network modeling

A broad spectrum of engineering challenges has been effectively solved using a number of physics-based models. An accurate relationship between the boundary conditions and input-output variables is necessary for such techniques. The Artificial Neural Network (ANN) approach has evolved over the last few decades as a beneficial technique for modeling material behavior and manufacturing processes that would otherwise be difficult to describe using analytical or mechanistic models, especially when the number of variables is high and the input-output relationship is nonlinear. In recent years, soft computational techniques, such as ANN, fuzzy logic, and evolutionary algorithms, have grown into beneficial instruments for tackling tough engineering challenges. ANN is a data-driven model that analyses data about a system by establishing relationships between the variables that make up the system. When enough sets of input-output data are available, connections between the state variables can be made, even if the precise physical behavior of the system is unknown. Additionally, ANN provides a rapid solution in comparison to other physics-based models.

The feed-forward back-propagation neural network (BPNN) model is one of many neural network models that is frequently utilized, especially when adequate data sets are available. The input layer, the hidden layer or layers, and the output layer are the three unique layers that make up this structure. Numerous neurons make up each layer. The output of one layer's neurons is used as the input for the next layer's neurons. The input layer receives data from the user. The second layer,i.e., the hidden layer, has no direct contact with the outside world. This layer is important as it facilitates the network to learn the relationships among the datasets. Depending on the complexity of the problem, there may be a need to have more than one hidden layer. However, the majority of engineering problems were solved using an architecture having a single hidden layer architecture. The final layer, known as the output layer, is where users get information.

The backpropagation algorithm minimizes the disparity between the predicted and actual output values. It is a variant of the gradient descent optimization method. The input signals travel from the network input during the forward pass. The input vector values are fed to the network at the input layer and propagated to the output layer with weights and activation

functions to produce an output in this pass. This value is compared to the output value once the data reaches the output layer. The difference in values between that predicted by the neural network and the actual one, is calculated and relayed backward as error signals. The weights and bias at each neuron are adjusted to minimize the error when these error signals travel backward from the output layer to the input layer. This feedback method is known as training. To minimize the error arising from the adjustments of weight , any effective optimisation technique can be employed. Various pattern recognition and functional approximation problems have been trained using a variety of back-propagation training algorithms, including Levenberg-Marquardt (trainlm), Bayesian regulation (trainbr), scaled conjugate gradient (trainscg), resilient (trainrp), gradient descent with momentum (traingdm), etc. Hegan [170] found the Levenberg-Marquardt technique to be quite effective after testing it on a variety of function approximation situations.

Once the training of the network is completed, it becomes capable of computing the output values associated with the fresh input vectors. By providing testing data, the trained neural network must be put to the test. The network is considered to have over-fit the data if the testing error is significantly higher than that of the training error. An adequately fitted network will produce almost equal training and testing errors. A review of work done previously by various researchers on ANN is given below.

ANN technique successfully modeled high-temperature deformation behavior and the generation of processing maps for metalworking with high accuracy [171]. Here, the flow stress was predicted successfully by considering the strain, strain rate, and temperature as the input parameter. ANN techniques have also been employed to predict the corrosion and degradation behavior of metals [172, 173]. ANN has been found to be a potent tool for successfully predicting the high-temperature flow stress of materials[174–177], high-temperature deformation behavior [178, 179], and mechanical properties in the dynamic strain aging regime[180]. Hong et al. successfully predicted the yield and tensile strength of ferrite-pearlite steels with the help of the ANN technique [181]. The model was developed using alloying elements and microstructural variables as inputs and tensile properties as outputs. Deshpande et al. developed an ANN model for forecasting surface roughness as a function of cutting parameters, force, sound, and vibration during the machining of Inconel 718[182]. The model predicted surface roughness with 90% accuracy. Maleki and Unal successfully developed an ANN model to explore the influence of shot peening on AISI316L steel [183].

The depth of the deformed layer was shown to be more influenced by the surface coverage. Another study used the ANN technique for predicting the surface hardness of shot penned surfaces of different carbon steels, finding that the penning duration was the most important factor in improving surface hardness [184]. Researchers have demonstrated the applicability of ANN for the prediction of creep rupture life of ferritic steel, 9Cr–1Mo–V–Nb steel, and polymers [185–187]. Kwon and Lim developed an ANN model for simulating the creep-fatigue life of AISI 316 stainless steel as a function of total strain range, plastic strain range, tensile hold time, and compressive hold time [188]. The model could predict the creep fatigue life within an average error of 15.6%. Sarkar et al. used the ANN approach to model the diametrical creep rate of P.T.s. The model was developed by taking the mechanical properties, alloy composition, tube thickness, temperature, and fluence as the input parameter[26]. This study revealed that the amount of oxygen concentration and mechanical properties had more influence on calculating the creep rate.

From the literature, it can be seen that the ANN model could effectively predict the rupture life and creep rate materials. The methods generally used for predicting the creep life of materials are typically parametric methods or constitutive relationships that employ data obtained from accelerated creep tests. The procedure for developing a physics-based relationship between creep strain, stress, and temperature is complicated by the fact that a creep curve is a superimposition of three different creep regions having different relationships in each stage. Artificial neural network (ANN) modeling was used for predicting the creep curve of HP40Nb micro-alloyed steel [18]. The ANN architecture was developed using data from accelerated creep tests. In the study, 98% of the total data was predicted to have a deviation of ±10% from the experimental data. The correlation coefficient between the actual and estimated data was reported to be 0.992. It may be noted that the material used in this study was HP40Nb micro-alloyed steel which has a single-phase austenitic structure from melting temperature to room temperature. The Zr-2.5Nb alloy exists as a two-phase ($\alpha + \beta$) structure in the range of 610-900 °C [6]. This alloy exists as a single-phase material (α-Zr) with a hexagonal closed-pack crystal structure till 600°C. Above 600 °C α-Zr phase starts transforming to body-centered cubic structure β-Zr phase, and the relative amount of β-Zr increases with the increase in temperature. Above ~ 900°C, the alloy completely transforms to the β-Zr phase [189]. The creep deformation mechanism is complicated by the variation of constituent phases as temperature increases. The temperature of the pressure tubes may

abruptly rise to above 800 °C in the case of the postulated design accident scenario, LOCA. Hence, predicting creep deformation in this dual-phase alloy becomes essential. In such cases, traditional methods of predicting creep curves may be ineffective. Therefore, the present study was conducted to conduct accelerated creep tests on Zr-2.5Nb alloy and investigate the creep deformation behavior by various models.

2.14 Technical gaps

Based on the literature survey, the following research gaps have been identified.

1. Results of systematic investigation of the temperature dependent mechanical properties and fracture of Zr-2.5Nb alloy pressure tube and its correlation to the microstructure are not much in the open literature.
2. Creep behavior of this material along both the longitudinal and transverse directions of the pressure tubes has not been investigated in detail.
3. Investigation of the creep behavior of Zr-2.5Nb alloy pressure tube using constitutive relationships has not been thoroughly studied.
4. Modeling of a complete creep curve of Zr-2.5Nb alloy with reasonable accuracy has not been reported in the literature. It seems that data-driven modeling techniques are capable of predicting the creep curve.
5. Prediction of the creep rupture life by parametric technique.

2.15 Research objectives

The main objectives of the thesis are as follows.

1. To investigate the tensile creep behavior of Zr-2.5Nb alloy at different temperatures and stresses along the longitudinal and transverse directions of the pressure tube.
2. To develop creep constitutive equations and determine the creep damage tolerance factor for the alloy.
3. To develop an ANN model for predicting the creep curve of Zr-2.5Nb alloy.
4. To predict the creep life of the alloy using the Larson-Miller parameter technique.
5. To study the $C_{L\text{-}M}$ in the Larson-Miller parameter technique for Zr-2.5Nb alloy.

A summary of relevant literature is presented in this chapter. The main research gaps in the area of elevated temperature creep of Zr-2.5Nb alloys have been underlined, and the objectives of the work have been identified. The methodology used to achieve the objectives is given in depth in the following chapter.

Chapter 3 Research Methodology

3.1 Introduction

Chapter 2 highlighted the objectives of the present thesis work. The methodology i.e., the experimental procedures and techniques of result analysis followed for meeting these objectives are presented in this chapter. This includes constant stress creep testing setup, creep testing procedures, microstructural characterization using Scanning Electron Microscope (SEM), Transmission Electron Microscope (TEM), energy dispersive X-ray (EDX) analysis, and X-ray diffraction (XRD) technique. The creep test results were analyzed using constitutive and parametric models, and the creep curve was predicted using MLR and ANN modeling. Finally, the creep life assessment of the alloy under various conditions was determined by a modified Larson-Miller technique. However, in the present study, the degradation of creep life due to the radiation effect has not been taken into account. The methodology adopted has been explained in detail in the following subsections.

3.2 Experimental procedures

3.2.1 Raw material

The material used for the present work was Zr-2.5Nb alloy pressure tubes, as shown in Figure 3.1, having an outside diameter of 90 mm and 3.6 mm wall thickness, provided by Bhabha Atomic Research Centre (BARC) Mumbai, India. The production sequence of this material, reported by Srivastava et al. [6] are, hot extrusion at 850°C, first stage of pilgering where 50-55% reduction occurs, annealing at 550°C, second stage of pilgering for 20-25% reduction and finally autoclaving at 400°C for stress relieving.

Figure 3.1 Photograph of the as-received Zr-2.5Nb Pressure tubes.

3.2.2 Scanning Electron Microscopy

Samples were sliced from the pressure tubes using wire-cut EDM (WDEM) and polished following the standard metallurgical specimen preparation techniques. The polished samples were gold coated using a plasma sputter coater and observed under Scanning Electron Microscope (SEM) (Make: Zeiss, Model: Sigma 300) fitted with a backscattered electron (BSE) detector. SEM imaging was carried out with accelerating voltages in the range of 10-20 kV. The composition of various phases present in the matrix was analyzed using an energy-dispersive X-ray spectroscope (EDX) attached to the SEM. The X-ray elemental mapping technique obtained qualitative distribution of various elements in the specimen matrix over a specific area.

3.2.3 X-ray Diffraction

Phase identification of the alloy was carried out using an X-ray diffractometer (Make: Rigaku Technologies, JAPAN, Model: Smartlab) operated at 45 kV and 200 mA using Cu-Kα radiation (λ=1.540 Å). Samples of size 10 mm × 10 mm × 3 mm were sectioned by WEDM and cleaned with acetone. XRD analysis was carried out in (a) the as-received condition and (ii) samples tensile tested at elevated temperatures. Before conducting XRD analysis, the samples were polished using the standard metallographic technique. Scanning was performed from 30^{o} to 100^{o} with a scan rate of 0.5^{o}/min. The peak position and intensity of the XRD patterns were indexed by comparing with the JCPDS datasheet to establish the phases present in the alloy.

3.2.4 Transmission Electron Microscopy

The crystal structure of the samples was investigated using a TEM (Make: JEOL, Model:2100F) equipped with an energy-dispersive X-ray spectrometer (EDS) and operated at an accelerating voltage of 200 kV. TEM specimens were prepared by slicing fine pieces of the sample using a low-speed diamond cutter and then polishing them down to 80-100 μm thickness using SiC papers. Discs having 3 mm diameter were punched out from these thin slices. The final thinning of the TEM specimen was done using twin-jet electropolishing machine at -35°C and at an applied voltage of 20V using an electrolyte of 10% perchloric acid + 90% ethanol solution. The samples were then investigated under TEM. Selective area electron diffraction (SAED) patterns were obtained, which were then indexed to identify the

structure of the particles. Inter-planar spacing of the crystal was determined from the HRTEM images.

3.3 Mechanical property testing

The following sub-sections discuss the testing conditions and the methodology adopted for the tensile and creep tests.

3.3.1 Tensile test

Tensile specimens having a gauge length of 25 mm and cross-sectional area of 6.5 × 3.6 mm^2 were machined from the pressure tube by WEDM. The specimen was prepared such that the axis of the sample was parallel to the longitudinal axis of the pressure tube. Slicing was also done to obtain circumferential sections. These were then split and straightened, from which transverse testing specimens were machined. Figure 3.2(a) illustrates schematically the orientation of the longitudinal and transverse specimens.

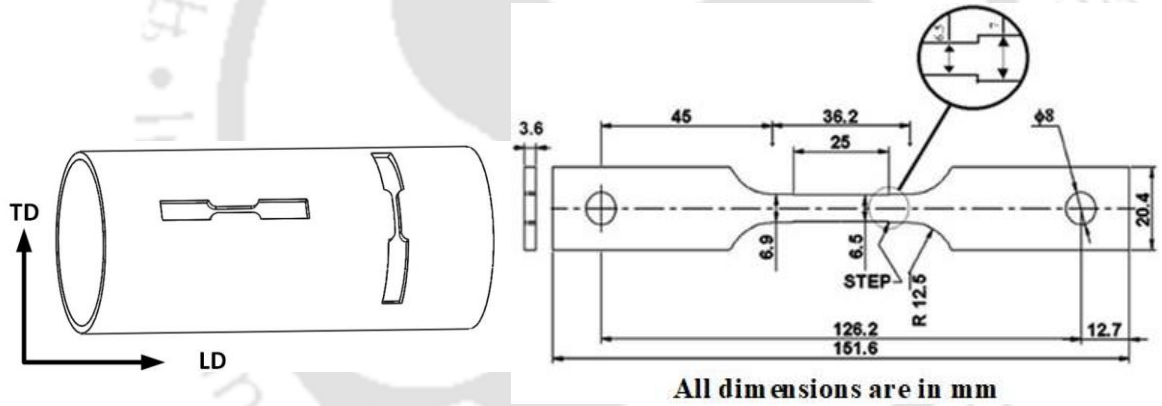

(a) (b)

Figure 3.2(a) Schematic of (a) orientation of the test specimen (TD-Transverse direction and LD- Longitudinal direction) and (b) sample geometry.

Uniaxial tensile tests were conducted in a Universal Testing Machine (Model-Median 250, Make - BISS) equipped with a resistance-type electric furnace. The chamber of the furnace comprised two independent heating regions, each of which contained two heating elements. The temperature of both the heating zones was measured using two internal thermocouples placed within the furnace. The furnace was heated at the required rate, and the temperature was maintained constant with a deviation of ±2°C from the set value by a PID controller attached to the furnace. A high-temperature extensometer (Make: Epsilon) of 25 mm gauge length with a maximum travel range of ± 2.5 mm was used to measure the strain

during the tensile testing. Tensile tests were conducted at a nominal strain rate of $1x10^{-4}$ s^{-1} and temperatures ranging from 25-800°C at an interval of 100°C. Strain rate jump tests were also performed in the same Universal Testing Machine in the strain rate range of 2×10^{-3} to 2×10^{-1} s^{-1} with a dwell time of 1 second before each strain rate change. The strain rate tests were carried out at temperatures of 600, 700, and 800°C.

The samples for high-temperature tensile testing were fixed to the UTM using high-temperature extension rods. This was placed inside the furnace and heated to the test temperature. In order to minimize oxidation during the tests, the furnace chamber was purged with argon gas. After achieving the set temperature, the sample was further soaked for 30 minutes at this temperature. The load-displacement data generated during the test were recorded using a data acquisition system integrated with the machine. 0.2% offset yield strength (YS), ultimate tensile strength (UTS), Young's modulus(E), and the strain hardening exponent (n) were determined using the load-displacement data. The percentage elongation was determined by measuring the fractured specimens. The fracture surfaces of the tensile tested specimens were investigated by SEM. True stress- true strain (σ-ε) data were generated from the load elongation curve. The true stress-true strain (σ -ε) plot obtained was assumed to follow the Holloman equation, which is of the form $\sigma = K\ \varepsilon^n$ [190] where σ is true stress, K is the strength coefficient,ε the true plastic strain, and n is the strain-hardening exponent. The strain hardening exponent, n, for various test temperatures was calculated using the equation [191]:

$$n = \left[\frac{\partial(\log\sigma)}{\partial(\log\varepsilon)}\right]_{T,\dot{\varepsilon}} \qquad (3.1)$$

The work hardening parameters, viz. σ_s, φ_o, and n_v of the K–M model for the linear portion of stage-III work hardening [90, 91], were evaluated for both the longitudinal and transverse specimens [Eq-2.17]. The graph of φ with σ at 400° C for Zr-2.5Nb alloy for a longitudinal sample is shown in Figure 3.3. The figure explains how the various work hardening parameters were calculated for each case. Transient stage (T.S.), marked in Figure 3.3, represents the initial rapid decrease in φ. Characteristic work hardening of stage III, as defined by the K–M approach, is reflected in the gradual decline in φ at higher stresses. Extrapolation of the best-fit K-M line gives the value of saturation stress ($\sigma_{s,K\text{-}M}$) at the X-axes

intercept. The Y-axes intercept presents the value of the initial rate of strain hardening ($\varphi_{o,\,K\text{-}M}$). The rate of decrease of work hardening with stress at various temperatures attained from the slope of $\varphi - \sigma$ graph is indicated by $n_{v,K-M}$.

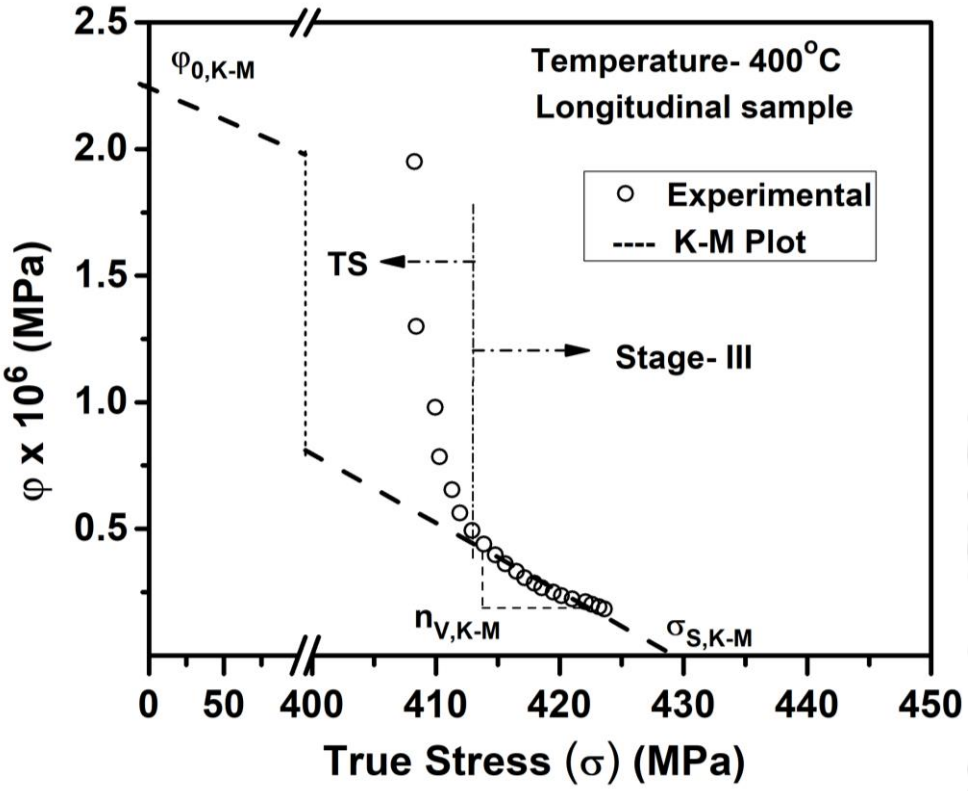

Figure 3.3 Variations of φ with σ at 400° C in Zr-2.5Nb for a longitudinal sample. (The line of best fit is represented as a dashed line in stage-III hardening.)

3.3.2 Creep test

The pressure tube used for the current study had an outside diameter of 90 mm having a wall thickness of 3.6 mm. The creep tests were conducted on the specimens machined from the pressure tubes in accordance with the orientation and geometry shown in Figure 3.2.Creep testing was performed on both the longitudinal and transverse specimens under constant true stress conditions. The details regarding the working of the creep test setup are given in the subsequent sub-section.

3.3.2.a Constant stress creep test set-up

Figure 3.4 shows a schematic of the experimental setup used for the creep tests. The setup consists of a load frame, impedance heater, infrared (IR) pyrometer, high-definition

video camera, and data acquisition system for measuring and recording the temperature and loads acting on the sample. Complete description and working of each part are given below:

a) Load frame: The load frame is made up of four vertical cylindrical columns that are rigidly attached to a steel frame. The steel frame has a top and a bottom plate. The top plate allows a power screw with a nut at the top end to slide through freely. A disc made of mild steel is attached to the screw's bottom end. When the nut is rotated, there is an axial movement of the power screw as well as the disc. Four guide rods are attached to the top plate and pass through four brass bushes that are put into the disc to limit the disc's rotation. The top portion of a tension spring is attached to the steel disc, and the bottom portion of the spring is connected to an S-type load cell with the help of a rod. The Load cell, in turn, is connected to the upper extension rod. The specimen is secured between the upper extension rod and the lower extension rod with the help of pins. The lower extension rod is attached to the bottom of the insulation chamber using a nut and screw. When the nut connected to the top plate of the frame is rotated, it results in the axial movement of the mild steel disc, which in turn loads the spring to the required value. This results in the storage of elastic energy in the spring. This energy gets released gradually when the specimens experience tensile extension with a rise in temperature. Single springs with spring constants of 1.16 N/mm, 1.78 N/mm, 2.34 N/mm, and 2.96 N/mm were utilized to conduct creep tests on longitudinal specimens at constant stresses of 2 MPa, 3 MPa, 4 MPa, and 5 MPa, respectively. Similarly, springs with spring constants of 12.76N/mm, 18.68N/mm, and 28.48N/mm were used for carrying out creep tests on transverse specimens at constant stresses of 22MPa, 38MPa, and 58MPa, respectively. The detailed calculations of the spring constants are given in the Appendix.

b) Infra-red pyrometer: The temperature of the sample was continuously monitored with the help of an IR pyrometer (Make: Accurate Sensors Technologies Ltd., Model: AST 250).

c) Video camera: A video camera (Make: Sony, Model: HVR-Z7P) was used for capturing the video of the specimen during the creep tests. These video frames were then used for calculating the elongation of the gauge length of the specimen during the creep deformation using image analysis technique.

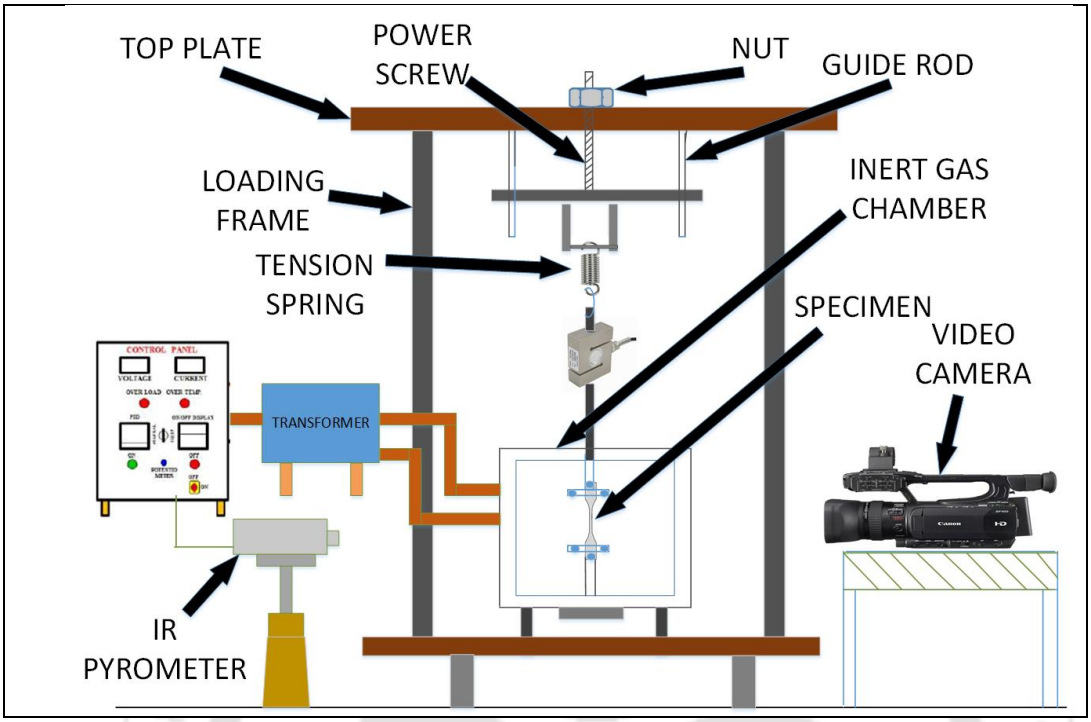

Figure 3.4 Schematic diagram of creep setup.

d) Impendence heater system: An impedance heater system was used to heat the specimen and keep it at the desired temperature. Figure 3.5 illustrates the assembly of the impedance heater. The test specimen is held in the test setup with the help of extension rods (Part-D). The specimen is heated to the desired temperature by the impedance heater (Part G). The temperature of the sample was measured with the help of an IR pyrometer (Part E). The specimen temperature was carefully controlled by manually adjusting the amount of input current to the transformer with a very sensitive potentiometer (Part F). The specimen was enclosed in a chamber made of stainless steel fitted with quartz windows so that video capturing of the specimen could be done during the experiment. In order to minimize oxidation, argon gas was purged inside the chamber at regular intervals.

e) Data acquisition system: The load acting on the sample was measured using an S-type load cell (Make: Haris Sensor Technologies Private Ltd., Model: SL). Detailed specification of the load cell is given in Appendix. The output of the load cell was connected to a digital load cell indicator. The load cell indicator gave the values of the load acting on the specimen. The digital load cell indicator was attached to a data acquisition (DAQ) system (Make: Agilent, Model: 34972A LXI). The DAQ was

connected to the computer system with an RS232 cable. The load on the sample was continuously acquired by Agilent Benchlink acquisition software. The average load acquisition rate was every 5 seconds.

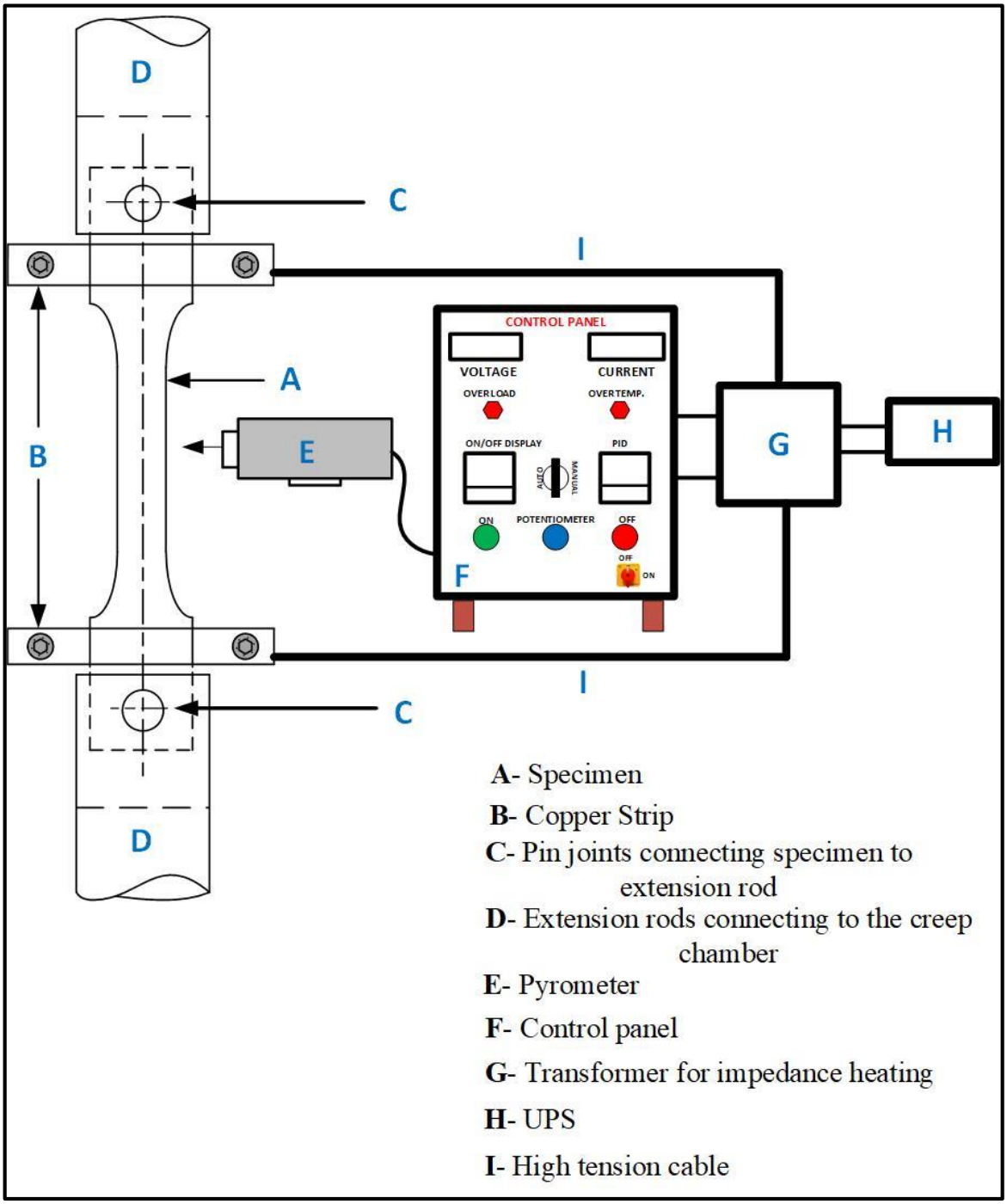

Figure 3.5 Schematic of the impedance heater assembly.

Inconel 718 was used for the extension rods that connected to the creep samples.

Figure 3.6 shows the photograph of the entire constant stress creep testing arrangement taken during a test. Details regarding the calibration of the load cell and the strain measurement technique are explained in the following sections.

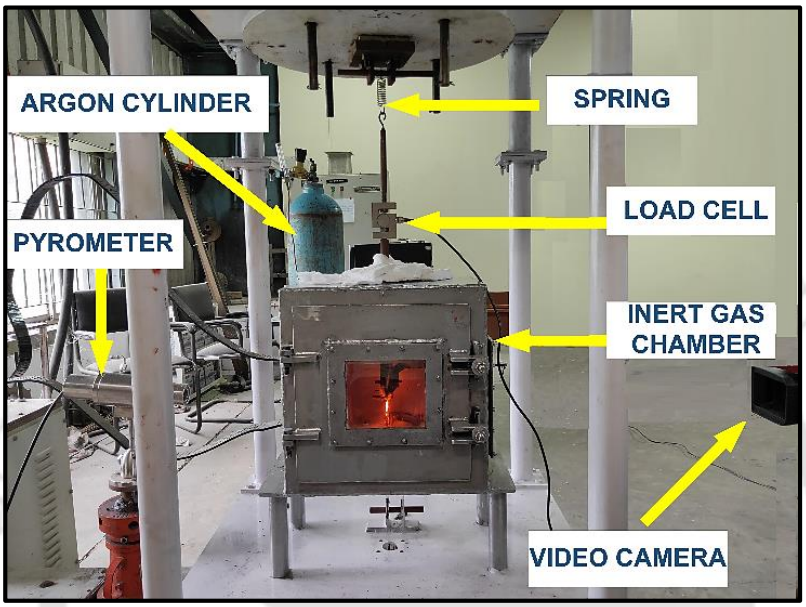

Figure 3.6 Photo of creep testing apparatus with a pyrometer, load cell, video camera, and inert gas chamber.

The following assumptions were used for the creep setup.

a) During creep deformation, the volume of the gauge length remains constant till the end of the secondary creep.
b) Strain across the thickness direction is assumed negligible.
c) The creep setup was designed for a gauge length extension of 20 mm.

In order to maintain the constant volume relationship, the area of the gauge length decreases continuously during the creep strain. The external load on the specimen must continuously decrease as the gauge length increases so as to maintain a consistent true stress condition. The load vs. gauge length extension for a constant stress(σ) at any instant can be obtained as follows:

Let, L_0, W_0 and t_0 be the initial length, width, and thickness of the gauge section of the specimen, respectively. The instantaneous load F_i on the specimen is given by:

$$F_i = \sigma \times A_i \tag{3.2}$$

From the constant volume relationship, the instantaneous area of the gauge section A_i is related to the change in gauge length Δ and initial area A_0 by the relation:

$$A_i = \frac{L_{gauge} \times A_0}{L_{gauge} + \Delta} \tag{3.3}$$

Combining Eq. (3.2) and Eq. (3.3), we get the expression:

$$F_i = \sigma . A_i = \sigma \times \frac{L_{gauge} \times A_{initial}}{L_{gauge} + \Delta} \tag{3.4}$$

Figure 3.7 (a) and (b) shows the load vs. elongation plot for constant true stresses of 2, 3, 4, and 5 MPa for longitudinal creep tests and for stresses of 22,38 and 58 MPa for transverse creep tests for a gauge length of 25 mm. From the figure, it can be seen that the load varies non-linearly with the elongation. However, straight lines having R^2 value $\geq$ 97% can be fitted onto the curves as shown in the figure. So, it was decided to conduct the creep tests considering a linear relationship between the load and the gauge length elongation. The symbols in the graph represent the actual load vs. elongation values.

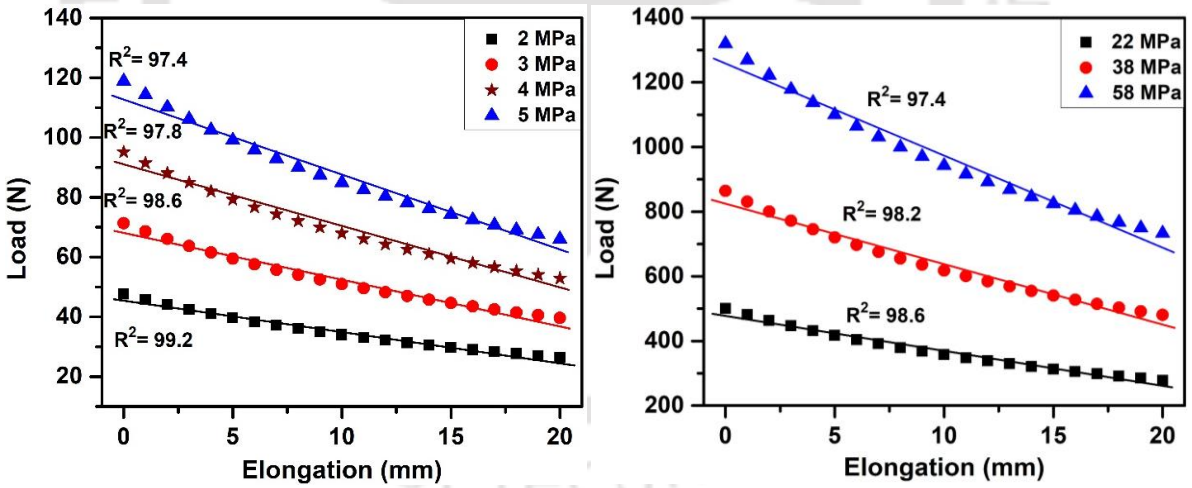

Figure 3.7 Plots of load vs. elongation required for constant stresses with straight line fit for (a) Longitudinal and (b) Transverse creep tests.

3.3.2.b Calibration of load cell

The S-type load cell(Figure 3.8(a)) used in the creep tests was calibrated using the UTM (Make: BISS, Model: Median 250). The S-type load cell was fixed to the grips of the UTM with the help of the extension rods. The output of the load cell was connected to the

digital load indicator, which in turn was connected to the DAQ system. The DAQ was connected to the computer system through an RS232 cable to record the load change continuously. The load cell was loaded monotonically in the UTM at 0.5 mm/minute crosshead speed. The load vs. time data obtained from the UTM and the DAQ system of the S-type load cell were compared. Figure 3.8(b) shows the plot of the load obtained from the UTM vs. that obtained from the S-type load cell using the DAQ system.

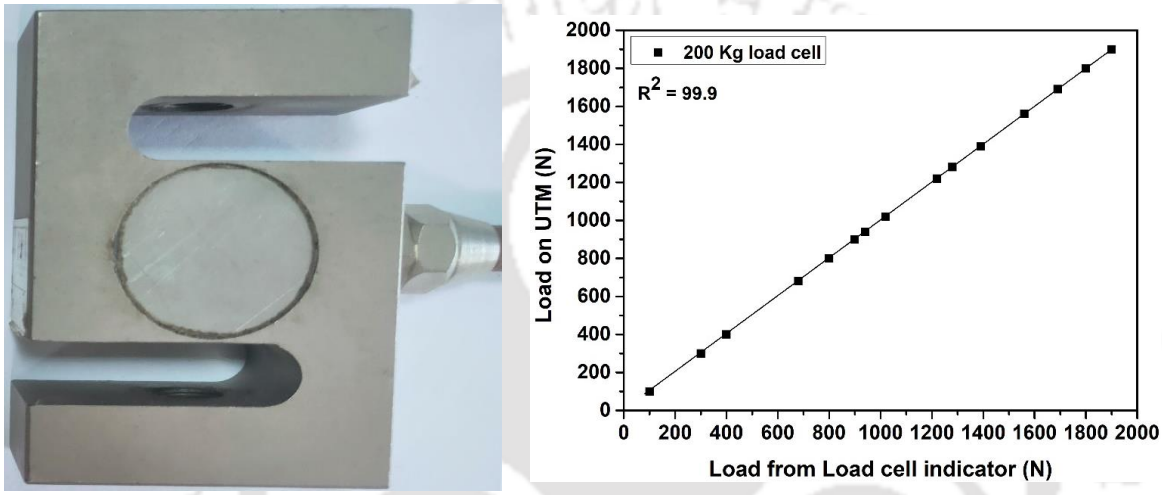

(a) (b)

Figure 3.8 (a) S-type load cell and (b) plot of load on UTM vs. load on the load cell indicator for a 200kg load cell.

3.3.2.c Calibration of strain measurement system

The elongation of the gauge length during the creep tests was expected to be~20 mm. High-temperature extensometers available in the market generally have a travel range of around ± 5 mm. So, it was not possible to measure the elongation using extensometers. For this reason, a digital HD video camera (Make: Sony, Model: HVR-Z7P) was used to capture the gauge length extension during the creep tests. It is necessary to establish the accuracy of the strain measurement technique. For this purpose, tensile tests were conducted on a 3 mm thick flat tensile specimen made of stainless steel in UTM (Make: BISS, Model: Median 250). Two parallel lines were drawn on the flat tensile specimen 25mm apart. For comparison, a 25mm gauge extensometer (Make: Epsilon) was attached to the specimen in such a manner that each end of the extensometer coincides with the parallel lines drawn earlier. The

specimen was loaded monotonically, with a cross-head speed of 0.5 mm/minute. Video recording of the two parallel lines was recorded, and the change in distance between the lines was determined using image processing. Simultaneously, the data from the extensometer was also recorded. The change in specimen extension obtained from the image analysis technique and that from the extensometer reading is compared and shown in Figure 3.9. The plot shows a straight line fit having an R^2 value of 99.4. This demonstrates that the creep strain during creep experiments may be measured using the approach of strain measurement using video recording.

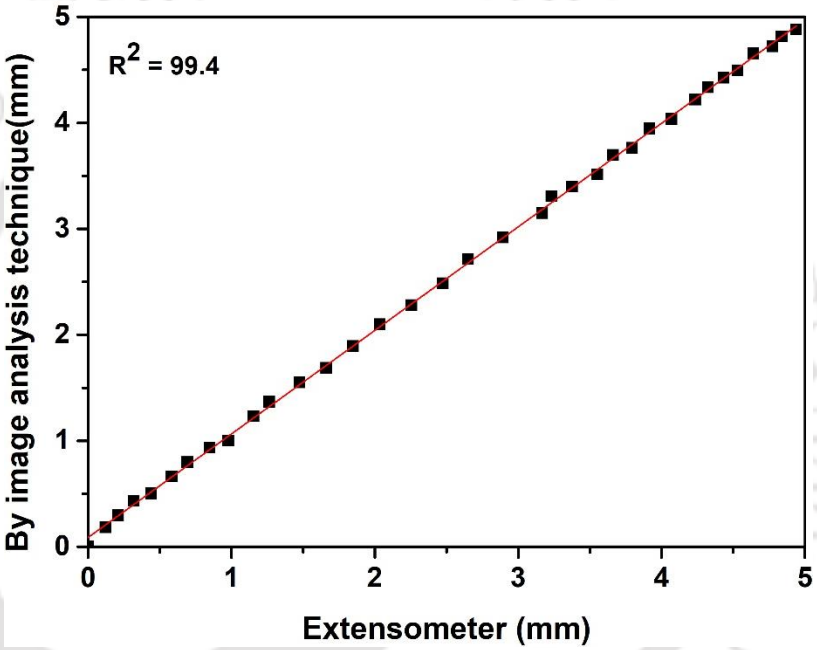

Figure 3.9 Plot of sample extension using image analysis vs. extensometer reading.

3.3.2.d Creep testing procedure

The tensile creep specimen was connected to the extension rods, as shown in Figure 3.10. The specific spring was used for each stress level to produce the necessary load vs. displacement plot for the particular constant true stress tests. The sample was connected electrically to the impedance heater. The specimen was heated to the desired temperature in less than 30 seconds and maintained constant within ± 3°C by manually controlling the input current of the heating system using the attached potentiometer. The current(ampere) required for maintaining the constant temperature was pre-determined before the start of the actual experiment. The IR pyrometer continuously recorded the specimen's temperature. Video

recording of the sample extension was also carried out continuously during creep tests till failure. Argon purging was done at regular intervals in order to minimize oxidation. Figure 3.11(a) and (b) show the photos of the impedance heating system and non-contact IR pyrometer, respectively.

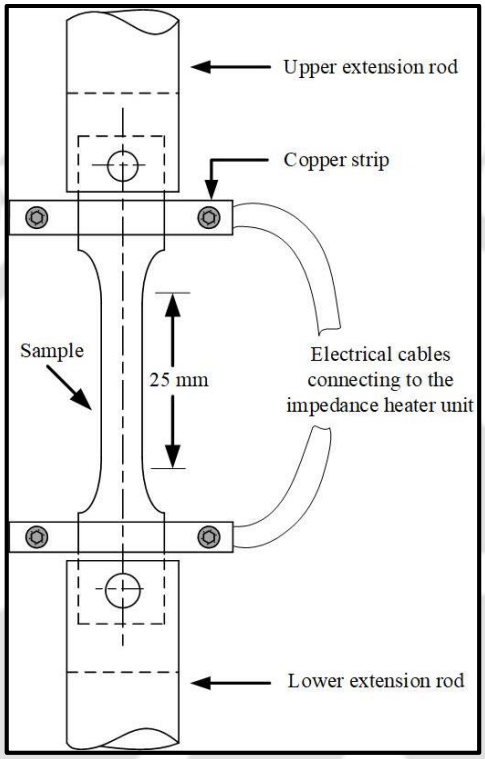

Figure 3.10 Schematic of the specimen attachment.

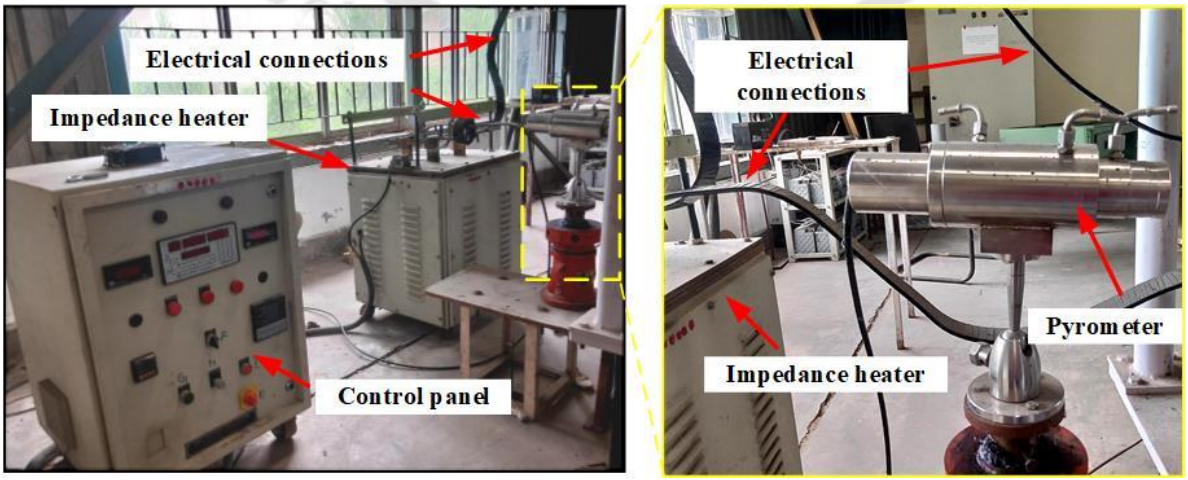

(a) (b)

Figure 3.11 Photographs of (a) impedance heating system and (b)non-contact IR

pyrometer.

Gauge length elongation during creep test was determined using image analysis technique. From the digital video recording, picture frames at regular time intervals were extracted by image capture software (Make: VideoLAN, Version: VLC 3.0.17). From each picture frame, the change in gauge length was determined using image analysis technique. The elongation was determined in terms of pixels by picture manager (Make: Microsoft Corporation, Version: Picture Manager 14.0). Finally, pixel value was converted to engineering unit by comparing it with an image taken before loading.,

3.3.3 Creep test matrix

In the present work, it was decided to perform accelerated creep experiments, and the creep life of the material will be evaluated from the data using extrapolation techniques. The experimental matrix for the longitudinal and transverse specimens is shown in Table 3.1 and 3.2, respectively. Due to the long duration of tests, it was decided to conduct only one experiment for each test condition.

Table 3.1 Experimental matrix for creep-rupture test for longitudinal specimens ("✓" indicates the experiments carried out)

Temperature	Constant true stress (MPa)			
(˚C)	2	3	4	5
600	✓	✓	✓	✓
650	✓	✓	✓	✓
700	✓	----	✓	✓
750	✓	✓	✓	✓
800	✓	✓	----	✓
850	✓	✓	✓	✓

Table 3.2 Experimental matrix for creep-rupture test for transverse specimens ("✓" indicates the experiments carried out)

Temperature	Constant true stress (MPa)		
(˚C)	22	38	58
600	✓	✓	✓
650	✓	----	✓
700	✓	✓	✓
750	✓	✓	✓
800	✓	✓	----
850	✓	✓	✓

3.4 Analysis of creep test data

The data obtained from the creep tests were used for

1. developing constitutive equation for calculating the minimum creep rate
2. validating the Monkman-Grant and Modified Monkman-Grant relationships for the alloy
3. studying the Larson-Miller parametric technique for obtaining the creep life of the material
4. developing the MLR and ANN model and using it to predict the creep curves for various combinations of stress and temperature.

The details are given in the subsequent sub-sections

3.4.1 Constitutive modeling of creep behavior

The creep stress exponent(n_c)and apparent activation energy for creep(Q_{app})of power law creep (Eq. 2.2) for minimum creep rate($\dot{\varepsilon}_s$)were evaluated from the experimental creep data (i.e. creep strain vs. time). The value of n_c was calculated from the slope of a double logarithmic plot of minimum creep rate vs. applied stress for constant temperatures. Q_{app} at constant stresses was determined graphically by plotting $\ln(\dot{\varepsilon}_s)$ vs. 1/T. The slope of these plots provides the values of $-Q_{app}/R$ for the particular stress. The values of n_c and Q_{app} are obtained graphically by considering either temperature or stress as a constant. However, in order to find out n_c and Q_{app} for a combination of stress and temperatures, the creep constitutive equations are used, as explained in Section 2.5. Equations 2.2-2.4 from section 2.5 are reproduced here again for clarity.

$$\dot{\varepsilon}_s = A_1 \sigma^{n_c} \exp\left(-\frac{Q_{app}}{RT}\right) \tag{3.5}$$

$$\dot{\varepsilon}_s = A_2 \exp(\beta\sigma) \exp\left(-\frac{Q_{app}}{RT}\right) \tag{3.6}$$

$$\dot{\varepsilon}_s = A_3 [\sinh(\alpha\sigma)] \exp\left(-\frac{Q_{app}}{RT}\right) \tag{3.7}$$

The material constants A_1, A_2, A_3, n_c, β and α of Eq. 3.5, Eq. 3.6 and Eq. 3.7 were calculated using least square method. The method has been described in detail elsewhere [192]. In the present study, the method applied to Eq 3.5 only is explained in detail below. Taking logarithms on both sides, Eq. 3.5 can be rewritten as[192]:

$$\ln \dot{\varepsilon}_s = \ln A_1 + n_c \ln \sigma - \frac{Q_{app}}{RT} \tag{3.8}$$

Error E_i, is defined by [192],

$$E_i = \ln \dot{\varepsilon}_s - \ln A_1 - n_c \ln \sigma + \frac{Q_{app}}{RT} \tag{3.9}$$

The error is minimized by carrying out the partial derivatives of $\sum_{i=1}^{N_{obs}} E_i^2$ with respect to $\ln A_1$, n_c and $\frac{Q_{app}}{R}$ and equating them to zero, where N_{obs} is the number of observations. By taking the partial derivatives, equations are obtained as:

$$\sum_{i=1}^{N_{obs}} \ln A_1 + \sum_{i=1}^{N_{obs}} (n_c \ln \sigma) - \sum_{i=1}^{N_{obs}} \frac{Q_{app}}{RT} = \sum_{i=1}^{N_{obs}} \ln(\dot{\varepsilon}_s) \tag{3.10}$$

$$\sum_{i=1}^{N_{obs}} (\ln \sigma \ln A_1) + \sum_{i=1}^{N_{obs}} (n_c (\ln \sigma)^2) - \sum_{i=1}^{N_{obs}} \frac{(\ln \sigma \, Q_{app})}{RT} = \sum_{i=1}^{N_{obs}} \ln \sigma \ln(\dot{\varepsilon}_s) \tag{3.11}$$

$$-\sum_{i=1}^{N_{obs}} \left(\frac{\ln A_1}{T}\right) - \sum_{i=1}^{N_{obs}} \frac{(n_c \ln \sigma)}{T} + \sum_{i=1}^{N_{obs}} \left(\frac{Q_{app}}{RT^2}\right) = -\sum_{i=1}^{N_{obs}} \left(\frac{\ln(\dot{\varepsilon}_s)}{T}\right) \tag{3.12}$$

Equations 3.10-3.12 form a set of three linear equations which can be written in the matrix form as

$$\begin{bmatrix} N_{obs} & \sum_{i=1}^{N_{obs}} \ln \sigma & -\sum_{i=1}^{N_{obs}} \left(\frac{1}{T}\right) \\ \sum_{i=1}^{N_{obs}} \ln \sigma & \sum_{i=1}^{N_{obs}} (\ln \sigma)^2 & -\sum_{i=1}^{N_{obs}} \left(\frac{\ln \sigma}{T}\right) \\ -\sum_{i=1}^{N_{obs}} \left(\frac{1}{T}\right) & -\sum_{i=1}^{N_{obs}} \left(\frac{\ln \sigma}{T}\right) & \sum_{i=1}^{N_{obs}} \frac{1}{T^2} \end{bmatrix} \begin{bmatrix} \ln A_1 \\ n_c \\ \frac{Q_{app}}{R} \end{bmatrix} = \begin{bmatrix} \sum_{i=1}^{N_{obs}} \ln(\dot{\varepsilon}_s) \\ \sum_{i=1}^{N_{obs}} \ln \sigma \ln(\dot{\varepsilon}_s) \\ -\sum_{i=1}^{N_{obs}} \left(\frac{\ln(\dot{\varepsilon}_s)}{T}\right) \end{bmatrix} \tag{3.13}$$

Eq. 3.13 is of the form [A][x] = [b], where the elements of [A] and [b] are obtained from the experimental data. The three unknown parameters $\ln A_1$, n and $\frac{Q_{app}}{R}$ of the Eq. 3.5 are calculated by solving [x]= $[A]^{-1}$ [b]. The constitutive parameters of Eqs. 3.6 and 3.7 are also determined by following the above-explained method.

3.4.2 Multiple Linear Regression modeling

Multiple linear regression (MLR) is a statistical tool that uses a linear equation to fit experimental data to establish a relationship between two or more variables. The data is analyzed, and the output parameters are predicted using linear predictor functions in these tools. It is based on the principle of minimization of the sum of the squares of the differences between the actual and predicted values. In the present study, creep strain (ε) is expressed as a function of applied stress (σ), temperature (T), and time (t). [29]i.e.,

$$\varepsilon = f(\sigma, T, t) \tag{3.14}$$

Eq. 3.14 can be expressed in the form [29]:

$$\varepsilon = A\,\sigma^m T^n t^l \tag{3.15}$$

where *A, m, n,* and *l* are constants. Taking logarithm of Eq. 3.15, it can be transformed into linear form

$$\log(\varepsilon) = \log(\mathrm{A}) + m\log(\sigma) + n\log(T) + l\log(t) \tag{3.16}$$

The datasets obtained from the experiments were used to determine *A, m, n,* and *l* by MLR analysis using the "REGRESS" function available in MATLAB® (Make: Math Works Inc., Version: R2016a). Once these values were determined, the time-dependent creep strains were predicted using Eq. 3.15.

3.4.3 Artificial Neural Network modeling

A three-layer feed-forward back propagation (BP) - ANN network was developed to simulate the creep strain(ε). The model consisted of three neurons in the input layer viz., applied stress(σ), temperature (T), and time (t), and creep strain(ε) as the output. The typical ANN architecture used for the present study is shown schematically in Figure 3.12. The ANN model was developed by applying the inbuilt neural network toolbox of MATLAB® software (Make: Math Works Inc., Version: R2016a). The network was trained with the help of the trainlm function. During the training process, the values of the weights and bias are updated by a feed-forward back-propagation network using the Levenberg–Marquardt (LM) optimization algorithm. The LM algorithm has proven to be highly effective in solving nonlinear optimization problems.

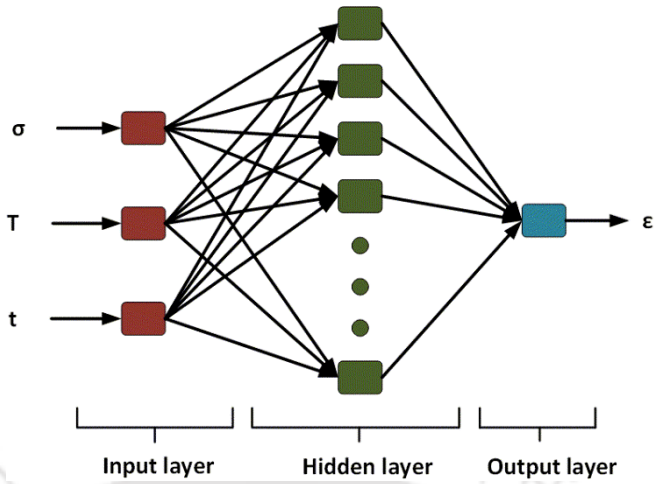

Figure 3.12 Schematic of the ANN architecture.

ANN modeling was done separately for the longitudinal and transverse creep tests. A total of 664 input-output data sets were taken from 22 creep experiments for the longitudinal creep tests. From this, 365,199 and 100 data sets were separated out for network training, testing, and validation, respectively. In the case of the transverse creep tests, the total number of input-output datasets was taken as 588 from 16 experiments. Out of these, 322, 168, and 98 datasets were taken for training, testing, and validation, respectively.

Before the data was fed into the network, normalization of all input and output parameters values was done so that the values lie between 0.1 and 0.9. Training was carried out to achieve the optimum network architecture by conducting a series of numerical experiments. A combination of the following factors was carried out during the training process: (i) using different activation functions viz, *tansig*, *logsig*, *purelin*, (ii) changing the number of neurons of the hidden layer, (iii) by varying the error goal between 0.0001 and 0.00001 and (iv) keeping the error value between the predicted and experimental minimum. Both the training and testing errors were calculated independently.

The following error norms were initially set for arriving at the best network architecture: (a) minimum root-mean-square functional error (RMS_{err}^{f}), (b) the effective error during training and testing should be nearly equal, (c) the maximum deviation between the experimental and predicted strain values must lie within ± 15% error, and (d) 95% of the estimated data fall within ± 10% error. The RMS_{err}^{f} is expressed as

$$RMS_{err}^{f} = \sqrt{\frac{\sum(E_i - P_i)^2}{NE_i^2}} \quad (3.17)$$

where E_i is the actual output, P_i is the predicted output, and N is the total number of data. To ensure that suitable weights and biases are generated and assigned during the training phase, the ANN model was also parallelly tested with the data set aside for testing. The training and testing errors were calculated individually. The effective error for training and testing data is expressed as:

Effective error = maximum of [RMS_{err}^{f} of training data, RMS_{err}^{f} of testing data] (3.18)

A series of computational trial experiments were carried out to achieve the best network design. The most suitable ANN architecture was frozen for the case with: (1) the RMS_{err}^{f} was minimum during the training and testing phase, (2) 98% of the estimated data were within an error of ± 5 % and (3) 95% of estimated data were within an error % of ±10 of the actual results, (4) maximum deviation error between the estimated and experimental value as 7.19% and 7.86% for the longitudinal and transverse case, respectively.

The training and testing experiments were carried out simultaneously to attain the best network architecture. After carrying out a number of experiments, the best neural network architecture having minimum RMS functional error for both the training and testing was finalized. *Tansig* was identified to be the most suitable activation function as the input to the hidden layer, and *Purelin* was found to be the most appropriate from the hidden to the output layer. The *tansig* function calculates output based on the following equation:

$$\text{Output of the neuron} = \frac{e^{XY} - e^{-XY}}{e^{XY} + e^{-XY}} \quad (3.19)$$

where Y represents the input to the neuron, X is a constant. *Purelin* function calculates output according to the equation:

$$\text{Output of the neuron} = XY \quad (3.20)$$

For longitudinal tests, during the training phase, the RMS functional error and maximum deviation error for the best network architecture were 0.007 and 7.19 %, respectively. The corresponding values obtained during the testing were 0.0056 and 7.17%,

respectively. It was found that a network having 25 neurons best represented the experimental data. The details of the best ANN architecture obtained for the longitudinal creep tests are given in Table 3.3.

Table 3.3 ANN architecture for the longitudinal creep tests.

No. of neurons in the input layer	3
No. of hidden layers	1
No. of neurons in the hidden layer	25
No. of neurons in the output layer	1
No. of Training data	365
No. of Testing data	199
Processing function at the hidden layer	*tansig*
Processing function at the output layer	*purelin*
Error goal fixed	0.00001
Epochs required	4396

In the case of the transverse tests, during training , the RMS functional error and maximum deviation error for the best network architecture were 0.0044 and 7.86 %, respectively. The corresponding values obtained during the testing were 0.0048 and 7.76%, respectively. A network having 28 neurons gave the optimal result. The details of the best ANN architecture obtained for transverse creep tests are given in Table 3.4.

Table 3.4 ANN architecture for the transverse creep tests.

No. of neurons in the input layer	3
No. of hidden layers	1
No. of neurons in the hidden layer	28
No. of neurons in the output layer	1
No. of Training data	322
No. of Testing data	168
Processing function at the hidden layer	*tansig*
Processing function at the output layer	*purelin*
Error goal fixed	0.00001
Epochs required	3220

The algorithm proposed by Garson was used to quantify the relative significance of each input parameter on the output parameter [193]. In the Garsons method, the hidden-output connection weights of the networks are partitioned into components that are linked with the input neuron using the absolute values of weights and were obtained by the following expression:

$$I_j = \frac{\sum_{m=1}^{m=N_h}((|w_{jm}^{ih}| \div \sum_{k=1}^{N_i}|w_{km}^{ih}|) \times |w_{mn}^{ho}|)}{\sum_{k=1}^{k=N_i}\{\sum_{m=1}^{m=N_h}((|w_{jm}^{ih}| \div \sum_{k=1}^{N_i}|w_{km}^{ih}|) \times |w_{mn}^{ho}|)\}} \quad (3.21)$$

where I_j refers to the relative importance of the j^{th} input variable on the output variable, $N_i$and N_h are the no. of neurons in the input and hidden layer, respectively. The subscripts 'i', 'h', and 'o' indicate the input, hidden, and output layers, respectively, w are the connection weights. Subscripts 'k', 'm', and $'n'$ denote the input, hidden, and output neurons.

Standard statistical tools were used to study the effectiveness of both models. In this study, the coefficient of correlation (R^2), mean relative error (MRE), and average root-mean-square (RMS) error have been employed to analyze the predictability of the proposed models. These are expressed as:

$$R^2 = \frac{\sum_{i=1}^{N}(E_i - \bar{E})(P_i - \bar{P})}{\sqrt{\sum_{i=1}^{N}(E_i - \bar{E})^2 \sum_{i=1}^{N}(P_i - \bar{P})^2}} \quad (3.22)$$

$$MRE\ (\%) = \frac{1}{N}\sum_{i=1}^{N}\frac{|E_i - P_i|}{E_i} \times 100 \quad (3.23)$$

$$RMSE = \sqrt{\frac{1}{N}\sum_{i=1}^{N}(E_i - P_i)^2} \quad (3.24)$$

where $E_i$and P_i are the actual and estimated values, $\bar{E}$ and $\bar{P}$ gives the average values of $E_i$and P_i , and N is the number of total data used.

After completion of training and testing, the most suitable ANN architecture was frozen. This architecture was used to validate the 100 and 98 input-output data sets for the longitudinal and transverse tests, which have not been used previously. Subsequently, the frozen ANN architecture was used for the simulation of creep curves for different combination of stresses and temperatures.

3.4.4 Larson-Miller parametric technique

The Larson-Miller constant $C_{L\text{-}M}$ of Eq. 2.23 was determined from the plot of $\log_{10}(t_r)$ vs. $1/T$. Generally, researchers take the value of $C_{L\text{-}M}$ = 20. This is under the assumption that the plot of $\log_{10}(t_r)$ vs. $1/T$ meet at a single point at $1/T = 0$. However, in the present case, this iso-stress lines were not meeting at a single point. Hence, $C_{L\text{-}M}$ was taken as a linear function

of stress,i.e., $C_{L\text{-}M} = f(\sigma)$. The creep life was determined using $C_{L\text{-}M} = f(\sigma)$ from the L-M master curves. The creep life so obtained was compared with the creep life taking $C_{L\text{-}M} = 20$ for various combinations of stress and temperature.

3.4.5 Monkman-Grant relationships

The creep data were analyzed by the Monkman-Grant relationship using the data obtained from the creep experiments. The terminologies used for analyzing the data are shown schematically in Figure 3.13. The slope of the secondary creep region corresponds to the minimum strain rate $\dot{\varepsilon}_s$. A line drawn tangent to the creep curve showing the minimum creep rate was extended to meet the Y-axis at $t = 0$ and $t = t_r$ at points A and B, respectively. The primary creep strain ε_1 and the secondary creep strain ε_2 are shown by the distance OA and BF, respectively. The total failure strain is given by ε_f, and so the tertiary creep strain ε_3 was calculated as $\varepsilon_f-(\varepsilon_1+\varepsilon_2)$. The time t_{os} and t_{ot} was the time needed for the beginning of secondary creep and tertiary creep region, respectively. The time $t_t = t_r - t_{ot}$ was referred to as the time during the tertiary creep deformation, where t_r is rupture time. The Monkman-Grant ductility (MGD) was the product of $\dot{\varepsilon}_s$ and t_r, which is taken as equal to the secondary creep strain ε_2. The time taken to reach Monkman-Grant ductility(t_{MGD}) was the time taken to attain the tertiary creep strain. According to Eq. 2.22, tertiary creep strain ε_3 and strain to failure ε_f, were expressed in terms of creep damage tolerance factor (λ), minimum strain rate $\dot{\varepsilon}_s$ and rupture time t_r, as shown in the figure. The rupture time predicted using the Monkman-Grant relationships was compared with those obtained experimentally for various combinations of stresses and temperatures.

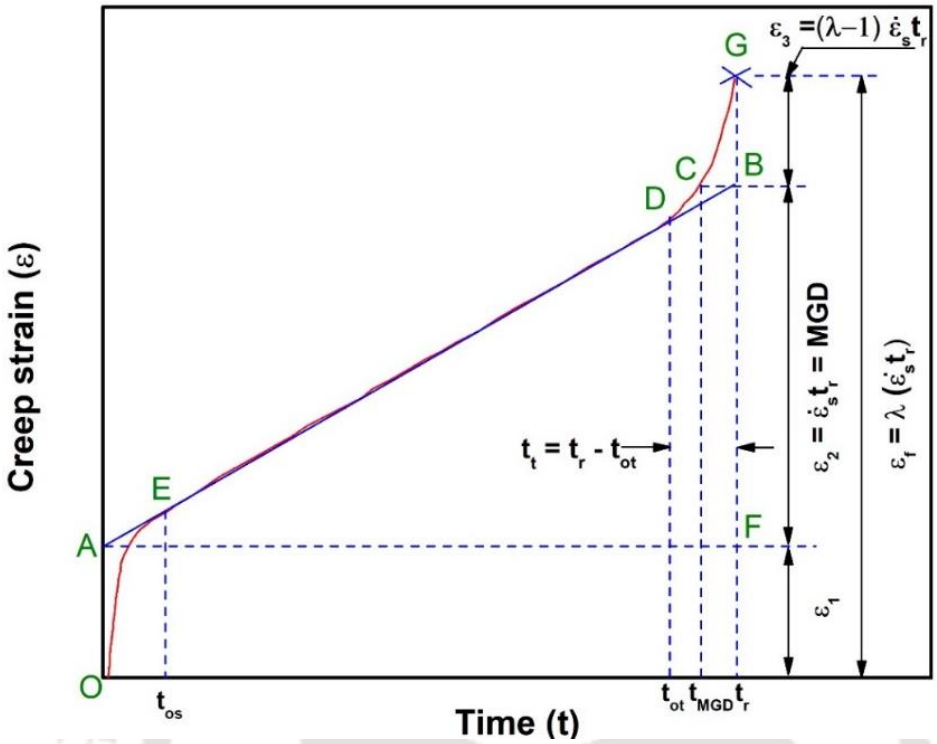

Figure 3.13 A typical creep curve demonstrating the various material parameters used for explaining creep behavior[194].

The methodology adopted for achieving the objectives of the present thesis has been discussed in the current chapter. The results obtained are presented and discussed in detail in chapter 4.

Chapter 4 Results and Discussions

4.1 Introduction

This chapter discusses the results of (a) microstructure characterization by SEM/EDS, TEM, and XRD, (b) tensile properties viz. flow stress, Young's modulus (E), yield stress(YS), ultimate tensile strength (UTS) and strain hardening exponent (*n*) from room temperature to 800 °C, and (c) creep testing under different combination of temperature and stresses. Correlations of the tensile properties with temperature were developed. Creep behavior of the alloy is explained, and parametric models are studied. The creep life of the material is determined using Larson-Miller parametric technique. An investigation is carried out to predict the creep curve of Zr-2.5Nb alloy using Multiple Linear Regression (MLR) and Artificial Neural Network (ANN). Detailed discussions of the results obtained are presented in the following sub-sections.

4.2 Microstructure of the as-received alloy

The microstructure of the as-received alloy was investigated using SEM and TEM, phase identification by XRD and micro-chemical analysis by EDS. Figure 4.1 shows the SEM micrograph of the as-received alloy using a high-definition backscattered electron detector (HDBSD). Two distinct phases are evident: the dark continuous α-Zr phase matrix and the light grey discontinuous Nb-rich β-Zr phase. Similar features are reported in the literature[19, 195]. The XRD pattern shown in Figure 4.1(b) reveals the presence of these two phases. The 2θ values of 35.2°, 36.8°, 48.2°, 57.3°, 63.8°, 68.8°, 73.9°, and 100° correspond to reflections from planes of (0002), $(10\bar{1}1)$, $(10\bar{1}2)$, $(11\bar{2}0)$, $(10\bar{1}3)$, $(11\bar{2}2)$, (0004), and $(11\bar{2}4)$ of α-Zr having a hexagonal close-packed (HCP) structure. The peaks corresponding to the 2θ values of 38.8°, 82.8°, and 96.4° have been identified as reflections from planes of (110), (310), and (222) from the body-centered cubic (BCC) structured Nb-enriched β-Zr phase[196]. The intensity of peaks corresponding to α-Zr is very high compared to the reflections from the β phase, indicating that the alloy is basically α-Zr matrix with minor quantities of β-Zr phase.

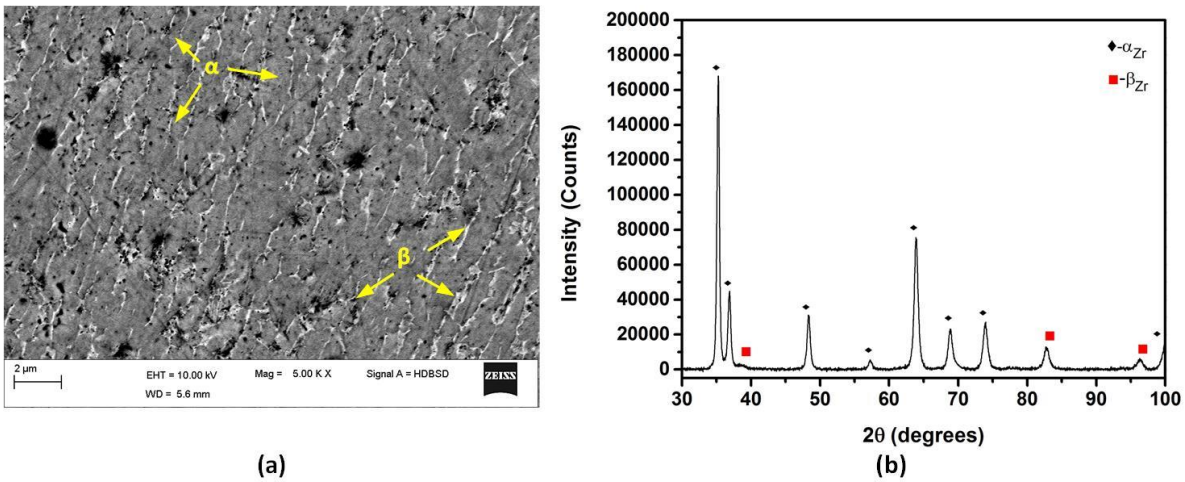

Figure 4.1 (a) SEM micrographs (HDBSD mode) and (b) XRD plot of the Zr-2.5Nb alloy in as-received condition.

The TEM micrograph of the as-received sample is presented in Figure 4.2(a). The figure shows that fine spherical precipitates are distributed uniformly in the matrix. Analysis of the EDS spectrum from the fine particles shown in Figure 4.2(c) reveals that these are Nb-enriched. Figure 4.3(a) depicts the image of the as-received alloy matrix by high-resolution TEM (HRTEM). Analysis of the IFFT image in Figure 4.3(b) estimated the d_{0002} of the α-Zr phase as 2.62 Å, which is almost the same (deviation of only ~2%) as that of the value obtained by the XRD analysis.

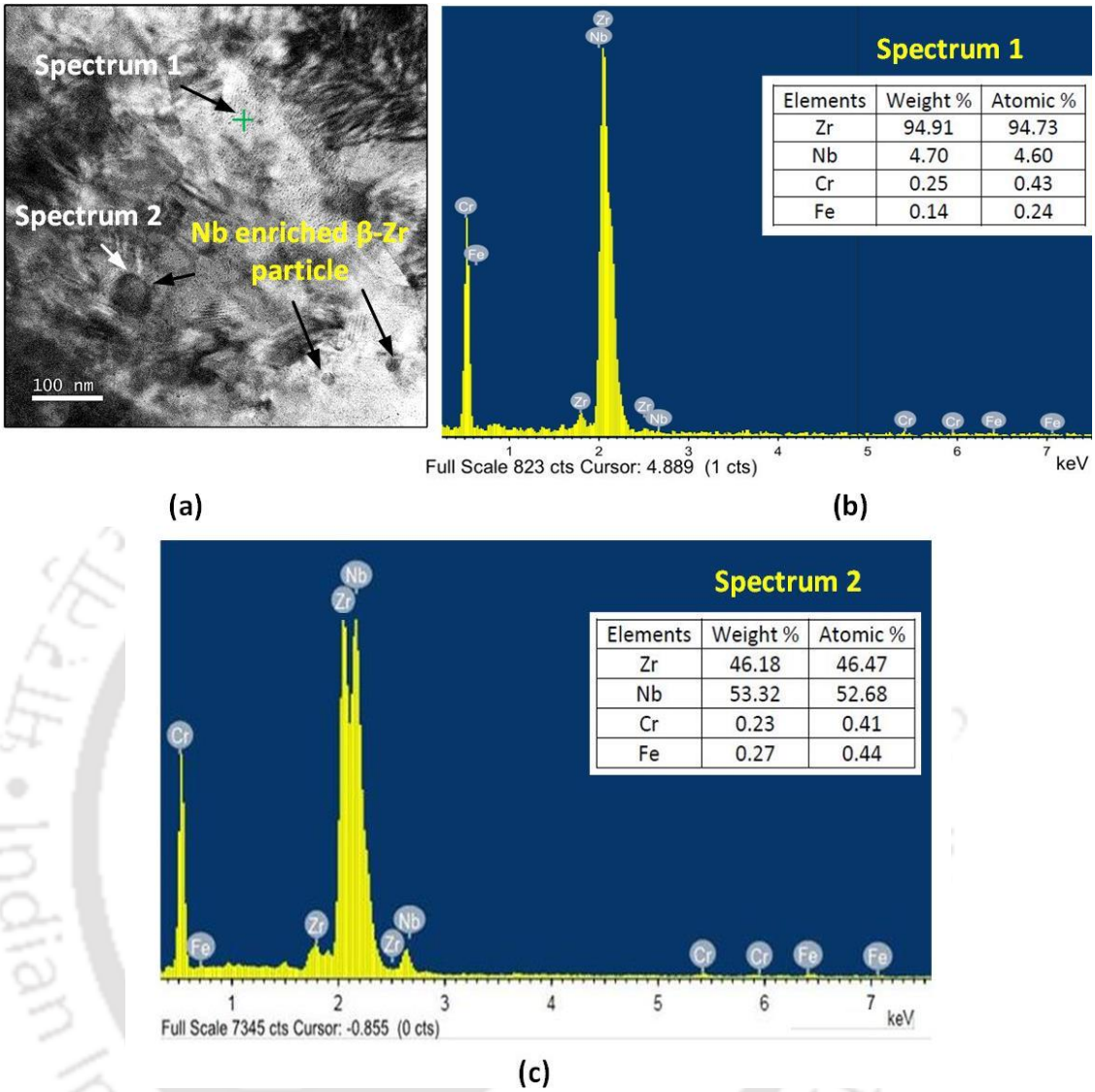

Figure 4.2 (a) TEM micrograph of the as-received sample, EDS spectrum of the (b) matrix and (c) particle marked in (a).

In summary, the as-received alloy is an α-Zr alloy with very small quantities of discontinuous Nb-rich β-Zr particles distributed almost uniformly in the matrix.

4.3 Mechanical properties

4.3.1 Stress-Strain curves

The stress-strain curves obtained from the load-displacement data of the tensile tests carried out at the temperature in the range of 25-800°C for both the longitudinal and transverse samples are given in Figure 4.3 (a) and (b). It can be seen from the figures that the peak flow stress decreased with a rise in temperature. The total tensile ductility increased appreciably in both cases with an increase in temperature. Flow hardening was visible in all the stress-strain

curves during the initial deformation stage. Samples tested at higher temperatures show flow softening upon achieving the peak stress. The tensile properties as a function of temperature are discussed in detail in the subsequent sections.

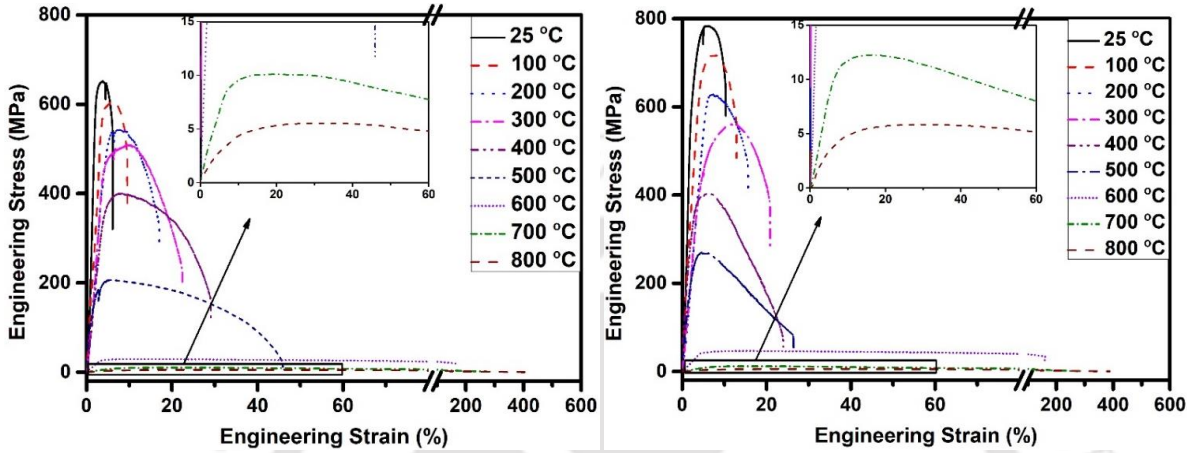

Figure 4.3 Stress-strain plots of the Zr-2.5Nb alloy tested at various temperatures for (a) longitudinal and (b) transverse specimens. The inset shows the stress-strain graphs obtained from tests done at 700 and 800°C.

4.3.2 High-temperature tensile test

The variation in UTS, YS, and ductility with temperature for the longitudinal and transverse specimens is given in Figure 4.4(a-f). In the case of the longitudinal specimen, as the temperature increased from 25°C - 300°C, UTS decreased by ~22% (Figure 4.4(a)). With the rise in temperature from 300°C to 600°C, the UTS drastically decreased by ~ 94%. However, above 600°C, only a marginal decrease was observed. Figure 4.4(b) depicts a similar trend for YS. The YS decreased by ~21% as the temperature was increased to 300°C and decreased further by ~96% as the temperature increased from 300°C to 600°C. From 600°C to 800°C, YS decreased by 7%. In the case of the transverse specimens (Figure 4.4(d)), there was an almost 27% decrease in the value of UTS in the temperature regime of 25-300°C. Between 300-600°C, UTS reduced significantly by ~92%, and above 600°C, the UTS decreased by 9%. The YS variation depicts the same trend (Figure 4.4(e)). The corresponding variation in the YS values for the transverse samples for the exact temperature ranges was ~27%, ~93%, and 8%, respectively. Figures 4.4(d&e) indicate a significant decrease (> 90%) in UTS and YS values beyond 300°C.

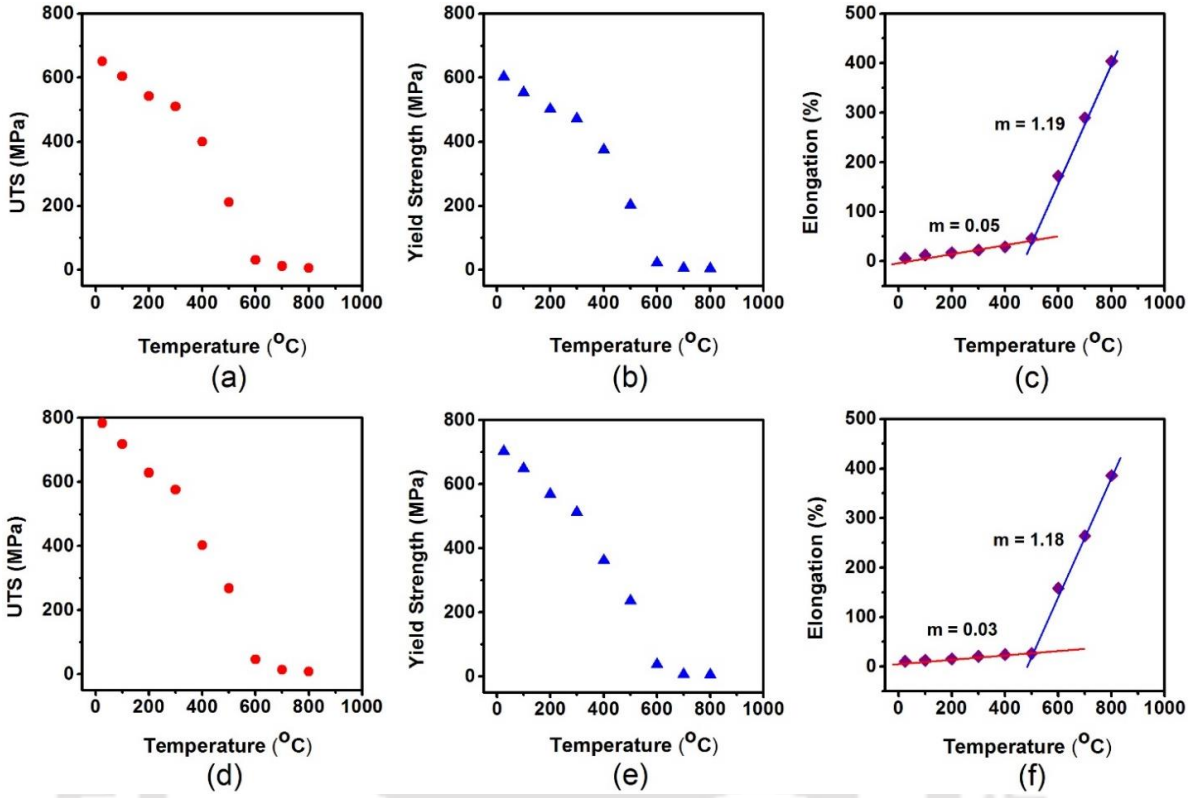

Figure 4.4 Variation of UTS, YS, and % elongation for (**a,b,c**) longitudinal and (**d,e,f**) transverse specimens.

In the case of longitudinal specimens, the percentage elongation increased linearly with an increase in temperature. Figure 4.4(c) shows that the slope of the elongation vs. temperature plot in the temperature region from 25-500°C is 0.05. The percentage elongation increased drastically from ~46 % at 500°C to ~406% at 800°C, indicating that the slope of the plot beyond 500 °C changed to 1.19. A similar trend was observed for the transverse samples (Figure 4.4(f)), where the slopes of the lines were 0.03 and 1.18, respectively, for temperatures up to 500 °C and beyond 500 °C. In the case of transverse samples, the elongation increased from 26 % at 500°C to ~386% at 800°C. From the results obtained, it can be inferred that the Zr-2.5%Nb alloy exhibits superplasticity in the temperature range of 600 °C – 800 °C, which is in agreement with earlier reports [19, 20].

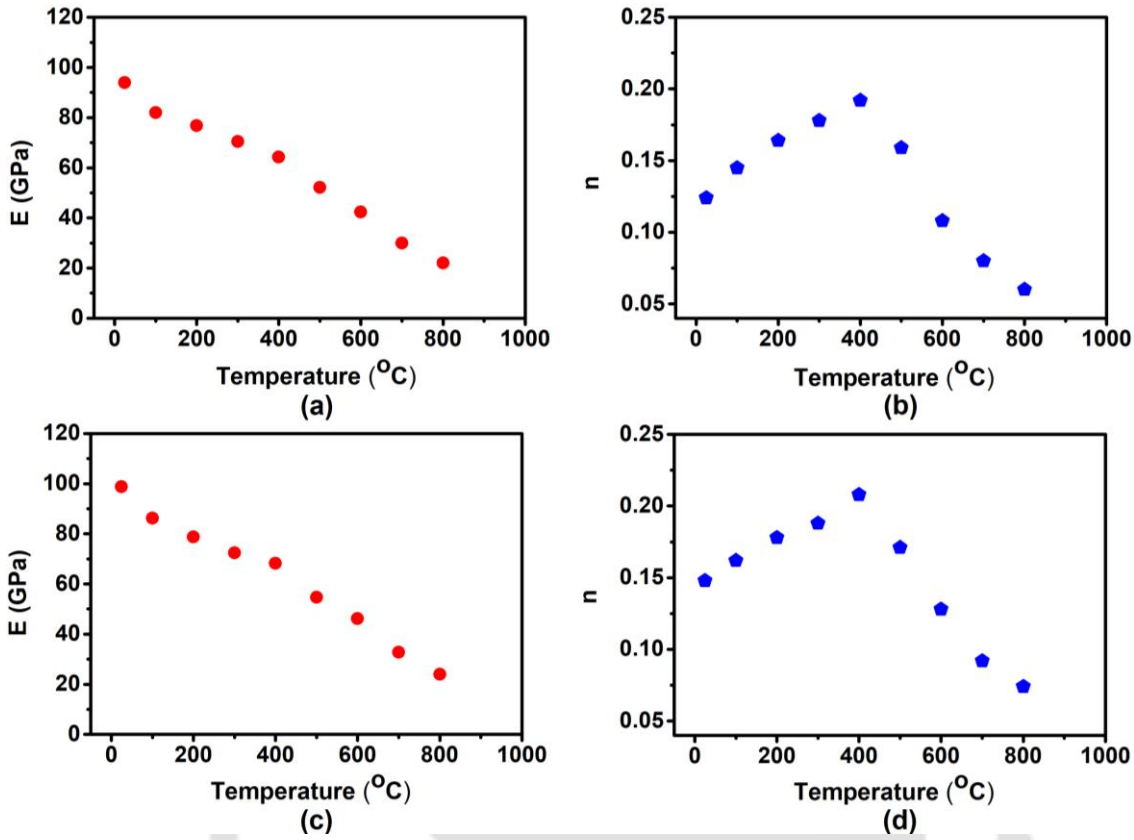

Figure 4.5 Variation of Young's modulus(E) and strain hardening exponent(*n*) with temperature for (**a,b**)longitudinal specimens and (**c,d**) transverse specimens.

The E vs. temperature plot for the longitudinal specimens shown in Figure 4.5(a) demonstrates that between 25-100°C, E is reduced by ~20%. E value decreased by ~52% as the temperature increased from 100 to 600°C. Beyond 600°C, the E value decreased monotonically. The E vs. temperature plot for the transverse specimens, as shown in Figure 4.5(c), demonstrates that between 25-100°C, E was reduced by ~22%. In the temperature range of 100-600°C, E decreased by ~50%. The value of E was ~22GPa at 800°C for both specimen orientations. The E values are comparable to those reported in the literature[197, 198]

The value of the strain hardening exponent (*n*) was calculated from the true stress-true strain plots using the relation,

$$n = \frac{d\log\sigma}{d\log\varepsilon} \tag{4.1}$$

where σ represents true stress corresponding to true strain(ε).The *n*-value was 0.125 and 0.148

for the longitudinal and transverse samples at room temperature. The *n* -value increased almost linearly with temperature and reached a maximum value of 0.19 and 0.21 at 400 °C, respectively (Figure 4.5(b&d)) for the longitudinal and transverse specimens, respectively. Increasing the test temperature further resulted in a decrease in the *n*-value. The respective *n*-values for the longitudinal and transverse specimens are 0.06 and 0.07 at 800 °C. Annihilation of dislocations at elevated temperatures was the primary reason for the decrease in the value of *n.*

The values of YS and UTS for both the longitudinal and transverse specimens decrease at temperatures above 300 ˚C. The flow stress of material at a certain temperature depends on the number of active slip systems at that temperature [8]. In the present alloy, slip generally occurs on the basal plane (0001) along $\langle 11\bar{2}0 \rangle$ direction. At high temperatures, the slip happens on $\{10\bar{1}0\}$ prismatic plane along $\langle 1\bar{2}10 \rangle$ direction[19]. With a rise in temperature, the likelihood of basal slip rises despite the dominance of $\{10\bar{1}0\}$ $\langle 1\bar{2}10 \rangle$ slip systems [19]. Thus, it is seen that more slip systems become available with the rise in temperature, which in turn decreases the flow stress above 300 ˚C. On comparing the tensile behavior of both the longitudinal and transverse specimens, it could be seen that the longitudinal samples showed lower strength but higher ductility at all temperatures. Zr-2.5Nb alloy possesses a duplex microstructure of elongated HCP α-grains surrounded by a nearly continuous BCC β-phase. The α-grains have been reported to be heavily textured, with ~43% and ~54% of the basal poles aligned along the radial and circumferential directions, respectively[6]. Principal slip systems for α-Zr grains are the prismatic planes. The likelihood of deformation of α-grains by prismatic slip is more for the longitudinal specimens(~97%) than the transverse ones(~43%)[19]. As a result, transverse samples exhibited higher strength than longitudinal ones. Bulk of the α-Zr grains does not participate in the plastic deformation in the case of transverse samples[19]. This leads to a large amount of stress concentration at the unfavorably aligned grains, resulting in lower ductility[29]. These differences in the tensile behavior between the specimen orientations indicate that the resistance of the PTs to circumferential expansion is more than the resistance to longitudinal sagging at the test temperatures.

4.3.3 Empirical relationships of temperature dependent tensile properties

An in-depth understanding of the deformation behavior of the PTs with temperature is essential to predict the component's performance in accidental conditions like LOCA.

Empirical relations have been used in the past to study the work-hardening behavior of alloys [199, 200]. However, these did not consider the flow softening behavior and eventually failed to predict the material behavior under LOCA conditions. Singh et al. [19] modeled the flow behavior of this alloy using a constitutive relationship in the temperature range of 25- 550°C. In the present work, the tensile properties obtained have been correlated with a wide range of temperatures for longitudinal as well as transverse samples, as given in Tables 4.1 and 4.2. The empirical relationships generated in the tables can be used to compute the high-temperature deformation behavior, thereby predicting the pressure tube's failure during LOCA. The R^2 value, of the empirical relations is above 0.99 for all the cases indicating a perfect fit. This shows that these equations can be effectively used to model the tensile properties of this alloy over a wide range of temperatures.

Table 4.1 Empirical relations of variation of tensile properties with temperature for longitudinal specimens.

Tensile properties	Temperature (°C)	Correlation	R^2- value (%)
UTS (MPa)	25-500	$UTS = -11 \times 10^{-4}T^2 - 0.4748T + 788.8$	99.08
	600-800	$UTS = 12 \times 10^{-4}T^2 - 1.8762T + 740.16$	99.99
YS (MPa)	25-500	$YS = -11 \times 10^{-4}T^2 - 0.4076T + 706.6$	99.44
	600-800	$YS = 14 \times 10^{-4}T^2 - 2.1276T + 808.64$	99.99
Elongation (%)	25-500	$Elongation = 0.0364T - 0.5588$	99.72
	600-800	$Elongation = 1.1844T - 885.02$	99.84
E (GPa)	25-500	$YM = 3 \times 10^{-6}T^2 - 0.0808T + 93.56$	99.76
	600-800	$YM = 2 \times 10^{-4}T^2 - 0.4026T + 206.4$	99.99
n	25-400	$n = 0.0002T + 0.01454$	99.18
	500-800	$n = 6 \times 10^{-7}T^2 - 0.0012T + 0.586$	99.9

Table 4.2 Empirical relations of variation of tensile properties with temperature for transverse specimens.

Tensile properties	Temperature (°C)	Correlation	R^2 (%)
UTS (MPa)	25-500	$UTS = -7 \times 10^{-6}T^2 - 1.1726T + 680.28$	99.84
	600-800	$UTS = 7 \times 10^{-4}T^2 - 1.048T + 421.6$	99.99
YS (MPa)	25-500	$YS = -14 \times 10^{-4}T^2 - 0.5882T + 868.2$	99.88
	600-800	$YS = 7 \times 10^{-4}T^2 - 1.0804T + 416.6$	99.99
Elongation (%)	25-500	$Elongation = 0.0592T - 10.948$	99.23
	600-800	$Elongation = 1.198T - 874.28$	99.94
E (GPa)	25-500	$YM = 3 \times 10^{-5}T^2 - .0972T + 98.68$	99.37
	600-800	$YM = 2 \times 10^{-4}T^2 - 0.422T + 222.2$	99.99
n	25-400	$n = 0.0002T + 0.0762$	99.93
	500-800	$n = 8 \times 10^{-7}T^2 - 0.0014T + 0.638$	99.8

4.3.4 Effect of temperature and sample orientation on the σ–ε and φ–σ behavior

True stress-true strain(σ–ε) data are shown in Figure 4.6 (a) and (b) for both specimen orientations. A systematic decrease is observed in the flow stress with the rise in temperature. For transverse samples, although the flow stress was higher than that of the longitudinal ones at all temperatures, its ductility was less as compared to the longitudinal ones. This type of behavior of Zr-2.5Nb alloy has been reported before by Singh et al. [19]. The variations of φ with σ $\left(=\frac{d\sigma}{d\varepsilon}\right)$ in the temperature range of 25-600°C shown in Figure 4.7(a and b) depicts two stages of work hardening. Persistent reduction in φ with the increase in stress reflects stage-III work hardening as defined by the Kocks-Mecking approach [90, 91]. The effect of temperature on the behavior of σ–ε and φ –σ brings out three separate temperature regimes that are in line with those reported for the Zr-2.5Nb alloy [19, 201]. The phenomenon of dynamic strain aging (DSA) has been identified as the underlying reason for this type of behavior in this particular alloy. From Figure 4.7 (a) and (b), it is seen that the slopes of φ – σ plots increase with temperature rise, particularly in stage III of strain hardening. A sudden drop in the flow stress and a quick change in φ –σ at lower stresses with the rise in temperature is also observed. The dominance of recovery processes has been reported as the underlying phenomenon behind this behavior in this particular alloy [19].

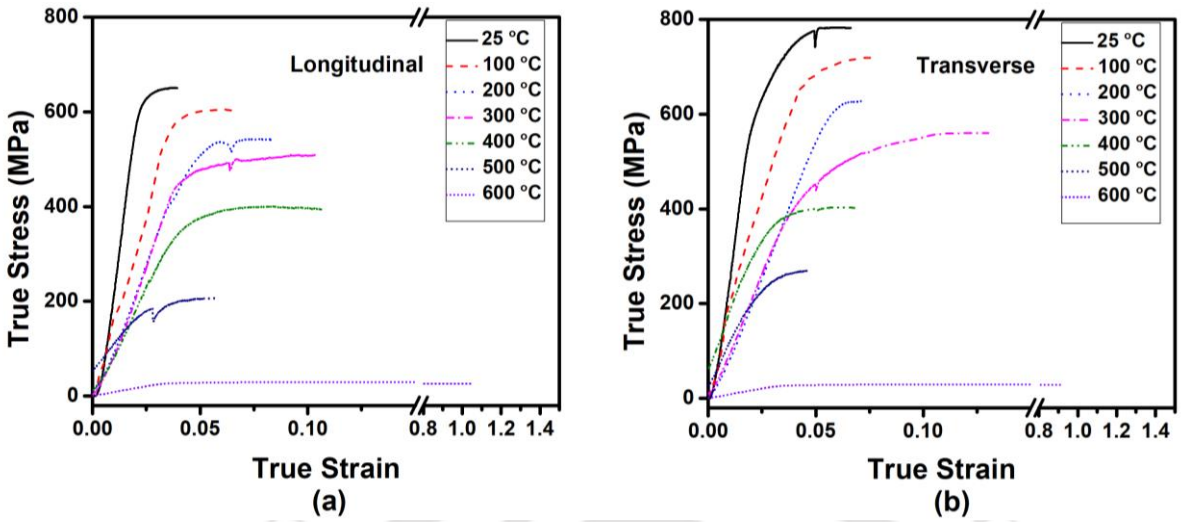

Figure 4.6 Plot of σ vs. ε for (a)longitudinal and (b) transverse samples.

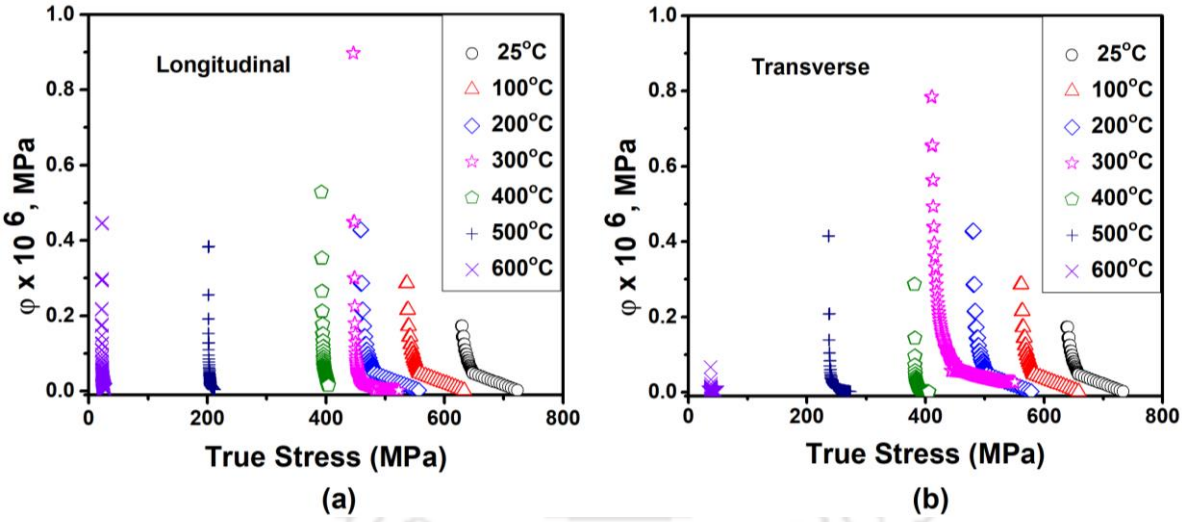

Figure 4.7 Plot of φ vs. σ for (a) longitudinal and (b) transverse samples

4.3.5 Variation of strain hardening parameters with temperature

For Zr-2.5Nb alloy, the variation of strain hardening parameters with respect to temperature was determined for both longitudinal and transverse directions and is shown in Figure 4.8. These include initial work hardening rate ($\varphi_{o,\,K\text{-}M}$), saturation stress ($\sigma_{s,\,K\text{-}M}$), and rate of decrease of strain hardening with stress ($n_{v,\,K\text{-}M}$) obtained by the K-M model. Since the modulus of elasticity (E) was measured at the specific test temperatures the normalized values of the work hardening parameters were taken. The change in the rate of normalized initial

strain hardening ($\varphi_{o,\,K\text{-}M}/E$) showed a rise of ~ 46% from 25-200°C (Figure 4.8 (a)). Between 200-300°C, $\varphi_{o,K\text{-}M}/E$ varied by ~ 4%, followed by a rise of ~ 198% above 300°C. The difference in the value of $\varphi_{o,K\text{-}M}/E$ between transverse and longitudinal samples increased rapidly above 500°C. It can be observed from Figure 4.8 (b) that $\sigma_{s,K\text{-}M}/E$ decreased by ~ 20% between 25-200°C. Further increase in the temperature showed that the value of $\sigma_{s,K\text{-}M}/E$ increased by about ~ 80% above 300°C. The rate parameter $n_{v,K\text{-}M}$ showed a rise of ~ 44% from 25-200°C, followed by a rapid rise of ~ 122% above 400°C (Figure 4.8(c)). However, in all the cases it is seen that the value of $n_{v,K\text{-}M}$ for the longitudinal samples is less than that of the transverse ones. All the variations in the parameters of strain hardening calculated with the K–M method showed plateaus in the temperature range of 200-300°C rather than a monotonic decrease. The graph of flow stress and work-hardenability of some alloys display plateaus in certain ranges of temperatures, which is observed in the present case[202, 203].

In the present study, a sharp rise in $\varphi_{o,\,K\text{-}M}/\mathrm{E}$ and $n_{v,\,K\text{-}M}$ value with a concomitant drop in $\sigma_{s,\,K\text{-}M}/E$ is observed at elevated temperatures (Figure 4.8(a),(c),(b)). Similar trend was observed in 9Cr-1Mo ferritic steel and P9 steel [93, 96, 97], where the sudden rise in $\varphi_{o,K\text{-}M}$ /E and $n_{v,\,K\text{-}M}$ values were attributed to the mechanism of deformation control changing from cross-slip to dislocation climb. In Figure 4.8 (d), the variation of normalized true yield strength (σ_Y/E) with respect to temperature has been shown. A systematic sharp decrease in σ_y/E with the temperature above 300°C for both the longitudinal and transverse samples are clearly evident in Figure 4.8 (d). The plastic portion of stress normalized by Young's Modulus ($(\sigma_{S,K\text{-}M} - \sigma_Y)/E$) with temperature for both samples is shown in Figure 4.8 (e). The figure reveals higher values of the plastic component of the saturation stress at all temperatures for the transverse samples. The increased work-hardening characteristics of the transverse samples at all temperatures agree with previously reported findings for the Zr-2.5Nb alloy [19, 189, 201].

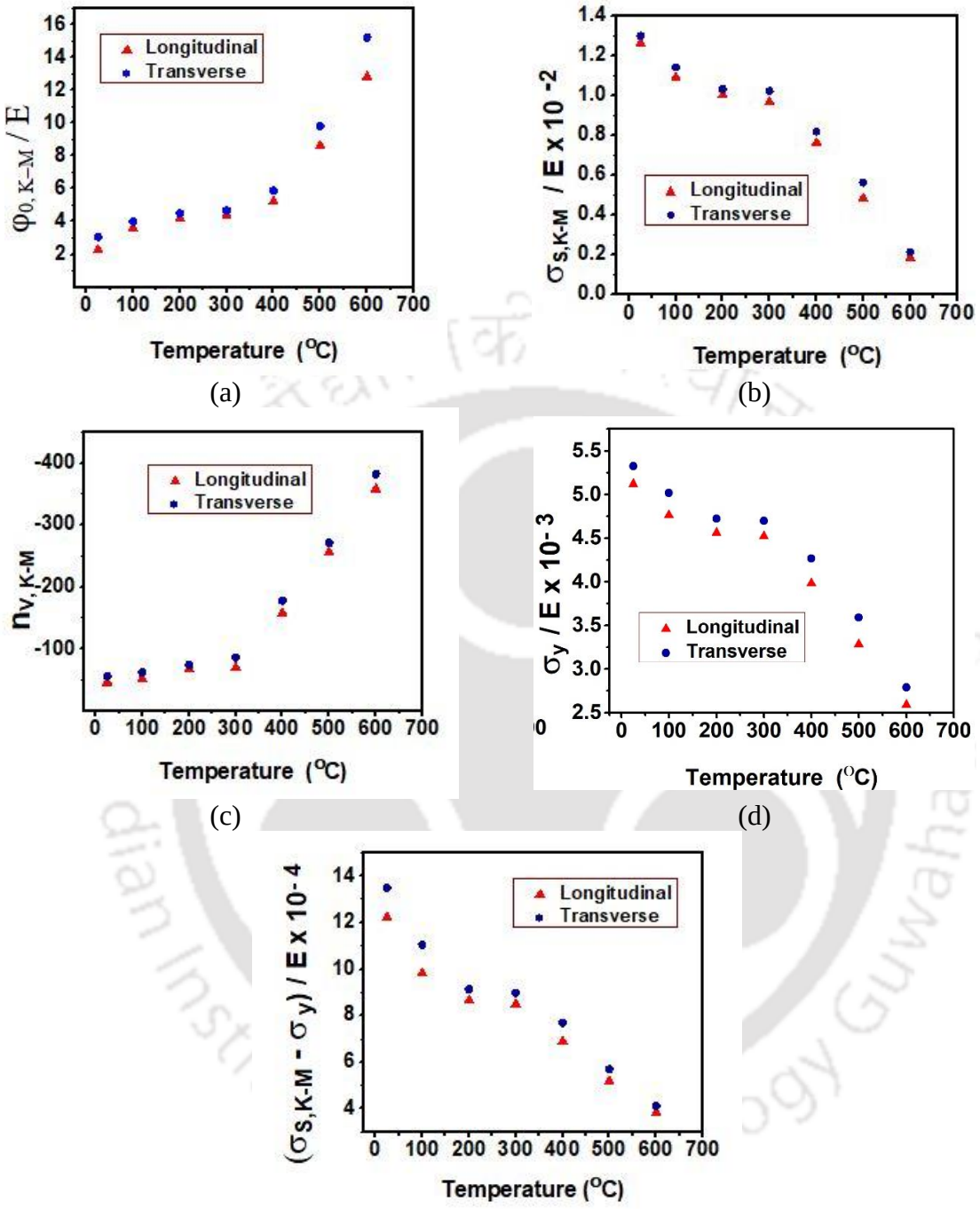

Figure 4.8 Variation of (a) $\varphi_{o,\,K\text{-}M}/E$, (b) $\sigma_{s,\,K\text{-}M}/E$, (c) $n_{v,\,K\text{-}M}$, (d) σ_Y/E, (e) $(\sigma_{s,\,K\text{-}M} - \sigma_Y)/E$ with respect to temperature for Zr-2.5Nb for the longitudinal and transverse samples.

4.3.6 Microstructure of Zr-2.5Nb alloy tensile tested at 800°C

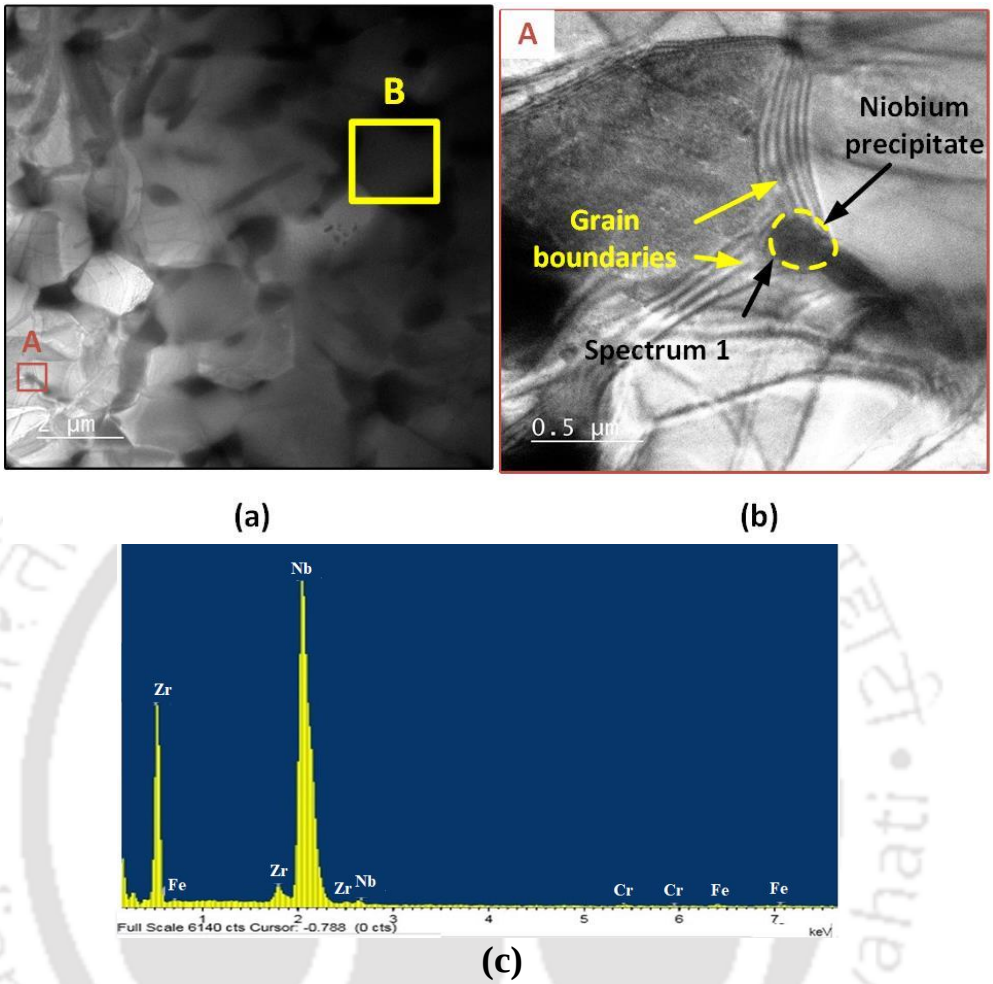

Figure 4.9 (a) Bright-field TEM micrographs of sample tensile tested at 800°C, (b) Magnified image of inset **A** showing the presence of grain boundaries and Niobium precipitates. (c) Point EDS of the precipitate.

TEM micrograph of the sample, tensile tested at 800°C, is shown in Figure 4.9(a). Figure 4.9(b) presents a magnified view of a portion of Figure 4.9(a). EDX analysis of the particle at grain boundaries reveals it as Nb- enriched, as shown in Figure 4.9(c). The X-ray elemental mapping of the area inset labelled B in Figure 4.9(a) depicts Nb- enriched particles distributed around the grain boundaries along with Zirconium, Chromium, and Iron, as shown in Figure 4.10.

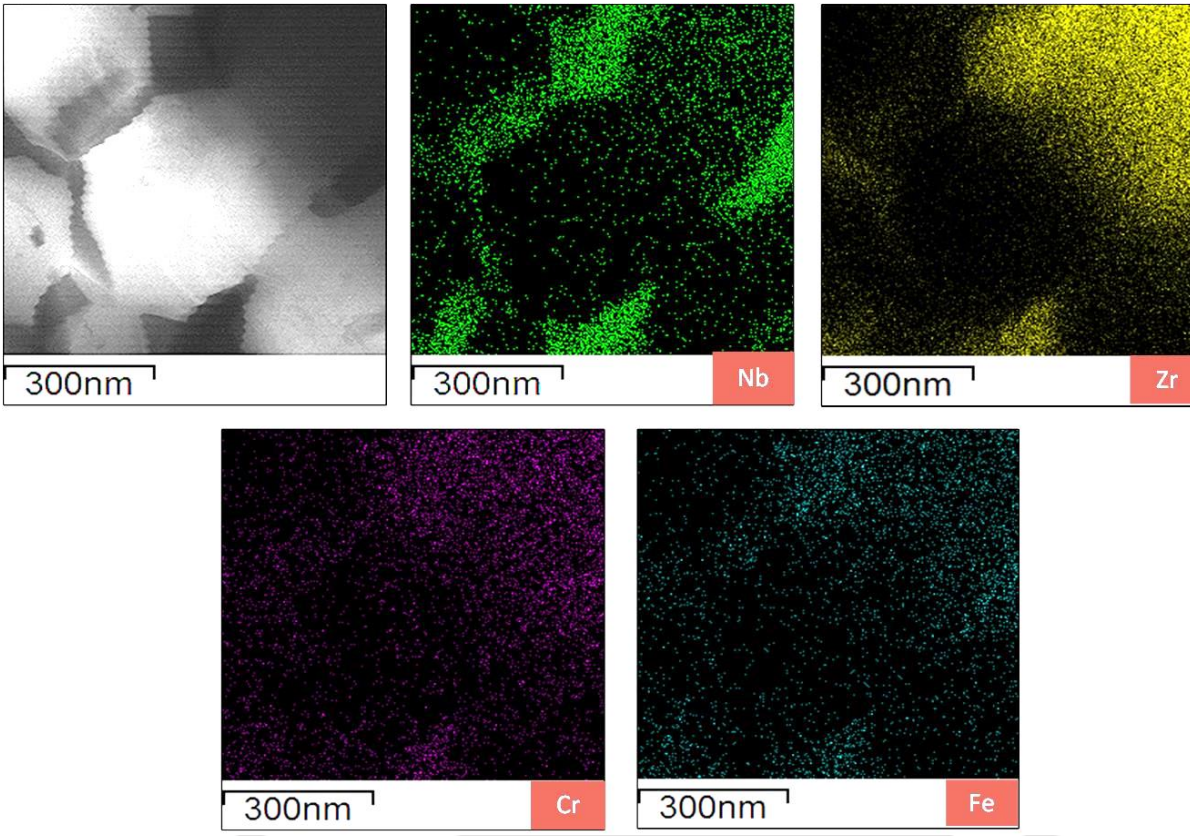

Figure 4.10 EDS mapping of inset **B** of Fig 4.9 (a) shows Niobium, Zirconium, Chromium, and Iron distribution at grain boundaries.

The general conditions accepted by researchers for achieving structural superplasticity are: (i) microstructure consists of two phases: a hard discontinuous phase surrounded by a soft ductile phase; (ii) fine grain size (< 5 µm); (iii) deformation taking place at low strain rates and high temperatures and (iv) high strain rate sensitivity at the deformation temperature[29, 204]. At 800°C, the α- phase grains became equiaxed with an average size of ~2µm (Figure 4.9(a)). TEM micrograph of the as-received sample revealed uniform distribution of Nb-enriched precipitates in the matrix (Figure 4.2(a)). Literature reveals that the BCC β-phase is softer than the HCP α-phase[6, 205]. At localized regions, harder α- phase grains are seen to have become enveloped by the softer β-phase. Grain-boundary sliding along with grain rotation increases the curvature of the α – grains, leading to the formation of β-phase around the α -phase grains [7].

According to the Zr-Nb phase diagram, the β-phase increases with the rise in temperature, and the alloy exist as a dual phase (α Zr + β Zr) in the temperature range of 600-800°C[6]. The volume fraction of the β-phase is ~30% at 800°C [206]. i.e., envelopment of α-phase by

the β-phase is more prevalent at higher temperatures. Singh et al. [7] proposed that after a certain amount of deformation, α-grains become rounded, as observed in the present study, and the β-phase forms an envelope around the α-grains. Subsequently, due to the localized deformation of the β-phase, superplastic deformation prevails by grain boundary sliding [207, 208].

4.3.7 Fractography

Fractography of tensile-tested samples at different temperatures is given in Figure 4.11. At 200°C, the fractographs of both longitudinal and transverse specimens displayed dimple features indicating ductile fracture (Figure 4.11(a)&(b)). The ductility of the alloy increased with increase in temperature. In the case of the longitudinal specimen, a significant portion of the grain boundaries is parallel to the load axis, whereas it is normal to the load axis in the case of the transverse specimen. The features in Figure 4.11(c) reveal the failure of longitudinal samples by microvoid coalescence at 600 °C. However, voids are present at grain boundary regions in the transverse tensile surface tested at 600 °C (Figure 4.11(d)). The fracture features also reveal intergranular failure in the transverse specimen. This is mainly because the grain boundaries are oriented normal to the tensile load axis, thereby favoring grain boundary failure. This results in lower ductility in the transverse specimen compared to that in the longitudinal specimen.

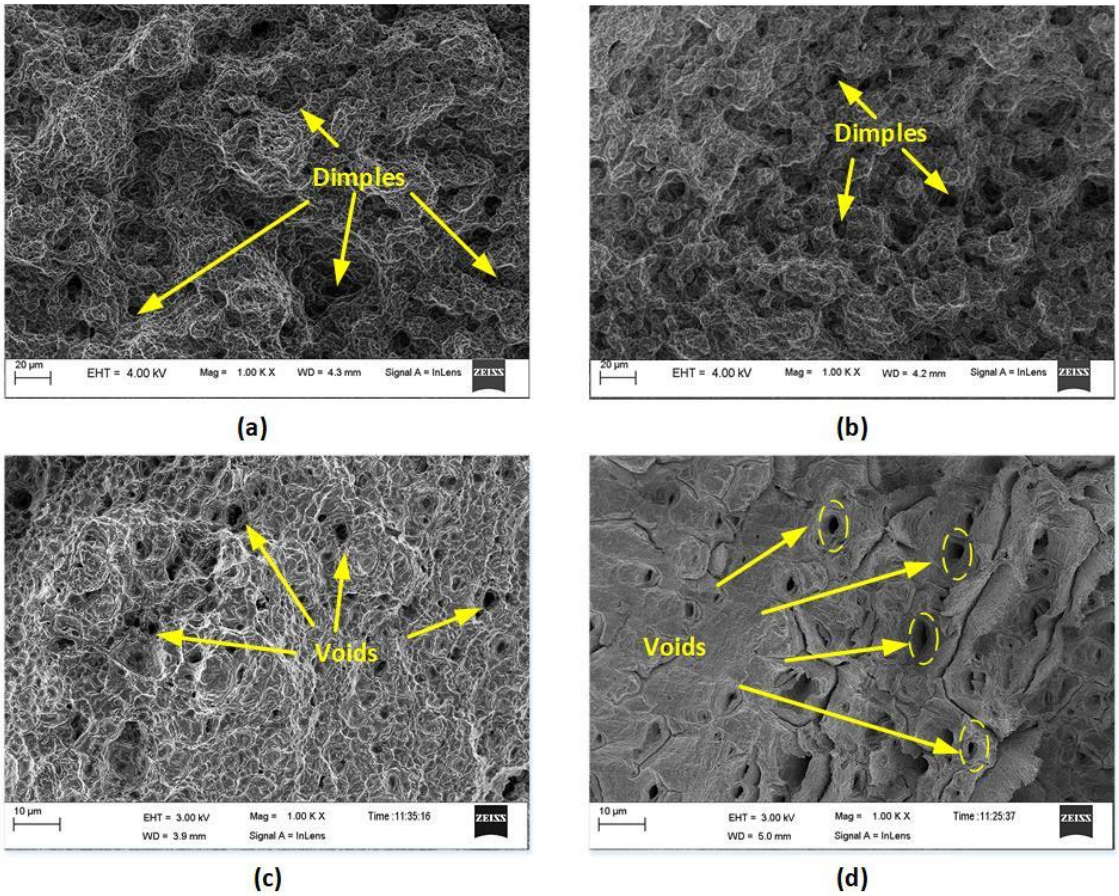

Figure 4.11 Fractographs of samples tensile tested at (a&b)- 200°C, (c&d)-600°C. **a**, **c** are of longitudinal specimens, and **b**,**d** of transverse specimens.

4.3.8 Strain rate jump test

Figure 4.4 (c) and (f) indicates the possibility of superplastic deformation at temperatures above 500 °C. Strain rate sensitivity (*m*) is a critical parameter for superplastic deformation, as its value characterizes the ability of an alloy to resist necking during deformation. Hence the strain rate jump tests were carried out at temperatures in the range 600 °C to 800 °C, and the value of *m* is determined by the σ vs $\dot{\varepsilon}$ data using Eq. 4.2:

$$m = \left(\frac{\partial \log \sigma}{\partial \log \dot{\varepsilon}}\right)_T \tag{4.2}$$

where T is the temperature in Kelvin. Flow stress values were obtained from the strain rate jump test done in the strain rate range of 2×10^{-3}- 4×10^{-2} s^{-1}, as shown in Figure 4.12(a). The corresponding σ - $\dot{\varepsilon}$ is plotted in the logarithmic scale as given in Figure 4.12(b). The maximum value of *m* = 0.68 is observed at 800°C in the case of the longitudinal specimen. However, for the transverse sample *m* decreases with decrease in temperature and attains a

lowest value of 0.31 at 600°C. The activation energy for deformation was determined using the expression:

$$Q = \frac{R}{m}\left(\frac{\partial \log \sigma}{\partial \left(\frac{1}{T}\right)}\right) \tag{4.3}$$

where R is the universal gas constant (kJ/mol K). Figure 4.13 shows the plot of peak stress vs. 1/T for different strain rates. The calculated activation energy for superplastic deformation is in the range of 162 to 236 kJ/mol for the longitudinal orientation and 142-208 kJ/mol for the transverse orientation. In the strain rate range of 2×10^{-2} to 4×10^{-2} s^{-1}, the scatter in the value of activation energy is around 14%, and in the range of 2×10^{-3} to 4×10^{-3} s^{-1}, the scatter is about 8%. Rodchenkov et al.[189] reported an activation value of 202 kJ/mol in the $(\alpha + \beta)$ region at 10^{-4} s^{-1}. The value of Q decreased with the rise in temperature, suggesting that the barrier to deformation decreased with an increase in temperature.

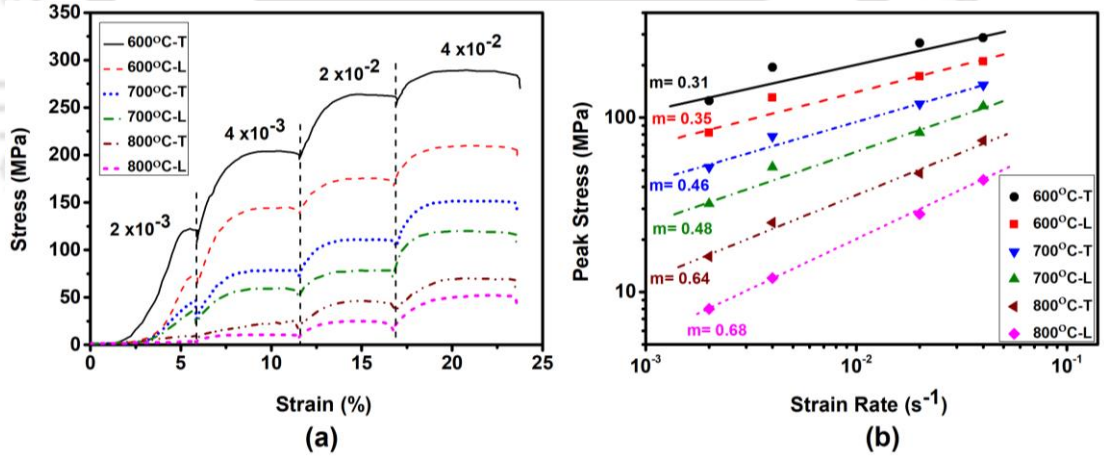

Figure 4.12 (a) Strain rate curves for Zr-2.5Nb alloy deformed at various temperatures and strain rates, (b)plot showing the variation of peak stress vs strain rate at various temperatures. L and T denote longitudinal and transverse specimens, respectively.

The higher the strain rate sensitivity value, the higher the superplastic elongation [209]. When the strain rate sensitivity becomes ~0.5, grain boundary sliding (GBS) becomes the primary deformation mechanism during superplastic flow [209, 210]. Considering superplastic deformation as $m \geq 0.38$, the superplasticity sets in at ~622°C and ~636°C for longitudinal and transverse samples, respectively. According to the Zr-Nb phase diagram, the β-phase in the $\alpha + \beta$ region of the alloy increases with the rise in temperature[211]. An

increase in the volume fraction of the β phase with temperature increases the strain rate sensitivity during superplastic deformation[212].

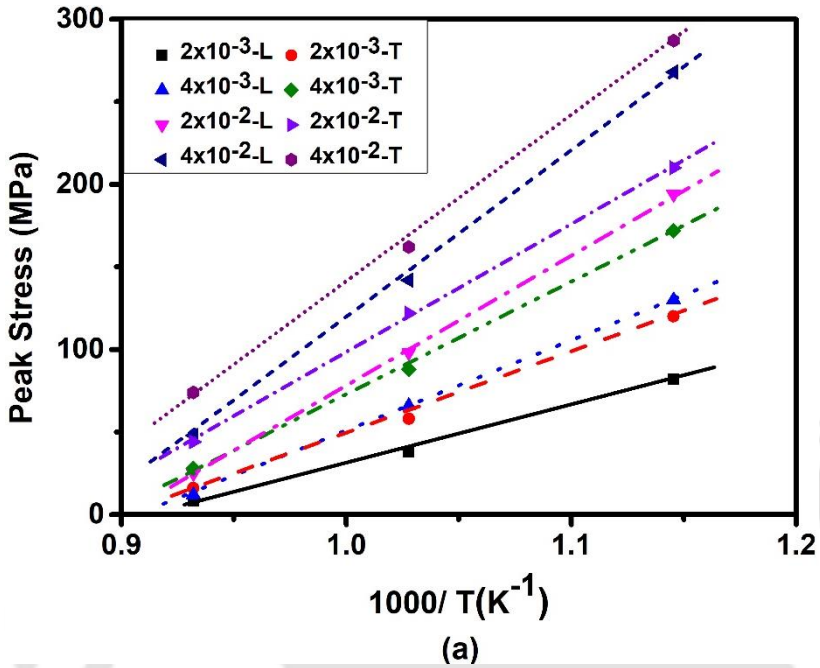

Figure 4.13 Plots of peak stress vs. 1/T for various strain rates. L and T denote longitudinal and transverse specimens, respectively.

At elevated temperatures, the higher volume fraction of the *β* phase primarily governs the superplastic deformation. Studies on Ti–6Al–4V alloys have shown that the β-phase controls the superplastic deformation in the dual-phase region[213]. The strain rate jump tests were carried out in the superplastic deformation domain of the specimen. When the value of *m* is around 0.3, the mechanism of superplastic deformation is primarily grain boundary sliding, accompanied by an accommodation mechanism [204, 214, 215]. This accommodation process, in turn, is controlled by diffusive mechanisms involving either/or grain boundary, phase boundary, or lattice. In the present study, in the strain rate range of 2×10^{-3}- 4×10^{-3} s^{-1}, the activation energy values are in the range of 224-236 and 198-208 kJ/mol for longitudinal and transverse samples, respectively. Literature reveals that the activation energy for lattice diffusion for Zr and Nb in β-Zr and Zr in α-Zr is around 212, 243, and 190 kJ/mol, respectively[67]. For the strain rate range of 2×10^{-2}- 4×10^{-2} $s^{-1,}$ the *Q*-values are in the range of 162-184 and 142-172 kJ/mol for the longitudinal and transverse specimens, respectively. The activation energy for grain boundary diffusion for Nb in *β*-Zr is 145 kJ/mol[67]. Based on the obtained *Q*-values, it can be attributed that the accommodation mechanism at high

strain rates is controlled by a combination of grain boundary and lattice diffusion, whereas, at a lower strain rate range, it is by lattice diffusion for the tested temperature domain.

4.4 Creep Test

The findings of the creep tests conducted on longitudinal and transverse samples of Zr-2.5Nb alloy tubes are presented and discussed in this section. Comparison between the load-displacement curve obtained during experiments with the theoretical load-displacement curve is presented. Typical creep curves obtained for each test condition are illustrated. Analysis of the creep curves and modeling using constitutive equations, Monkman-Grant and modified Monkman-Grant relationship, Larson-Miller parameter, and machine learning techniques are presented and discussed in the subsequent sub-sections.

4.4.1 Load-Displacement behavior

The load vs. displacement graphs obtained from the longitudinal and transverse creep tests on Zr-2.5Nb alloy at various temperatures and stresses are shown in Figures 4.14 and 4.15. The maximum percentage deviation from the required values and RMS error for some of the creep tests are given in Tables 4.3 and 4.4, indicating a satisfactory value. The R^2 values for all the cases are more than 0.99, which shows that the variation of the theoretical load-displacement curve with that of the curve obtained during experiments is within acceptable limit.

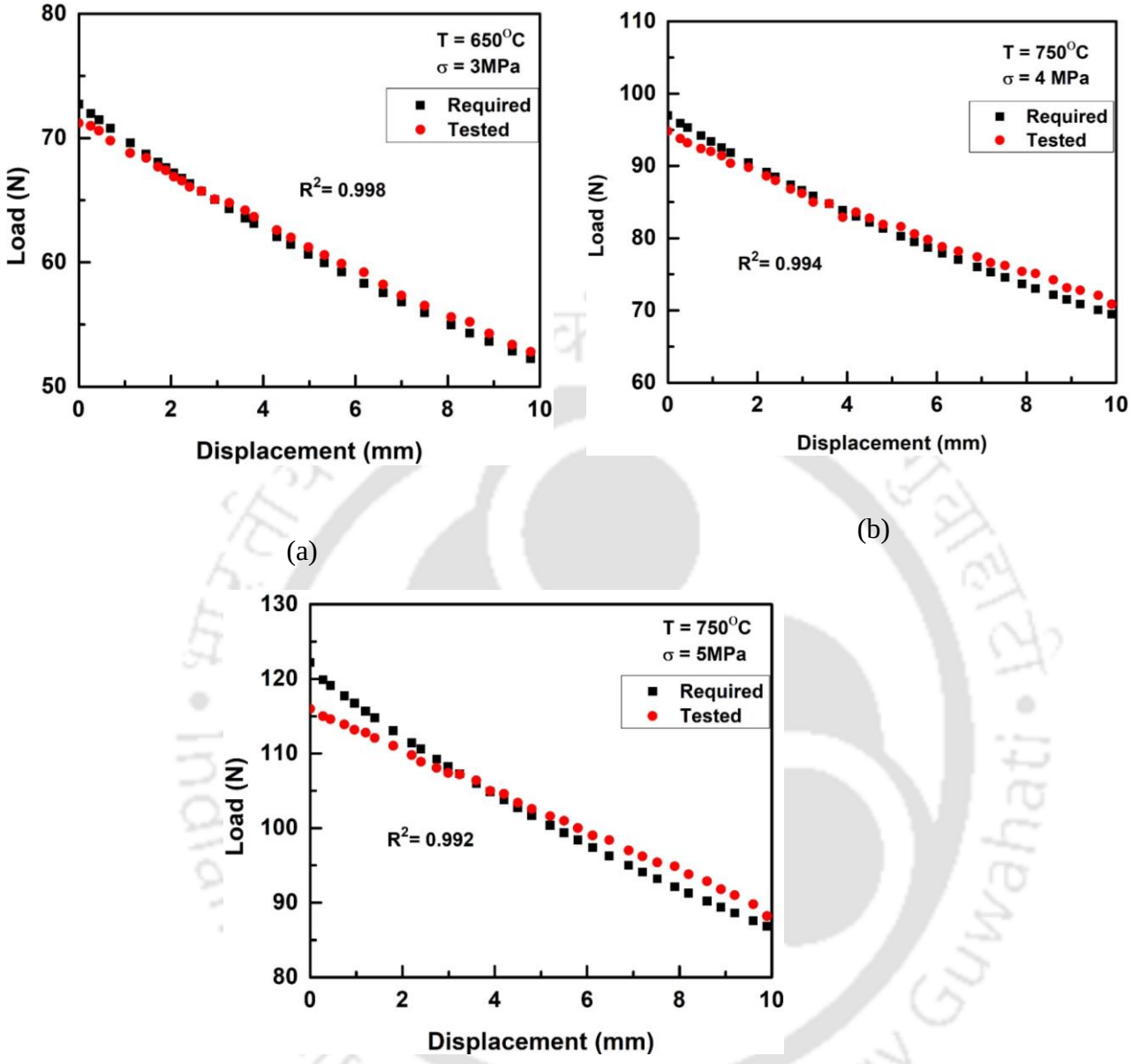

Figure 4.14 Load vs. displacement plot for creep tests carried out at (a) 650 °C/3 MPa, (b) 750 °C/4 MPa, and 750 °C/5 MPa.

Table 4.3 Maximum percentage deviation and RMS error for various true stresses and temperatures for longitudinal creep tests.

True Stress (MPa)	Temperature (°C)	Maximum deviation (%)	RMSE
3	650	+2.2 -1.6	0.66
4	750	+2.18 -2.86	1.28
5	750	+5.08 -3.22	2.4

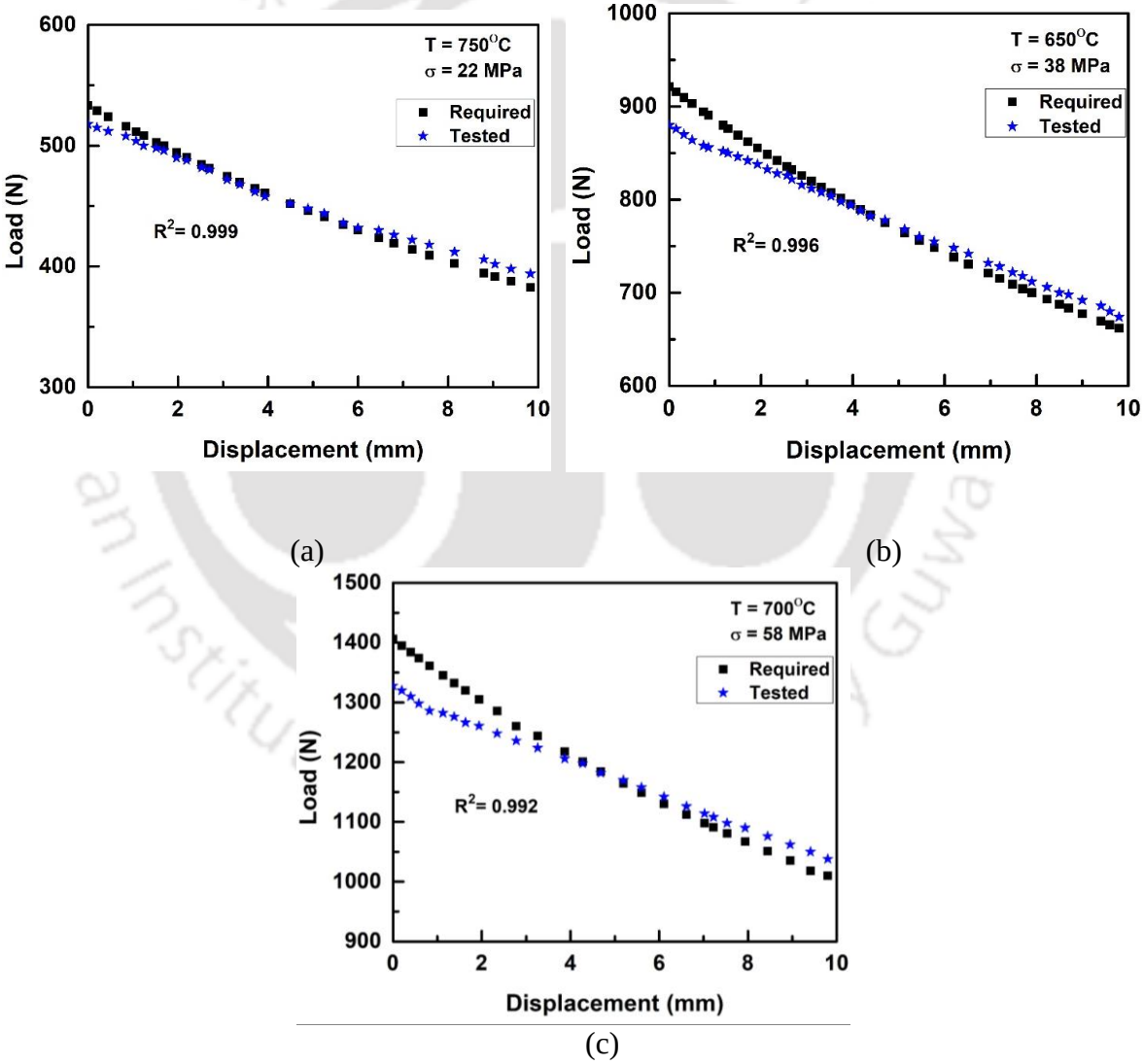

Figure 4.15 Load vs. displacement plot for creep tests carried out at (a) 750 °C/22 MPa, (b) 650 °C/38 MPa, and 700 °C/58 MPa.

Table 4.4 Maximum percentage deviation and RMS error for various true stresses and temperatures for transverse creep tests.

True Stress (MPa)	Temperature (°C)	Maximum deviation (%)	RMSE
22	750	+2.8 -2.9	7.46
38	650	+4.08 -4.34	18.4
58	700	+5.58 -4.24	38.78

4.4.2 Creep curves

The creep curves generated from the experimental load-displacement data obtained for the longitudinal samples tested at different stress and temperature are shown in Figures 4.16 to 4.19. The test temperature and applied stresses affect the nature of the creep curves. From the creep curves of both the longitudinal and transverse creep tests, the following observations are made:

- The failure time decreased with an increase in temperature at a specified applied stress.
- At a given temperature, an increase in applied stress reduced the failure time.
- The three distinct creep regions are observed for low or intermediate applied stresses and temperature combinations.

Figure 4.16 shows the creep curves of Zr-2.5Nb alloy tested at 2MPa stress and temperatures of 700°C, 800°C, and 850°C. At 700°C, the three creep regions are distinct. The transition between the primary and the secondary creep region is more prominent at this temperature. The creep curve enters the tertiary creep region after reaching a strain of 0.32. The total rupture strain at this combination of stress and temperature is 0.44. From Fig. 4.16, it can be seen that the steady state creep rate keeps increasing with the rise in temperature. Similar pattern was observed in the creep curves obtained when tested at 3 MPa, 4 MPa, and 5 MPa.

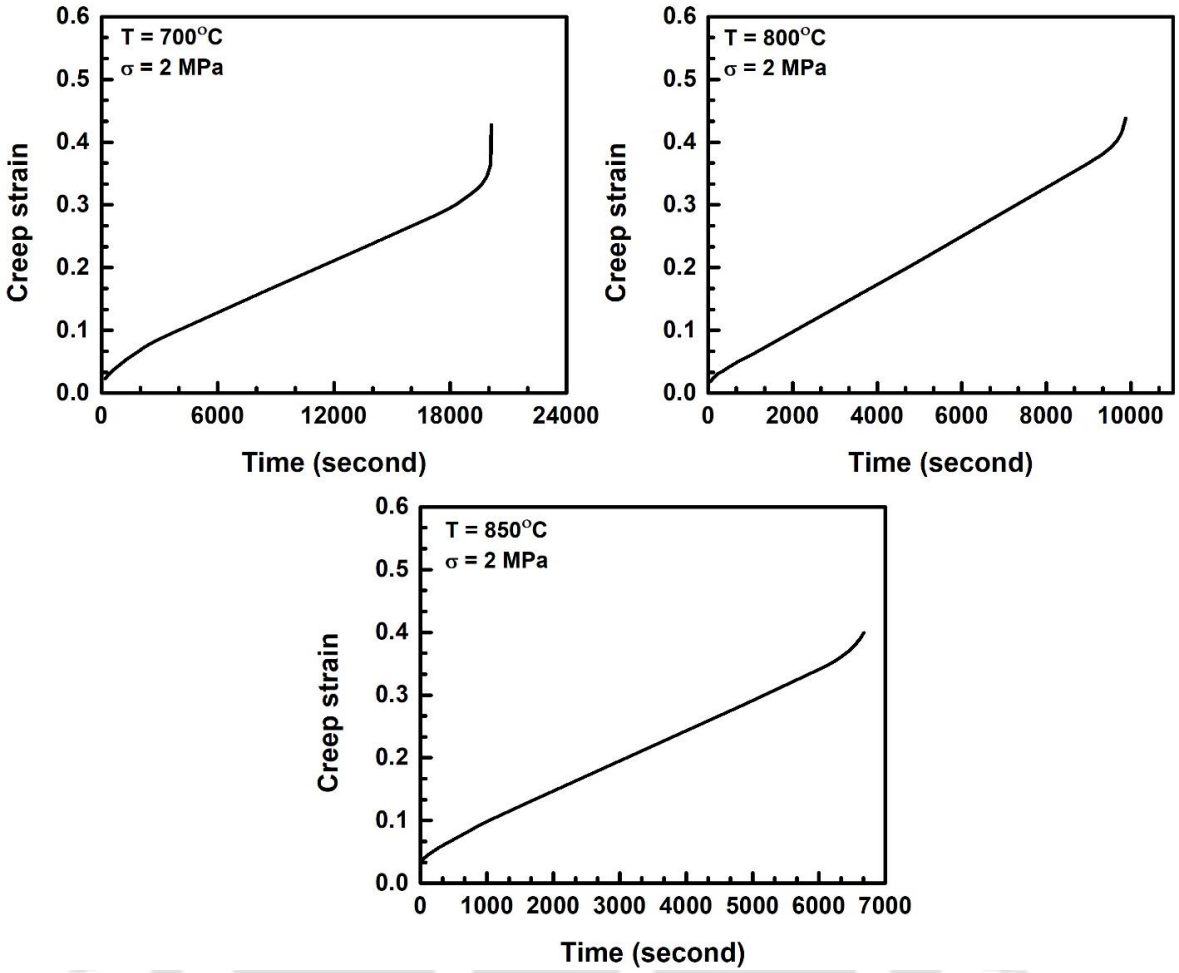

Figure 4.16 Typical creep curves obtained from experiments conducted on longitudinal samples at stresses of 2 MPa for different temperatures.

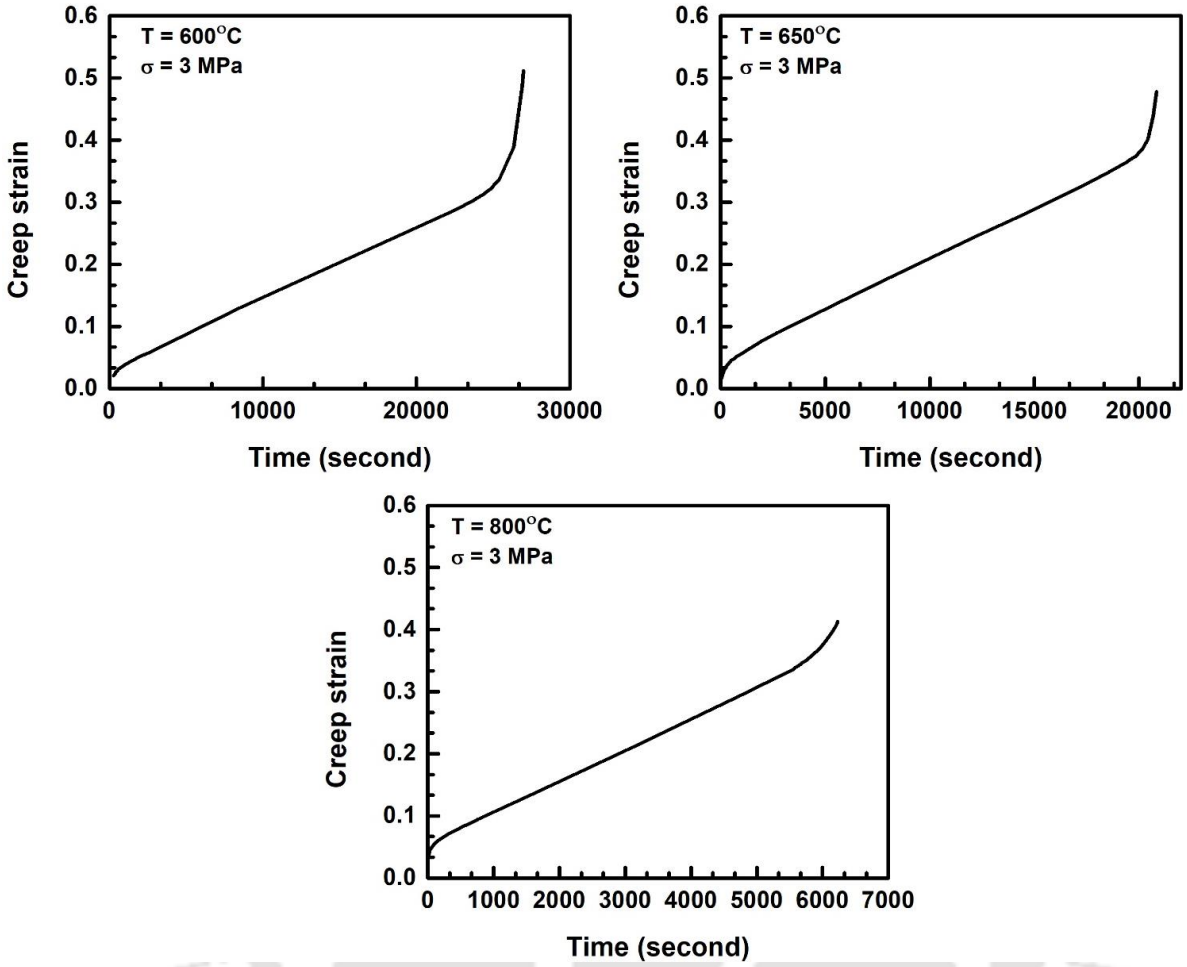

Figure 4.17 Typical creep curves obtained from experiments conducted on longitudinal samples at stresses of 3 MPa at different temperatures.

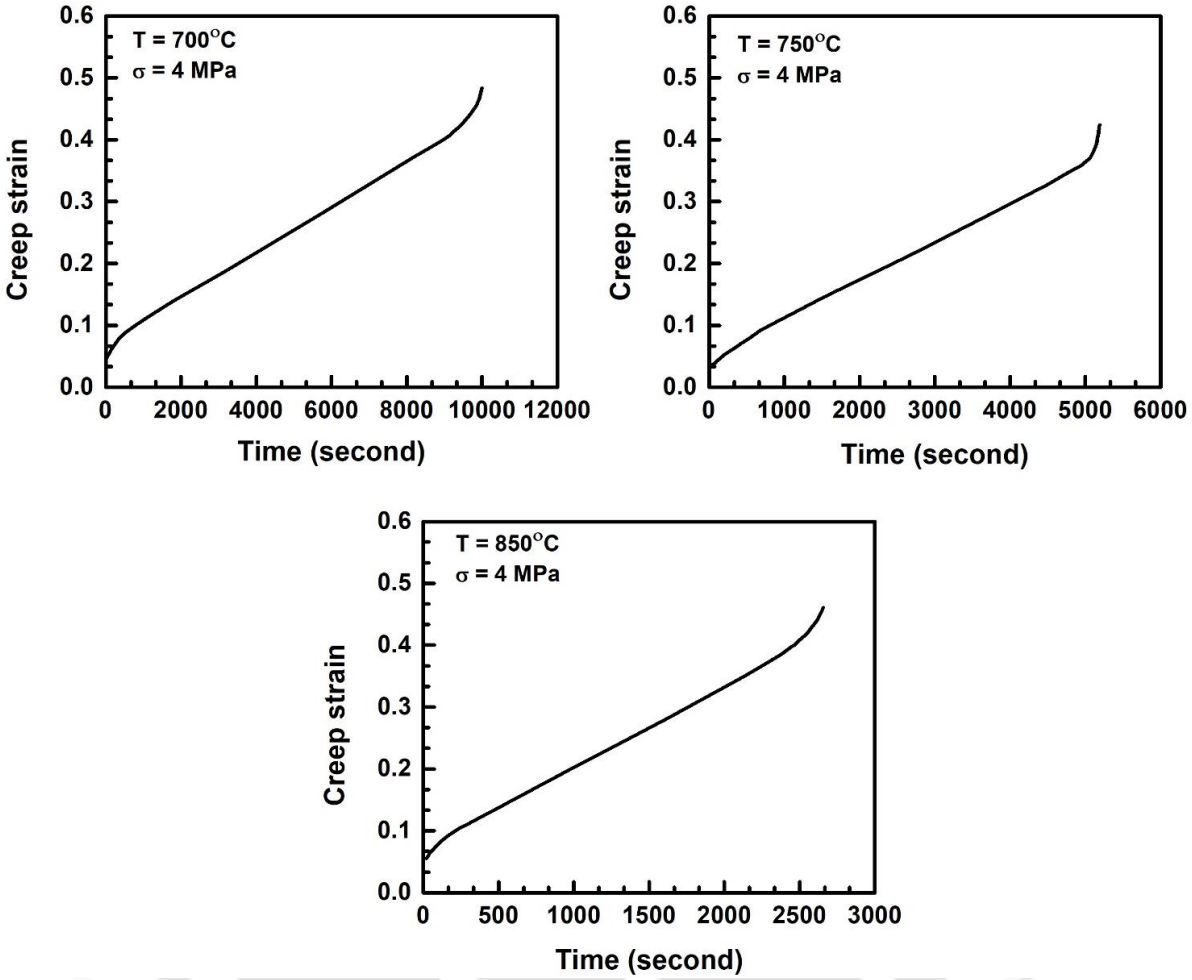

Figure 4.18 Typical creep curves obtained from experiments conducted on longitudinal samples at stresses of 4 MPa at different temperatures.

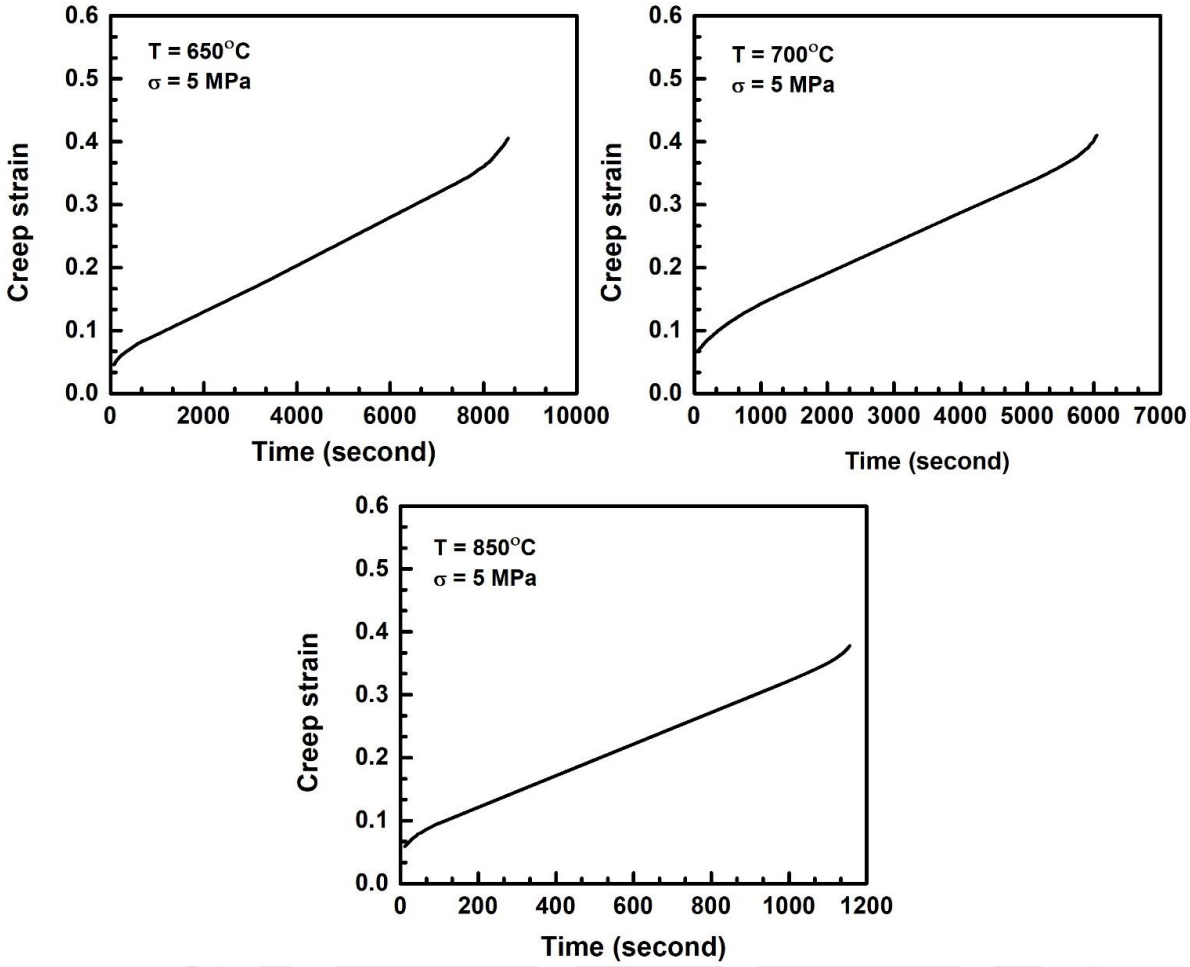

Figure 4.19 Typical creep curves obtained from experiments conducted on longitudinal samples at stresses of 5 MPa at various test temperatures.

The creep curves generated from the experimental data obtained for transverse samples tested at different conditions are shown in Figures 4.20 to 4.22. Figure 4.20 shows the creep curves of the investigated alloy at 22MPa stress and temperatures of 600°C, 750°C, and 800°C. The creep curve obtained at 600°C shows the three creep regions (primary, secondary, and tertiary) very clearly. The secondary region is followed by a rapid increase in the strain rate with time. The total failure strain of the alloy tested at this stress and temperature was around 0.36. From Fig. 4.20, it is seen that the steady state creep rate keeps increasing with the temperature rise. Similar observations were made in the creep curves obtained at 38 MPa and 58 MPa.

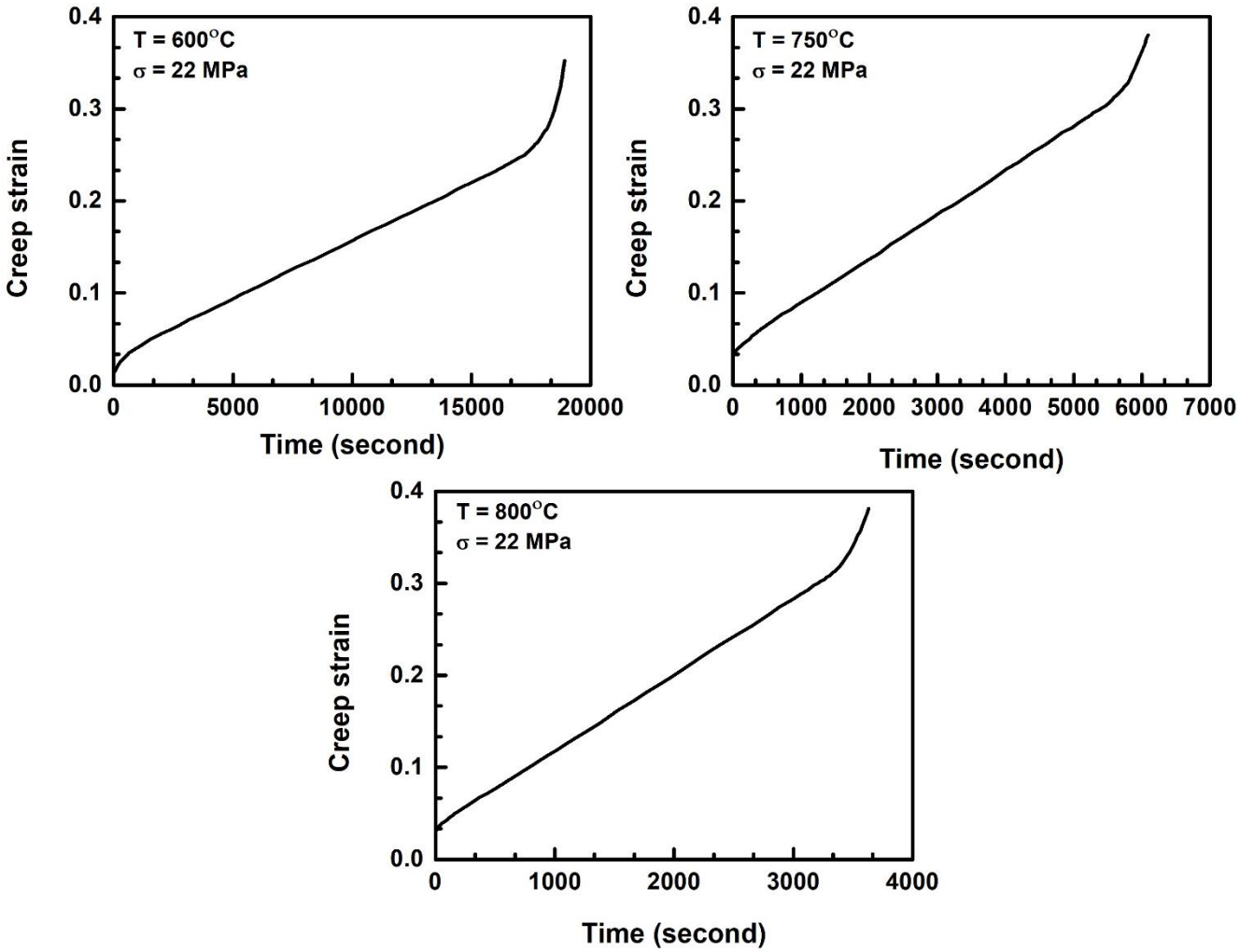

Figure 4.20 Typical creep curves obtained from experiments conducted on transverse samples at stresses of 22 MPa at different temperatures.

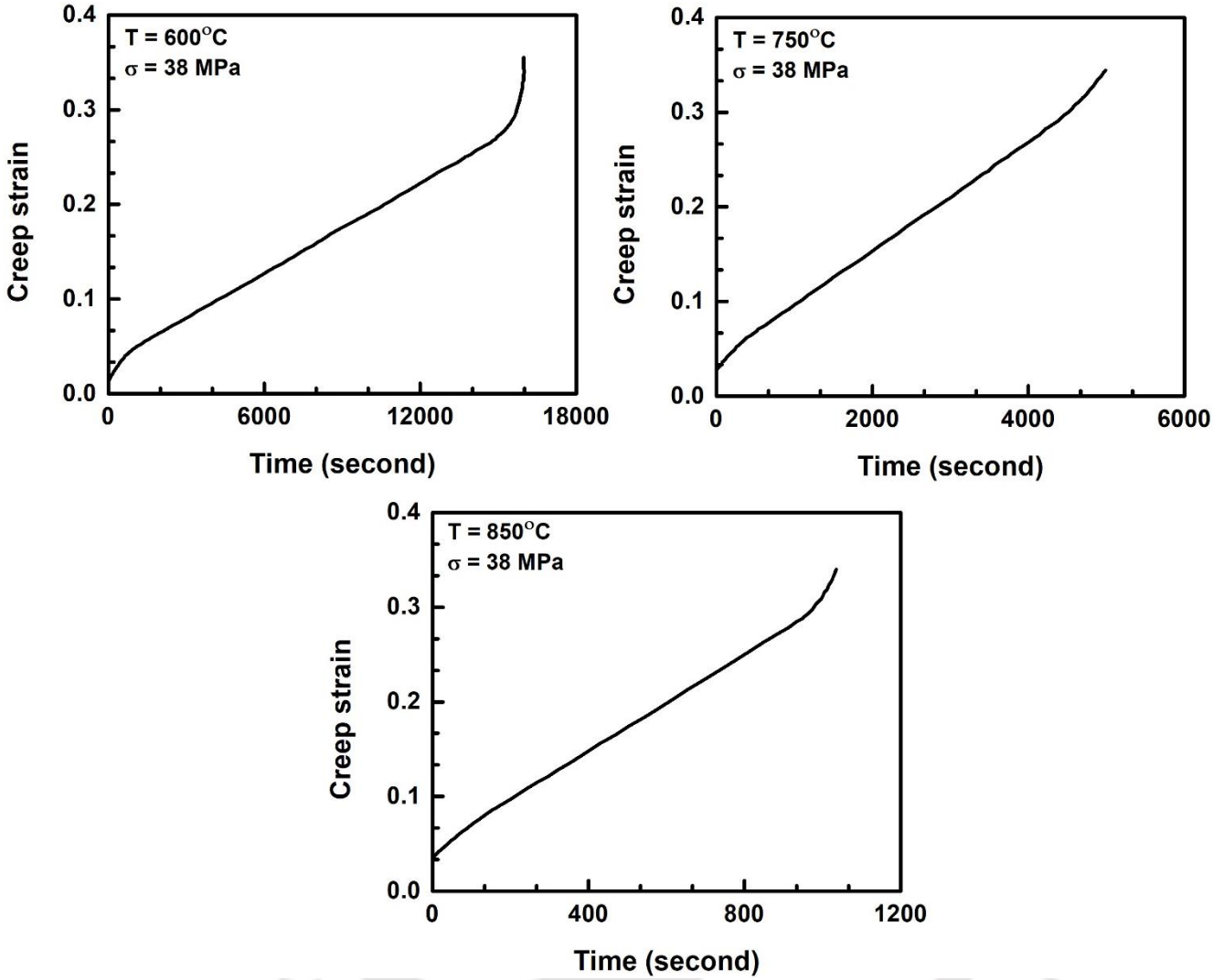

Figure 4.21 Typical creep curves obtained from experiments conducted on transverse samples at stresses of 38 MPa at various test temperatures.

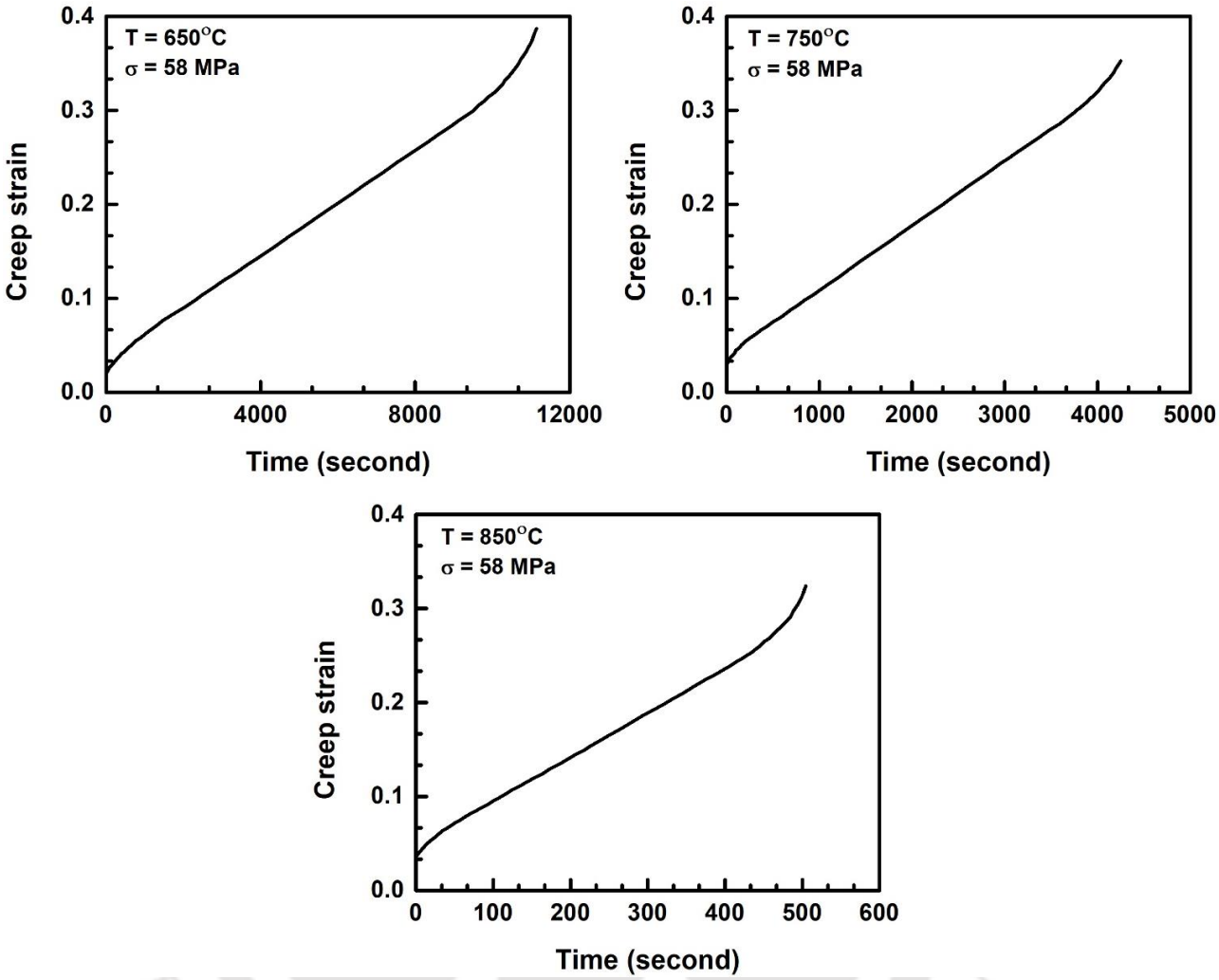

Figure 4.22 Typical creep curves obtained from experiments conducted on transverse samples at stresses of 58 MPa at various test temperatures.

Figure 4.23 (a) and (b) shows the plot of the creep curve obtained from tests conducted on longitudinal samples at constant stress and temperature of 3 MPa and 750 °C, respectively. At combinations of high stress and temperature, the primary creep region is reduced, and the creep curve enters the secondary creep region almost immediately after the test begins. Creep curves with three clearly defined stages are observed at lower temperatures and stresses.

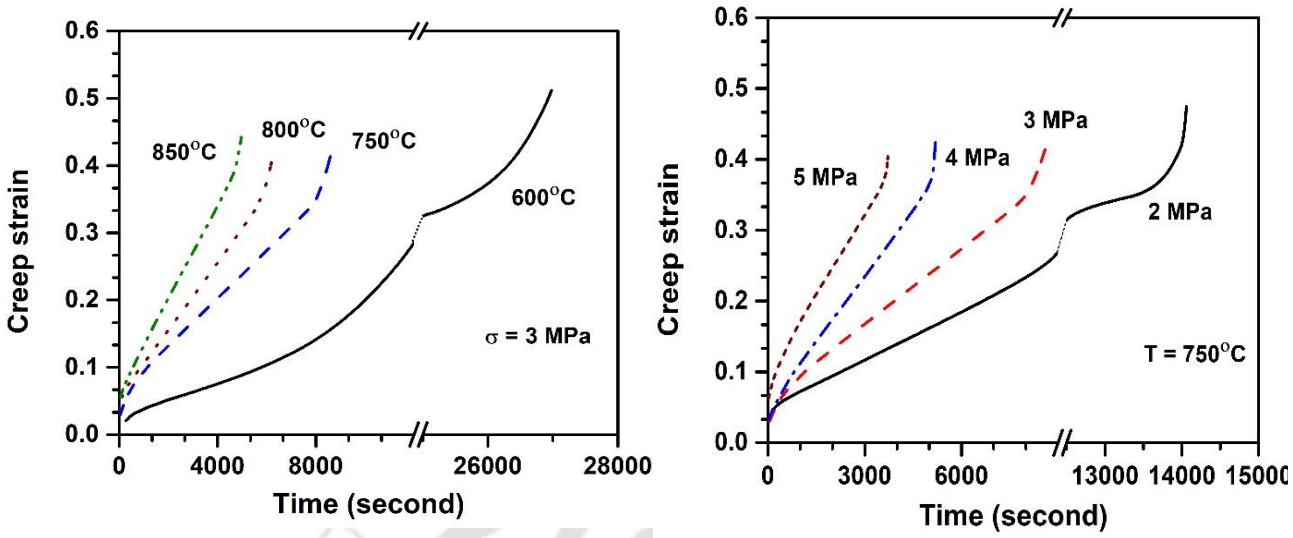

(a) (b)

Figure 4.23 Creep curves at constant (a) stress of 3 MPa and (b) temperature of 750 °C for longitudinal samples

Figure 4.24 (a) and (b) shows the variation of the creep curve obtained from tests conducted on transverse samples at a constant stress and temperature of 38MPa and 700 °C, respectively. Here also, the primary creep region is reduced when tests are conducted at high stresses and temperatures. Primary, secondary, and tertiary creep regions are more distinct at low temperatures and stress combinations.

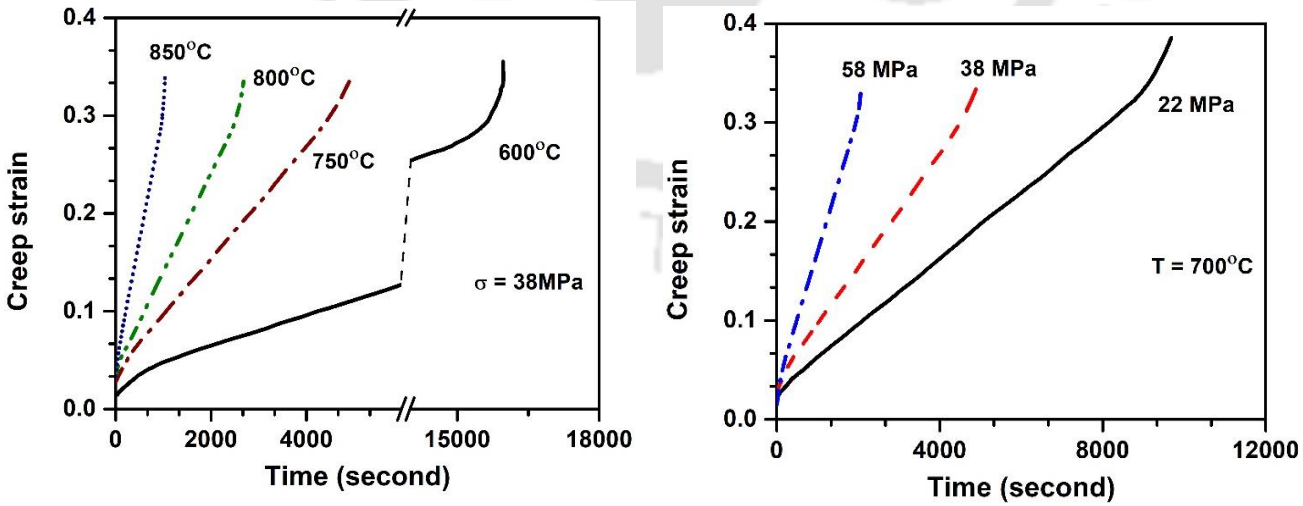

(a) (b)

Figure 4.24 Creep curves at constant (a) stress of 38 MPa and (b) temperature of 700 °C for transverse samples.

Figures 4.25 and 4.26 show the plot of creep strain rate vs. strain for the applied stresses for both the longitudinal and transverse creep tests, respectively. The early stage of creep deformation is characterized by a steadily decreasing strain rate. This happens because the motion of dislocations becomes extremely difficult at lower temperatures or stresses as the density of dislocations and other lattice defects increases with strain. The thermal activation permits the flow of metal at elevated temperatures. The combined influence of the phenomena, as mentioned above, causes the strain rate in the primary creep region to decrease continuously. The process continues until the rates of metal flow and softening due to recovery are comparable to the rate of work hardening. The total strain in the secondary creep region determines the material's effective creep life. Defects such as void nucleation cause a reduction in the effective cross-sectional area, thereby increasing the stresses. Under these circumstances, it's possible for the voids to expand, which would speed up the creep rate and cause the deformation to move into the tertiary creep region. As soon as the tertiary stage is attained, the void expansion quickens, leading to an increase in creep rate and an increase in strain, which eventually causes the final failure.

At higher temperatures, the metal flows at a rapid rate. Due to the annihilation of dislocations or vacancies at elevated temperatures, the strain hardening rate decreases, resulting in softening of the metal. The creep rate accelerates as a result of the combination of these two phenomena. For longitudinal creep tests, at stresses 2, 3, 4, and 5 MPa, the range for minimum creep rate lies between $\dot{\varepsilon}_s = 8.2 \times 10^{-6} - 4.8 \times 10^{-5} s^{-1}$,$\dot{\varepsilon}_s = 1.6 \times 10^{-5} - 6.8 \times 10^{-5} s^{-1}$,$\dot{\varepsilon}_s = 1.8 \times 10^{-5} - 1.2 \times 10^{-4} s^{-1}$,and $\dot{\varepsilon}_s = 2.8 \times 10^{-5} - 2.5 \times 10^{-4} s^{-1}$ respectively. In the case of the transverse creep tests, the minimum creep rates lie between $\dot{\varepsilon}_s = 2.2 \times 10^{-6} - 1.8 \times 10^{-5}$ s^{-1} , $\dot{\varepsilon}_s = 1.2 \times 10^{-5} - 2.4 \times 10^{-4} s^{-1}$,and $\dot{\varepsilon}_s = 8.8 \times 10^{-5} - 4.6 \times 10^{-4}$ s^{-1} for 22, 38, and 58MPa, respectively.

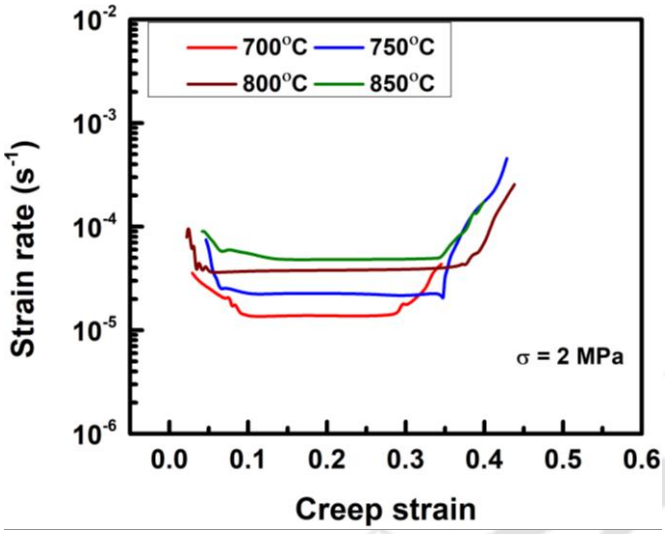

(a)

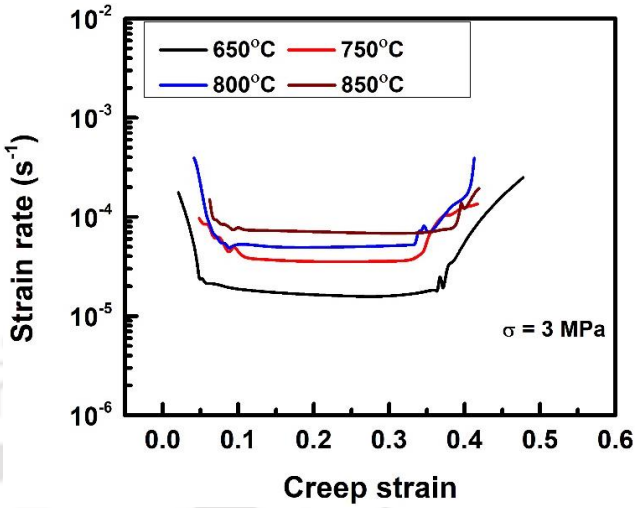

(b)

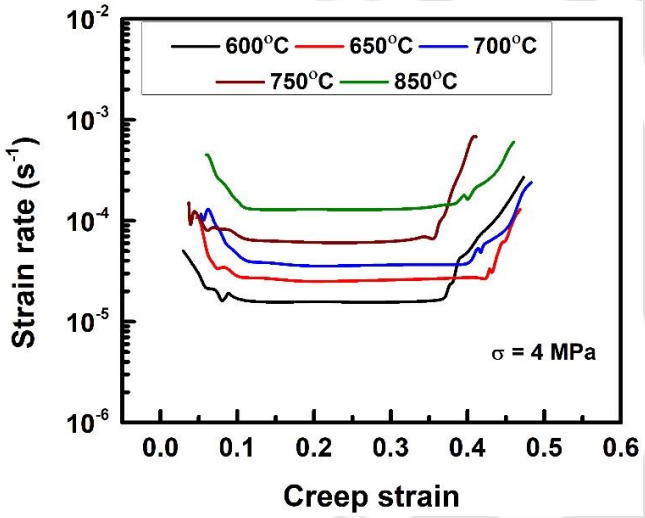

(c)

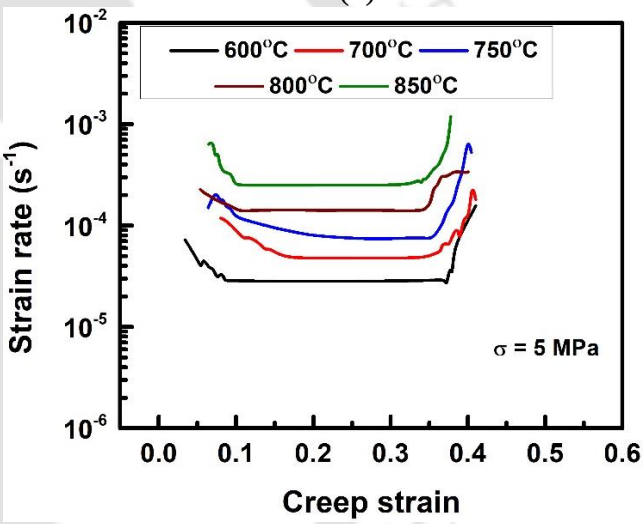

(d)

Figure 4.25 Plot of creep strain rate($\dot{\varepsilon}$) vs. creep strain at stresses (a) 2 MPa, (b) 3 MPa, (c) 4 MPa, and (d) 5 MPa at different temperatures for longitudinal samples.

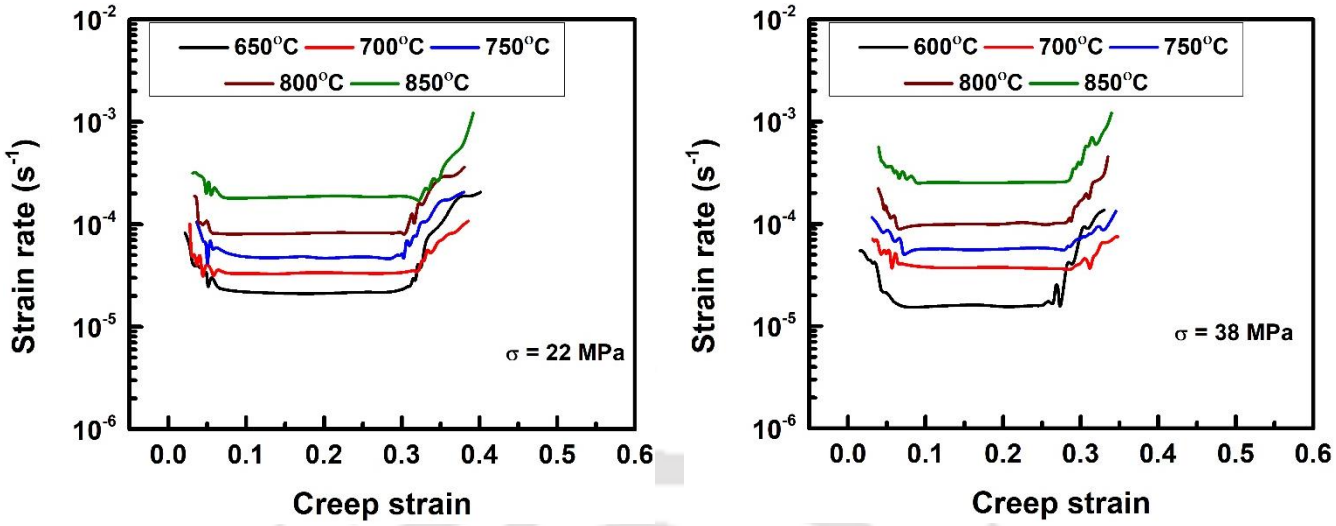

(a) (b)

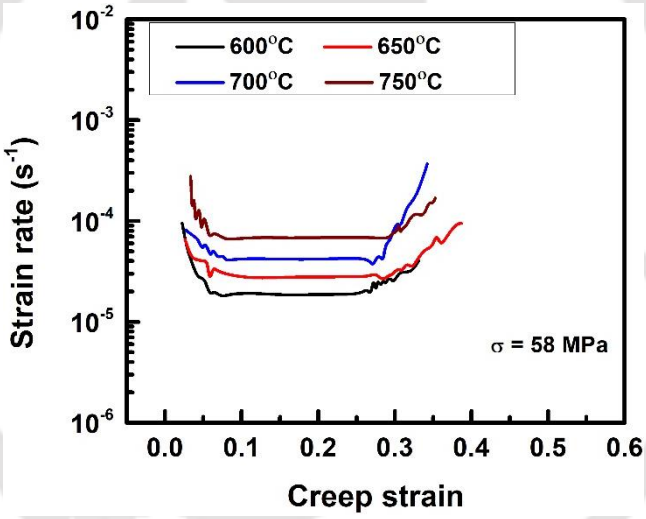

(c)

Figure 4.26 Plot of creep strain rate ($\dot{\varepsilon}$) vs. creep strain at stresses (a) 22 MPa, (b) 38 MPa, and (c) 58 MPa at different temperatures for transverse samples.

4.4.3 Creep strains and rupture time

The variation of primary (ε_1), secondary(ε_2), tertiary creep(ε_3) strains, failure strain (ε_f), and minimum creep rate $\dot{\varepsilon}_s$, with respect to stress and temperature for both the longitudinal and transverse creep test of the Zr-2.5Nb alloy pressure tube, are discussed in the following subsections. The notations used for the data analysis have been explained in Section 3.4.5 and are again reproduced schematically in Figure 4.27.

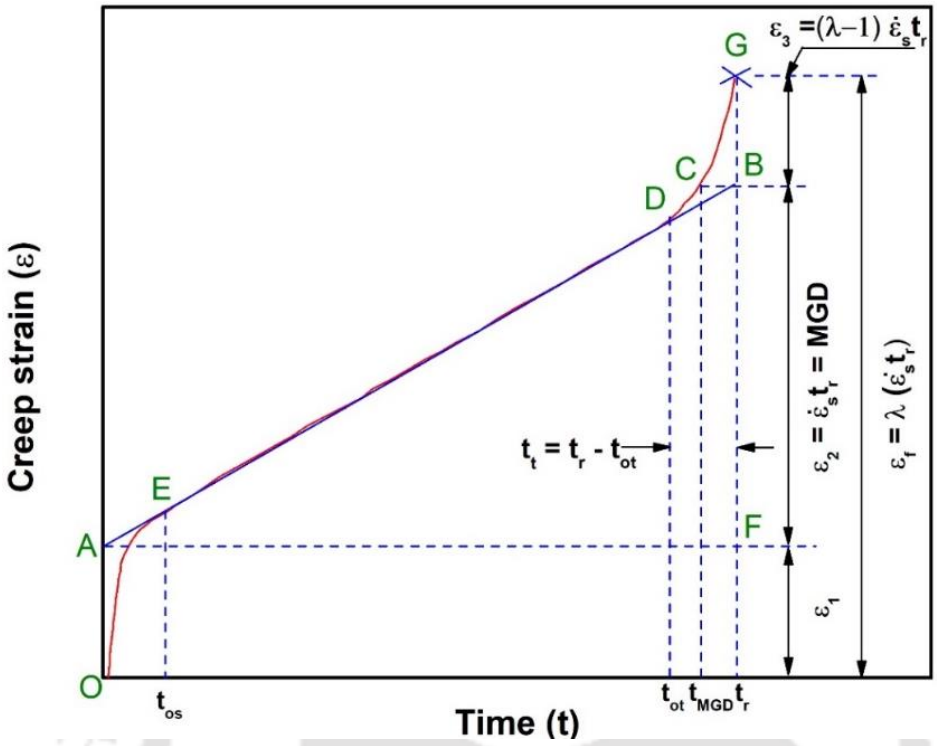

Figure 4.27 Typical creep curve showing different terms[194].

4.4.3.a Longitudinal creep tests

Figure 4.28 (a) shows the variation in the minimum creep rate ($\dot{\varepsilon}_s$) with applied stress (σ) at a constant temperature. The figure shows that the value of $\dot{\varepsilon}_s$ increases with an increase in applied stress at a particular temperature. Variation of minimum creep rate($\dot{\varepsilon}_s$) with temperature at constant stress is given in Figure 4.28 (b). At constant applied stress, the $\dot{\varepsilon}_s$ value increases with the increase in temperature.

Figure 4.29(a) shows the plot of rupture strain(ε_f) and secondary creep strain(ε_2) vs. minimum creep rate. From Figure 4.29(a), the maximum values of ε_f and ε_2 were found to be 0.52 and 0.39, respectively. It can be observed that the strains (ε_2 and ε_f) tend to decrease with the increase in $\dot{\varepsilon}_s$. Figure 4.29(b) shows the variation of the relative primary ($\varepsilon_1/\varepsilon_f$), secondary ($\varepsilon_2/\varepsilon_f$), and tertiary creep strain ($\varepsilon_3/\varepsilon_f$). Figure 4.29(b) shows that the relative secondary creep strain tends to increase with increasing $\dot{\varepsilon}_s$, whereas the contribution of relative primary and tertiary strain tends to decrease. The average values for the relative secondary strain and tertiary strains are 72 % and 18 %, respectively.

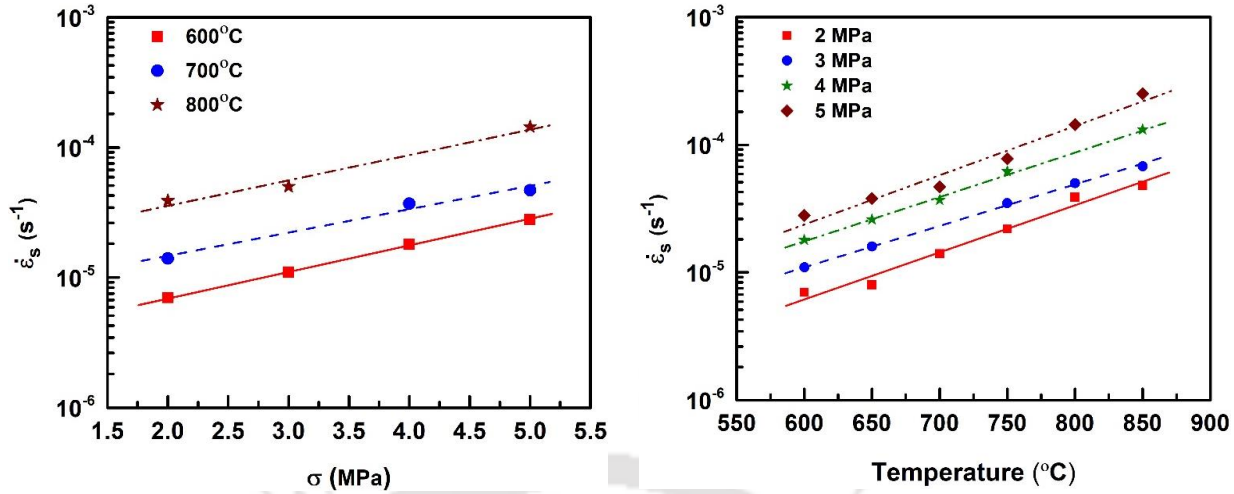

(a) (b)

Figure 4.28 Plot of minimum creep rate vs. (a) stress and (b) temperature for the longitudinal creep tests.

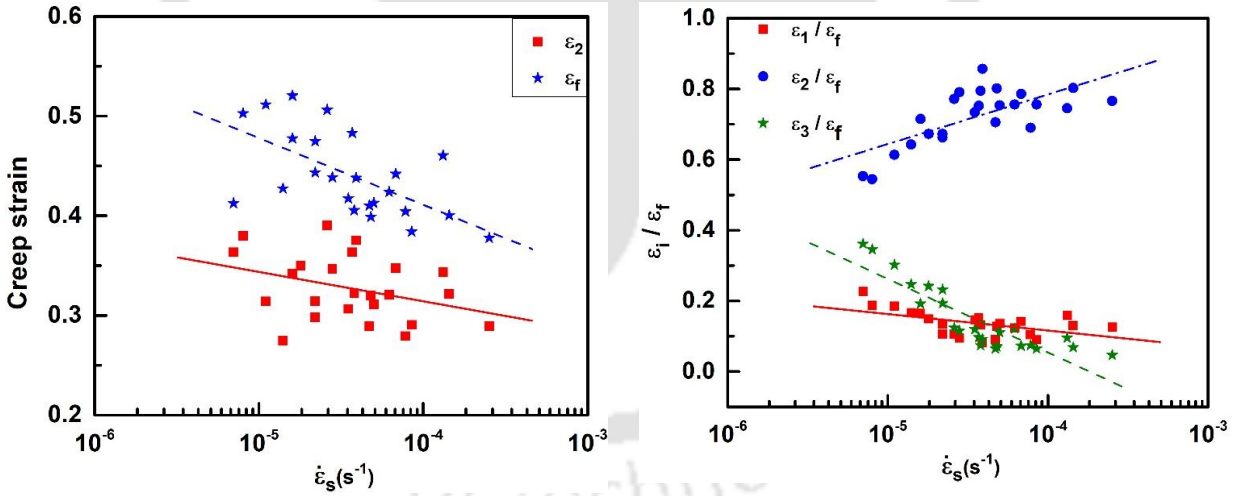

(a) (b)

Figure 4.29 Plot of (a) rupture strain(ε_f) and secondary creep strain (ε_2) and (b) relative creep strains of the three creep regions vs. minimum creep rate determined from longitudinal creep tests of the Zr-2.5Nb alloy.

Figure 4.30 (a) shows the variation of ε_2 and ε_f with stress for particular temperatures of 650 ˚C and 750˚C. For both cases, ε_2 and ε_f decrease with the increase in stress. Figure 4.30 (b) shows the variation of $\varepsilon_2 / \varepsilon_f$ as a function of applied stress at constant temperatures. The

figure shows that $\varepsilon_2/\varepsilon_f$ increases with an increase in stress. Similar trend was observed for other test temperatures also.

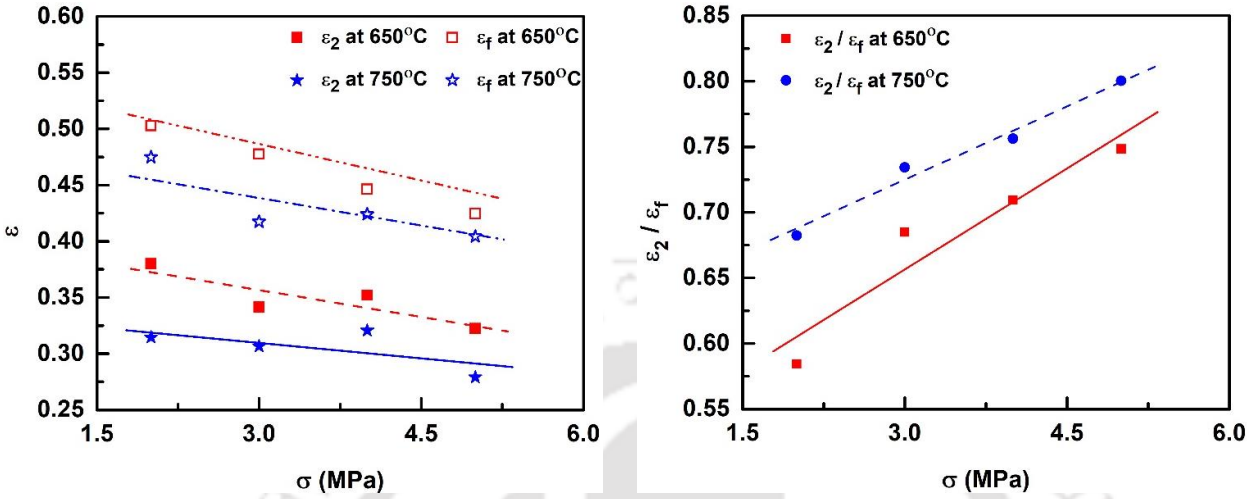

(a) (b)

Figure 4.30 Plot of (a) rupture strain(ε_f) and secondary creep strain (ε_2) and (b) relative secondary creep strain ($\varepsilon_2 / \varepsilon_f$) vs. stress at temperatures of 650°C and 750 ˚C for longitudinal creep tests.

The variation of ε_2 and ε_f with temperature at constant stresses of 3 MPa and 4 MPa is shown in Figure 4.31 (a). The figure shows that the secondary creep strain(ε_2) and rupture strain (ε_f) decreased with the rise in temperature. Figure 4.31 (b) shows the contribution of ε_2 to ε_f . The plot shows that $\varepsilon_2/\varepsilon_f$ increases with an increase in temperature at a constant applied stress. Similar trend was observed for other test temperatures and applied stresses also.

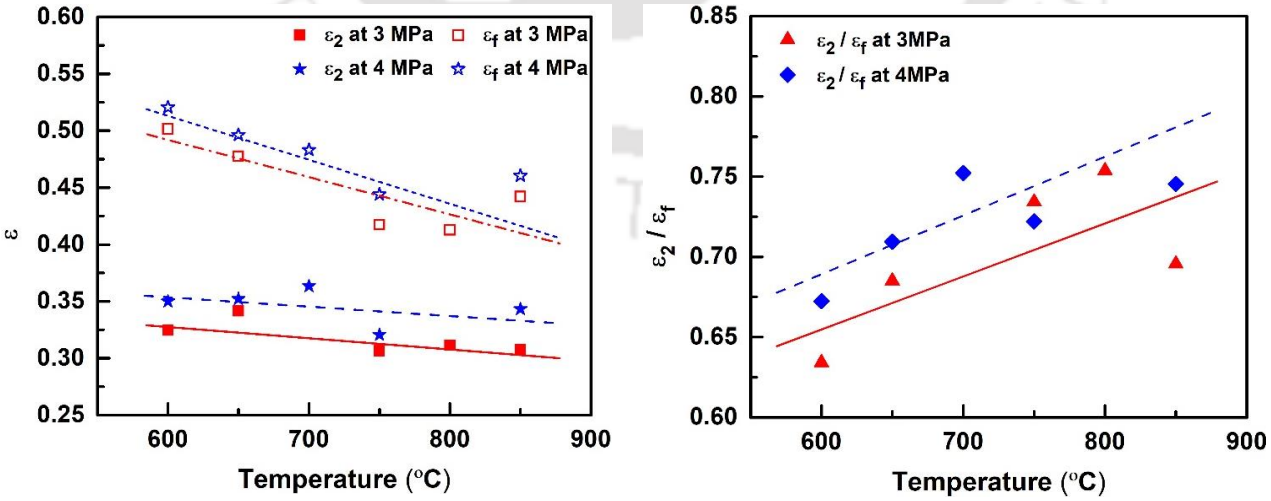

(a) (b)

Figure 4.31 Plot of (a) rupture strain(ε_f) and secondary creep strain (ε_2) and (b) relative secondary creep strain ($\varepsilon_2 / \varepsilon_f$) vs. temperature at stresses of 3 MPa and 4 MPa for longitudinal creep tests.

Figure 4.32(a) shows the double logarithmic plots of stress(σ) vs. rupture time (t_r) at temperatures of 600 °C, 700 °C and 800 °C. The graph shows that with the increase in applied stress, the rupture time decreases at a constant temperature. Maximum rupture time of 34320 seconds (9.5 hours) was obtained when the sample was creep tested at 600 °C/2 MPa. The effect of temperature on t_r at constant stress is shown in Figure 4.32(b). The figure clearly shows that the rupture time decreases for all stresses as temperature increases.

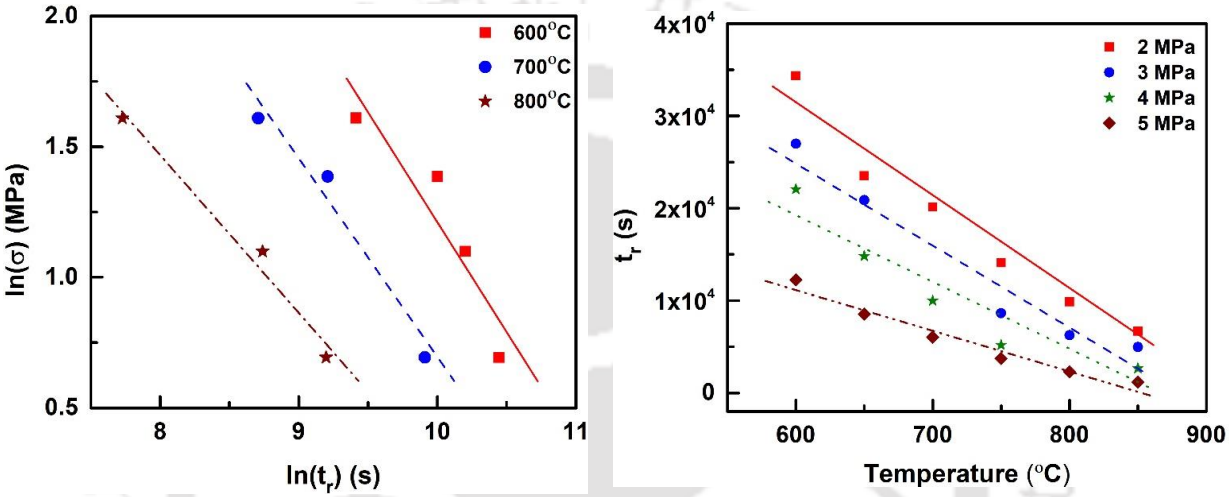

(a) (b)

Figure 4.32 Plot of (a) ln(σ) vs. ln (t_r), (b) t_r vs. temperature for the longitudinal creep tests.

4.4.3.b Transverse creep tests

Figure 4.33 (a) shows the variation in minimum creep rate ($\dot{\varepsilon}_s$) with applied stress (σ) at constant temperature for the transverse tests. The figure shows that $\dot{\varepsilon}_s$ increases as the applied stress is increased at a constant temperature. The plot of the minimum creep rate($\dot{\varepsilon}_s$) vs. temperature is shown in Figure 4.33 (b). At constant temperature, the $\dot{\varepsilon}_s$ value increases with the increase in temperature and $\dot{\varepsilon}_s$ increases with the increase in applied stress at a constant temperature.

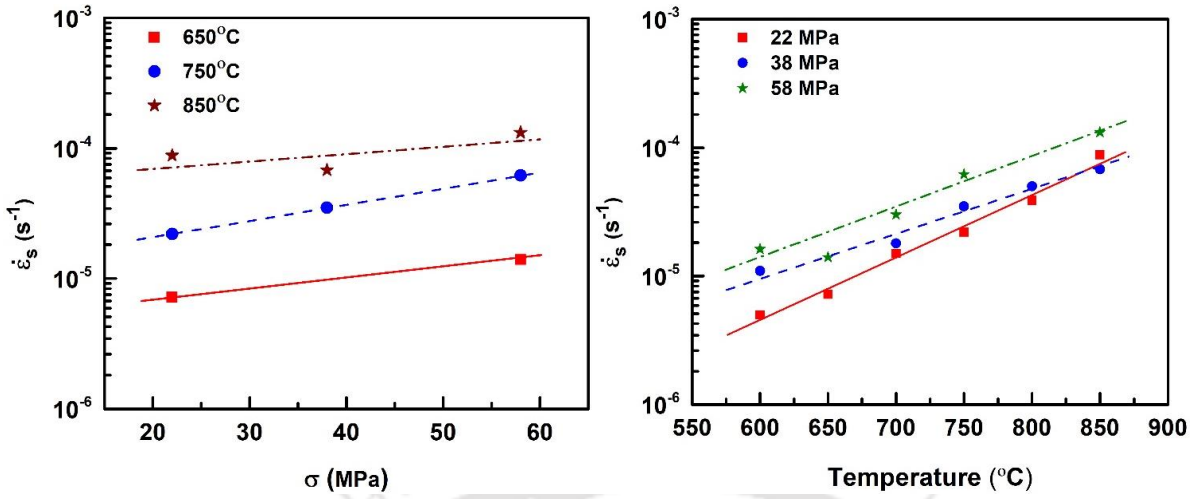

(a) (b)

Figure 4.33 Plot of minimum creep rate($\dot{\varepsilon}_s$) vs. (a) stress and (b) temperature for the transverse creep tests.

Figure 4.34(a) and (b) show semi-logarithmic plots of ε_2 and ε_f, and relative strains ($\varepsilon_i/\varepsilon_f$) vs. minimum creep rate $\dot{\varepsilon}_s$, obtained from the creep tests done on the transverse samples of the alloy. From figure 4.34(a), the maximum values of ε_f and ε_2 were found to be 0.4 and 0.34, respectively. From the figure, it can be seen that ε_2 and ε_f decreases as $\dot{\varepsilon}_s$ increases. Trend lines shown in Figure 4.34(b) show that the relative secondary strain tends to increase with increasing $\dot{\varepsilon}_s$. Whereas the contribution of relative primary and tertiary strain tend to decrease. The average values for the relative secondary creep strain and tertiary creep strains are 78 % and 10 %, respectively.

Figure 4.35 (a) shows the variation of ε_2 and ε_f with stress for test temperatures of 700 ˚C and 850˚C. For both cases, ε_2 and ε_f decrease with an increase in stress. Figure 4.35 (b) shows the variation of $\varepsilon_2/\varepsilon_f$ as a function of applied stress at constant temperatures. The figure shows that $\varepsilon_2/\varepsilon_f$ increases with an increase in stress.

The effect of temperature on ε_2 and ε_f at 22 MPa and 58 MPa is shown in Figure 4.36(a). The figure shows a marginal increase in ε_2 with temperature for the stress of 22 MPa, whereas ε_2 decreased for the applied stress of 58MPa. The strain to rupture for both stresses decreased with the rise in temperature. Figure 4.36(b) shows the variation of secondary creep strain to the total rupture strain for 22 and 58 MPa. The plot shows that similar to the longitudinal creep tests, here also the ratio of secondary creep strain to rupture strain increases with the rise in temperature at constant stress.

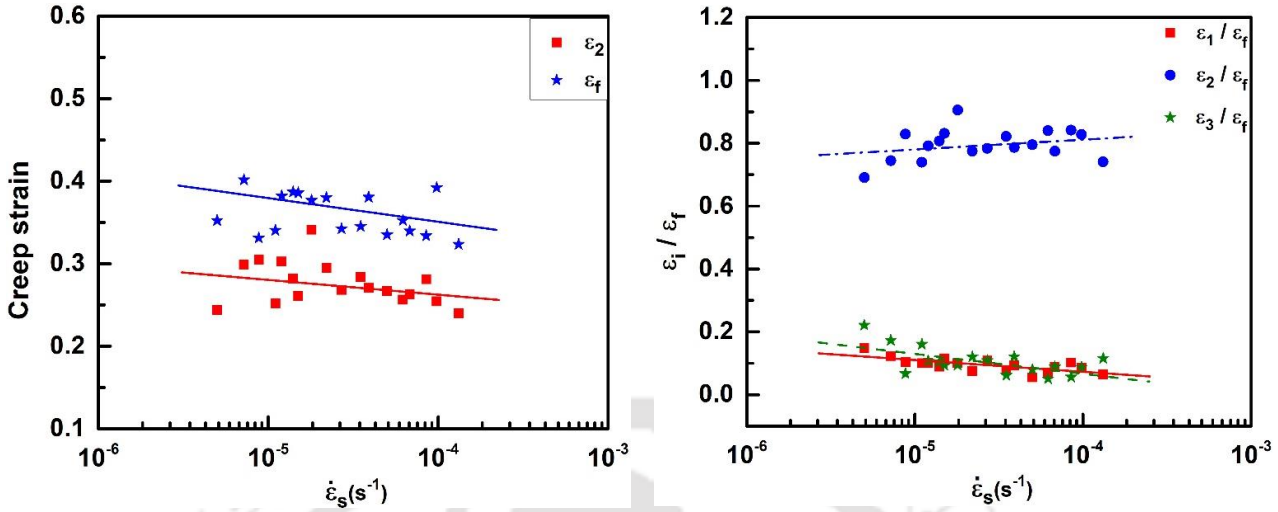

(a) (b)

Figure 4.34 Plot of (a) rupture strain(ε_f) and secondary creep strain (ε_2) and (b) relative creep strains of the three creep regions vs. minimum creep rate for the transverse creep tests of the alloy.

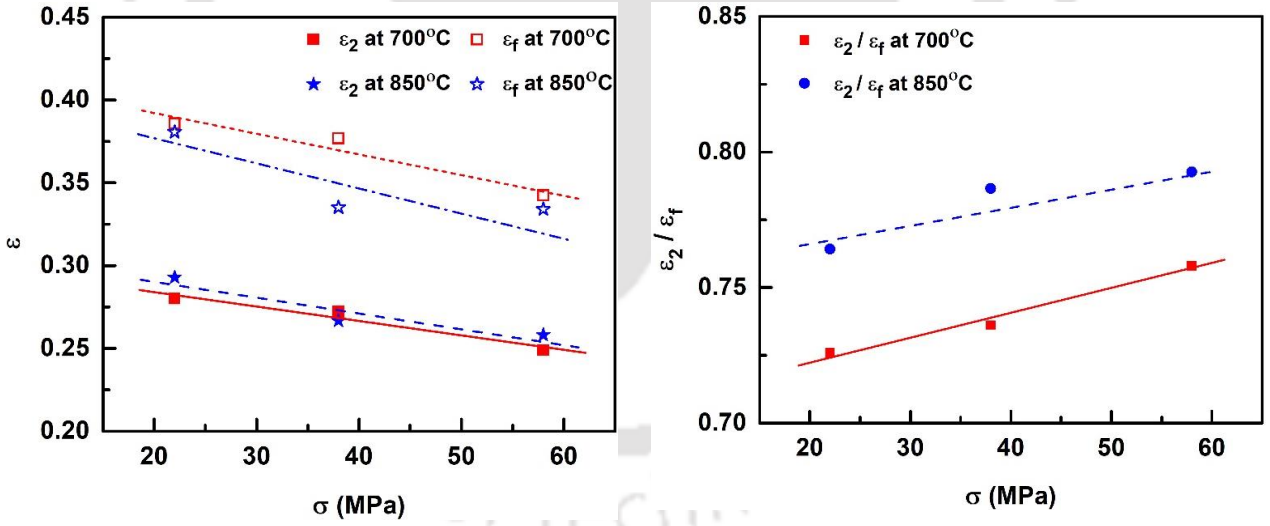

(a) (b)

Figure 4.35 Plot of (a) rupture strain(ε_f) and secondary creep strain (ε_2) and (b) relative secondary creep strain ($\varepsilon_2 / \varepsilon_f$) vs. stress at temperatures of 700°C and 850 ˚C for the transverse creep tests.

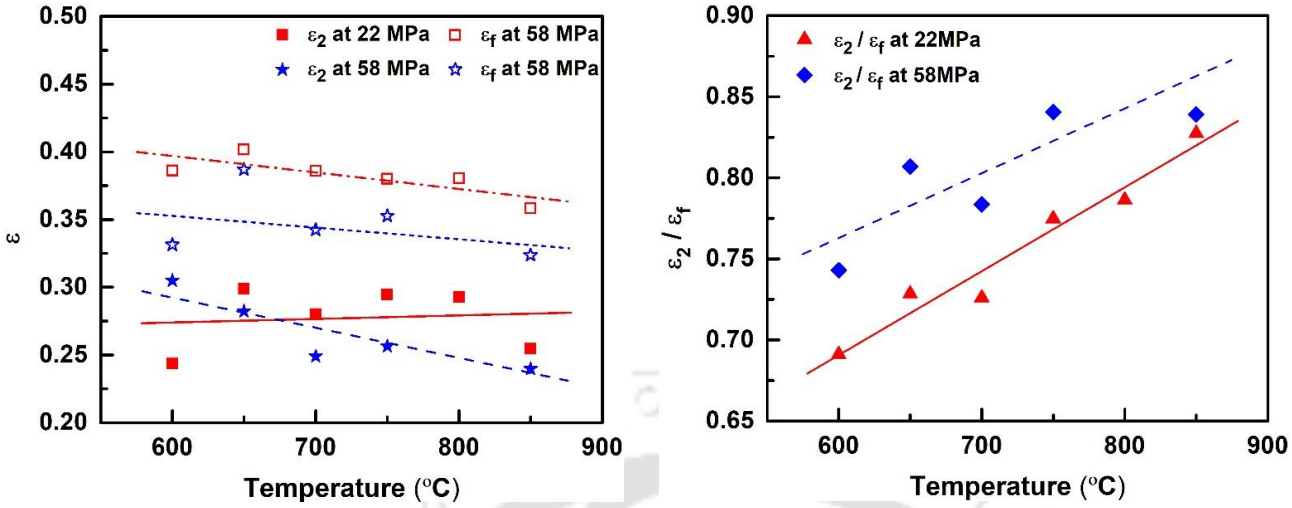

(a) (b)

Figure 4.36 Plot of (a) rupture strain(ε_f) and secondary strain (ε_2) and (b) relative secondary creep strain ($\varepsilon_2 / \varepsilon_f$) vs. temperature at stresses of 22 MPa and 58 MPa for transverse creep tests.

Figure 4.37(a) shows the double logarithmic plots of stress(σ) vs. rupture time (t_r) at temperatures of 650 °C, 750 °C and 850 °C. The graph shows that with the increase in applied stress, the rupture time decreases at a constant temperature. The maximum rupture time of 13702 seconds (3.8 hours) was obtained when creep tested at 600 °C/22 MPa. The effect of temperature on t_r at constant stress is shown in Figure 4.37(b). The figure shows that the rupture time decreases for all stresses as temperature increases.

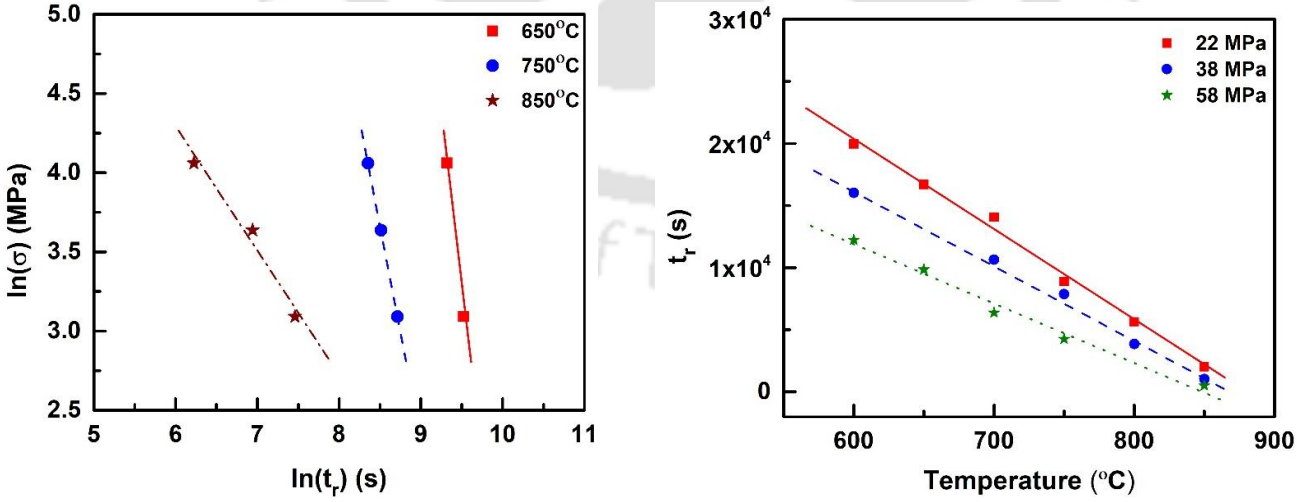

(a) (b)

Figure 4.37 Plot of (a) ln(σ) vs. ln (t_r), (b) t_r vs. temperature for the transverse creep tests.

4.4.4 Constitutive modeling

As discussed in section 2.5, The creep constitutive equations relating minimum creep rate ($\dot{\varepsilon}_s$) to temperature (T) and stress (σ) has been discussed in section 2.5. For ease of reading, the equations have been reproduced here again as follows:

$$\dot{\varepsilon}_s = A_1 \sigma^{n_c} \exp\left(-\frac{Q_{app}}{RT}\right) \tag{4.4}$$

$$\dot{\varepsilon}_s = A_2 \exp(\beta\sigma) \exp\left(-\frac{Q_{app}}{RT}\right) \tag{4.5}$$

$$\dot{\varepsilon}_s = A_3 [\sinh(\alpha\sigma)] \exp\left(-\frac{Q_{app}}{RT}\right) \tag{4.6}$$

where A_1, A_2, A_3 are pre-exponential factors, n_c, β, α are constants, Q_{app} is the apparent activation energy for creep, and R is the universal gas constant (8.314 J K^{-1} mol^{-1}). Pre-exponential factors, n_c, β, and α, are physical constants that can be determined from the creep test data. Constant n_c is also known as the creep stress exponent. The observed activation energy depends on the different operating mechanisms of creep. Multiple creep mechanisms may take place simultaneously depending on the combinations of stress and temperature. Therefore, the activation energy for creep is referred to as the apparent activation energy for creep (Q_{app}). Among the three relationships mentioned above, Eq. 4.4 is extensively used due to its simplicity. The stress exponent n_c and apparent activation energy for creep Q_{app} of both the longitudinal and transverse creep test of the Zr-2.5Nb alloy are determined and presented in the following subsections. The constitutive equations have been obtained for each case, and their efficacy in determining the minimum creep rate has also been discussed.

4.4.4.a Longitudinal creep tests

Figure 4.38 (a) shows the double logarithmic graph of minimum strain rate($\dot{\varepsilon}_s$) vs. applied stress (σ). The slope of the linear fits gives the value of n_c as shown in the figure. The values of n_c were in the range of 1.4-2.7 with an average value of 1.8. Figure 4.38(b) gives the plot of calculated n_c vs. temperature(T). It can be seen from the figure that the stress exponent (n_c) varies non-linearly with temperature (T).

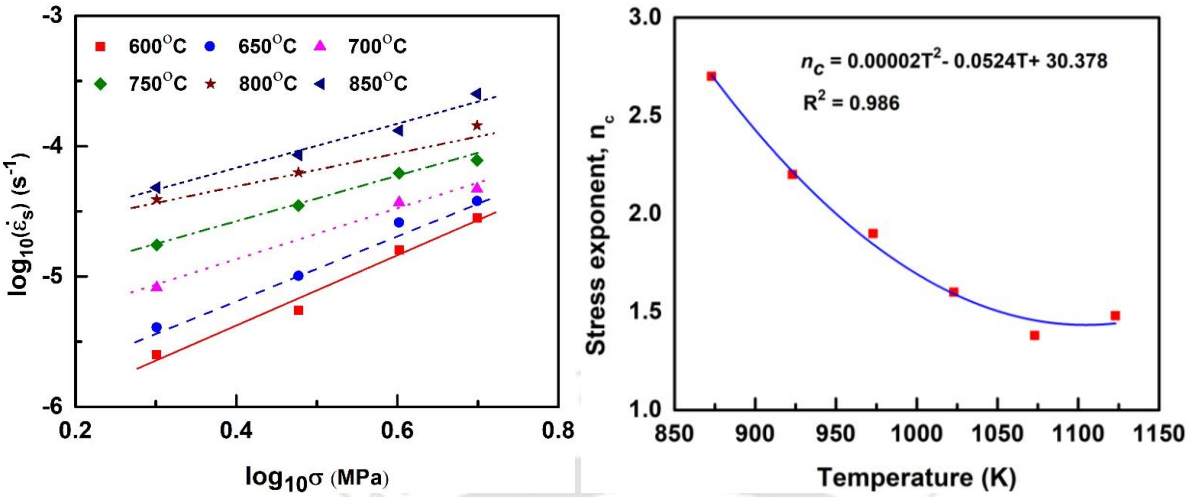

(a) (b)

Figure 4.38 Plot of (a) log ($\dot{\varepsilon}_s$) vs. log (σ) and (b) n_c vs. T for longitudinal sample.

Stress exponent (n_c) can be related to the test temperature (T) by a second-order polynomial equation of the form:

$$n_c = 0.00002T^2 - 0.0524T + 30.378 \quad (4.7)$$

where T is the test temperature in Kelvin.

The apparent activation energy (Q_{app}) was calculated from the plot of log ($\dot{\varepsilon}_s$) vs. 1/T corresponding to each stress, as shown in Figure 4.39(a). The Q_{app} for the stresses of 2, 3, 4, and 5 MPa are 315.2 kJ/mol, 296.4 kJ/mol, 268 kJ/mol, and 258.4 kJ/mol, respectively. The average Q_{app} is calculated as 284.4 kJ/mol. Figure 4.39(b) shows a non-linear relationship between Q_{app} and σ. Q_{app} can be related to σ with a polynomial equation of the form:

$$Q_{app} = 2.5\sigma^2 - 37.2\sigma + 380.8 \quad (4.8)$$

where Q_{app} is in kJ/mol and σ is in MPa.

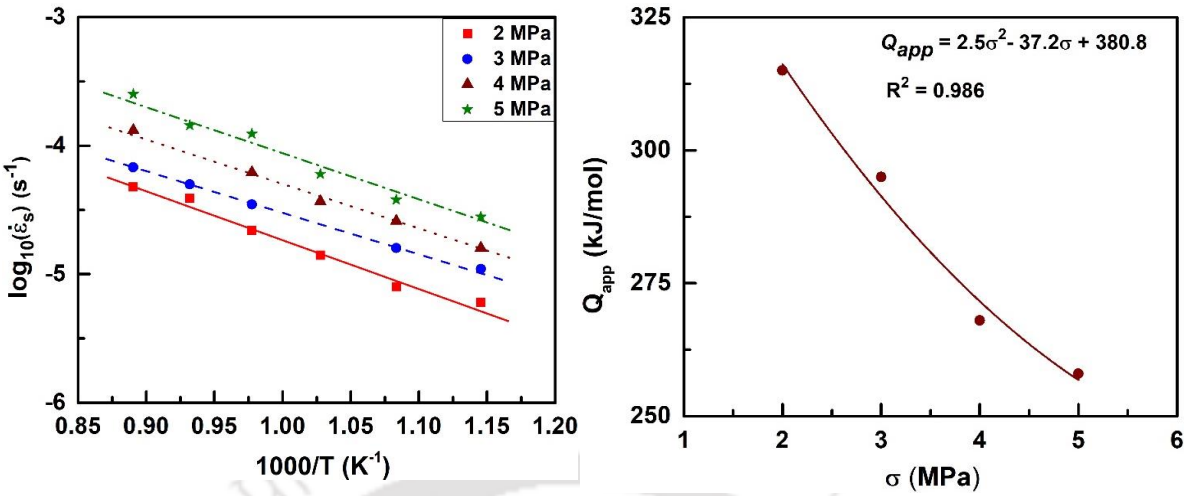

(a) (b)

Figure 4.39 Plot of (a) log ($\dot{\varepsilon}_s$) vs. 1/T and (b) Q_{app} vs. σ for longitudinal samples.

Since n_c is a function of temperature and Q_{app} is a function of stress, a precise determination of constants (A_1, A_2, A_3) is difficult. A least square fit technique, elaborated in Section 3.4.1, was used for determining the creep constitutive parameters. The constitutive parameters obtained by the technique for Eqs. 4.4 - 4.6 are shown in Table 4.5.

Table 4.5 Creep constitutive parameters of Eq. 4.4, 4.5, and 4.6 and corresponding R^2- values.

Eq. 4.4	A_1	Q_{app} (kJ/mol)	n_c	R^2
	8.02×10^{-6}	292.48	2.2	0.98
Eq. 4.5	A_2	Q_{app} (kJ/mol)	β	R^2
	4.22×10^{-5}	288.54	0.2428	0.94
Eq. 4.6	A_3	Q_{app} (kJ/mol)	α	R^2
	2.42×10^{-5}	282.36	0.2184	0.74

Based on the data given in Table 4.5, the following constitutive relationships for the longitudinal creep tests are obtained for $\dot{\varepsilon}_s$:

$$\dot{\varepsilon}_s = 8.02 \times 10^{-6} \sigma^{2.2} exp\left(-\frac{292480}{RT}\right) \quad (4.9)$$

$$\dot{\varepsilon}_s = 4.22 \times 10^{-5} \exp(0.2428\sigma)\exp(-\frac{288540}{RT}) \quad (4.10)$$

$$\dot{\varepsilon}_s = 2.42 \times 10^{-5}[sinh(0.2184\sigma)]exp\left(-\frac{282360}{RT}\right) \quad (4.11)$$

From the R^2- values given in Table 4.5, the best creep constitutive equation is the power law equation (Eq. 4.9).Figure 4.40 (a) and (b) compare the plot of $\dot{\varepsilon}_s$ vs.$1/T$ and $\dot{\varepsilon}_s$ vs. σ obtained experimentally with the values of $\dot{\varepsilon}_s$ obtained using Eq. 4.9 for different stresses and temperatures, respectively.

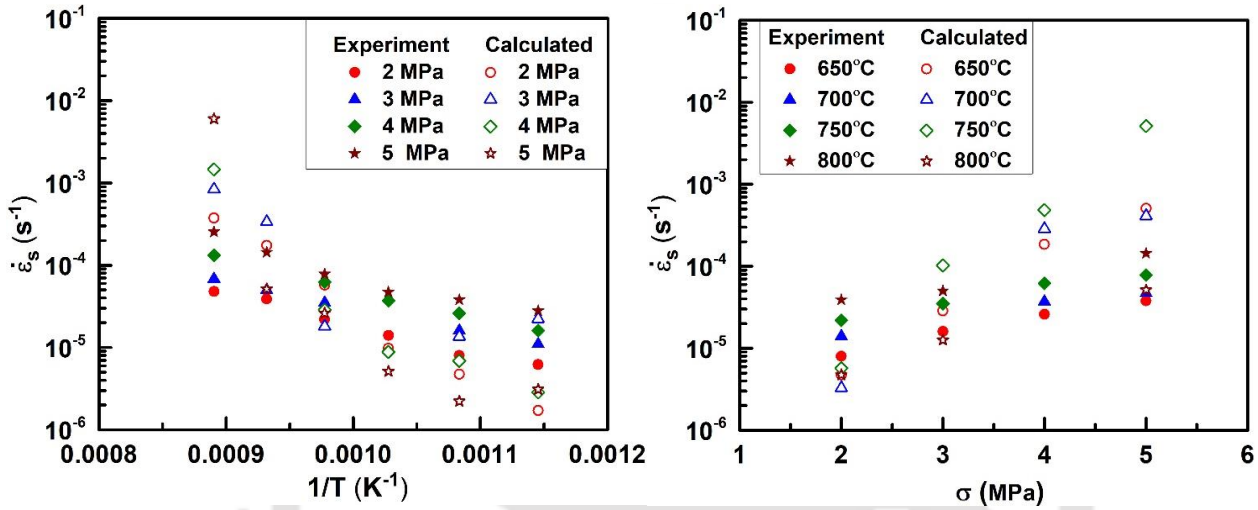

(a) (b)

Figure 4.40 Variation of experimentally obtained $\dot{\varepsilon}_s$ and calculated $\dot{\varepsilon}_s$ using Eq. 4.9 with (a) $1/T$ and (b) σ for longitudinal creep tests.

4.4.4.b Transverse creep tests

Figure 4.41(a) shows the double logarithmic graph of the minimum strain rate($\dot{\varepsilon}_s$) vs. applied stress (σ). The slope of the linear fits gives the value of n_c as shown in the figure. The values of n_c were in the range of 1.8-2.8 with an average value of 2.2. Figure 4.41(b) gives the plot of calculated n_c vs. temperature(T). Similar to the longitudinal tests, here also n_c varied non-linearly with the test temperatures (T) and is expressed by the form:

$$n_c = 0.00003T^2 - 0.054T + 32.218 \quad (4.12)$$

where T is the test temperature in Kelvin. The value for the stress exponent n_c for both the longitudinal and transverse creep tests is comparable to values reported in the literature for Zr alloys [19].

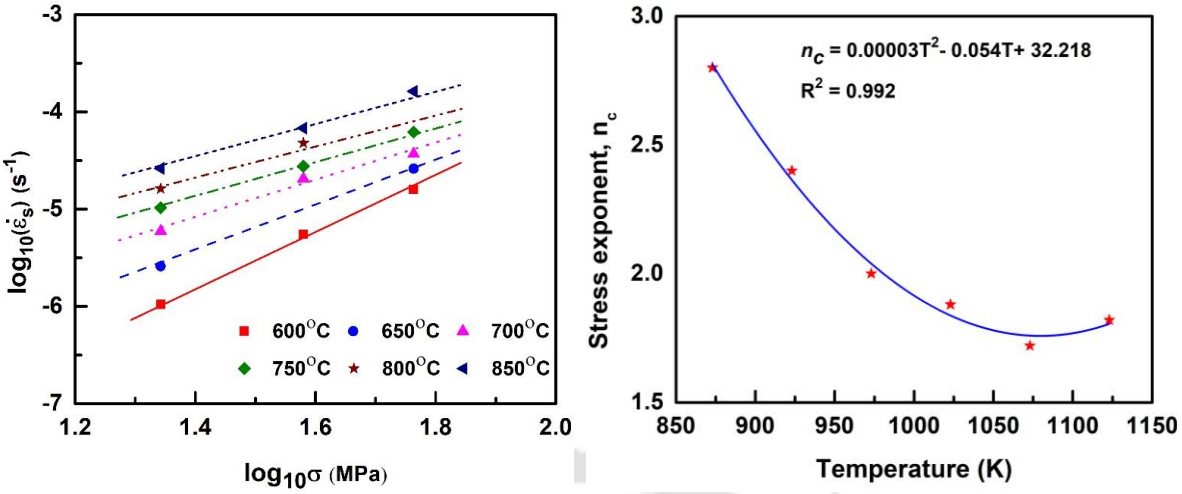

(a) (b)

Figure 4.41 Plot of (a) log ($\dot{\varepsilon}_s$) vs. log (σ) and (b) n_c vs. T for transverse samples.

The apparent activation energy (Q_{app}) was determined from the graph of log ($\dot{\varepsilon}_s$) vs. 1/T as shown in Figure 4.42(a). The Q_{app} for the stresses of 22, 38, and 58 MPa are 330.2 kJ/mol, 322.4 kJ/mol, and 308.8 kJ/mol, respectively. The average Q_{app} for the transverse creep tests is calculated as 320.6 kJ/mol. The graph of Q_{app} vs. σ shown in Figure 4.42(b) illustrates a linear relationship between Q_{app} and σ , which can be expressed by the relation:

$$Q_{app} = -0.598\sigma + 342.96 \qquad (4.13)$$

A least square fit technique, as discussed in the Section 3.4.1 was used for determining the creep constitutive parameters of the transverse creep tests. The constitutive parameters obtained by the method are shown in Table 4.6.

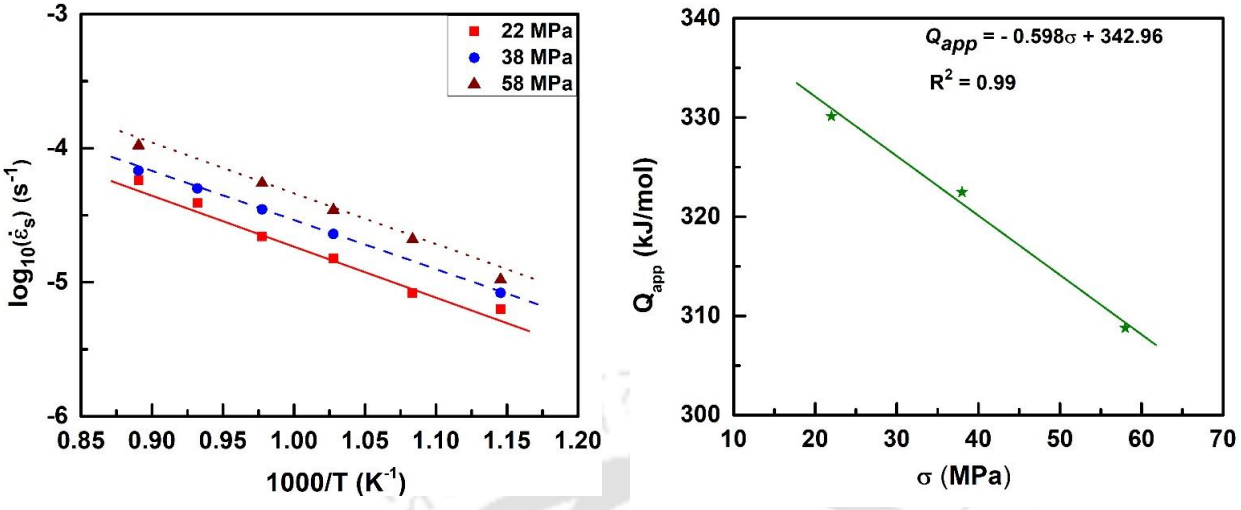

(a) (b)

Figure 4.42 Plot of (a) log ($\dot{\varepsilon}_s$) vs. 1/T and (b) Q_{app} vs. σ for transverse samples.

Table 4.6 Creep constitutive parameters of Eq. 4.4, 4.5 and 4.6 and corresponding R^2- values.

Eq. 4.4	A_1	Q_{app} (kJ/mol)	n_c	R^2
	4.08×10^{-6}	302.68	2.6	0.98
Eq. 4.5	A_2	Q_{app} (kJ/mol)	β	R^2
	2.06×10^{-5}	296.2	0.2088	0.95
Eq. 4.6	A_3	Q_{app} (kJ/mol)	α	R^2
	1.88×10^{-5}	286.04	0.1988	0.77

Based on the data shown in Table 4.6, the following constitutive relationships for the transverse creep tests are obtained for $\dot{\varepsilon}_s$:

$$\dot{\varepsilon}_s = 4.08 \times 10^{-6} \sigma^{2.6} exp\left(-\frac{302680}{RT}\right) \quad (4.14)$$

$$\dot{\varepsilon}_s = 2.06 \times 10^{-5} \exp(0.2088\sigma) exp\left(-\frac{296200}{RT}\right) \quad (4.15)$$

$$\dot{\varepsilon}_s = 1.88 \times 10^{-5} [sinh(0.1988\sigma)] exp\left(-\frac{286040}{RT}\right) \quad (4.16)$$

It can be inferred from the R^2 values given in Table 4.6 that the best creep constitutive equation is the power law equation (Eq. 4.14). Figure 4.43 (a) compares the plot of $\dot{\varepsilon}_s$ vs. $1/T$ obtained experimentally with $\dot{\varepsilon}_s$ values obtained using Eq. 4.11 for different stresses. Figure

4.43 (b) illustrates the plot comparing the values of $\dot{\varepsilon}_s$ obtained experimentally with that calculated using Eq.4.14 for different temperatures.

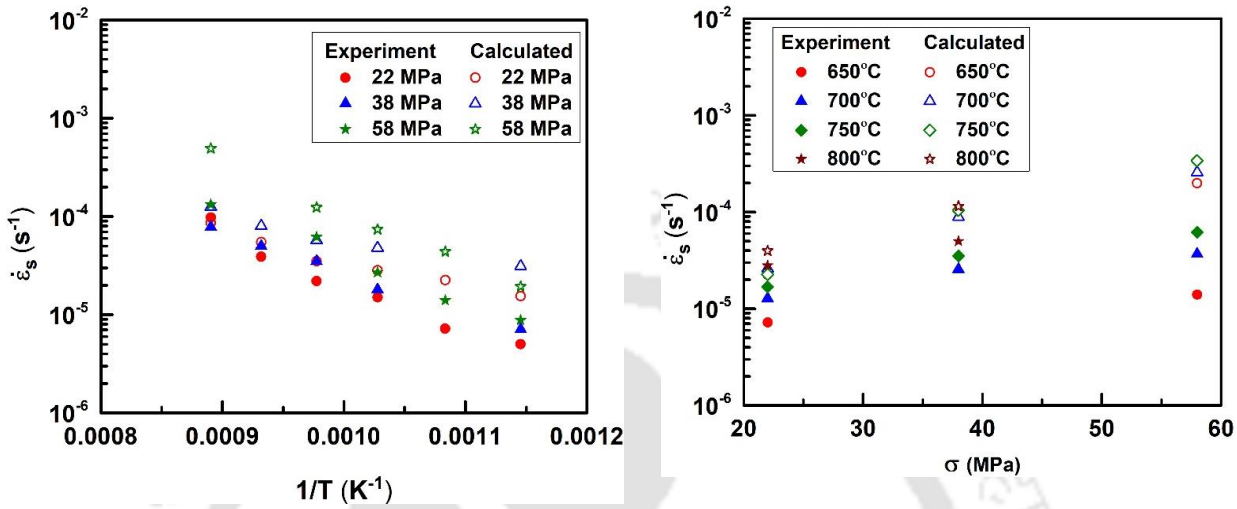

(a) (b)

Figure 4.43 Variation of experimental $\dot{\varepsilon}_s$ and calculated $\dot{\varepsilon}_s$ using Eq. 4.14 with (a) $1/T$ and (b) σ for transverse creep tests.

From figures 4.40 and 4.43, it can be seen that there is a good correlation between the calculated values and the experimental data in the variation of $\dot{\varepsilon}_s$ with $1/T$ or applied stress(σ) for both the longitudinal and transverse creep tests. In the case of modeling of creep, a variation of one order of magnitude between experimentally obtained value $\dot{\varepsilon}_s$ and that obtained by the constitutive equation is generally acceptable [216]. Hence, the constitutive relationship obtained by Eqs. 4.9 and 4.14 is acceptable for the creep deformation of the Zr-2.5Nb alloy along the longitudinal and transverse directions, respectively.

4.4.5 Monkman-Grant relationships

The Monkman-Grant as well as the modified Monkman-Grant (MMG)relationships are useful in determining the creep rupture time of the material. The significance of these relationships has been presented in section 2.11.1. The results of the analysis of the data obtained from the longitudinal and transverse creep test with respect to Monkman-Grant and modified Monkman-Grant relationships are presented and discussed in the following subsections.

4.4.5.a Longitudinal creep tests

The plot of rupture time(t_r) vs. $\dot{\varepsilon}_s$ for the longitudinal creep tests conducted at different temperatures and stresses is given in Figure 4.44(a). The figure shows a straight line fit having an R^2 value of 0.984. The value of Monkman-Grant exponent *m* and constant *C* in Eq. 2.18 is 1.024 and 0.228, respectively. Since it is reasonable to assume the value of *m* as unity, Eq. 2.18 can be re-written as:

$$\dot{\varepsilon}_s . t_r = C_{MG} = 0.228 \tag{4.17}$$

Figure 4.44(a) indicates that t_r is inversely proportional to $\dot{\varepsilon}_s$, and the Monkman-Grant relationship can be utilized for predicting the time to rupture of Zr-2.5Nb alloy. Figure 4.44(b) shows the log-log plot of t_r / ε_f vs. $\dot{\varepsilon}_s$ for the alloy. The plot gives a straight-line fit with an R^2 value of 0.988. Modified Monkman-Grant exponent *m'* and constant *C'* (Eq. 2.19) are found to be 0.99 and 0.348, respectively. Approximating the value of *m'* to be equal to unity, the modified Monkman-Grant expression can be obtained as

$$\dot{\varepsilon}_s . \frac{t_r}{\varepsilon_f} = C_{MMG} = 0.348 \tag{4.18}$$

This shows that the t_r / ε_f is inversely proportional to $\dot{\varepsilon}_s$. The MMG relationship expressed in the above form can be used with reasonable accuracy for estimating the rupture time from the minimum creep rate and fracture strain of the alloy.

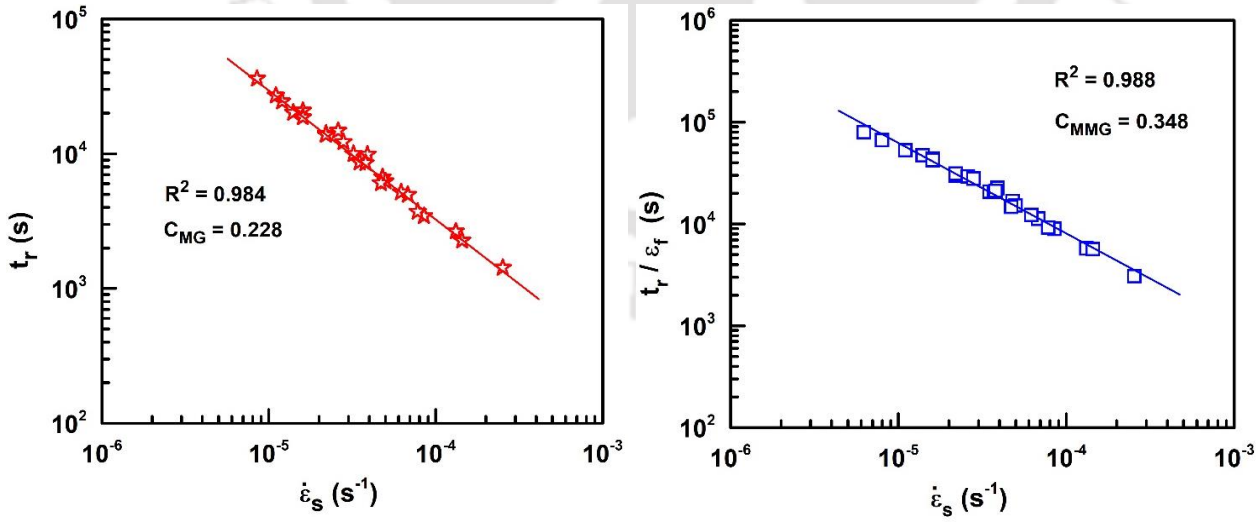

(a) (b)

Figure 4.44 Plot of (a) rupture time vs. $\dot{\varepsilon}_s$ and (b) t_r / ε_f vs. $\dot{\varepsilon}_s$ for the longitudinal creep tests.

Analogous to MMG relationship, Choudhary et al. [130] proposed relationships

correlating minimum strain rate ($\dot{\varepsilon}_s$), with time for onset of secondary creep, t_{os} and time for onset of tertiary creep t_t. Time t_{os} can be obtained using the relationship:

$$\dot{\varepsilon}_s{}^a . \frac{t_{os}}{\varepsilon_1} = K \tag{4.19}$$

where a and K are constants. A logarithmic plot of t_{os}/ε_1 vs. $\dot{\varepsilon}_s$ obtained using the longitudinal creep data is shown in Figure 4.45 (a). From the straight line fit, the values for a and K are determined as 0.998 and 0.44, respectively, with $R^2 = 0.992$. In the present case, assuming a =1, Eq. 4.19 can be expressed as:

$$\dot{\varepsilon}_s . \frac{t_{os}}{\varepsilon_1} = 0.44 \tag{4.20}$$

Similarly, the time for onset of tertiary creep, t_t can be obtained by the relationship

$$\dot{\varepsilon}_s{}^b . \frac{t_t}{\varepsilon_3} = K' \tag{4.21}$$

where b and K' are constants. From the logarithmic plot of t_t/ε_3 vs. $\dot{\varepsilon}_s$ shown in Figure 4.45(b), b and K' were determined to be 1.02 and 0.52, respectively. Considering b = 1, Eq. 4.21 can be expressed as:

$$\dot{\varepsilon}_s . \frac{t_t}{\varepsilon_3} = K' = 0.52 \tag{4.22}$$

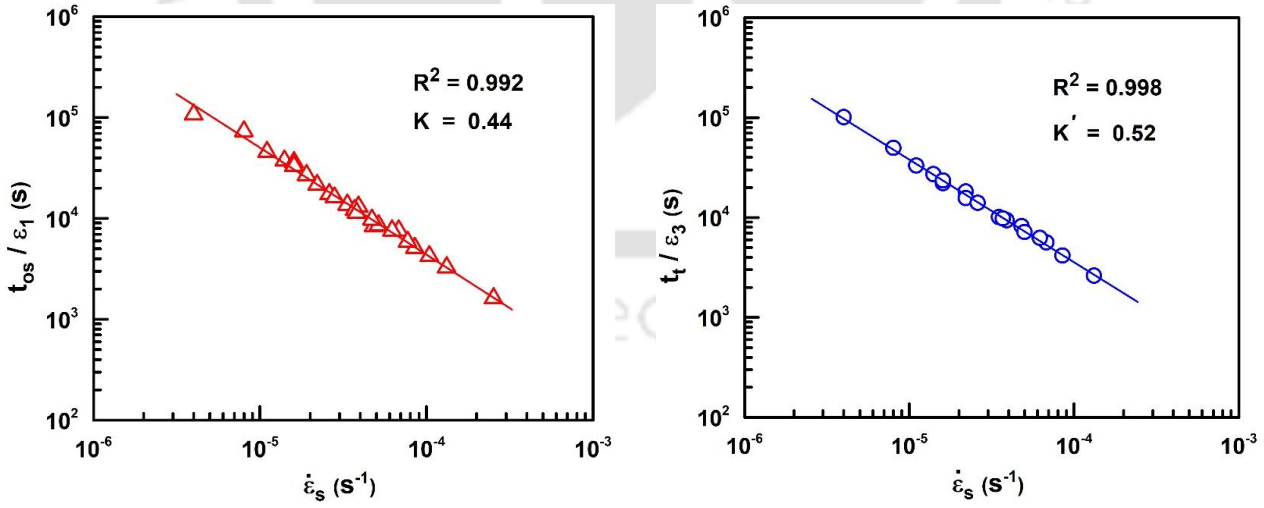

(a) (b)

Figure 4.45 Plot of (a) t_{os}/ε_1 vs. $\dot{\varepsilon}_s$ and (b) t_t/ε_3 vs. $\dot{\varepsilon}_s$ for longitudinal creep tests.

Figure 4.45 shows that relationship involving the steady state creep and transient creep is

valid for the alloy. The minimum creep rate, which is the effective creep life of a component can be obtained using Eqs. 4.20 and 4.22, considering other parameters are known.

4.4.5.b Transverse creep tests

The plot of t_r vs. $\dot{\varepsilon}_s$ for the transverse creep tests conducted at different temperatures and stresses is given in Figure 4.46(a). The figure shows a straight line fit with R^2 =0.99. The value of MG exponent *m* and constant *C* in Eq. 2.18 are 0.998 and 0.326, respectively. Considering *m* as unity, Eq. 2.18 for the transverse creep tests can be written in the form:

$$\dot{\varepsilon}_s . t_r = C_{MG} = 0.326 \tag{4.23}$$

From Eq. 4.23 it can be seen that t_r is inversely proportional to $\dot{\varepsilon}_s$. Figure 4.46 (b) represents the log-log plot of t_r / ε_f vs. $\dot{\varepsilon}_s$ at various temperatures and stresses. The plot gives a straight line fit having an R^2 = 0.994. The value of MMG exponent *m'* and constant *C'* (Eq. 2.19) are calculated as 1.01 and 0.544, respectively. Since the value of *m'* is almost unity, the MMG expression can be expressed as

$$\dot{\varepsilon}_s . \frac{t_r}{\varepsilon_f} = C_{MMG} = 0.544 \tag{4.24}$$

This shows that t_r / ε_f is inversely proportional to $\dot{\varepsilon}_s$. Similar to the longitudinal case, in the case of transverse creep tests, the modified Monkman-Grant relationship expressed in the above form can be used for estimating the rupture time. From the values of the coefficient of determination for Eq. 4.17, 4.18, 4.23, and Eq. 4.24, one can conclude that both Monkman-Grant and modified Monkman-Grant relationships can be successfully used to correlate the time to rupture and minimum creep rate for the Zr-2.5Nb alloy in both longitudinal and transverse directions.

The proposed relationship by Choudhary et al. [130] correlating $\dot{\varepsilon}_s$, t_{os} and t_t (Eq. 4.19 and 4.21) was used for the transverse creep tests also . From the straight line fit in Figure 4.47(a), *a* and *K* are determined as 0.999 and 0.48 respectively, having R^2 = 0.992. Considering *a* =1, Eq. 4.19 can be rewritten as

$$\dot{\varepsilon}_s . \frac{t_{os}}{\varepsilon_1} = K = 0.48 \tag{4.25}$$

Similarly, from the plot of t_t/ε_3 vs. $\dot{\varepsilon}_s$ shown in Figure 4.47(b), *b* and K' were determined to be 1.04 and 0.64, respectively. Assuming *b* = 1, Eq. 4.21 can be rewritten in the form

$$\dot{\varepsilon}_s . \frac{t_t}{\varepsilon_3} = K' = 0.64 \qquad (4.26)$$

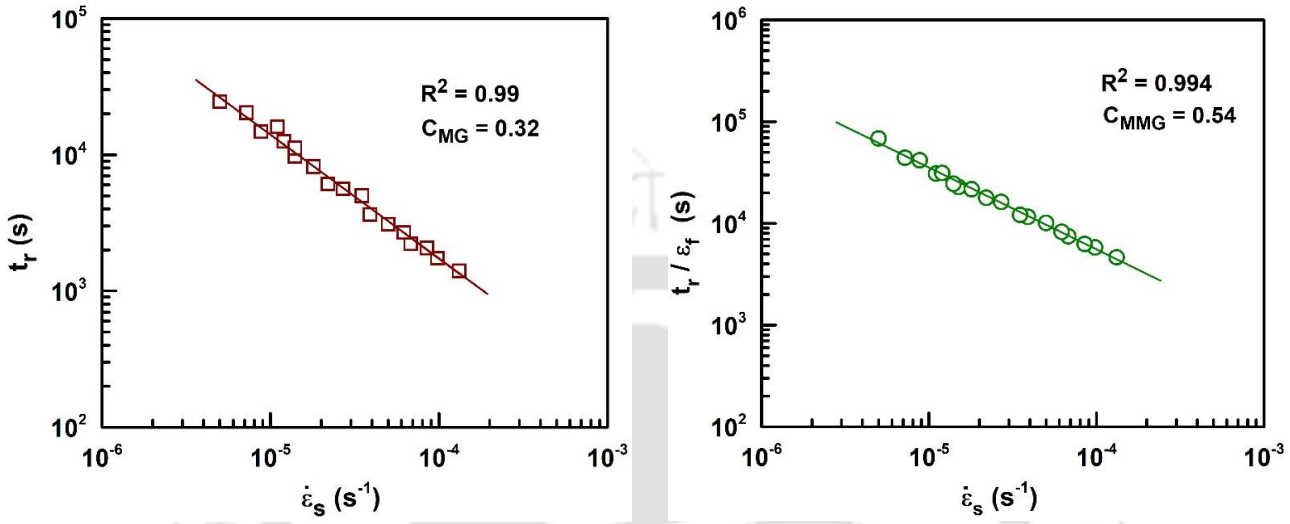

(a) (b)

Figure 4.46 Plot of (a) rupture time vs. $\dot{\varepsilon}_s$ and (b) t_r / ε_f vs. $\dot{\varepsilon}_s$ for transverse creep tests.

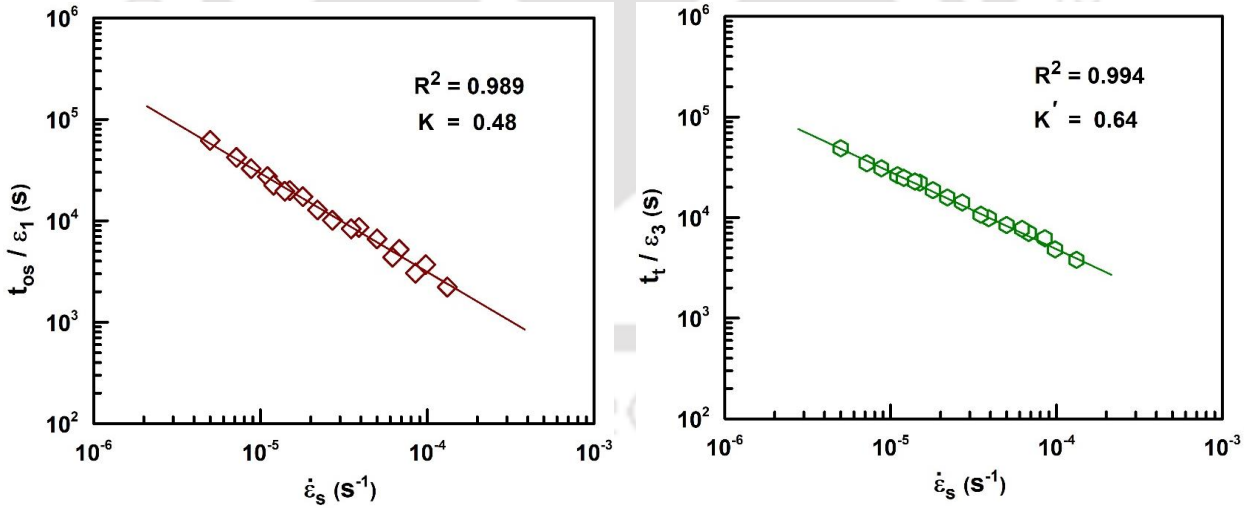

(a) (b)

Figure 4.47 Plot of (a) t_{os}/ε_1 vs. $\dot{\varepsilon}_s$ and (b) t_t/ε_3 vs. $\dot{\varepsilon}_s$ for transverse creep tests.

Figure 4.48 (a) and (b) compares the rupture time obtained experimentally with that calculated using modified Monkman-Grant relationships. It can be seen that for the longitudinal and transverse creep tests, the rupture time calculated using MMG equation gives

a R^2 value of more than 0.99 and MRE value ≤ 9.6%. This shows a very good correlation between the experimentally obtained rupture time and that obtained using MMG equation.

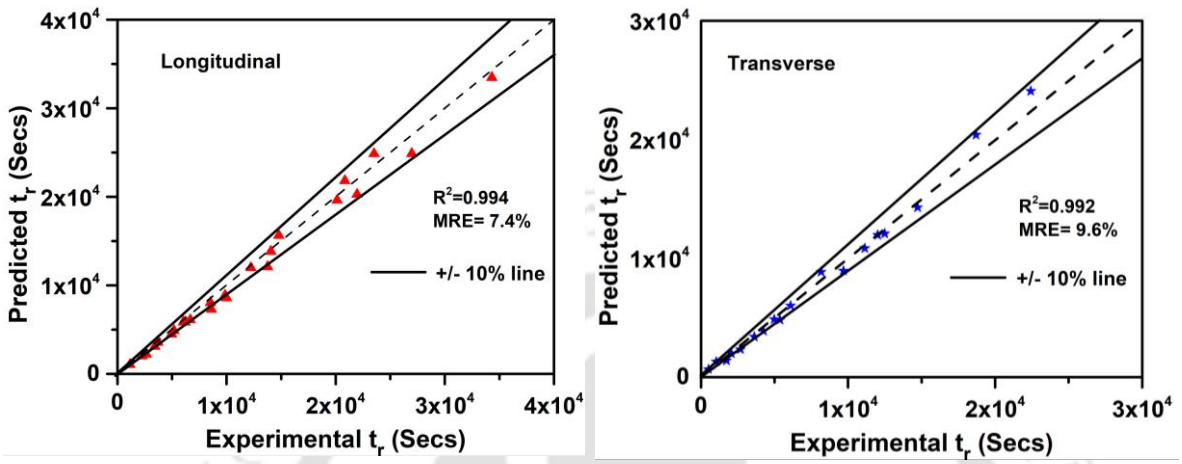

(a) (b)

Figure 4.48 Comparison between rupture time calculated using MMG equation and obtained experimentally for (a) longitudinal and (b) transverse creep tests.

4.4.6 Creep Damage Tolerance Factor

Components used at high temperatures are built for a specific permissible stress depending on the stress required to reach a certain strain. In this approach, the creep ductility is not considered while arriving at the allowable stress. The Monkman-Grant relationship states that creep deformation and damage are interrelated. According to continuum creep damage mechanics (CDM), the critical damage criterion is defined and can be expressed by Eq. 2.22.

A double logarithmic plot of average creep rate (ε_f / t_r) vs. minimum creep rate($\dot{\varepsilon}_s$) for both the longitudinal and transverse creep tests are shown in Figure 4.49(a) and (b). From the figure, λ in Eq. 2.22 is calculated as 2.8 and 1.8 for longitudinal and transverse tests, respectively. This is in agreement with the trend reported for Zirconium alloys [1]. However, it has been reported that for bulk samples, λ is in the range of 1.5 – 10 [138]. The beginning of the tertiary creep region is typically where microcracks and cavities begin to form during creep. The deformation that occurs during tertiary creep is significantly influenced by the existence of these defects at the grain boundary area.

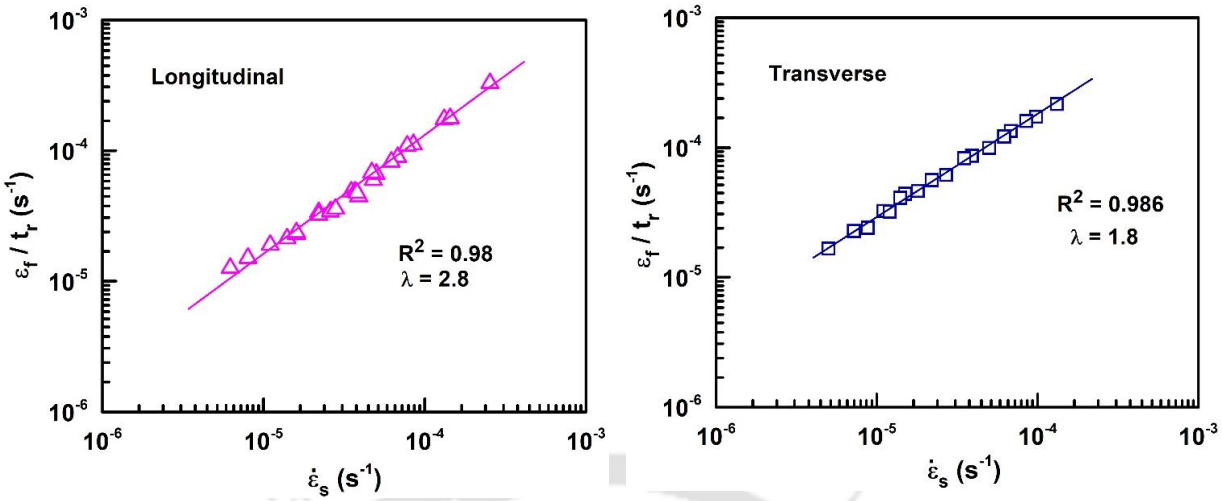

(a) (b)

Figure 4.49 Plot of average creep rate vs. minimum strain rate for (a) longitudinal and (b) transverse creep tests.

According to the model proposed by Ashby and Dyson [217, 218], when the value of λ = 1, the material shows low creep fracture strain, which is indicative of a typical brittle fracture without much plastic deformation. When the values of λ lie between 1.5 - 2.5, the creep damage is controlled by the mechanism of cavity growth [123, 219]. A value of 2.5–5, indicates the formation of the neck in the gauge section. When the value of λ is more than 5, it's an indication of damage resulting from microstructural degradation [217]. For HP40Nb micro-alloyed steel, the value of λ has been reported as 1.2 and 2.5 in the stress regime of 47-68 and 80-120MPa, respectively[194]. In the present investigation, the value of λ = 2.8 for the longitudinal creep tests suggests that the material has undergone localized strain concentration. Moreover, in case of the transverse creep tests, the creep damage is by cavity growth mechanism.

Figure 4.50 (a) and (b) illustrate the t_{MGD} vs. t_r plot for both the longitudinal and transverse creep tests, respectively. From the figure, the values of f_{CDM} are found to be 0.704 and 0.764, respectively. It is to be noted that the value of f_{CDM} calculated using Eq. 2.23 for λ= 2.8 and λ = 1.8 for the present alloy is 0.708 and 0.768, respectively, which is almost equal to the values obtained from Figure 4.50. This shows that the value of f_{CDM} obtained by MG relationship is in accordance with that obtained by CDM technique.

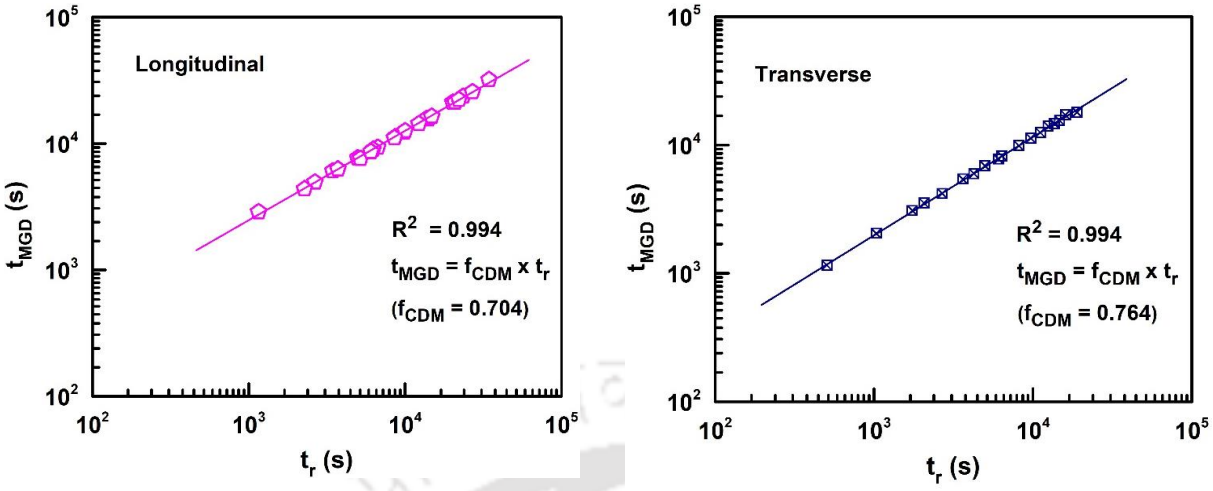

(a) (b)

Figure 4.50 Plot of t_{MGD} vs. t_r for (a) longitudinal and (b) transverse creep tests.

To conclude, the creep curve can be divided into two regions. The first region is a safe region that extends up to t_{MGD}. Here, the creep damage occurs slowly and is almost uniform. The second region, lying between t_{MGD} and $t_{r,}$ is considered unsafe due to localized creep damage, which accelerates the creep process. A transition exists between these two regions where the size of the cavity reaches a critical value causing an accelerated creep rate[220]. For engineering components, f_{CDM} can be utilized as a creep design criterion as it quantifies the degradation of the material during service [221]. From the current investigation, the more conservative value of f_{CDM} equal to 0.708 can be used as a factor of safety in creep design for the Zr-2.5Nb alloy.

4.5 Modeling of creep curve by Multiple Linear Regression and Artificial Neural Network

Various creep deformation models, like constitutive models, Monkman-Grant relationship, etc., exist, each with its own advantages and disadvantages. The constitutive equations can predict the minimum creep rate and express only the secondary creep region of a creep curve. Parametric techniques like the L-M parametric technique and Monkman-grant relationships can predict the creep rupture life of the material. None of these techniques can predict a full creep curve of a material based on available experimental data. In the present work, an attempt was made to predict the creep curve by data-driven techniques like MLR and ANN modeling.

4.5.1 Multiple Linear Regression modeling

Multiple linear regression (MLR) analysis was carried out by assuming that the creep strain(ε) is related to the applied stress (σ), test temperature (T), and exposure time (t) by the relationship given in Eq. 3.15. The values of the constants *A*, *m*, *n*, and *l* were determined using MLR. Eq. 3.15 can be rewritten as Eq. 4.27 and 4.28 for the longitudinal and transverse samples, respectively.

$$\dot{\varepsilon} = 8.41 \times 10^{-14} \sigma^{1.04} T^{3.56} t^{0.52} \quad (4.27)$$

$$\dot{\varepsilon} = 6.72 \times 10^{-14} \sigma^{0.16} T^{2.48} t^{0.28} \quad (4.28)$$

Creep curves were generated using Eq. 4.27 and 4.28 and compared with the actual experimental values. The prediction capability was substantiated by determining the statistical parameters, viz., R^2, MRE, and RMSE. Figure 4.51 (a) and (b) compares the MLR predicted and experimentally obtained creep curves tested at 850 °C/5 MPa °C and 700 °C/ 4 MPa for the longitudinal creep tests and 700 °C/22 MPa °C and 850 °C/ 58 MPa for the transverse tests. Table 4.7 gives the values of R^2, MRE, and RMSE for the creep curves obtained for the above-mentioned test conditions. Figure 4.51(a) indicates that the MLR model could reasonably predict the primary creep strain for the longitudinal samples. However, the model overpredicted for the secondary creep region and underpredicted the tertiary creep strain. As shown in Figure 4.51, a comparison of the curves reveals no indication of the transition from secondary to tertiary creep during the MLR prediction. Furthermore, despite the material entering the tertiary creep region, there is no evidence that the secondary creep has terminated. In transverse samples (Figure 4.51(b)), the MLR model failed to predict the secondary and tertiary creep region. According to the findings of this inquiry, the MLR approach is unlikely to be effective in determining overall creep life.

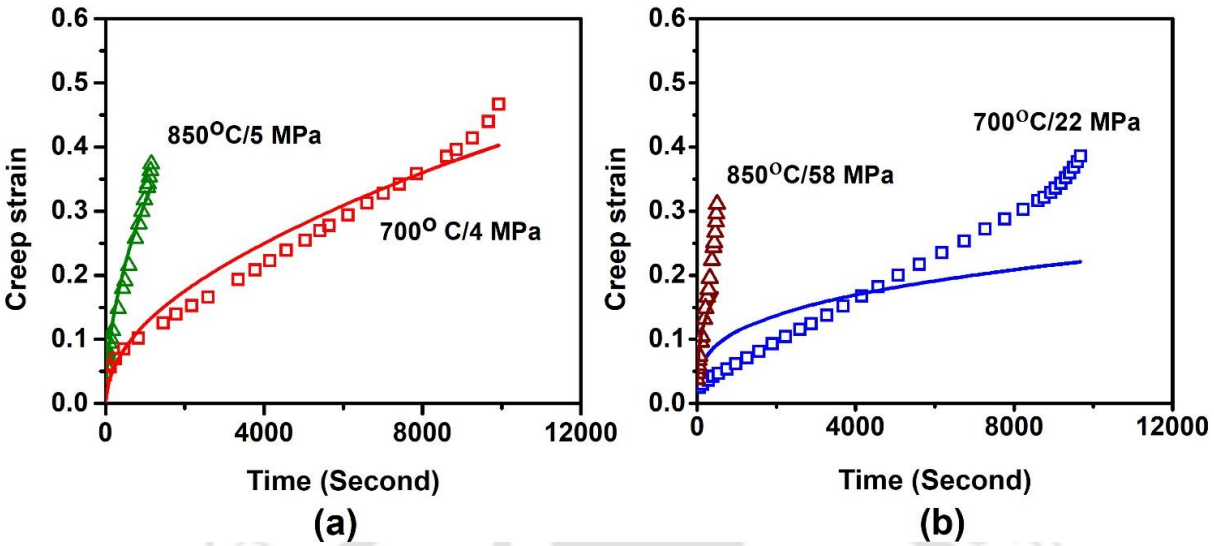

Figure 4.51 Comparison of MLR predicted curve and experimental curve. Symbols indicate the experimental curves, whereas the solid lines represent the MLR simulated curves.

Table 4.7 Values of R^2, MRE, and RMSE of the MLR predicted curve with respect to the experimental curves obtained from longitudinal and transverse creep tests.

Stress (MPa)	Temperature (°C)	R^2- value	MRE(%)	RMSE
4	700	0.904	14.8	0.046
5	850	0.926	11.74	0.028
22	700	0.824	58.74	0.086
58	850	0.862	28.22	0.072

4.5.2 Artificial Neural Network Modeling

The ANN model was developed based on the concept that creep strain is a function of applied stress σ, temperature T, and time t.

$$\varepsilon = f(\sigma, T, t) \tag{4.29}$$

Creep curve for a particular temperature and stress can be predicted by ANN using limited experimental data. In the present work, three-layered back-propagation ANN architecture was used to predict the creep curve. An input layer consists of three neurons representing input variables of σ, T, and t. The hidden layer consists of several neurons, and

the output layer contains one neuron representing the creep strain ε. The training process involves two stages. The first stage is the forward pass, where the input signals propagate from the input to the output network by generating weight and bias. The second stage is the reverse pass, where calculated error signals propagate backward through the network, and weights and biases are adjusted. Since the algorithm is termed as backpropagation algorithm, the trained ANN model has to be tested by supplying testing data set. The network can be said to be properly fitted when the network gives nearly equal training and testing errors. During the modeling, σ, T, and t values were transformed to lie within the range of 0.1 and 0.9. The output creep strain (ε) value was multiplied by 100 to get creep strain in terms of percentage. Both training and testing of the network were carried out using MATLAB® software (Make: Math Works Inc., Version: R2016a). In order to determine the best configuration of network architecture, several structures were considered with different numbers of hidden neurons. The *tansig*, *logsig*, *purelin* transfer functions, and *trainlm* training function based on the Levenberg–Marquardt optimization algorithm were used to achieve the best network architecture. The training, testing, and validation were conducted separately for the longitudinal and transverse creep tests.

During the training of the network, after a series of trials, it was found that a network having 25 and 28 neurons best represented the experimental data obtained from the longitudinal and transverse creep tests, respectively. In the training phase of longitudinal creep tests, the RMS functional error and maximum deviation error for the optimal network architecture were 0.007 and 7.19 %, respectively. The corresponding values obtained during the testing were 0.0056 and 7.17%, respectively. In the case of transverse tests, the RMS functional error and maximum deviation error were obtained as 0.0044 and 7.86 %, respectively. For the training, it was obtained as 0.0048 and 7.76%, respectively. The plot of the ANN-predicted creep strains vs. experimental creep strains during the training and testing for the longitudinal and transverse tests are presented in Figures 4.52 and 4.53, respectively. Points lying along the diagonal line in the plot (dashed line) indicate a perfect fit. The two lines on both sides of the diagonal lines indicate ± 5% deviation lines. For longitudinal creep tests, it can be observed that during training, 360 out of 365 (i.e., 98.63%) total data points lie within ± 5% error, where the maximum deviation error is 4.92%. The mean relative error (MRE) and the R^2 value of the training set of data is 0.14% and 0.998, respectively. On the other hand, in the case of testing phase, 194 out of 199 data points (i.e., 97.48%) could be

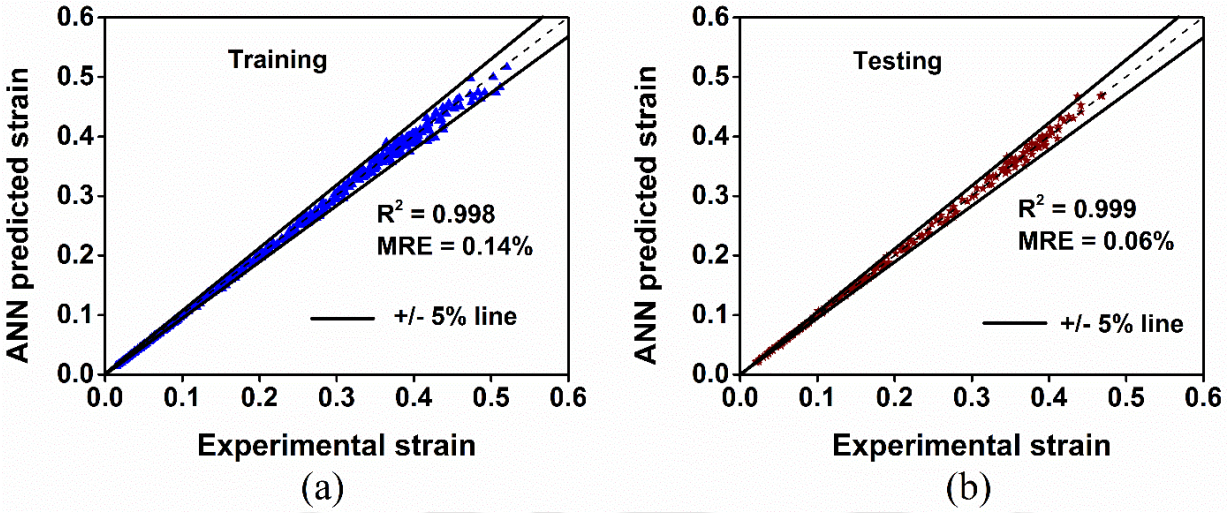

Figure 4.52 Correlation between neural network predicted and experimentally obtained creep strain from longitudinal creep tests after (a) training and (b) testing.

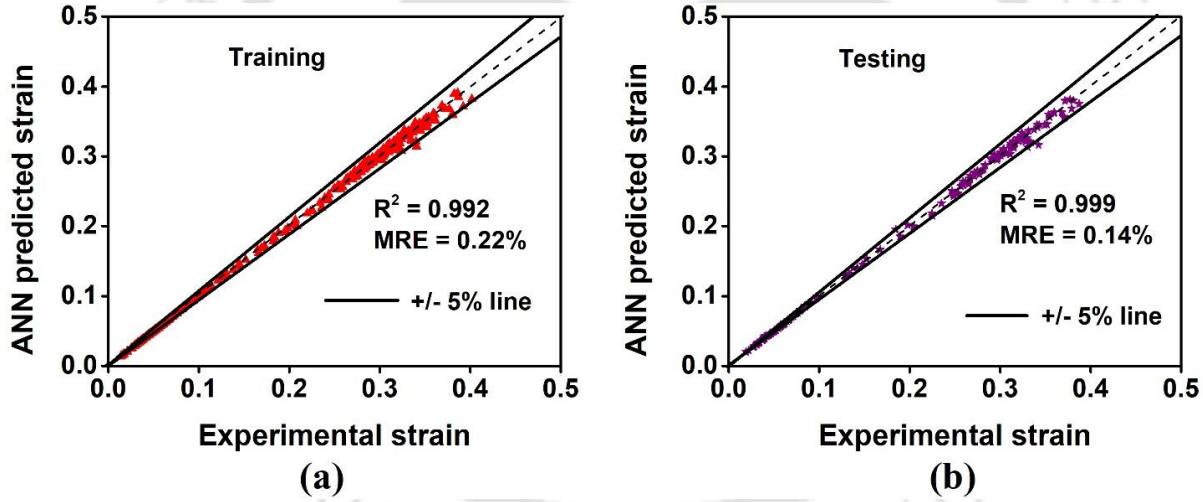

Figure 4.53 Correlation between neural network predicted and experimental creep strain after (a) training and (b) testing for transverse creep.

estimated within a deviation error of ± 5%, having a maximum error of 4.83%. The R^2- value and MRE in the case of the testing process were 0.999 and 0.06%, respectively. For transverse creep tests during training, it was observed that 314 out of 322 total data points lie within ± 5% error, with a maximum deviation error of 7.86%. The MRE and the R^2 value of the training set of data is 0.22% and 0.992, respectively. In the case of testing phase, 165 out of 169 data points could be predicted within a deviation error of ± 5%, with a maximum error of 7.76%. The R^2

value and MRE in the case of the testing process were 0.999 and 0.14%, respectively. In the creep modeling of HP40Nb micro-alloyed steel using a similar ANN model, it was reported that during the training and testing phase, 97.3% and 96.8% of the data lay within the deviation error of ± 15% error [18], which is more than that found in this study.

The efficacy of the developed ANN model was evaluated by determining the percentage relative error. The ANN-predicted values were compared with the experimental data, and the percentage relative errors were determined by the relationship:

$$\text{Relative error (\%)} = \frac{E_i - P_i}{E_i} \times 100 \qquad (4.30)$$

where $E_i$and P_i are the experimentally obtained and predicted values. The result is shown graphically by the frequency counts with respect to the relative error in Figures 4.54 and 4.55. The figures represent more or less a typical Gaussian distribution. For the longitudinal tests, as shown in Figure 4.54, during the training and testing, ~ 92% and ~91% of the entire data sets were found to be within a relative error of ± 2%, respectively. In the case of transverse tests (Figure 4.55), ~ 89 and ~87 % of the entire data sets were found to be within a relative error of ±2%, respectively. This indicates that the predicted values were in good agreement with the actual values. Moreover, the overall relative error in the case of training and testing by using the ANN varied from 6.46% - 7.19% and 7.08% - 7.17% for longitudinal tests and 6.48% - 7.86% and 7.22% - 7.76% , for the transverse tests, respectively.

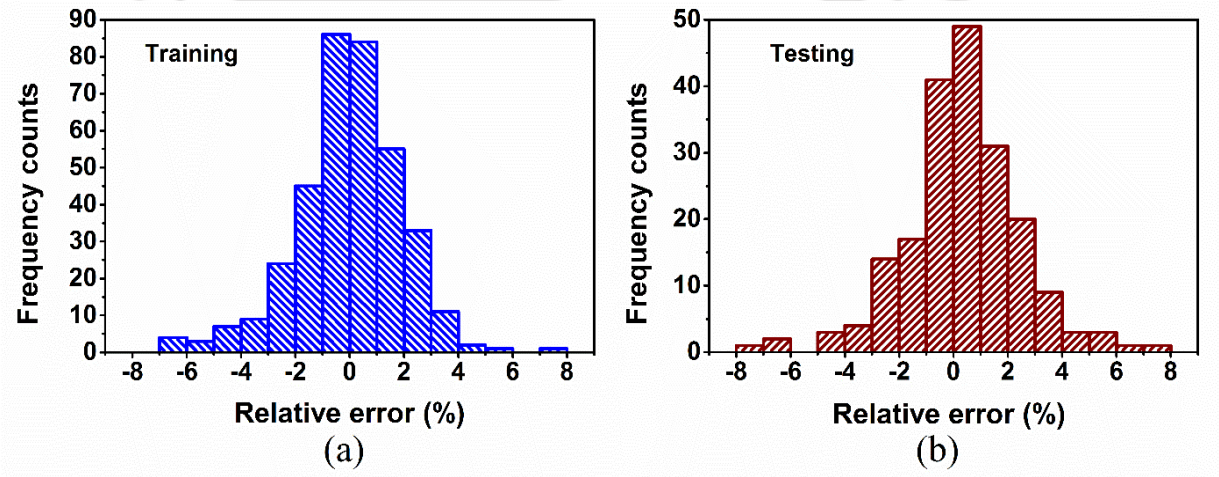

Figure 4.54 Relative error between neural network predicted and experimentally obtained creep strain from longitudinal creep tests after (a) training and (b) testing.

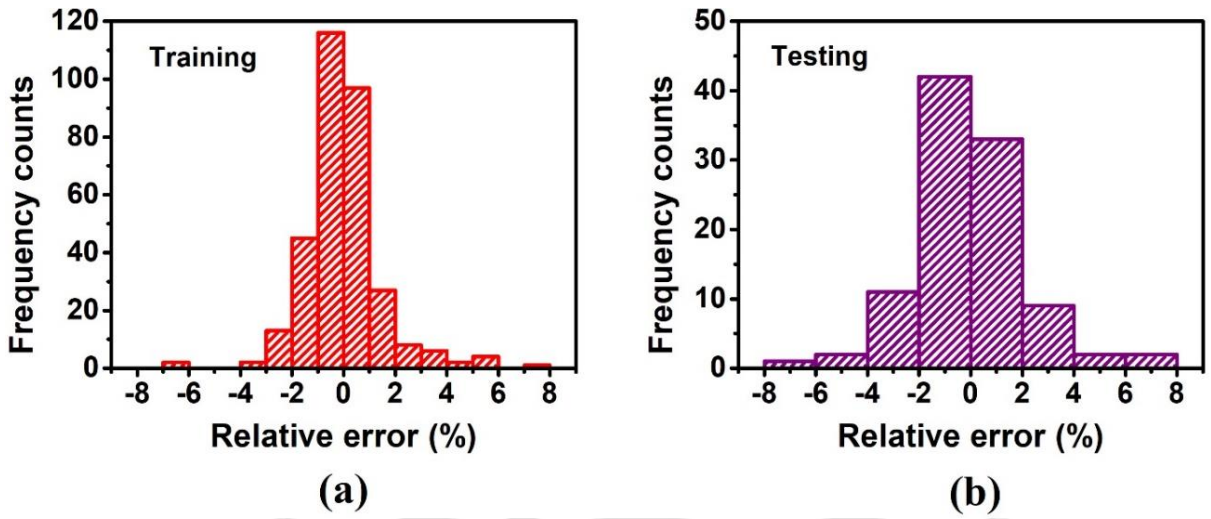

Figure 4.55 Relative error between neural network predicted and experimental creep strain after (a) training and (b) testing for transverse creep.

The predictability of the proposed ANN model was further investigated by determining the amount of variation between the ANN-predicted values and the experimental results. To accomplish this, residuals were computed as:

$$\text{Residuals} = E_i - P_i \tag{4.31}$$

The plot between the residuals and the ANN predicted strain is given in Figures 4.56 and 4.57 for both the longitudinal and transverse tests, respectively. From the plots, it can be seen that there is not much deviation in the residuals about the mean zero line at lower strain values. However, a comparatively higher scatter in the residuals is seen at higher values of strain., High variations were seen at larger strains since absolute values were chosen for computing the residuals, although the relative variation between predicted and experimental values was less. The variation in residuals for both the training and testing data sets for both cases was well within ± 0.04. Thus, it can be said that the proposed ANN model has good predictive capabilities and can be successfully used to predict the creep curves.

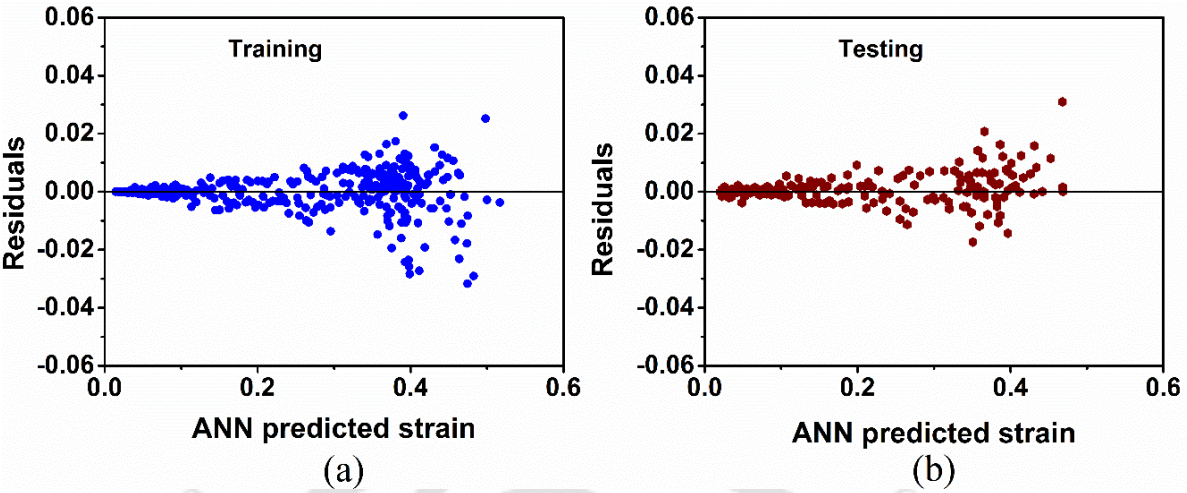

Figure 4.56 The graph between residuals and neural network estimated creep strain after (a) training and (b) testing in case of longitudinal creep test.

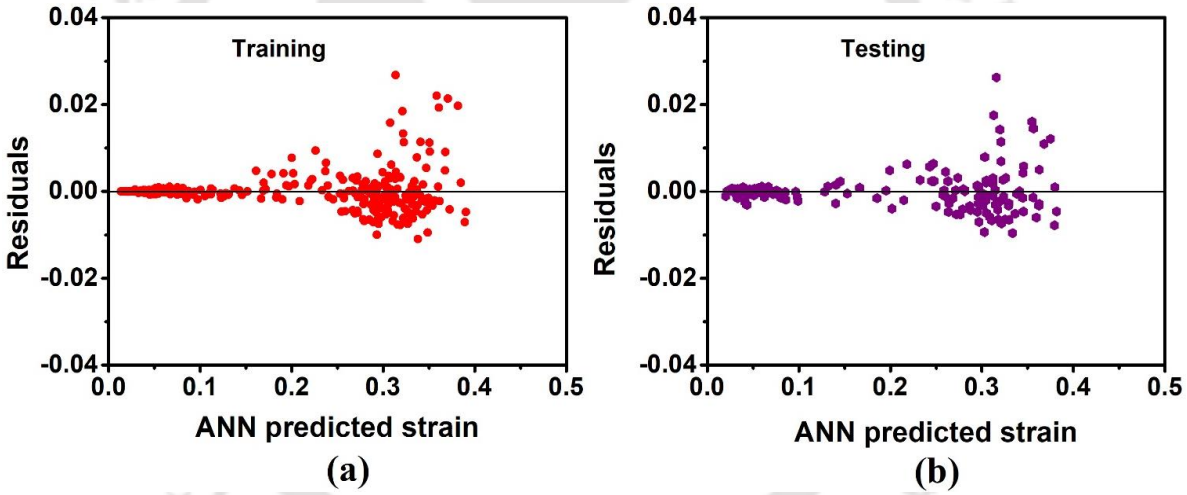

Figure 4.57 The graph between residuals and neural network estimated creep strain after (a) training and (b) testing for transverse creep tests.

The most effective network architecture was frozen after the training and testing phase. This network was then independently validated using the data sets not previously utilized during training and testing. The results obtained have been discussed separately in the following subsections.

4.5.2.a Longitudinal Creep Curve

The plot of the ANN predicted values vs. the experimental values using the 100 data sets kept aside for validation is shown in Figure 4.58 (a). While validating, 99% of the strain

data was predicted within a deviation error of ± 5%. The value of RMSE, R^2 and MRE was found to be 0.0048, 0.999, and 1.46%, respectively. Figure 4.58 (b) represents a histogram plot of frequency counts vs. relative error, indicating a Gaussian distribution with a maximum relative error of 5.06 %. Figure 4.58 (c) shows the randomly distributed values of the residuals about the line of zero mean obtained from the data set used for validation. Hence, the predictive capability of the neural network method is established based on the results of the 100 independent data sets for the longitudinal creep tests.

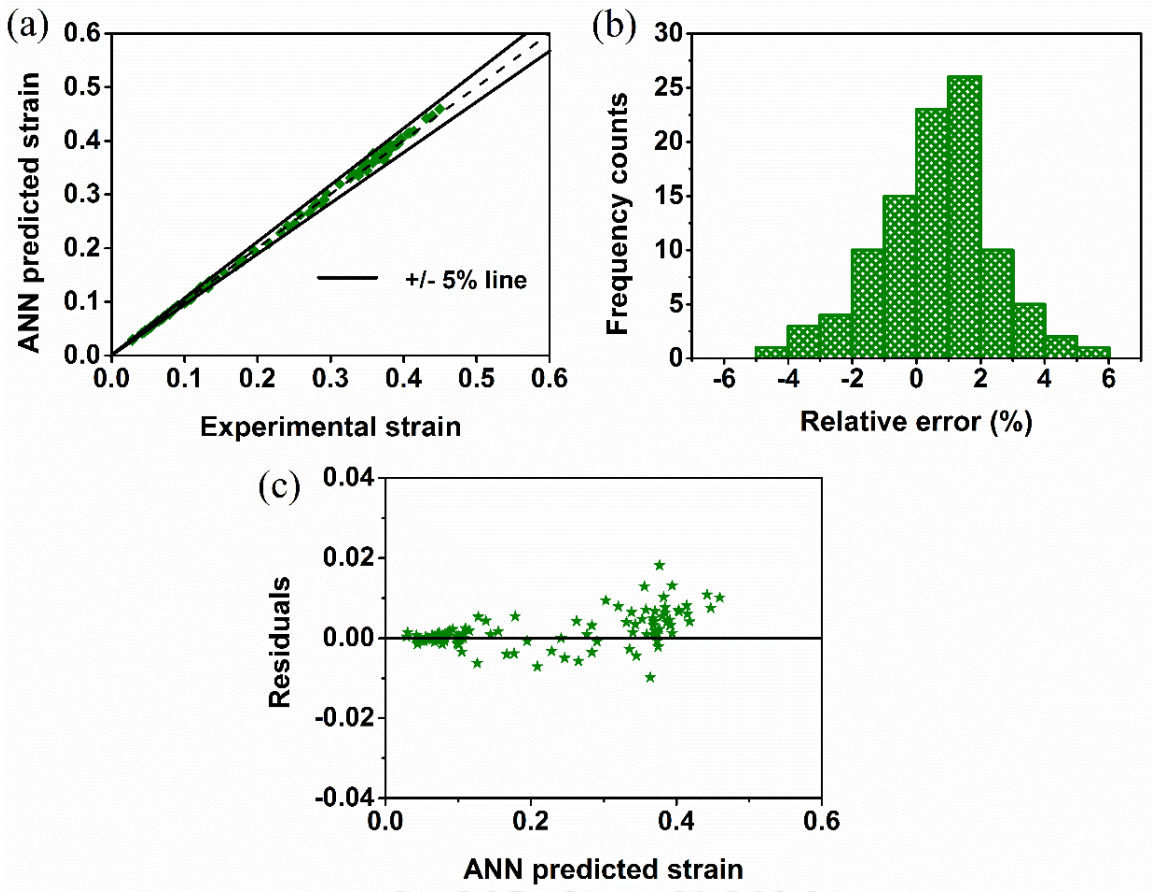

Figure 4.58 Plots of (a) ANN predicted strain vs. experimental strain, (b) frequency counts vs. relative error, and (c) residuals versus predicted strain values obtained during the validation phase for longitudinal creep curves.

Upon gaining confidence in the network architecture, it was used to simulate a few creep curves for the experimental conditions mentioned in Table 3.1. The comparison between the ANN-predicted creep curve and the ones attained from the longitudinal creep tests conducted at different stresses and temperatures are depicted in Figure 4.59. The ANN-predicted curves fit almost perfectly with the experimentally obtained creep curves. The

values of the fitting parameters viz., R^2, MRE and RMSE for these curves are given in Table 4.8. For all the creep curves, the range of values for R^2, MRE, and RMSE lie between 0.996-0.999, 1-2 %, and 0.0012-0.01, respectively, which indicates an almost perfect prediction by the ANN technique.

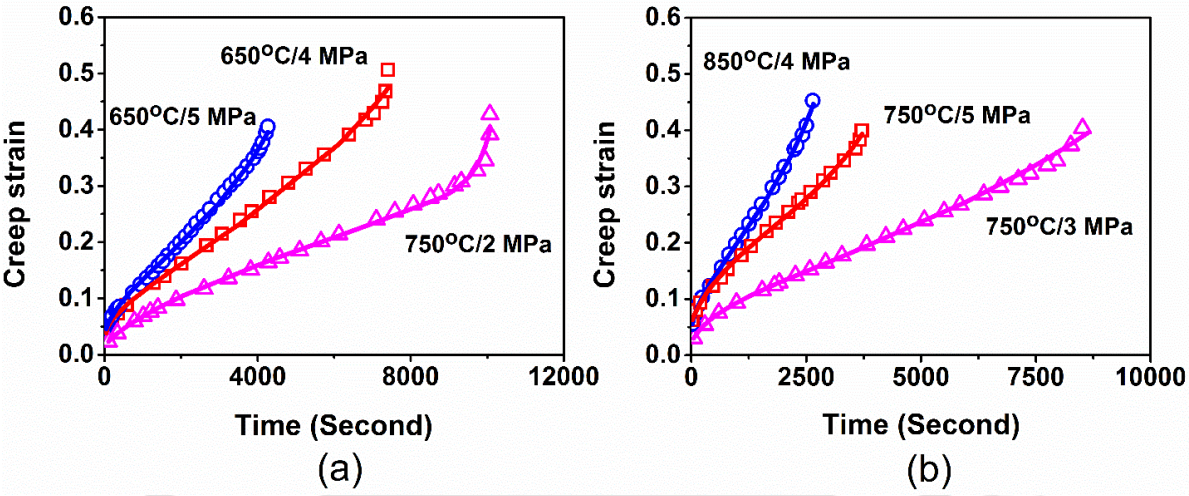

Figure 4.59 Comparison of creep curves obtained from ANN simulation and longitudinal creep experiments. Symbols denote experimental curves; solid lines indicate the simulated curves.

Table 4.8 Values of R^2, MRE, and RMSE of the ANN predicted curve with respect to the experimental curves obtained from longitudinal creep tests.

	Stress (MPa)	Temperature (°C)	R^2- value	MRE value (%)	RMSE
Fig. 4.59(a)	2	700	0.996	2.08	0.01
	4	650	0.998	1.85	0.006
	5	650	0.999	1.28	0.0036
Fig. 4.59(b)	3	750	0.998	1.58	0.0082
	5	750	0.999	1.4	0.0046
	4	850	0.999	1.04	0.004

4.5.2.b Transverse Creep Curve

After the training and testing phase, the optimal network architecture was selected. Similar to the longitudinal case, here also, this network was independently validated using the 98 data sets not previously utilized during training and testing. The plot of the ANN predicted values vs. the experimental values obtained using the validation data sets is shown in Figure 4.60 (a). 97% of the strain data was predicted within a deviation error of ± 5%. The value of RMSE, R^2 and MRE was found to be 0.0038, 0.999, and 1.5%, respectively. Figure 4.60 (b) represents a histogram plot of frequency counts vs. relative error, with a maximum relative error of 6.96 %. Figure 4.60 (c) shows the values of the residuals about the line of zero mean obtained from the data set used for validation. This shows the effectiveness of the neural network.

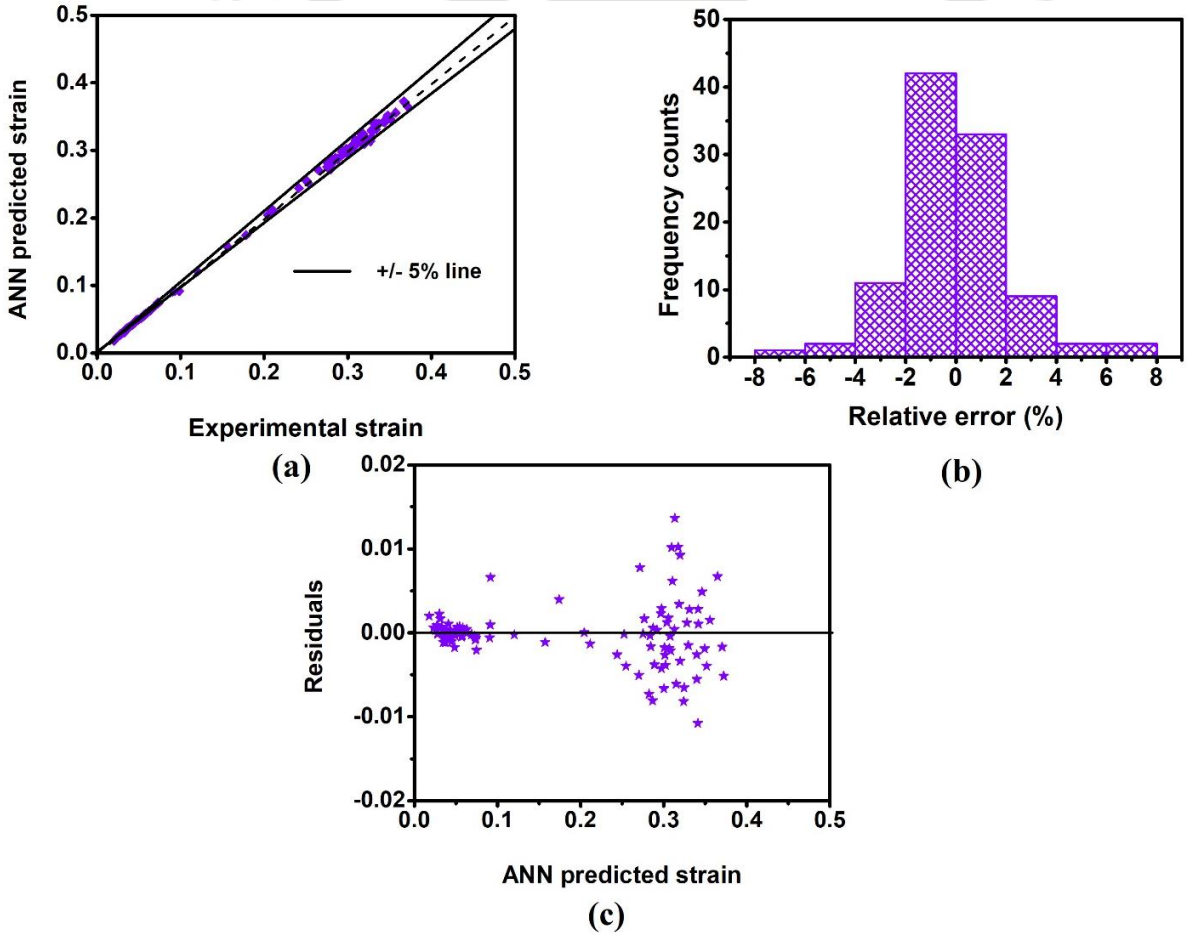

Figure 4.60 Plots of (a) ANN predicted strain vs. experimental strain, (b) frequency counts vs. relative error, and (c) residuals versus predicted strain values obtained during the validation of transverse creep.

Following the validation, the developed ANN model was used to simulate a few creep curves for the experimental conditions mentioned in Table 3.2. The comparison between the ANN-predicted creep curve and those obtained from transverse creep tests conducted at different stresses and temperatures are shown in Figure 4.61. The ANN-simulated curves fit almost perfectly with the experimentally obtained creep curves. The values of the fitting parameters viz., R^2, MRE, and RMSE for these curves are given in Table 4.9, indicating a good correlation.

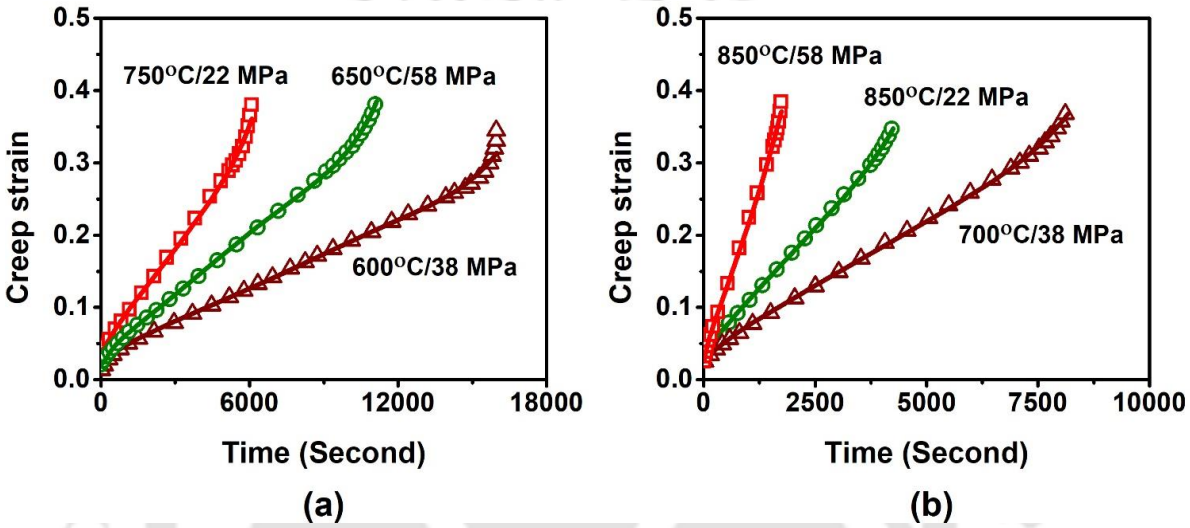

Figure 4.61 Comparison of creep curves obtained from ANN simulation and transverse creep experiments. Symbols denote experimental curves; solid lines indicate the simulated curves.

Table 4.9 Values of R^2, MRE, and RMSE of the ANN predicted curve with respect to the experimental curves obtained from transverse creep tests.

	Stress (MPa)	Temperature (°C)	R^2- value	MRE value (%)	RMSE
Fig. 4.61(a)	22	750	0.998	1.44	0.0052
	38	600	0.998	1.68	0.0066
	58	650	0.999	0.78	0.0016
Fig. 4.61(b)	22	850	0.999	1.22	0.0052
	38	700	0.997	1.02	0.0024
	58	850	0.999	1.64	0.0012

It can be observed that the developed network has the potential to represent the non-linearity of the creep curve for both the longitudinal and transverse creep tests. The ANN simulated curves accurately predicted the primary and secondary creep region perfectly. The notable observation is that during the prediction of creep curves by the ANN model, a definite shift is observed from the secondary to the tertiary creep regions based on the input combination of temperature and stress. This will aid in identifying the culmination of the secondary creep region, which is the effective creep life of the component.

Garson's equation (Eq.3.21) was used to quantify the relative influence of each input parameter on the output parameter. Figure 4.62 (a) and (b) depict the relative influence of the input parameters on the output parameters as described by Garson [193]. According to the technique, the higher the value of an input parameter in terms of relative importance, the more influence it has on the output parameter. Figure 4.62 shows that for both cases, the applied stress is the most influential factor for creep strain, followed by temperature and time, in that order.

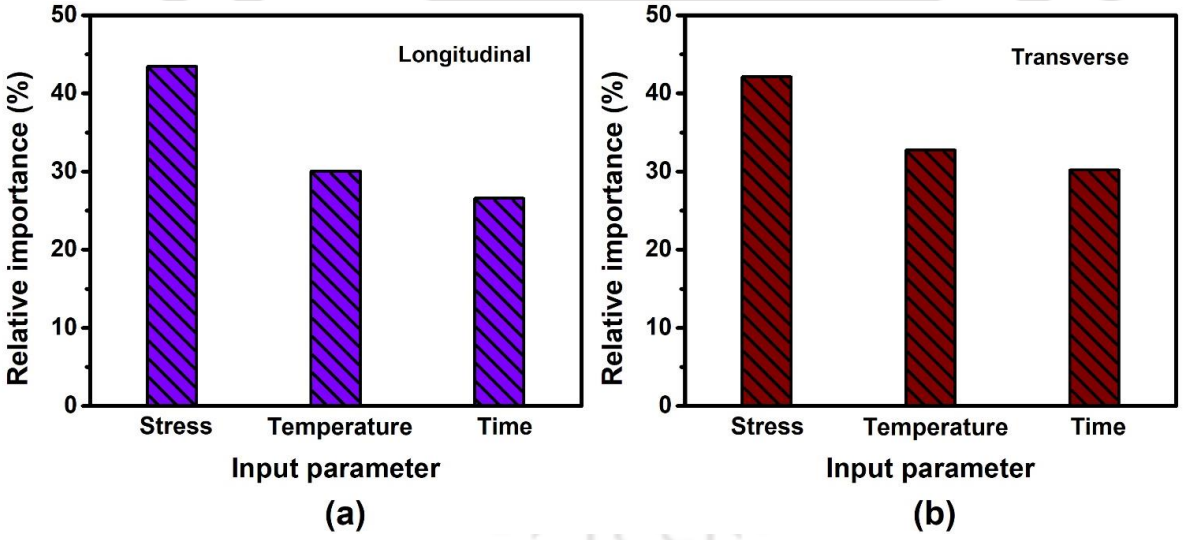

Figure 4.62 The relative importance of the three input parameters on the prediction of creep strain for (a) longitudinal and (b) transverse creep tests.

To authenticate the developed ANN model with test conditions not studied earlier, two sets of creep experiments were done for each specimen orientation. In the case of longitudinal specimens, creep tests were performed at 700 °C / 3 MPa and 800 °C / 4 MPa, and for transverse samples, tests were done at 650 °C / 38 MPa and 800 °C / 58 MPa. Figure

4.63 (a) and (b) compares the experimental, MLR predicted, and ANN-predicted creep curves for the above-stated test conditions. The values of R^2, MRE, and RMSE between the experimentally obtained graphs and the predicted curves are given in Table 4.10. It can be seen that for both experimental conditions, the creep curves predicted by ANN modeling (R^2-value ≥ 0.998, MRE ≤ 2.64 %, and RMSE ≤ 0.0074) were almost the same as that of the experimental creep curves. On the other hand, MLR technique failed to predict the curves effectively (R^2-value ≤ 0.964, MRE ≥ 14.04 %, and RMSE ≥ 0.02). Moreover, for the experiments mentioned above, 98% of the creep curve simulated by the ANN technique falls within a deviation error of ± 5%. In addition, referring to the curves for 700 °C / 3 MPa and 800 °C / 58 MPa test conditions, only two creep regions were observed for the curve simulated by the MLR technique. There was no indication of the termination of secondary creep or the beginning of tertiary creep.

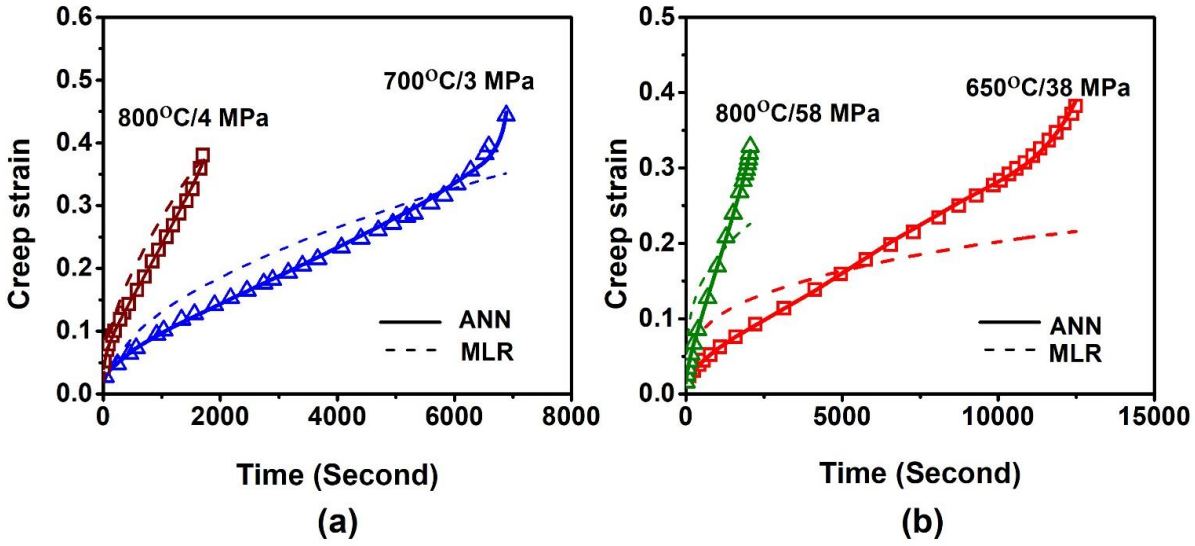

Figure 4.63 Comparison of graphs obtained from MLR and ANN model with that obtained from (a) longitudinal and (b) transverse creep tests. Symbols denote experimental curves.

Table 4.10 Comparison of ANN and MLR model.

Stress (MPa)	Temperature (°C)	ANN			MLR		
		R^2-value	MRE(%)	RMSE	R^2- value	MRE(%)	RMSE
3	700	0.998	2.64	0.0074	0.964	18.82	0.042
4	800	0.999	1.32	0.0048	0.942	14.04	0.022
38	650	0.999	0.92	0.0026	0.868	48.84	0.084
58	800	0.999	0.72	0.0028	0.848	58.26	0.066

It can be seen that the ANN simulated curve accurately predicted the three creep regions with distinct primary, secondary, and tertiary creep regions. Sarkar et al. [26] used the ANN approach to model the in-reactor diametrical creep rate of Zr-2.5Nb alloy. Mechanical properties (YS, UTS,%Elongation), alloy composition, temperature, and flux were the input parameters, whereas the creep rate was the output parameter. The creep life of the alloy was not taken into consideration in the study. In the present investigation, the creep strain was modeled as a function of applied stress, temperature, and time. Generally, the maximum creep life of a component is considered at the termination of the secondary creep region, and this ANN model could efficiently predict the secondary creep region. Therefore, it is reasonable to conclude that the ANN modeling could be effectively applied to predict the creep curve of components and, thereby, its safe creep life.

4.5.3 Comparison of minimum creep rate

Creep tests were carried out on both the longitudinal and transverse samples for different combinations of stresses and temperatures. The minimum creep rate($\dot{\varepsilon}_s$) obtained from the experiments were compared with the power law constitutive equation (Eq. 4.9 and 4.14) and the ANN model. Figures 4.64 and 4.65 shows the comparison for the longitudinal and transverse creep tests, respectively. Figure 4.64(a) shows the plot of $\dot{\varepsilon}_s$vs. 1/T. The plots indicate that the minimum strain rate values computed using the power law constitutive model deviate by one to two orders of magnitude compared to the experimental value. Whereas the ANN predicted $\dot{\varepsilon}_s$ values are in good agreement with experimental values of $\dot{\varepsilon}_s$. Figure 4.64(b) shows the comparison of $\dot{\varepsilon}_s$ values vs. the applied stress(σ). Table 4.11 compares the $\dot{\varepsilon}_s$values obtained experimentally with that predicted using constitutive equation and ANN

model.

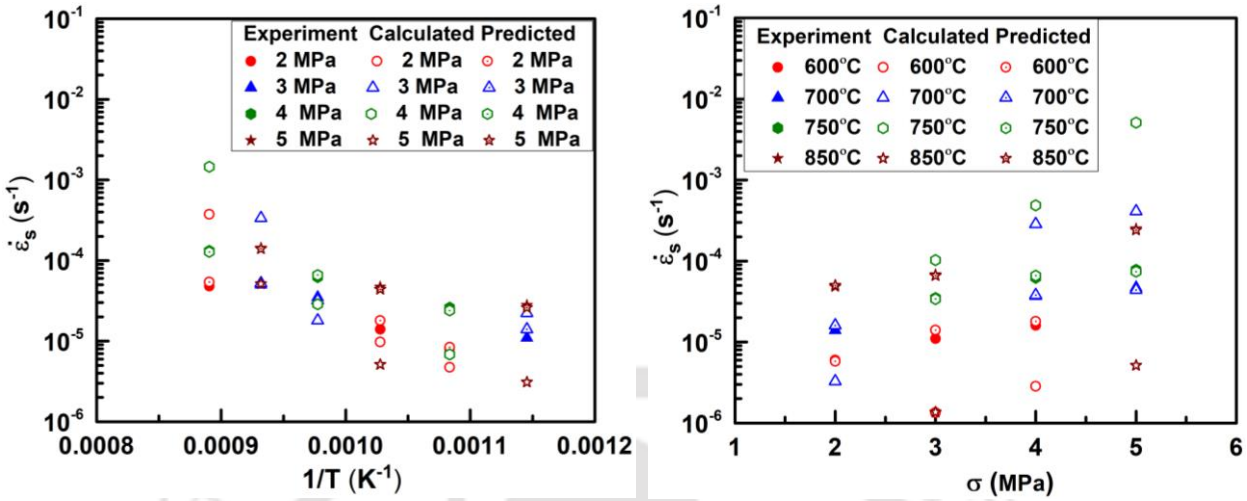

(a) (b)

Figure 4.64 Plot showing the comparison of experimentally obtained, calculated using power law(Eq. 4.9) and ANN predicted $\dot{\varepsilon}_s$with (a) $1/T$ for constant stresses and (b) σ for constant T for the longitudinal creep tests.

Table 4.11 Comparison of the minimum strain rate obtained experimentally, calculated using Eq. 4.9 and predicted by ANN technique for the longitudinal creep tests.

Stress (MPa)	Temperature (°C)	Minimum strain rate($\dot{\varepsilon}_s$)		
		Experimental	By Eq. 4.9	ANN
2	650	8.22×10^{-6}	7.28×10^{-5}	8.42×10^{-6}
2	700	1.42×10^{-5}	1.88×10^{-4}	1.46×10^{-5}
2	850	4.86×10^{-5}	4.22×10^{-5}	4.84×10^{-5}
3	600	1.12×10^{-5}	1.84×10^{-4}	1.22×10^{-5}
3	750	3.54×10^{-5}	2.24×10^{-5}	3.62×10^{-5}
3	800	5.28×10^{-5}	4.88×10^{-5}	5.22×10^{-5}
4	650	2.66×10^{-5}	2.02×10^{-4}	2.72×10^{-5}
4	750	6.28×10^{-5}	5.46×10^{-5}	6.24×10^{-5}
4	850	1.46×10^{-5}	1.22×10^{-5}	1.48×10^{-5}
5	600	2.82×10^{-5}	2.82×10^{-4}	2.86×10^{-5}
5	700	4.88×10^{-5}	3.94×10^{-4}	4.84×10^{-5}
5	800	1.24×10^{-5}	1.08×10^{-5}	1.28×10^{-5}

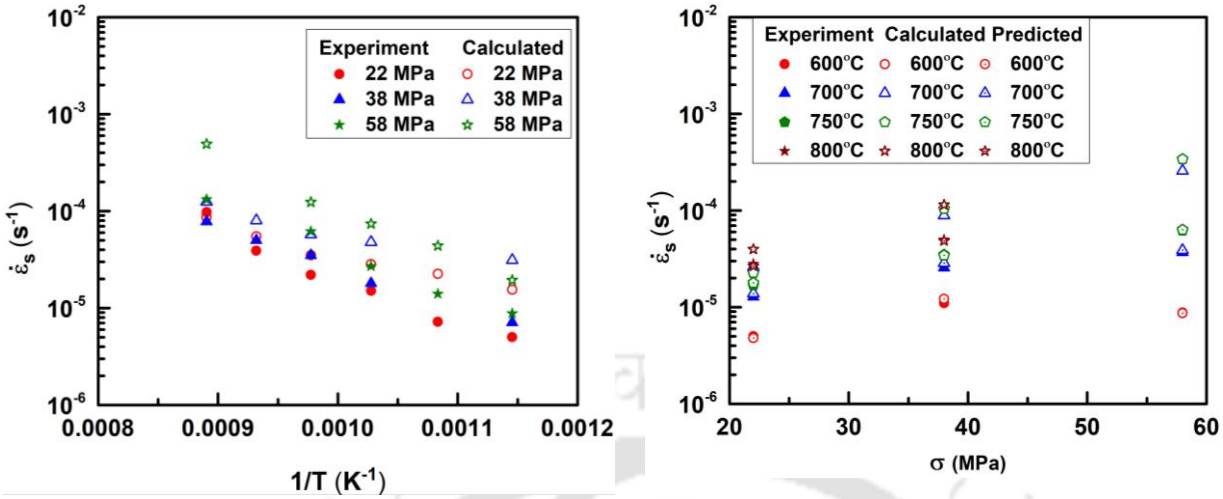

(a) (b)

Figure 4.65 Plot showing the comparison of experimentally obtained, calculated using power law(Eq. 4.14) and ANN predicted $\dot{\varepsilon}_s$with (a) 1/T for constant stresses and (b) σ for constant T for the transverse creep tests.

Similarly, Figure 4.65(a) shows the graph of $\dot{\varepsilon}_s$vs. 1/T . Plot of $\dot{\varepsilon}_s$ vs. σ is shown in Figure 4.65(b). Table 4.12 compares the predictability of $\dot{\varepsilon}_s$ values obtained from the power law equation (Eq. 4.14) and ANN predicted creep curve for the transverse creep tests. Table 4.11 and 4.12 shows that the minimum strain rate ($\dot{\varepsilon}_s$) values predicted using the ANN model are in good agreement with the values obtained experimentally. From the above analysis, it can be summarized that the ANN model is a reliable tool for the prediction of $\dot{\varepsilon}_s$ compared to the constitutive model for the tested stress and temperature conditions.

Table 4.12 Comparison of the minimum strain rate obtained experimentally, calculated using Eq. 4.14 and predicted by ANN technique for the transverse creep tests.

Stress (MPa)	Temperature (°C)	Minimum strain rate($\dot{\varepsilon}_s$)		
		Experimental	By Eq. 4.14	ANN
22	600	5.22×10^{-6}	3.66×10^{-5}	5.64×10^{-6}
22	700	1.56×10^{-5}	2.88×10^{-5}	1.62×10^{-5}
22	800	3.98×10^{-5}	6.22×10^{-5}	3.82×10^{-5}
38	600	7.24×10^{-6}	6.84×10^{-5}	7.28×10^{-5}
38	750	3.22×10^{-5}	4.64×10^{-5}	3.42×10^{-5}
38	850	2.38×10^{-5}	6.72×10^{-5}	2.34×10^{-5}
58	650	1.46×10^{-6}	6.86×10^{-5}	1.48×10^{-5}
58	700	4.78×10^{-5}	6.44×10^{-5}	4.72×10^{-5}
58	750	2.46×10^{-5}	4.48×10^{-5}	2.42×10^{-5}

4.6 Creep life prediction by Larson-Miller parametric technique

In parametric modeling techniques, the creep failure time of a material at particular service conditions of temperature and pressure is determined. The advantage of these techniques is that the long time life of the material can be predicted using data obtained from short-time accelerated creep tests. Larson–Miller parametric technique is the most extensively used extrapolation technique for predicting the creep life of metallic materials. In the present work, the data obtained from the accelerated creep test experiments are used to predict the creep life using Larson–Miller parametric technique. As described in section 2.11.2, the Larson-Miller parameter $P_{L\text{-}M}$ is expressed as:

$$P_{L-M} = T(C_{L-M} + log_{10}t_r) \times 10^{-3} \tag{4.32}$$

where T is the test temperature, t_r is the total rupture time, and $C_{L\text{-}M}$ is a constant obtained graphically, as discussed in section 2.11.2. Figure 2.11 shows the typical plot of $log_{10}(t_r)$ vs 1/T at constant stresses. The Larson-Miller parametric technique is under the assumption that the iso-stress lines, when extended, intersect the vertical axis at 1/T = 0 at a particular point. This value of $log_{10}(t_r)$ is taken as the value of $C_{L\text{-}M}$. Using the σ vs. $P_{L\text{-}M}$ master curve, the creep life at any temperature and stress is estimated by the expression:

$$t_r = 10^{\left[\left(1000 \times \frac{P_{L-M}}{T}\right) - C_{L-M}\right]} \tag{4.33}$$

Close observation of the $\log_{10}(t_r)$ vs.1/T plots for different applied stresses reveal that the iso-stress curves, when extended, intersect the vertical axes at different points, each point corresponding to a different value of $C_{L\text{-}M}$. A plot of $C_{L\text{-}M}$ vs. σ by Ghatak and Robi for HP40Nb reformer tube [15] indicated a straight-line fit which could be expressed as:

$$C_{L-M} = a_2 + a_3\sigma \tag{4.34}$$

where a_2 and a_3 are constants. By substituting Eq. 4.34 for the $C_{L\text{-}M}$ in Eq. 4.32, the $P_{L\text{-}M}$ relationship can be modified as:

$$P_{L-M}(\sigma) = T(log_{10}t_r + (a_2 + a_3\sigma)) \times 10^{-3} \tag{4.35}$$

Zr-2.5Nb pressure tubes fail due to creep either along the longitudinal direction (longitudinal creep) or in the diametric direction (transverse creep) of the pressure tubes by

ballooning or sagging. For this reason, the creep life of the tube has been analyzed and discussed separately for both the longitudinal and transverse directions in the following sub-sections.

4.6.1 Longitudinal creep life by L-M parameter

Creep tests were conducted on the samples taken from the longitudinal direction of the pressure tube in the stress range of 2-5MPa and at temperatures ranging from 600°C-850°C. Figure 4.66(a) and (b) show the plots of $\log_{10}(t_r)$ vs. 1/T for different constant stresses. It is clear from Figure 4.66 (b) that the constant stress lines, when extended, intersect the $\log_{10}(t_r)$ axis at different points, indicating different $C_{L\text{-}M}$ values. The values of $C_{L\text{-}M}$ obtained from the iso-stress lines are 18.4, 17.8, 17.4, and 17.06 for constant stresses of 2 MPa, 3 MPa, 4 MPa, and 5 MPa, respectively. The plot of $C_{L\text{-}M}$ vs. σ shown in Figure 4.66(c) indicates a linear relationship between $C_{L\text{-}M}$ and the applied stress. The constants a_2 and a_3 in Eq. 4.34 are determined as 19.22 and -0.44, respectively.

The Larson–Miller constant ($C_{L\text{-}M}$) for Zr-2.5Nb alloy is generally taken as 20 for determining the rupture time[195]. The plot of σ versus $P_{L\text{-}M}$ considering $C_{L\text{-}M}$ as 20 and as a function of stress is shown in Figure 4.67(a). Figure 4.67(b) shows the master plot of σ vs. $P_{L\text{-}M}$ considering the average values of stresses. It may be noted that the R^2 value for the σ versus $P_{L\text{-}M}$ plot, considering $C_{L\text{-}M}$ as a constant, was 0.924. However, the master plot considering $C_{L\text{-}M}(\sigma)$ has an R^2 value of 0.992 which appears to be more realistic for the prediction of the long-term creep rupture life of the alloy.

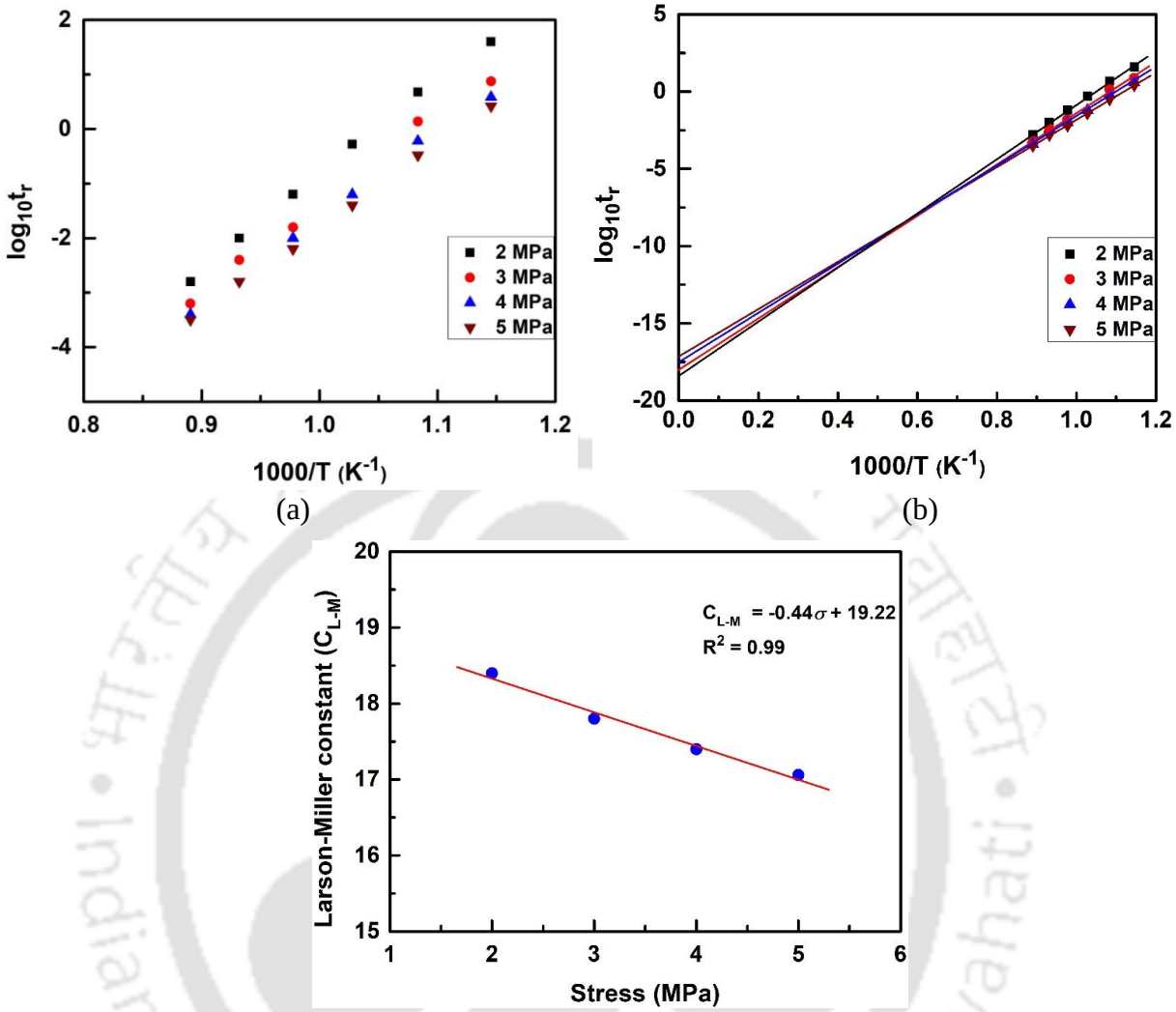

Figure 4.66 Plot of (a) $\log_{10}(t_r)$ vs. 1000/T, (b) $\log_{10}(t_r)$ vs. 1000/T with extrapolated curves up to 1000/T = 0, and (b) $C_{L\text{-}M}$ vs. applied stress (σ) calculated from the longitudinal creep tests.

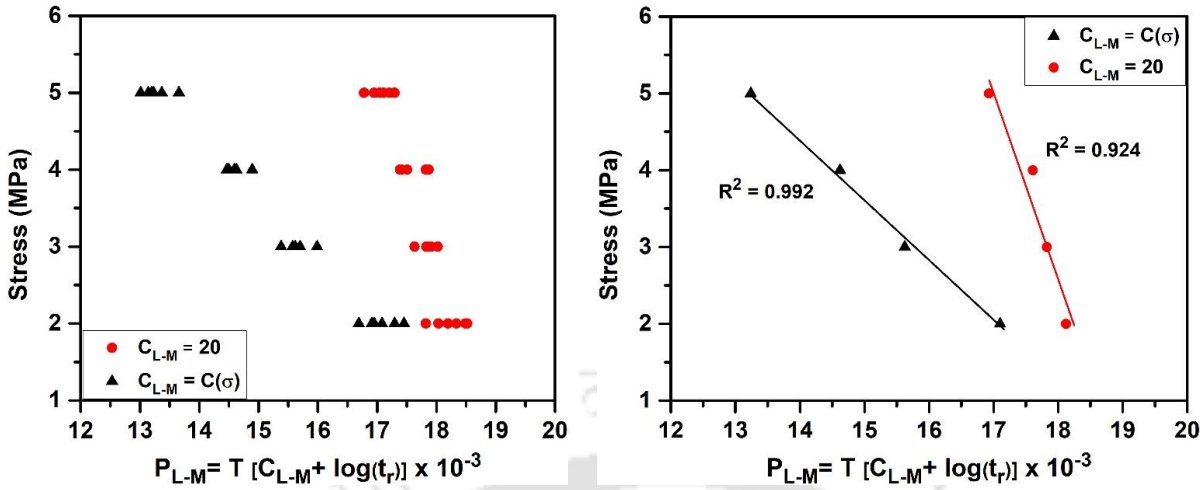

(a) (b)

Figure 4.67 Plot of (a) σ vs. P_{L-M} and (b) σ vs. average P_{L-M} calculated from the longitudinal creep tests.

The P_{L-M} value is obtained by extrapolating the master curve for the prediction of the creep life of the material at service conditions. The extrapolated values of P_{L-M} determined for stresses in the range 8-12MPa for the Zr-2.5Nb alloy are given in Table 4.13.

Table 4.13 P_{L-M} and C_{L-M} values at different stresses.

Stress (MPa)	P_{L-M} for constant C_{L-M} ($\times 10^{-3}$)	C_{L-M} as a function of stress	P_{L-M} for C_{L-M} as a function of stress ($\times 10^{-3}$)
8	16.2	13.2	14.6
9	15.8	12.6	14.2
10	15.5	11.8	13.6
11	15.1	10.9	13.2
12	14.8	10.16	12.8

The creep life of the Zr-2.5Nb alloy pressure tube along the longitudinal direction for both the cases, i.e., C_{L-M} =20 and C_{L-M} (σ) is determined by Eq. 4.36 and Eq. 4.37, respectively.

$$t_r = 10^{\left[\left(1000\times\frac{P_{L-M}}{T}\right)-20\right]} \quad (4.36)$$

$$t_r = 10^{\left[\left(1000\times\frac{P_{L-M}}{T}\right)-(-0.44\sigma+19.22)\right]} \quad (4.37)$$

It is evident from Figure 4.68(a) and (b) that the creep life decreases with an increase in temperature. From Figures 4.68-4.70, it can be seen that the creep life of the alloy predicted by considering C_{L-M} =20 is higher than that predicted by considering C_{L-M} (σ). Figure 4.68(a)

and (b) show the plot of temperature vs. creep life of the alloy. Both the figures show that the creep life decreases with an increase in stress. At 250 °C and 12 MPa, the estimated creep life of the alloy is 24.6 years and 18.4 years for the case $C_{L\text{-}M}$ =20 and $C_{L\text{-}M}$ (σ), respectively.

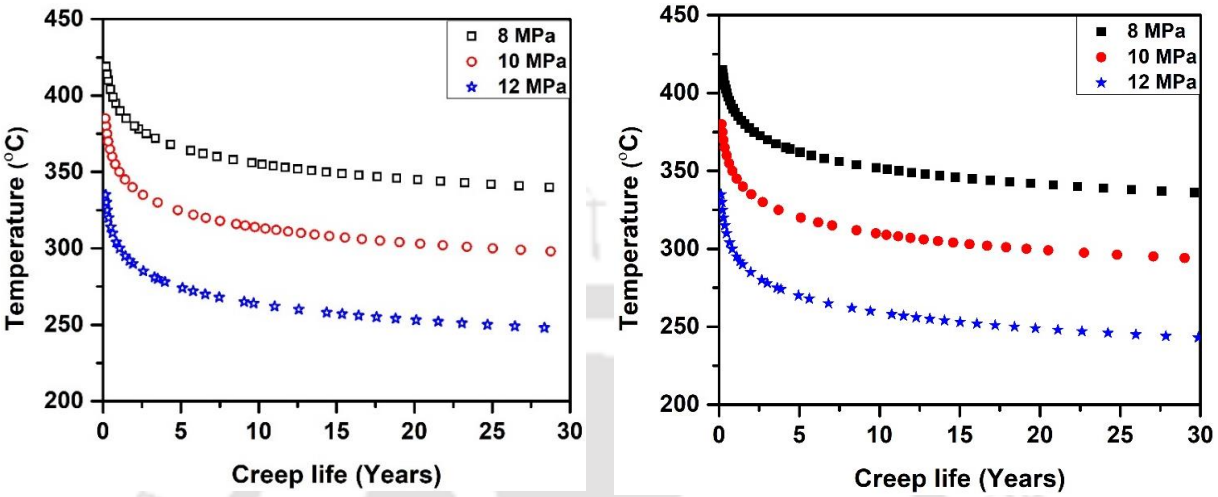

(a) (b)

Figure 4.68 Creep life prediction using (a) $C_{L\text{-}M}$ =20 and (b) $C_{L\text{-}M}$ =$C_{L\text{-}M}$ (σ) at different stresses.

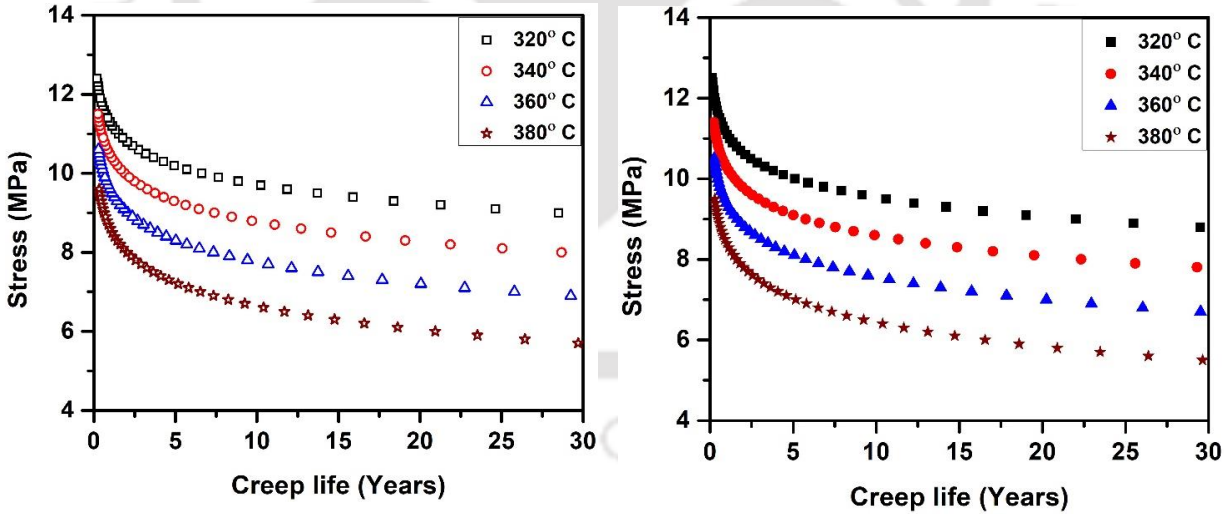

(a) (b)

Figure 4.69 Creep life prediction using (a) $C_{L\text{-}M}$ =20 and (b) $C_{L\text{-}M}$ =$C_{L\text{-}M}$ (σ) at different temperatures.

Figure 4.69 (a) and (b) compare the creep life of the alloy predicted for different combinations of stresses and temperatures by considering $C_{L\text{-}M}$ =20 and $C_{L\text{-}M}$ (σ). At 340 °C and 8 MPa, the estimated creep life of the alloy is 28.6 years and 22.2 years for the case of

$C_{L\text{-}M}$ =20 and $C_{L\text{-}M}$ (σ), respectively. At 310 °C and 10 MPa, the estimated creep life of the alloy is 12.7 years and 9.8 years for $C_{L\text{-}M}$ =20 and $C_{L\text{-}M}$ (σ), respectively. A comparison of creep life of the alloy obtained by considering constant $C_{L\text{-}M}$ and $C_{L\text{-}M}$ (σ) at various temperatures and stresses is given in Table 4.14. The Zr-2.5Nb pressure tubes are designed to operate for a life of 30 years in the reactor under normal working conditions [222]. According to the present study, the creep life of the tube obtained, considering normal service conditions, is lower for $C_{L\text{-}M}$ (σ) than that obtained using $C_{L\text{-}M}$ =20. This indicates that the prediction of the creep life using $C_{L\text{-}M}$ (σ) is very conservative.

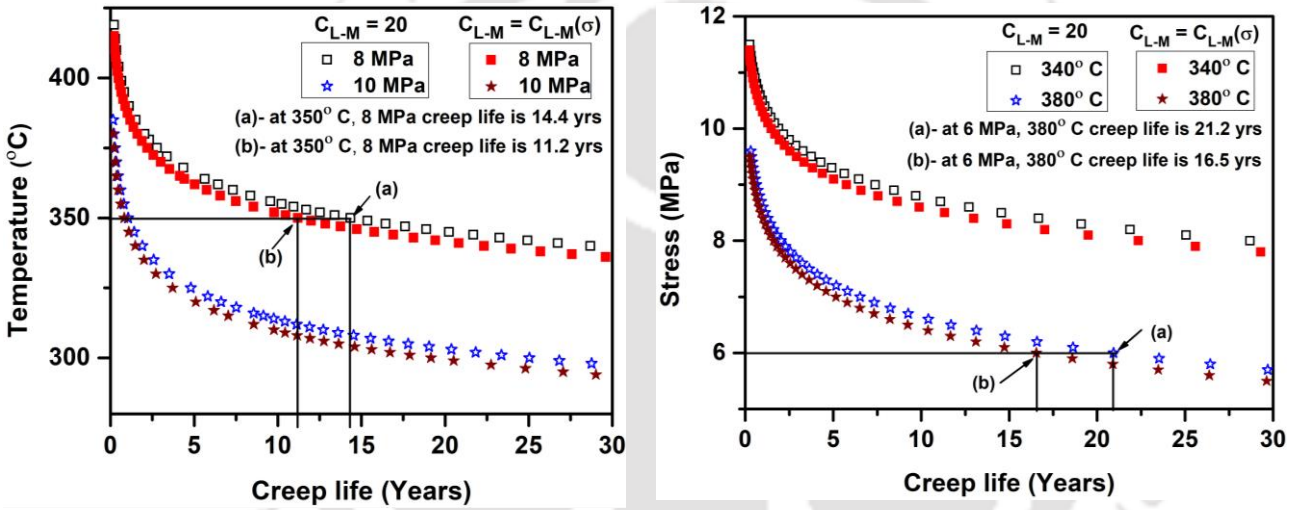

(a) (b)

Figure 4.70 Plot of comparison of creep life prediction by using $C_{L\text{-}M}$ =20 and $C_{L\text{-}M}$ =$C_{L\text{-}M}$ (σ) at (a) different stresses and (b) temperatures for longitudinal creep tests.

Table 4.14 Creep life of the Zr-2.5Nb alloy along the longitudinal axis for different stress and temperature combinations.

Stress (MPa)	Temperature (˚C)	Creep life (years)	
		Using constant $C_{L\text{-}M}$	Using $C_{L\text{-}M}$ as a function of stress
8	350	14.34	11.22
10	300	24.02	18.28
12	250	25.06	19.68

4.6.2 Transverse creep life by L-M parameter

Creep tests were conducted on the samples taken from the transverse direction of the Zr-2.5Nb pressure tube in the stress range of 22-58 MPa and at temperatures ranging from

600°C-850°C. Figure 4.71(a) and (b) show the plots of $\log_{10}(t_r)$ vs. 1/T for different constant stresses. Similar to the longitudinal case, here also it is evident from Fig. 4.71(b) that the constant-stress lines intersect the $\log_{10}(t_r)$ axis at different points rather than a single point indicating different $C_{L\text{-}M}$ values. The values of $C_{L\text{-}M}$ obtained from the iso-stress lines are 15.22, 14.02, and 12.98 for constant stresses of 22 MPa, 38 MPa, and 58 MPa, respectively. The plot of $C_{L\text{-}M}$ vs. σ shown in Fig. 4.71(c) indicates that for the given stress ranges, $C_{L\text{-}M}$ varies linearly with stress. The constants a_2 and a_3 in Eq. 4.34 are determined as 16.22 and -0.056, respectively.

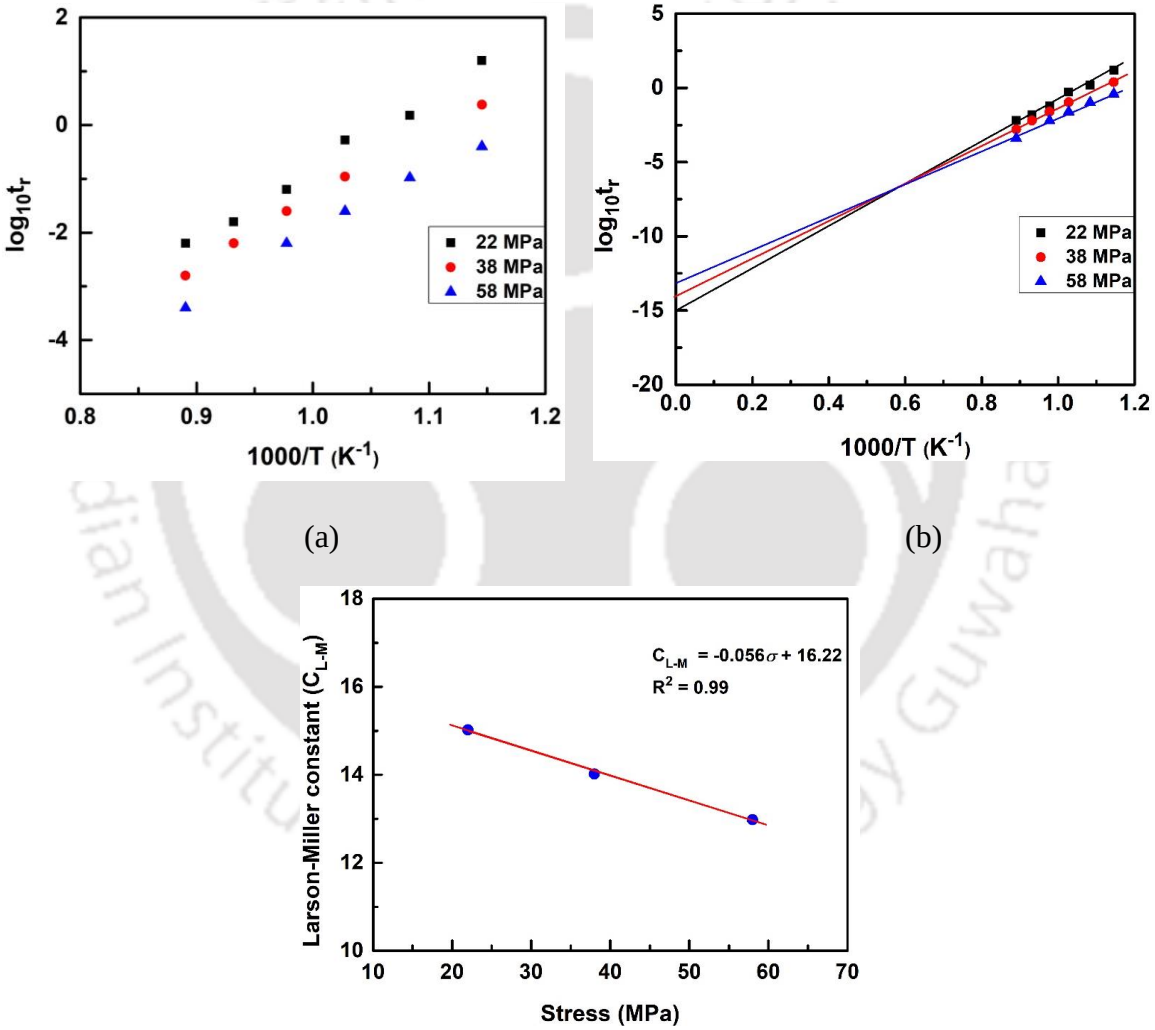

Figure 4.71 Plot of (a) $\log_{10}(t_r)$ vs. 1000/T, (b) $\log_{10}(t_r)$ vs. 1000/T with extrapolated curves up to 1000/T = 0 and (b) $C_{L\text{-}M}$ vs. applied stress (σ) calculated from transverse creep tests.

The plot of σ vs. $P_{L\text{-}M}$ considering $C_{L\text{-}M}$ as 20 and as a function of stress is shown in

Figure 4.72(a). Figure 4.72(b) shows the master plot of σ vs. $P_{L\text{-}M}$ considering the average values of stresses. It may be noted that the R^2 value for the master plot of σ vs. $P_{L\text{-}M}$, considering $C_{L\text{-}M}$ as a constant, was 0.902. The master plot considering $C_{L\text{-}M}(\sigma)$ with an R^2 value of 0.998 is more realistic for the prediction of the long-term creep rupture life of Zr-2.5Nb alloy.

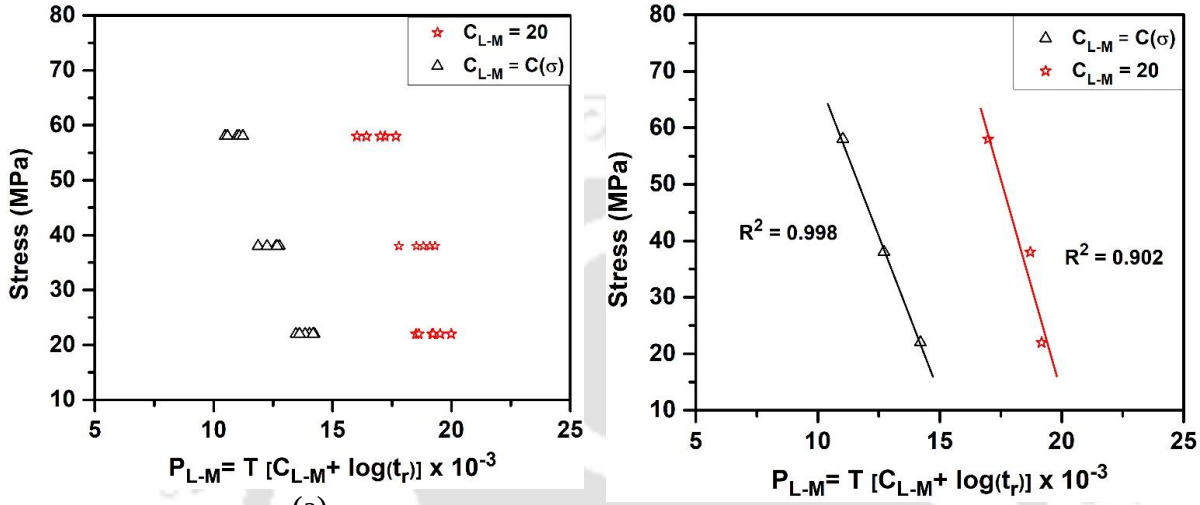

Figure 4.72 Plot of (a) σ vs. $P_{L\text{-}M}$ and (b) σ vs. average $P_{L\text{-}M}$ calculated from the transverse creep tests.

For the creep life prediction of the material at service conditions, the $P_{L\text{-}M}$ value is obtained by extrapolating the master curve. The extrapolated values of $P_{L\text{-}M}$ determined for stresses in the range 80-100MPa for the Zr-2.5Nb alloy are given in Table 4.15 for both cases.

Table 4.15 $P_{L\text{-}M}$ and $C_{L\text{-}M}$ values at different stresses.

Stress (MPa)	$P_{L\text{-}M}$ for constant $C_{L\text{-}M}$ ($\times 10^{-3}$)	$C_{L\text{-}M}$ as a function of stress	$P_{L\text{-}M}$ for $C_{L\text{-}M}$ as a function of stress ($\times 10^{-3}$)
80	15.4	11.8	14.2
85	15.2	11.4	13.6
90	14.8	11.2	13.2
95	14.5	10.8	12.9
100	14.2	10.4	12.4

The creep life of the Zr-2.5Nb alloy pressure tube along the transverse direction for both the cases, i.e., $C_{L\text{-}M}$ =20 and $C_{L\text{-}M}$ (σ) are determined by Eq. 4.38 and Eq. 4.39, respectively.

$$t_r = 10^{\left[\left(1000\times\frac{P_{L-M}}{T}\right)-20\right]} \quad (4.38)$$

$$t_r = 10^{\left[\left(1000\times\frac{P_{L-M}}{T}\right)-(-0.056\sigma+16.22)\right]} \quad (4.39)$$

It can be seen from Figures 4.73-4.75 that the creep life of the alloy predicted by considering $C_{L\text{-}M}$ =20 is higher compared to that predicted by considering $C_{L\text{-}M}$ (σ). Figure 4.73 (a) and (b) shows the plot of temperature vs. creep life of the alloy as a function of stress. Figure 4.74(a) and (b) shows the plot of σ vs. creep life of the investigated alloy as a function of temperature. Both the figures show that the creep life decreases with an increase in stress. At 340 °C and 90 MPa, the estimated creep life of the alloy is 21.2 years and 19.8 years for the case $C_{L\text{-}M}$ =20 and $C_{L\text{-}M}$ (σ), respectively.

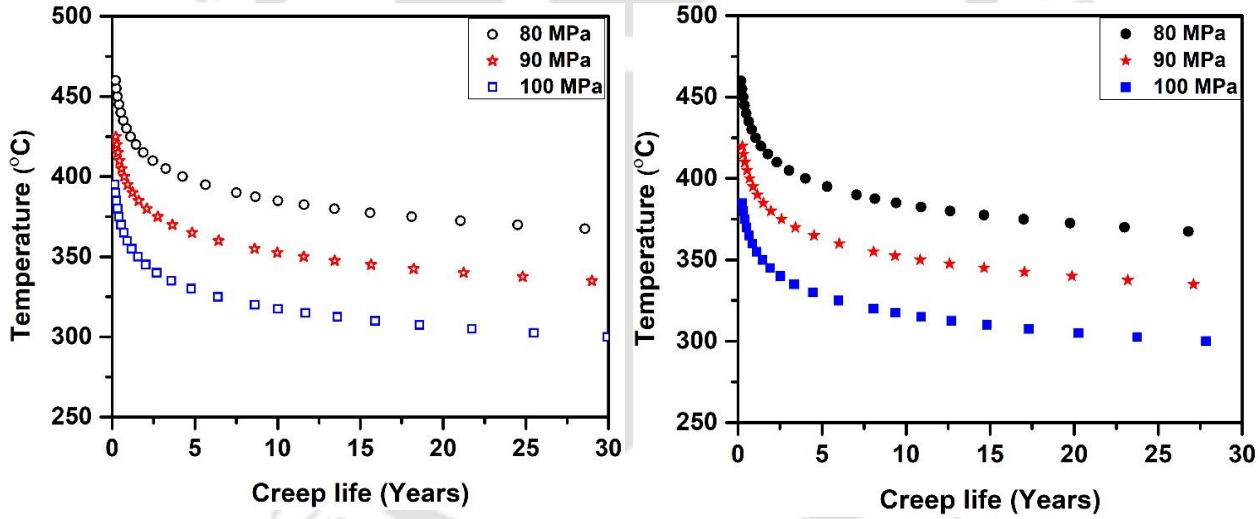

(a) (b)

Figure 4.73 Creep life prediction using(a) $C_{L\text{-}M}$ =20 and (b) $C_{L\text{-}M}$ =$C_{L\text{-}M}$ (σ) at different stresses.

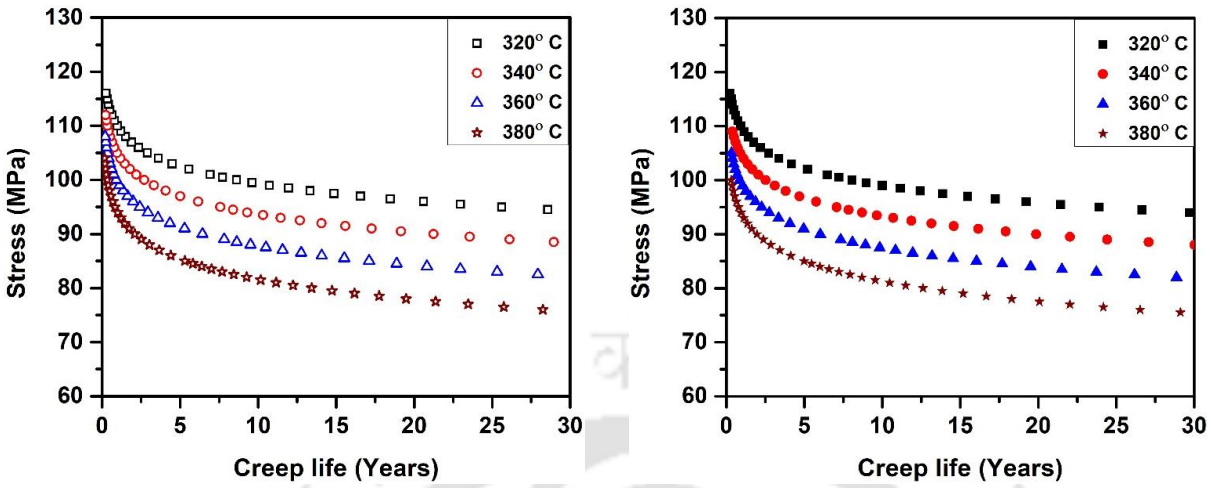

Figure 4.74 Creep life prediction using(a) $C_{L\text{-}M}$ =20 and (b) $C_{L\text{-}M}$ =$C_{L\text{-}M}$ (σ) at different temperatures.

Figure 4.75 (a) and (b) compare the creep life of the alloy predicted for different combinations of stresses and temperatures by considering $C_{L\text{-}M}$ =20 and $C_{L\text{-}M}$ (σ). At 370 °C and 80 MPa, the estimated creep life of the alloy is 24.6 years and 22.9 years for the case $C_{L\text{-}M}$ =20 and $C_{L\text{-}M}$ (σ), respectively. At 310 °C and 100 MPa, the predicted creep life of the alloy is 15.8 years and 14.6 years for the case $C_{L\text{-}M}$ =20 and $C_{L\text{-}M}$ (σ), respectively. Comparison of creep life of the alloy obtained by considering constant $C_{L\text{-}M}$ and $C_{L\text{-}M}$ (σ) at various temperatures and stresses is given in Table 4.16. It can be seen that for all the combinations of stress and temperature, the creep life predicted by considering $C_{L\text{-}M}$ =20 is higher than that predicted by considering $C_{L\text{-}M}$ (σ).

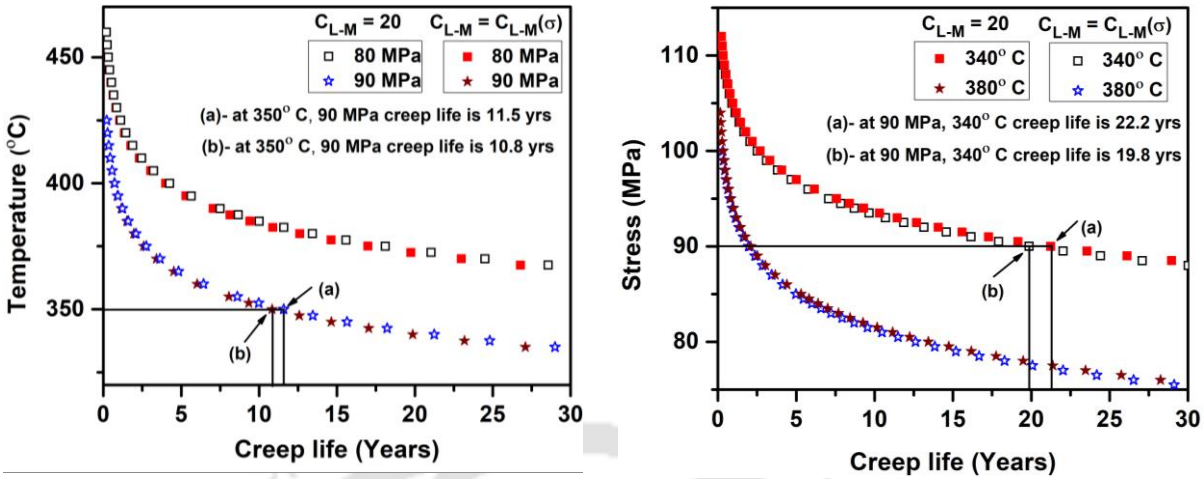

(a) (b)

Figure 4.75 Plot of comparison of creep life prediction by using C_{L-M} =20 and C_{L-M} = C_{L-M} (σ) at (a) different stresses and (b) temperatures for transverse creep tests.

Table 4.16 Creep life of the Zr-2.5Nb alloy along the transverse axis for different stress and temperature combinations.

Stress (MPa)	Temperature (˚C)	Creep life (years)	
		Using constant C_{L-M}	Using C_{L-M} as a function of stress
80	400	4.26	4.02
90	350	11.68	10.84
100	300	29.62	27.88

In the present study, the iso-stress lines were not meeting at a single point. The values of C_{L-M} changed with the stress linearly. Creep life prediction was done taking C_{L-M} = 20 as well as C_{L-M} = C_{L-M} (σ). The creep life obtained using C_{L-M} = C_{L-M} (σ) gave a lower value than that obtained using C_{L-M} = 20. Thus, it can be concluded that the creep life determined by considering C_{L-M} (σ) is more conservative from the design point of view.

4.7 Summary

The experimental results from the microstructural analysis, high-temperature tensile tests, and creep tests on both the longitudinal and transverse specimens of the Zr-2.5Nb alloy pressure tubes are presented in this chapter. The tensile tests reveal that at all temperatures, the longitudinal samples displayed lower strength but higher ductility than the transverse

ones. Superplasticity was observed for both the longitudinal and tensile samples. The strain rate jump tests suggested that superplasticity sets in at a temperature of ~622°C and ~636°C for the longitudinal and transverse samples, respectively. Constitutive modeling was developed to determine the minimum creep rate using the data obtained from the creep curves. Monkman-Grant and Modified Monkman- Grant relationships were validated for the alloy and were used to predict the rupture time of the Zr-2.5Nb alloy. Creep curves could be successfully predicted by ANN modeling, where 98 % of the data could be predicted within a deviation error of ± 5%. The creep life of the material was estimated by the Larson-Miller technique. The creep life prediction by Larson-Miller method is sensitive to the $C_{L\text{-}M}$ value. A more conservative value of the creep life is obtained if the $C_{L\text{-}M}$ in the $P_{L\text{-}M}$ expression is a stress-dependent function.

Chapter 5 Conclusion and Scope for Future Work

5.1 Introduction

In the present work, tensile properties at room and elevated temperatures and microstructural evolution with temperature and creep testing were performed on both the longitudinal and transverse samples of Zr-2.5Nb alloy pressure tube material. The correlation of tensile properties with temperature was developed. An extensive analysis of short-time accelerated creep test results were carried out. Various techniques like constitutive modeling, MLR, and ANN modeled the creep deformation of this material. The creep life prediction of the Zr-2.5Nb alloy was carried out by Larson-Miller parametric technique by extrapolating accelerated creep test results. The conclusions that can be derived from the current study are given below:

- The pressure tube material was more prone to failure due to longitudinal sagging compared to the diametrical expansion.
- The strain hardening exponent of the alloy increased with the increase in temperature up to 400 °C and decreased with a further increase in temperature.
- As received samples were characterized by uniform distribution of Nb-enriched precipitates in the matrix. With the increase in temperature, Nb-enriched β-Zr phase increased and formed a network around the α- phase leading to grain boundary sliding at elevated temperatures.
- The Zr-2.5 Nb alloy deformed by superplastic deformation at temperatures above ~622°C and ~636°C for the longitudinal and transverse samples, respectively. The highest value of strain rate sensitivity (m) was obtained at 800°C, and the value of m at this temperature was 0.62 and 0.58 for the longitudinal and transverse samples, respectively.
- Good correlations between the tensile properties and temperature were obtained with an R^2 value of 0.99 for the longitudinal and transverse samples. These equations could be effectively used for modeling the failure in the case of LOCA in nuclear power plants.
- The mechanism of failure of the longitudinal samples above 600 °C was by microvoid coalescence.

- Failure of transverse samples at elevated temperature was by intergranular failure and was facilitated by void nucleation at grain boundary regions.
- At constant applied stress, the minimum creep rate ($\dot{\varepsilon}_s$) increased with the increase in temperature. The value of $\dot{\varepsilon}_s$ increased with an increase in applied stress at a constant temperature for both the longitudinal and transverse creep tests.
- The contribution of relative secondary creep strain increased with an increase in temperature at constant stress for both the longitudinal and transverse creep tests.
- Creep deformation ($\dot{\varepsilon}_s$) was correlated to the applied stress and temperature by a Power-law expression. The stress exponent and apparent activation energy for creep decreased with the increase in temperature and stress, respectively.
- Monkman-Grant and Modified Monkman-Grant relationships were successfully used to correlate the rupture time and steady-state creep rate for the Zr-2.5Nb alloy in longitudinal and transverse directions.
- Creep damage tolerance factor (λ) was found to be 2.8 and 1.8 for the longitudinal and transverse specimens, respectively.
- The MLR model could effectively predict the primary creep region but failed to predict the secondary and tertiary creep regions of the creep curve. Transition between the secondary and the tertiary creep region could not be predicted by the model. An R^2 value of less than 0.92 was obtained, which showed that the model could not predict the creep curves very well.
- ANN model was successfully used for predicting creep curves within the range of investigated temperature and stresses. 98 % of the creep strains could be successfully predicted within a deviation error of ± 5%. Comparison of ANN predicted creep curve with experimental values showed an R^2 value greater than 0.99, indicating very good prediction capability.
- Garson's analysis revealed that the most influencing parameter for creep deformation is the applied stress, followed by temperature and time.
- The minimum creep rate obtained by the ANN model was found to be more accurate than that obtained by the constitutive modeling technique.

- Creep life prediction was carried out using the Larson-Miller parameter technique. The creep life prediction taking $C_{L\text{-}M}$ as a function of stress rather than a constant in the $P_{L\text{-}M}$ function gave a more conservative result from the design point of view.

5.2 Scope for future work

The present investigations were focused on investigating the high-temperature tensile and creep failure of the Zr-2.5Nb alloy. The work also demonstrated the capability of the ANN technique in simulating creep curves from the data obtained from limited experiments. Based on this work, the following areas are suggested for further research:

- Models for the creep deformation in the case of LOCA should be developed with the results obtained from the present work.
- An in-depth investigation of the high-temperature microstructure of this alloy by TEM should be carried out. This would shed more light on the nature of phase change during creep tests at high temperatures.
- Corrosion studies of this alloy would give an in-depth understanding of its behavior during service conditions.
- Modeling of the creep curves by other machine learning techniques should also be explored to predict the creep life of this alloy.
- The modified Larson-Miller parameter technique for predicting creep life can be validated for other alloys.

REFERENCES

1. Guguloth, K., Ghosh, M., Swaminathan, J., Mitra, R.: Tensile creep and rupture behavior along with evolution of microstructure in a Zr-2.5Nb alloy. Mater. Sci. Eng. A. 791, 139681 (2020). https://doi.org/10.1016/j.msea.2020.139681
2. Li, Y., Rogge, R., Holt, R.A.: Development of local microstructure and crystallographic texture in extruded Zr-2.5Nb tubes. Mater. Sci. Eng. A. 437, 10–20 (2006). https://doi.org/10.1016/j.msea.2006.04.048
3. Holt, R.A.: In-reactor deformation of cold-worked Zr-2.5Nb pressure tubes. J. Nucl. Mater. 372, 182–214 (2008). https://doi.org/10.1016/j.jnucmat.2007.02.017
4. Christodoulou, N., Turner, P.A., Tomé, C.N., Chow, C.K., Klassen, R.J.: Analysis of steady-state thermal creep of Zr-2.5Nb pressure tube material. Metall. Mater. Trans. A Phys. Metall. Mater. Sci. 33, 1103–1115 (2002). https://doi.org/10.1007/s11661-002-0212-4
5. Li, W., Holt, R.A., Daymond, M.R., Xu, F.: Influence of prior dislocation structure on anisotropy of thermal creep of cold-worked Zr-2.5Nb tubes. J. Nucl. Mater. 412, 138–144 (2011). https://doi.org/10.1016/j.jnucmat.2011.02.044
6. Srivastava, D., Dey, G.K., Banerjee, S.: Evolution of microstructure during fabrication of Zr-2.5 Wt pct Nb alloy pressure tubes. Metall. Mater. Trans. A. 26, 2707–2718 (1995). https://doi.org/10.1007/BF02669427
7. Singh, R.N., Kishore, R., Singh, A.K., Sinha, T.K., Kashyap, B.P.: Microstructural instability and superplasticity in a Zr-2.5 Wt Pct Nb pressure-tube alloy. Metall. Mater. Trans. A Phys. Metall. Mater. Sci. 32, 2827–2840 (2001). https://doi.org/10.1007/s11661-001-1033-6
8. Khandelwal, H.K., Singh, R.N., Bind, A.K., Sunil, S., Chakravartty, J.K., Ghosh, A., Dhandharia, P., Bhachawat, D., Shekhar, R., Kumar, S.J.: Tensile properties and fracture toughness of Zr-2.5Nb alloy pressure tubes of IPHWR220. Nucl. Eng. Des. 293, 138–149 (2015). https://doi.org/10.1016/j.nucengdes.2015.07.048
9. Nene, S.S., Sharma, G., Singh, R.N., Kashyap, B.P.: Microstructural evolution in and

flow properties of Zr-2.5Nb pressure tube material at elevated temperature. J. Nucl. Mater. 449, 62–68 (2014). https://doi.org/10.1016/j.jnucmat.2014.03.002

10. Rodgers, D.K., Coleman, C.E., Griffiths, M., Bickel, G.A., Theaker, J.R., Muir, I., Bahurmuz, A.A., Lawrence, S.S., Resta Levi, M.: In-reactor performance of pressure tubes in CANDU reactors. J. Nucl. Mater. 383, 22–27 (2008). https://doi.org/10.1016/j.jnucmat.2008.08.037

11. Sawada, K., Tabuchi, M., Kimura, K.: Analysis of long-term creep curves by constitutive equations. Mater. Sci. Eng. A. 510–511, 190–194 (2009). https://doi.org/10.1016/j.msea.2008.06.057

12. Manson, S., Haferd, A.: A linear time-temperature relation for extrapolation of creep and stress-rupture data. (1953)

13. Sherby, O.D., Orr, R.L., Dorn, J.E.: Creep correlations of metals at elevated temperatures. Jom. 6, 71–80 (1954). https://doi.org/10.1007/bf03397983

14. Larson, F.R., Miller, J.: A Time-Temperature Relationship for Rupture and Creep Stresses. Trans. ASME. 74, 765–771 (1952)

15. Ghatak, A., Robi, P.S.: Modification of Larson–Miller Parameter Technique for Predicting Creep Life of Materials. Trans. Indian Inst. Met. 69, 579–583 (2016). https://doi.org/10.1007/s12666-015-0803-6

16. Monkman, F., Grant, N.: An empirical relationship between rupture life and minimum creep rate in creep rupture tests. In: Proc. ASTM. pp. 593–620 (1956)

17. Dobeš, F., Milička, K.: The relation between minimum creep rate and time to fracture. Met. Sci. 10, 382–384 (1976). https://doi.org/10.1080/03063453.1976.11683560

18. Ghatak, A., Robi, P.S.: Prediction of creep curve of HP40Nb steel using artificial neural network. Neural Comput. Appl. 30, 2953–2964 (2018). https://doi.org/10.1007/s00521-017-2851-9

19. Singh, R.N., Mukherjee, S., Kishore, R., Kashyap, B.P.: Flow behaviour of a modified Zr-2.5wt%Nb pressure tube alloy. J. Nucl. Mater. 345, 146–161 (2005). https://doi.org/10.1016/j.jnucmat.2005.05.008

20. Shukla, S. V., Chandrashekharayya, C., Singh, R.N., Fotedar, R., Kishore, R., Sinha, T.K., Kashyap, B.P.: Effect of strain rate and test temperature on superplasticity of a

Zr-2.5 wt% Nb alloy. J. Nucl. Mater. 273, 130–138 (1999). https://doi.org/10.1016/S0022-3115(99)00037-9

21. Kombaiah, B.: Transitions in Creep Mechanisms of Zirconium Alloys, https://www.researchgate.net/publication/269107473_What_is_governance/link/548173090cf22525dcb61443/download%0Ahttp://www.econ.upf.edu/~reynal/Civil wars_12December2010.pdf%0Ahttps://think-asia.org/handle/11540/8282%0Ahttps://www.jstor.org/stable/41857625, (2015)

22. Murty, K.L.: Creep studies for zircaloy life prediction in water reactors. Jom. 51, 32–39 (1999). https://doi.org/10.1007/s11837-999-0184-6

23. Charit, I., Murty, K.L.: Creep behavior of niobium-modified zirconium alloys. J. Nucl. Mater. 374, 354–363 (2008). https://doi.org/10.1016/j.jnucmat.2007.08.019

24. K.L.Murty: Deformation mechanisms and transients in creep of zircaloys: Applications to nuclear technology. Trans. Indian Inst. Met. 53, 107–120 (2000)

25. Hayes, T.A., Kassner, M.E.: Creep of zirconium and zirconium alloys. Metall. Mater. Trans. A Phys. Metall. Mater. Sci. 37, 2389–2396 (2006). https://doi.org/10.1007/BF02586213

26. Sarkar, A., Sinha, S.K., Chakravartty, J.K., Sinha, R.K.: Artificial Neural Network modelling of in-reactor diametral creep of Zr2.5%Nb pressure tubes at Indian PHWRs. Ann. Nucl. Energy. 69, 246–251 (2014). https://doi.org/10.1016/j.anucene.2014.01.043

27. Nandan, G., Majumdar, P., Sahoo, P.K., Kumar, R., Chatterjee, B., Mukhopadhyay, D., Lele, H.G.: Study of ballooning of a completely voided pressure tube of Indian PHWR under heat up condition. Nucl. Eng. Des. 243, 301–310 (2012). https://doi.org/10.1016/j.nucengdes.2011.11.007

28. Ali, D.B.: Development of Non-Destructive Small Specimen Creep Testing Techniques, (2013)

29. G.E.Dieter: Mechanical Metallurgy. (1998)

30. Phillips, P.: The slow stretch in indiarubber, glass, and metal wires when subjected to a constant pull. London, Edinburgh, Dublin Philos. Mag. J. Sci. 9, 513–531 (1905). https://doi.org/10.1080/14786440509463303

31. Mcvetty, P.G.: Factors Affecting Choice of Working Stresses for High-Temperature Service. Trans. ASME. 55, 99 (1933)

32. Conway, J.B., Mullikin, M.J.: An evaluation of various first stage creep equations. In: Proceedings of AIME conference. , Detroit, Michigan (1962)

33. Norton, F.N.: The creep of steel at high temperature. McGraw – Hill (1929)

34. Prandtl, L.: Ein Gedankenmodell zur kinetischen Theorie der festen Körper. ZAMM - J. Appl. Math. Mech. / Zeitschrift für Angew. Math. und Mech. 8, 85–106 (1928). https://doi.org/https://doi.org/10.1002/zamm.19280080202

35. Nadai, A.: The influence of time upon creep, the hyperbolic sine creep law. In: S. Timoshenko Anniversary Volume. pp. 155–170. The Macmillian Co. (1938)

36. McHenry, D.: A new aspect of creep in concrete and its application to design. In: Proceedings of ASTM. p. 1069 (1943)

37. Rabotnov, Y.N., Leckie, F.A., Prager, W.: Creep problems in structural members. Presented at the (1969)

38. Sandstroem, R., Kondyr, A.: Model for tertiary-creep in Mo- and CrMo-steels. Pergamon, United Kingdom (1980)

39. Woodford, D.A.: Creep and rupture of an advanced fiber strengthened eutectic composite superalloy. Metall. Trans. A. 8, 639–650 (1977). https://doi.org/10.1007/BF02676987

40. Zhang, X.P., Yu, C.B., Zhang, Y.P., Shrestha, S., Dorn, L.: Processing treatment of a lead-free Sn-Ag-Cu-Bi solder by rapid laser-beam reflowing and the creep property of its soldered connection. J. Mater. Process. Technol. 192–193, 539–542 (2007). https://doi.org/10.1016/j.jmatprotec.2007.04.072

41. Holdsworth, S.R., Askins, M., Baker, A., Gariboldi, E., Holmström, S., Klenk, A., Ringel, M., Merckling, G., Sandstrom, R., Schwienheer, M., Spigarelli, S.: Factors influencing creep model equation selection. Int. J. Press. Vessel. Pip. 85, 80–88 (2008). https://doi.org/10.1016/j.ijpvp.2007.06.009

42. Kandare, E., Feih, S., Kootsookos, A., Mathys, Z., Lattimer, B.Y., Mouritz, A.P.: Creep-based life prediction modelling of aluminium in fire. Mater. Sci. Eng. A. 527, 1185–1193 (2010). https://doi.org/10.1016/j.msea.2009.10.010

43. Omprakash, C.M., Kumar, A., Kamaraj, M., Satyanarayana, D.V.V.: Creep Behaviour of Directionally Solidified Nickel-Base Superalloy CM 247: A Three-Dimensional Representation of Creep Curves. Trans. Indian Inst. Met. 74, 1787–1797 (2021). https://doi.org/10.1007/s12666-021-02275-w

44. Gao, J., Dong, Z.: Creep behavior and structure evolution of an advanced 9Cr-1.5Mo-1Co-VNbBN heat-resistant steel at elevated temperature. Appl. Phys. A Mater. Sci. Process. 126, 1–7 (2020). https://doi.org/10.1007/s00339-020-03842-6

45. Weertman, J.: Theory of steady-state creep based on dislocation climb. J. Appl. Phys. 26, 1213–1217 (1955). https://doi.org/10.1063/1.1721875

46. Dorn, J.E.: Some fundamental experiments on high temperature creep. J. Mech. Phys. Solids. 3, (1955). https://doi.org/10.1016/0022-5096(55)90054-5

47. Hayhurst, D.R., Vakili-Tahami, F., Zhou, J.Q.: Constitutive equation for time independent plasticity and creep of 316 stainless steel at 550 °C. Int. J. Press. Vessel. Pip. 80, 97–109 (2003). https://doi.org/10.1016/S0308-0161(03)00027-9

48. Sherby, O.D., Lytton, J.L., Dorn, J.E.: Activation Energies for Creep of High-Purity Aluminium. Acta Metall. 5, 219–227 (1957)

49. Sherby, O.D., Burke, P.M.: Mechanical behavior of crystalline solids at elevated temperature. Prog. Mater. Sci. 13, 323–390 (1968). https://doi.org/https://doi.org/10.1016/0079-6425(68)90024-8

50. Kassner, M.E., Pérez-Prado, M.-T.: Five-Power-Law Creep. (2004)

51. Tegart, W.J.M.G.: Activation energies for high temperature creep of polycrystalline magnesium. Acta Metall. 9, 614–617 (1961). https://doi.org/10.1016/0001-6160(61)90166-3

52. Holmes, J.J.: The activation energies for creep of zircaloy-2. J. Nucl. Mater. 13, 137–141 (1964). https://doi.org/10.1016/0022-3115(64)90035-2

53. Klein, M.J., Gulden, M.E.: The activation energy for creep of columbium (Niobium). Metall. Trans. 4, 2175–2180 (1973). https://doi.org/10.1007/BF02643284

54. Lund, R.W., Nlx, W.D.: On high creep activation energies for dispersion strengthened metals. Metall. Trans. A. 6, 1329 (1975). https://doi.org/10.1007/BF02641925

55. Purushothaman, S., Tien, J.K.: Role of back stress in the creep behavior of particle strengthened alloys. Acta Metall. 26, 519–528 (1978). https://doi.org/10.1016/0001-6160(78)90104-9

56. Hong, S.I.: Influence of dynamic strain aging on the apparent activation energy for creep. Mater. Sci. Eng. 64, 19–21 (1984)

57. Hong, S.I.: On the creep activation energies of alloys. Mater. Sci. Eng. 86, 211 – 218 (1987)

58. Buršíková, V., Buršík, J., Navrátil, V., Milička, K.: Creep behaviour of leaded brass. Mater. Sci. Eng. A. 324, 235–238 (2002). https://doi.org/10.1016/S0921-5093(01)01317-X

59. Raj, S. V.: Tensile creep of polycrystalline near-stoichiometric NiAl. Mater. Sci. Eng. A. 356, 283–297 (2003). https://doi.org/10.1016/S0921-5093(03)00137-0

60. Barret, C.R., Ardell, A.J., Sherby, O.D.: Influence of Modulus on Temperature Dependence of Activation Energy for Creep at High Temperatures. Trans. Metall. Soc. Aime. 20, 200 (1964)

61. El-Khalek, A.M.A.: Effect of pre-deformation and phase transformation on the creep behaviour of Ag-1wt% Cu alloy. Mater. Sci. Eng. A. 527, 4818–4822 (2010). https://doi.org/10.1016/j.msea.2010.04.026

62. Zhurkov, S.N., Sanfirova, T.P.: No Title. Sov. Phys. – Tech. Phys. 3, 1586 (1959)

63. Yan, J., Sun, Y., Xue, F., Xue, S., Xiao, Y., Tao, W.: Creep behavior of Mg-2 wt.%Nd binary alloy. Mater. Sci. Eng. A. 524, 102–107 (2009). https://doi.org/10.1016/j.msea.2009.06.008

64. Landon, P.R., Lytton, J.L.: The activation energies for creep of polycrystalline copper and nickel. CALIFORNIA UNIV BERKELEY MATERIALS RESEARCH LAB (1957)

65. Yamane, T., Genma, N., Takahashi, Y.: Creep behaviour of a 25wt % Cr-20wt % Ni austenitic stainless steel doped with antimony. J. Mater. Sci. 19, 263–269 (1984). https://doi.org/10.1007/BF02403134

66. Ruano, O.A., Wadsworth, J., Sherby, O.D.: Deformation mechanisms in an austenitic stainless steel (25Cr-20Ni) at elevated temperature. J. Mater. Sci. 20, 3735–3744

(1985). https://doi.org/10.1007/BF01113782

67. Brandes, E.A.: Smithells metals reference book, sixth edition. Butterworth Publishers,Stoneham, MA, United States (1983)

68. Kapoor, R., Chakravartty, J.K., Gupta, C.C., Wadekar, S.L.: Characterization of superplastic behaviour in the (α + β) phase field of Zr-2.5 wt.%Nb alloy. Mater. Sci. Eng. A. 392, 191–202 (2005). https://doi.org/10.1016/j.msea.2004.09.023

69. F.R.N. Nabarro.: Report of conference on Strength of Solids London: The Physical Society. (1948)

70. Herring, C.: Diffusional viscosity of a polycrystalline solid. J. Appl. Phys. 21, 437–445 (1950). https://doi.org/10.1063/1.1699681

71. T.H. Courtney: Mechanical behavior of materials. Waveland Press, Inc. (2000)

72. Harper, J., Dorn, J.E.: Viscous creep of aluminum near its melting temperature. Acta Metall. 5, 654–665 (1957). https://doi.org/10.1016/0001-6160(57)90112-8

73. Coble, R.L.: A Model for Boundary Diffusion Controlled Creep in Polycrystalline Materials. J. Appl. Phys. 34, 1679–1682 (1963). https://doi.org/10.1063/1.1702656

74. J.E. Bird, A.K. Mukherjee, J.E.D.: Correlations between high-temperature creep behavior and structure. In: Brandon DG, R.A. (ed.) Quantitative relation between properties and microstructure. pp. 255–342. Israel University press (1969)

75. Murty, K.L., Mohamed, F.A., Dorn, J.E.: Climb and Newtonian Viscous Deformation Mechanisms Of High Temperature Creep in Al-3mg. 20, (1972)

76. Mohamed, F.A., Murty, K.L., Morris, J.W.: Harper-dorn creep in al, pb, and sn. Metall. Trans. 4, 935–940 (1973). https://doi.org/10.1007/BF02645593

77. Kumar, P., Kassner, M.E., Langdon, T.G.: Fifty years of Harper-Dorn creep: A viable creep mechanism or a Californian artifact? J. Mater. Sci. 42, 409–420 (2007). https://doi.org/10.1007/s10853-006-0782-4

78. Yavari, P., Miller, D.A., Langdon, T.G.: An investigation of harper-dorn creep-I. Mechanical and microstructural characteristics. Acta Metall. 30, 871–879 (1982). https://doi.org/10.1016/0001-6160(82)90085-2

79. Poirier, J.-P.: Creep of Crystals: High-Temperature Deformation Processes in Metals,

Ceramics and Minerals. Cambridge University Press, Cambridge (1985)

80. Weertman, J.: Steady-state creep of crystals. J. Appl. Phys. 28, 1185–1189 (1957). https://doi.org/10.1063/1.1722604

81. Weertman, J.: Steady-State Creep through Dislocation Climb. J. Appl. Phys. 28, 362–364 (1957). https://doi.org/10.1063/1.1722747

82. T.H. Courtney: Mechanical behavior of materials. Overseas Press, Long Grove, IL (2006)

83. Robinson, S.L., Sherby, O.D.: Mechanical behavior of polycrystalline tungsten at elevated temperature. Acta Metall. 17, 109–125 (1969). https://doi.org/10.1016/0001-6160(69)90132-1

84. Barrett, C.R., Nix, W.D.: A model for steady state creep based on the motion of jogged screw dislocations. Acta Metall. 13, 1247–1258 (1965). https://doi.org/10.1016/0001-6160(65)90034-9

85. Mott, N.F.: Creep and fracture of metals at high temperatures. In: NPL Symposium. p. 21 (1956)

86. Čadek, J.: Creep in metallic materials. Elsevier Science Publishers B. V., Amsterdam (1988)

87. Poirier, J.P.: On the symmetrical role of cross-slip of screw dislocations and climb of edge dislocations as recovery processes controlling high-temperature creep. Rev. Phys. Appliquée. 11, 731–738 (1976). https://doi.org/10.1051/rphysap:01976001106073100

88. J.P.Poirier: Is power-law creep diffusion-controlled? 26, 629–637 (1977)

89. Friedel, J.: Dislocations Interactions and Internal Strains. In: Rassweiler, G. and Grube, W. (eds.) Proceedings of the symposium on Internal stresses and fatigue in metals. Elesevier Publishing Company (1958)

90. Kocks, U.F.: Laws for Work-Hardening and Low-Temperature Creep. J. Eng. Mater. Technol. 98, 76–85 (1976). https://doi.org/10.1115/1.3443340

91. Mecking, H., Kocks, U.F.: Kinetics of flow and strain-hardening. Acta Metall. 29, 1865–1875 (1981). https://doi.org/10.1016/0001-6160(81)90112-7

92. Kocks, U.F., Mecking, H.: Physics and phenomenology of strain hardening: the FCC

case. Prog. Mater. Sci. 48, 171–273 (2003). https://doi.org/10.1016/S0079-6425(02)00003-8

93. Choudhary, B.K., Christopher, J., Isaac Samuel, E.: Applicability of Kocks-Mecking approach for tensile work hardening in P9 steel. Mater. Sci. Technol. (United Kingdom). 28, 644–650 (2012). https://doi.org/10.1179/1743284711Y.0000000106

94. Bambach, M., Sizova, I., Bolz, S., Weiß, S.: Devising strain hardening models using kocks-mecking plots-a comparison of model development for titanium aluminides and case hardening steel. Metals (Basel). 6, (2016). https://doi.org/10.3390/met6090204

95. Angella, G., Donnini, R., Maldini, M., Ripamonti, D.: Combination between Voce formalism and improved Kocks-Mecking approach to model small strains of flow curves at high temperatures. Mater. Sci. Eng. A. 594, 381–388 (2014). https://doi.org/10.1016/j.msea.2013.11.088

96. Palaparti, D.P.R., Choudhary, B.K., Christopher, J., Samuel, E.I., Mathew, M.D.: Kocks-mecking approach to tensile work hardening behaviour of normalised and tempered and post-weld heat-treated modified 9cr-1mo steel. Mater. High Temp. 30, 295–305 (2013). https://doi.org/10.3184/096034013X13808197639117

97. Choudhary, B.K., Rao Palaparti, D.P.: Comparative tensile flow and work hardening behaviour of thin section and forged thick section 9Cr-1Mo ferritic steel in the framework of Voce equation and Kocks-Mecking approach. J. Nucl. Mater. 430, 72–81 (2012). https://doi.org/10.1016/j.jnucmat.2012.06.046

98. Ashby, M.F.: A first report on deformation-mechanism maps. Acta Metall. 20, 887–897 (1972). https://doi.org/10.1016/0001-6160(72)90082-X

99. Mohamed, F.A., Langdon, T.G.: Deformation mechanism maps based on grain size. Metall. Mater. Trans. B. 5, 2339–2345 (1974). https://doi.org/10.1007/BF02644014

100. Yavari, P., Langdon, T.G.: An examination of the breakdown in creep by viscous glide in solid solution alloys at high stress levels. Acta Metall. 30, 2181–2196 (1982). https://doi.org/https://doi.org/10.1016/0001-6160(82)90139-0

101. Stocker, R.L., Ashby, M.F.: On the empirical constants in the dorn equation. Scr. Metall. 7, 115–120 (1973). https://doi.org/https://doi.org/10.1016/0036-9748(73)90192-0

102. Singh, R.N.: Application of deformation-mechanism maps to the study of in-reactor behavior of carbide fuels. J. Nucl. Mater. 64, 167–173 (1977). https://doi.org/https://doi.org/10.1016/0022-3115(77)90020-4

103. Sargent, P.M., Ashby, M.F.: Deformation-mechanism maps for silicon carbide. Scr. Metall. 17, 951–957 (1983). https://doi.org/https://doi.org/10.1016/0036-9748(83)90269-7

104. Sargent, P.M., Malakondaiah, G., Ashby, M.F.: A deformation map for cobalt. Scr. Metall. 17, 625–629 (1983). https://doi.org/https://doi.org/10.1016/0036-9748(83)90390-3

105. Sargent, P.M., Ashby, M.F.: Deformation mechanism maps for alkali metals. Scr. Metall. 18, 145–150 (1984). https://doi.org/https://doi.org/10.1016/0036-9748(84)90494-0

106. Sargent, P.M., Ashby, M.F.: A deformation mechanism map for a III–V compound, indium antimonide. Scr. Metall. 18, 219–224 (1984). https://doi.org/https://doi.org/10.1016/0036-9748(84)90511-8

107. Carey, J.A., Sargent, P.M., Jones, D.R.H.: A deformation mechanism map for IN738LC superalloy. J. Mater. Sci. Lett. 9, 572–575 (1990). https://doi.org/10.1007/BF00725881

108. VERRALL, R.A., FIELDS, R.J., ASHBY, M.F.: Deformation-Mechanism Maps for LiF and NaCl. J. Am. Ceram. Soc. 60, 211–216 (1977). https://doi.org/https://doi.org/10.1111/j.1151-2916.1977.tb14108.x

109. Jeong, H.T., Kim, W.J.: Calculation and construction of deformation mechanism maps and processing maps for CoCrFeMnNi and Al0.5CoCrFeMnNi high-entropy alloys. J. Alloys Compd. 869, 159256 (2021). https://doi.org/10.1016/j.jallcom.2021.159256

110. Patnamsetty, M., Somani, M.C., Ghosh, S., Ahmed, S., Peura, P.: Processing map for controlling microstructure and unraveling various deformation mechanisms during hot working of CoCrFeMnNi high entropy alloy. Mater. Sci. Eng. A. 793, 139840 (2020). https://doi.org/10.1016/j.msea.2020.139840

111. Yu, Z., Xie, B., Zhu, Z., Xu, B., Sun, M.: High-temperature deformation behavior and processing maps of a novel AlNbTi3VZr1.5 refractory high entropy alloy. J. Alloys

Compd. 912, 165220 (2022). https://doi.org/10.1016/j.jallcom.2022.165220

112. Kawasaki, M., Langdon, T.G.: Developing superplasticity and a deformation mechanism map for the Zn-Al eutectoid alloy processed by high-pressure torsion. Mater. Sci. Eng. A. 528, 6140–6145 (2011). https://doi.org/10.1016/j.msea.2011.04.053

113. Xie, D.G., Zhang, R.R., Nie, Z.Y., Li, J., Ma, E., Li, J., Shan, Z.W.: Deformation mechanism maps for sub-micron sized aluminum. Acta Mater. 188, 570–578 (2020). https://doi.org/10.1016/j.actamat.2020.02.013

114. Jiang, H., Dong, J., Zhang, M., Zheng, L., Yao, Z.: Hot deformation characteristics of Alloy 617B nickel-based superalloy: A study using processing map. J. Alloys Compd. 647, 338–350 (2015). https://doi.org/10.1016/j.jallcom.2015.05.192

115. Sun, Y., MacIejewski, K., Ghonem, H.: A damage-based cohesive zone model of intergranular crack growth in a nickel-based superalloy. Int. J. Damage Mech. 22, 905–923 (2013). https://doi.org/10.1177/1056789512468917

116. Prasad, K., Sarkar, R., Ghosal, P., Kumar, V.: Simultaneous creep – fatigue damage accumulation of forged turbine disc of IN Materials Science & Engineering A Simultaneous creep – fatigue damage accumulation of forged turbine disc of IN 718 superalloy. Mater. Sci. Eng. A. 572, 1–7 (2013). https://doi.org/10.1016/j.msea.2013.02.003

117. ASHBY, M.F., GANDHI, C., TAPLIN, D.M.R.: Fracture – mechanism maps and their construction for f.c.c. metals and alloys. In: ASHBY, M.F. and BROWN, L.M.B.T.-P. in C.F. (eds.) Perspectives in Creep Fracture. pp. 1–31. Pergamon (1983)

118. Gaffard, V., Besson, J., Gourgues-Lorenzon, A.F.: Creep failure model of a tempered martensitic stainless steel integrating multiple deformation and damage mechanisms. Int. J. Fract. 133, 139–166 (2005). https://doi.org/10.1007/s10704-005-2528-8

119. Kim, W.G., Kim, S.H., Ryu, W.S.: Evaluation of Monkman-Grant parameters for type 316LN and modified 9Cr-Mo stainless steels. KSME Int. J. 16, 1420–1427 (2002). https://doi.org/10.1007/BF02985134

120. Isaac Samuel, E., Choudhary, B.K., Rao Palaparti, D.P., Mathew, M.D.: Creep deformation and rupture behaviour of P92 steel at 923 K. Procedia Eng. 55, 64–69

(2013). https://doi.org/10.1016/j.proeng.2013.03.220

121. Michel, B.: Formulation of a new intergranular creep damage model for austenitic stainless steels. Nucl. Eng. Des. 227, 161–174 (2004). https://doi.org/10.1016/j.nucengdes.2003.09.005

122. Rate, B.S., Failure, S.T.O., Time, L.: E.H. TOSCANO * and M. BOCEK. 96, 29–36 (1981)

123. Osman Ali, H., Tamin, M.N.: Modified Monkman-Grant relationship for austenitic stainless steel foils. J. Nucl. Mater. 433, 74–79 (2013). https://doi.org/10.1016/j.jnucmat.2012.08.048

124. Povolo, F.: Comments on the Monkman-Grant and the modified Monkman-Grant relationships. J. Mater. Sci. 20, 2005–2010 (1985). https://doi.org/10.1007/BF01112283

125. Baldan, A.: Effects of carbides and cavitation on the Monkman-Grant ductility of a nickel-base superalloy. J. Mater. Sci. Lett. 11, 1315–1318 (1992). https://doi.org/10.1007/BF00742189

126. Choudhary, B.K.: Tertiary creep behaviour of 9Cr-1Mo ferritic steel. Mater. Sci. Eng. A. 585, 1–9 (2013). https://doi.org/10.1016/j.msea.2013.07.026

127. Radhakrishnan, V.M.: The relationship between minimum creep rate and rupture time in Cr-Mo steels. J. Mater. Eng. Perform. 1, 123–128 (1992). https://doi.org/10.1007/BF02650043

128. Dobeš, F., Milička, K.: On the Monkman-grant relation for small punch test data. Mater. Sci. Eng. A. 336, 245–248 (2002). https://doi.org/10.1016/S0921-5093(01)01975-X

129. Ray, A.K., Diwakar, K., Prasad, B.N., Tiwari, Y.N., Ghosh, R.N., Whittenberger, J.D.: Long term creep-rupture behaviour of 813 K exposed 2.25-1Mo steel between 773 and 873 K. Mater. Sci. Eng. A. 454–455, 124–131 (2007). https://doi.org/10.1016/j.msea.2006.11.020

130. Choudhary, B.K., Phaniraj, C., Raj, B.: Interesting relationships for creep deformation and damage and their applicability for 9Cr-1Mo ferritic steel. Trans. Indian Inst. Met. 63, 675–680 (2010). https://doi.org/10.1007/s12666-010-0103-0

131. Choudhary, B.K., Isaac Samuel, E.: Creep behaviour of modified 9Cr-1Mo ferritic steel. J. Nucl. Mater. 412, 82–89 (2011). https://doi.org/10.1016/j.jnucmat.2011.02.024

132. Sundararajan, G.: The Monkman-Grant Relationship. Mater. Sci. Eng. A. 112, 205–214 (1989)

133. Phaniraj, C., Nandagopal, M., Mannan, S.L., Rodriguez, P.: The relationship between transient and steady state creep in AISI 304 stainless steel. Acta Metall. Mater. 39, 1651–1656 (1991). https://doi.org/10.1016/0956-7151(91)90253-W

134. Choudhary, B.K., Phaniraj, C., Rao, K.B.S., Mannan, S.L.: Creep deformation behaviour and kinetic aspects of 9Cr-1Mo ferritic steel. Isij Int. 41, 1298 (2001)

135. Phaniraj, C., Nandagopal, M., Mannan, S., Rodriguez, P., Kashyap, B.: Analysis of first order kinetics for tertiary creep in AISI 304 stainless steel. Acta Mater. 44, 4059–4069 (1996). https://doi.org/10.1016/S1359-6462(97)00117-6

136. Choudhary, B.K., Phaniraj, C., Bhanu Sankara Rao, K., Mannan, S.L.: Transient Creep Behaviour of Forged Thick Section 9Cr-1Mo Ferritic Steel. In: Creep and Fracture of Engineering Materials and Structures. pp. 437–444. Trans Tech Publications Ltd (1999)

137. Phaniraj, C., Choudhary, B.K., Bhanu Sankara Rao, K., Raj, B.: Relationship between time to reach Monkman-Grant ductility and rupture life. Scr. Mater. 48, 1313–1318 (2003). https://doi.org/10.1016/S1359-6462(03)00021-6

138. Phaniraj, C., Choudhary, B.K., Raj, B., Bhanu Sankara Rao, K.: A critical damage criterion for creeping solids. J. Mater. Sci. 40, 2561–2564 (2005). https://doi.org/10.1007/s10853-005-2074-9

139. Kachanov, L.M.: Rupture time under creep conditions. Int. J. Fract. 97, (1999). https://doi.org/10.1023/a:1018671022008

140. Rabotnov, Y.N., Leckie, F.A., Prager, W.: Creep Problems in Structural Members. J. Appl. Mech. 37, 249 (1970). https://doi.org/10.1115/1.3408479

141. Cane, B.J., Aplin, P.F.: Creep life assessment methods. J. Strain Anal. Eng. Des. 29, 225–232 (1994). https://doi.org/10.1243/03093247V293225

142. Cane, B.J.: Remaining creep life estimation by strain assessment on plant. Int. J. Press.

Vessel. Pip. 10, 11–30 (1982). https://doi.org/10.1016/0308-0161(82)90023-0

143. Leckie, F.A., Hayhurst, D.R.: Constitutive equations for creep rupture. Acta Metall. 25, 1059–1070 (1977). https://doi.org/10.1016/0001-6160(77)90135-3

144. Leckie, F.A., Hayhurst, D.R.: The damage concept in creep mechanics. Mech. Res. Commun. 2, 23–26 (1975). https://doi.org/10.1016/0093-6413(75)90020-8

145. Hollomon, J.H., Jaffe, L.D.: Time-Temperature Relations In Tempering Steel, (1945)

146. Ray, A.K., Whittenberger, J.D.: Stress rupture behavior of a thermal barrier coated AE 437A Ni-based superalloy used for aero turbine blades. 509, 111–114 (2009). https://doi.org/10.1016/j.msea.2009.01.033

147. Nakashiro, M., Kihara, S., Kishimoto, F., Fujimor, T.: Evaluation of Long-term Creep Strength of 2 . 25Cr-1Mo Heat Transfer Tube in Actual Service Stress Level Range. 30, 823–828 (1990)

148. Vasudevan, M., Venkadesan, S., Sivaprasad, P.V., Mannan, S..: Use of the Larson – Miller parameter to study the influence of ageing on the hardness of cold – worked austenitic stainless steel. J. Nucl. Mater. 211, 251–255 (1994)

149. Fujita, T.: Current progress in advanced high Cr ferritic steels for high – temperature applications. ISIJ Int. 32, 75–81 (1992)

150. Koul, A.K.: Larson – Miller parameter and its modified version. Scr. Metall. 16, 947 – 950 (1982)

151. Koul, A.K., Wallace, W.: A Note on the Microstructural Dependence of Creep Strength in Inconel 700. Metall. Trans. A. 13, 673–675 (1982). https://doi.org/10.1007/BF02644434

152. Kadoya, Y., Goto, T., Date, S., Yamauchi, T., Saida, T., Sada, T.: Assessment of remaining life of fossil power plant parts by means of a miniature creep rupture test. ISIJ Int. 30, 854–861 (1990)

153. Harada, Y., Maruyama, Y., Maeda, A., Chino, E., Shibazaki, H., Kudo, T., Hidaka, A., Hashimoto, K., Sugimoto, J.: Evaluation of High Temperature Tensile and Creep Properties of Light Water Reactor Coolant Piping Materials for Severe Accident Analyses Evaluation of High Temperature Tensile and Creep Properties of Light Water Reactor Coolant Piping Materials for Severe. J. Nucl. Sci. Technol. 37, 518–529

(2000). https://doi.org/10.1080/18811248.2000.9714925

154. Deng, S., Warren, R.: Creep Properties of Single Crystal Oxides Evaluated by a Larson-Miller Procedure. Jouurnal Eur. Ceram. Soc. 15, 513–520 (1995)

155. Sugita, Y., Kato, Y., Yokoyama, T., Sada, T., Sasuyama, F., Nishimura, N.: Evaluation of creep damage progress by metallurgical examination in aged power boiler pressure parts. ISIJ Int. 30, 895–904 (1990)

156. Nicoll, A.R.: The Larson – Miller C constant as applied to a cobalt – based directionally solidified eutectic alloy. J. Mater. Sci. 14, 1759–1761 (1979)

157. Furillo, F.T., Purushothaman, S., Tien, J.K.: Further discussion on "Understanding the Larson – Miller parameter. Scr. Metall. 12, 331–332 (1978)

158. Pahutová, M., Kuchařová, K., Čadek, J.: Some basic creep characteristics of ZrSnMo and ZrSnMoNb alloys part II. Fracture in creep. Mater. Sci. Eng. 27, 249–255 (1977). https://doi.org/10.1016/0025-5416(77)90208-7

159. Kim, H.: Assessment of creep life fraction for in-service high-temperature components. 12, 578–585 (2005). https://doi.org/10.1016/j.engfailanal.2004.09.001

160. Shlyakman, B.M., Yampolskii, O.N., Ratushev, D. V: A METHOD FOR DETERMINING CONSTANT C IN THE HOLLOMON PARAMETER. 52, 451–453 (2010)

161. Zhao, J., Li, D., Zhang, J., Feng, W., Fang, Y.: Introduction of SCRI model for creep rupture life assessment. Int. J. Press. Vessel. Pip. 86, 599–603 (2009). https://doi.org/10.1016/j.ijpvp.2009.04.004

162. Zhao, J., Han, S., Gao, H., Wang, L.: Remaining life assessment of a CrMoV steel using the Z-parameter method. 81, 757–760 (2004). https://doi.org/10.1016/j.ijpvp.2004.05.002

163. Kim, W., Park, J., Kim, S., Jang, J.: Reliability assessment of creep rupture life for Gr . 91 steel. J. Mater. 51, 1045–1051 (2013). https://doi.org/10.1016/j.matdes.2013.05.013

164. Kim, W., Park, J., Choudhary, B.K., Kim, S., Kim, M., Jang, J.: Influence of data size on the reliability assessment of creep life of grade 91 steel †. 28, 4493–4501 (2014). https://doi.org/10.1007/s12206-014-1049-7

165. Ferreira Schon, A., Apoena Castro, N., dos Santos Barros, A., Eduardo Spinelli, J., Garcia, A., Cheung, N., Luiz Silva, B.: Multiple linear regression approach to predict tensile properties of Sn-Ag-Cu (SAC) alloys. Mater. Lett. 304, (2021). https://doi.org/10.1016/j.matlet.2021.130587

166. Kusano, M., Miyazaki, S., Watanabe, M., Kishimoto, S., Bulgarevich, D.S., Ono, Y., Yumoto, A.: Tensile properties prediction by multiple linear regression analysis for selective laser melted and post heat-treated Ti-6Al-4V with microstructural quantification. Mater. Sci. Eng. A. 787, 139549 (2020). https://doi.org/10.1016/j.msea.2020.139549

167. Yang, D., Liu, Z.: Surface topography analysis and cutting parameters optimization for peripheral milling titanium alloy Ti-6Al-4V. Int. J. Refract. Met. Hard Mater. 51, 192–200 (2015). https://doi.org/10.1016/j.ijrmhm.2015.04.001

168. Milhomme, S., Lartigau, J., Brugger, C., Froustey, C.: Bead geometry prediction using multiple linear regression analysis: Application to Ti-6Al-4V beads made by laser metal powder deposition. Int. J. Adv. Manuf. Technol. 117, 607–620 (2021). https://doi.org/10.1007/s00170-021-07697-w

169. Lazo, Y., Suárez, L., Fernández, M., Fernández, L.: Modeling of lattice parameters of the γ and γ′ phases of the superalloys with base nickel by using a multiple linear regression analysis. Superlattices Microstruct. 45, 117–124 (2009). https://doi.org/10.1016/j.spmi.2009.01.001

170. Hagan, M.T., Menhaj, M.B.: Training feedforward networks with the Marquardt algorithm. 5, 2–6 (1994)

171. Robi, P.S., Dixit, U.S.: Application of neural networks in generating processing map for hot working. J. Mater. Process. Technol. 142, 289–294 (2003). https://doi.org/10.1016/S0924-0136(03)00579-X

172. Kamrunnahar, M., Urquidi-Macdonald, M.: Prediction of corrosion behavior using neural network as a data mining tool. Corros. Sci. 52, 669–677 (2010). https://doi.org/10.1016/j.corsci.2009.10.024

173. Yetim, A.F., Codur, M.Y., Yazici, M.: Using of artificial neural network for the prediction of tribological properties of plasma nitrided 316L stainless steel. Mater. Lett. 158, 170–173 (2015). https://doi.org/10.1016/j.matlet.2015.06.015

174. Ping, L., Kemin, X., Yan, L., Jianrong, T.: Neural network prediction of flow stress of Ti-15-3 alloy under hot compression. J. Mater. Process. Technol. 148, 235–238 (2004). https://doi.org/10.1016/j.jmatprotec.2003.07.013

175. Reddy, N.S., Lee, Y.H., Park, C.H., Lee, C.S.: Prediction of flow stress in Ti-6Al-4V alloy with an equiaxed α + β microstructure by artificial neural networks. Mater. Sci. Eng. A. 492, 276–282 (2008). https://doi.org/10.1016/j.msea.2008.03.030

176. Banerjee, S., Robi, P.S., Srinivasan, A.: Deformation processing maps for control of microstructure in Al-Cu-Mg alloys microalloyed with Sn. Metall. Mater. Trans. A Phys. Metall. Mater. Sci. 43, 3834–3849 (2012). https://doi.org/10.1007/s11661-012-1191-8

177. Asgharzadeh, A., Asgharzadeh, H., Simchi, A.: Role of Grain Size and Oxide Dispersion Nanoparticles on the Hot Deformation Behavior of AA6063: Experimental and Artificial Neural Network Modeling Investigations. Met. Mater. Int. (2021). https://doi.org/10.1007/s12540-020-00950-z

178. Kapoor, R., Pal, D., Chakravartty, J.K.: Use of artificial neural networks to predict the deformation behavior of Zr-2.5Nb-0.5Cu. J. Mater. Process. Technol. 169, 199–205 (2005). https://doi.org/10.1016/j.jmatprotec.2005.03.022

179. Rezaei Ashtiani, H.R., Shayanpoor, A.A.: Hot Deformation Characterization of Pure Aluminum Using artificial neural network (ANN) and Processing Map Considering Initial Grain Size. Met. Mater. Int. (2021). https://doi.org/10.1007/s12540-020-00943-y

180. Singh, S.K., Mahesh, K., Gupta, A.K.: Prediction of mechanical properties of extra deep drawn steel in blue brittle region using Artificial Neural Network. Mater. Des. 31, 2288–2295 (2010). https://doi.org/10.1016/j.matdes.2009.12.012

181. Hong, T.W., Lee, S.I., Shim, J.H., Lee, M.G., Lee, J., Hwang, B.: Artificial Neural Network for Modeling the Tensile Properties of Ferrite-Pearlite Steels: Relative Importance of Alloying Elements and Microstructural Factors. Met. Mater. Int. 27, 3935–3944 (2021). https://doi.org/10.1007/s12540-021-00982-z

182. Deshpande, Y. V., Andhare, A.B., Padole, P.M.: Application of ANN to estimate surface roughness using cutting parameters, force, sound and vibration in turning of Inconel 718. SN Appl. Sci. 1, 1–9 (2019). https://doi.org/10.1007/s42452-018-0098-4

183. Maleki, E., Unal, O.: Shot Peening Process Effects on Metallurgical and Mechanical Properties of 316 L Steel via: Experimental and Neural Network Modeling. Met. Mater. Int. 27, 262–276 (2021). https://doi.org/10.1007/s12540-019-00448-3

184. Maleki, E., Unal, O.: Optimization of Shot Peening Effective Parameters on Surface Hardness Improvement. Met. Mater. Int. 27, 3173–3185 (2021). https://doi.org/10.1007/s12540-020-00758-x

185. Wang, N., Tu, S.T., Xuan, F.Z.: A novel prediction method of creep rupture life of 9-12% chromium ferritic steel based on abductive network. Eng. Fail. Anal. 31, 302–310 (2013). https://doi.org/10.1016/j.engfailanal.2013.01.026

186. Liang, T., Liu, X., Fan, P., Zhu, L., Bi, Y., Zhang, Y.: Prediction of long-term creep life of 9Cr–1Mo–V–Nb steel using artificial neural network. Int. J. Press. Vessel. Pip. 179, 104014 (2020). https://doi.org/10.1016/j.ijpvp.2019.104014

187. Zhong, J., Yang, C., Ma, W., Zhang, Z.: Long-term creep behavior prediction of polymethacrylimide foams using artificial neural networks. Polym. Test. 93, 106893 (2021). https://doi.org/10.1016/j.polymertesting.2020.106893

188. Kwon, Y. Il, Lim, B.S.: A study of creep-fatigue life prediction using an artificial neural network. Met. Mater. Int. 7, 311–317 (2001). https://doi.org/10.1007/bf03186074

189. Rodchenkov, B.S., Semenov, A.N.: High temperature mechanical behavior of Zr-2.5% Nb alloy. Nucl. Eng. Des. 235, 2009–2018 (2005). https://doi.org/10.1016/j.nucengdes.2005.05.032

190. Hollomon, J.H.: Tensile deformation. Trans. Am. Instiute Min. 162, 268–290 (1945)

191. Luo, J., Li, M.Q.: Strain rate sensitivity and strain hardening exponent during the isothermal compression of Ti60 alloy. Mater. Sci. Eng. A. 538, 156–163 (2012). https://doi.org/10.1016/j.msea.2012.01.021

192. Ghatak, A., Robi, P.S.: A comparative study of constitutive equations for the creep deformation of HP40Nb micro-alloyed steel. Mater. Sci. Eng. A. 648, 418–427 (2015). https://doi.org/10.1016/j.msea.2015.09.087

193. Garson, G.D.: “Interpreting Neural-Network Connection Strengths.” AI Expert. 47–51 (1991)

194. Ghatak, A., Robi, P.S.: Analysis of Monkman-Grant relationships and damage tolerance factor for creep of 25Cr35NiNb micro-alloyed steel. Mater. Sci. Eng. A. 845, 143027 (2022). https://doi.org/10.1016/j.msea.2022.143027

195. Guguloth, K., Mitra, R., Chowdhury, S.G., Swaminathan, J.: Mechanism of creep deformation with evolution of microstructure and texture. Mater. Sci. Eng. A. 721, 286–302 (2018). https://doi.org/10.1016/j.msea.2018.02.035

196. JCPDF reference, code:00-018-0599.pdf

197. Kumawat, Bhupendra K, Sarkar, A., Singh, R.N.: TEMPERATURE DEPENDENT YOUNG'S MODULUS OF Zr-2.5Nb PRESSURE TUBE MATERIAL USED IN INDIAN PRESSURIZED HEAVY WATER REACTOR. (2021)

198. Northwood, D.O., London, I.M., Bähen, L.E.: Elastic constants of zirconium alloys. J. Nucl. Mater. 55, 299–310 (1975). https://doi.org/10.1016/0022-3115(75)90071-9

199. Swift, H.W.: Plastic instability under plane stress. J. Mech. Phys. Solids. 1, 1–18 (1952). https://doi.org/10.1016/0022-5096(52)90002-1

200. Voce, E.: A practical strain hardening function. Metallurgia. 51, 219–226 (1955)

201. Dureja, A.K., Sinha, S.K., Srivastava, A., Sinha, R.K., Chakravartty, J.K., Seshu, P., Pawaskar, D.N.: Flow behaviour of autoclaved, 20% cold worked, Zr-2.5Nb alloy pressure tube material in the temperature range of room temperature to 800 °c. J. Nucl. Mater. 412, 22–29 (2011). https://doi.org/10.1016/j.jnucmat.2011.01.023

202. Hayes, R.W.: On a proposed theory for the disappearance of serrated flow in f.c.c. Ni alloys. Acta Metall. 31, 365–371 (1983). https://doi.org/10.1016/0001-6160(83)90213-4

203. McCormigk, P.G.: A model for the Portevin-Le Chatelier effect in substitutional alloys. Acta Metall. 20, 351–354 (1972). https://doi.org/10.1016/0001-6160(72)90028-4

204. Sotoudeh, K., Bate, P.S.: Diffusion creep and superplasticity in aluminium alloys. Acta Mater. 58, 1909–1920 (2010). https://doi.org/10.1016/j.actamat.2009.11.034

205. Kiran Kumar, M., Samajdar, I., Venkatramani, N., Dey, G.K., Tewari, R., Srivastava, D., Banerjee, S.: Explaining absence of texture development in cold rolled two-phase Zr-2.5 wt% Nb alloy. Acta Mater. 51, 625–640 (2003). https://doi.org/10.1016/S1359-6454(02)00442-1

206. Nouduru, S.K., Kumar, M.K., Kain, V., Khanna, A.S., Saibaba, N., Dey, G.K.: High temperature and high pressure oxidation behavior of Zr-2.5Nb pressure tube material - Effect of β phase composition and surface machining. J. Nucl. Mater. 470, 197–207 (2016). https://doi.org/10.1016/j.jnucmat.2015.12.030

207. Gifkins, R.C.: The effect of grain size and stress upon grain-boundary sliding. Metall. Trans. A. 8, 1507–1516 (1977). https://doi.org/10.1007/BF02644853

208. Ashby, M.F., Verrall, R.A.: Diffusion-accommodated flow and superplasticity. Acta Metall. 21, 149–163 (1973). https://doi.org/10.1016/0001-6160(73)90057-6

209. Wang, X.G., Li, Q.S., Wu, R.R., Zhang, X.Y., Ma, L.: A Review on Superplastic Formation Behavior of Al Alloys. Adv. Mater. Sci. Eng. 2018, (2018). https://doi.org/10.1155/2018/7606140

210. Duan, Y.L., Xu, G.F., Peng, X.Y., Deng, Y., Li, Z., Yin, Z.M.: Effect of Sc and Zr additions on grain stability and superplasticity of the simple thermal-mechanical processed Al-Zn-Mg alloy sheet. Mater. Sci. Eng. A. 648, 80–91 (2015). https://doi.org/10.1016/j.msea.2015.09.049

211. Shewfelt, R.S.W., Lyall, L.W.: A high-temperature longitudinal strain rate equation for Zr-2.5 wt% Nb pressure tubes. J. Nucl. Mater. 132, 41–46 (1985). https://doi.org/10.1016/0022-3115(85)90391-5

212. R.N. SIngh, Kishore, R., T.K. Sinha, B.P.Kashyap: Superplastic behaviour of a Zr-2.5wt% Nb pressure tube alloy. Scr. Metall. Mater. 28, 937–942 (1993)

213. Kim, J.S., Kim, J.H., Lee, Y.T., Park, C.G., Lee, C.S.: Microstructural analysis on boundary sliding and its accommodation mode during superplastic deformation of Ti – 6Al – 4V alloy. 263, 272–280 (1999)

214. Cao, F.R., Ding, H., Li, Y.L., Zhou, G., Cui, J.Z.: Superplasticity, dynamic grain growth and deformation mechanism in ultra-light two-phase magnesium-lithium alloys. Mater. Sci. Eng. A. 527, 2335–2341 (2010). https://doi.org/10.1016/j.msea.2009.12.029

215. Tan, J.C., Tan, M.J.: Superplasticity and grain boundary sliding characteristics in two stage deformation of Mg-3Al-1Zn alloy sheet. Mater. Sci. Eng. A. 339, 81–89 (2003). https://doi.org/10.1016/S0921-5093(02)00097-7

216. Tahami, F.V., Daei-Sorkhabi, A.H., Biglari, F.R.: Creep constitutive equations for cold-drawn 304L stainless steel. Mater. Sci. Eng. A. 527, 4993–4999 (2010). https://doi.org/10.1016/j.msea.2010.04.055

217. Sargent, P.M., Ashby, M.F.: Deformation maps for titanium and zirconium. Scr. Metall. 16, 1415–1422 (1982). https://doi.org/https://doi.org/10.1016/0036-9748(82)90439-2

218. Ashby, M.F., Dyson, B.F.: CREEP DAMAGE MECHANICS AND MICROMECHANISMS. Presented at the (1984)

219. Yin, D.D., Wang, Q.D., Boehlert, C.J., Janik, V.: Creep and fracture behavior of peak-aged Mg-11Y-5Gd-2Zn-0.5Zr (wt pct). Metall. Mater. Trans. A Phys. Metall. Mater. Sci. 43, 3338–3350 (2012). https://doi.org/10.1007/s11661-012-1131-7

220. Davies, P.W., Williams, K.R.: Recovery measurements during tertiary creep of α-iron. Acta Metall. 17, 897–903 (1969). https://doi.org/https://doi.org/10.1016/0001-6160(69)90110-2

221. Dieter, G.E. ed: Materials Selection and Design. ASM International (1997)

222. Rodgers, D., Griffiths, M., Bickel, G., Buyers, A., Coleman, C., Nordin, H., Lawrence, S.S.: PERFORMANCE OF PRESSURE TUBES IN CANDU REACTORS. CNL Nucl. Rev. 5, 1–15 (2016). https://doi.org/10.12943/CNR.2016.00007

APPENDIX

Larson-Miller parameter

In 1952, F.R. Larson and J. Miller proposed that the creep rate is governed by the Arrhenius type equation as follows:

$$\dot{\varepsilon} = A_0 \exp\left(-\frac{Q_c}{RT}\right) \tag{A.1}$$

where $\dot{\varepsilon}$ is the minimum creep rate, A_0 is a constant, R is the universal gas constant, T is the absolute temperature, Q_c is the activation energy for the creep mechanism.

Since, the rupture time depends on the creep rate by $t_r(\frac{d\varepsilon}{dt})_{min}$ = constant, Eq A.1 may be written as

$$\frac{1}{t_r} = A_o \exp\left(-\frac{Q_c}{RT}\right) \tag{A.2}$$

where t_r is the time to rupture.

Taking the natural logarithm of both sides of Eq. A.2

$$-\ln(t_r) = \ln(A_o) - \frac{Q_c}{RT} \tag{A.3}$$

With some rearrangement

$$-\frac{Q_c}{R} = T(\ln(A_o) + \ln(t_r)) \tag{A.4}$$

The final relation becomes

$$T\left(C_{L-M} + log_{10}(t_r)\right) = \frac{Q_c}{2.3R} = P_{L-M} = \text{Constant (for constant stress)} \tag{A.5}$$

where $C_{L-M} = log_{10}(A_{10})$ = constant and P_{L-M} is Larson-Miller parameter.

Calculations of the spring constants

The spring stiffness for constant stresses was calibrated for 2 MPa, 3MPa, 4 MPa, 5MPa for longitudinal creep tests and 22MPa, 38MPa, and 58MPa for transverse creep tests. Before the beginning of each calibration test, the top plate was kept at such a position by rotating the power screw such that maximum load acts on the specimen with zero displacement in the gauge length. Axial movement of the top plate was measured from a reference point. The nut was rotated in the reverse direction, which resulted in the release of load on the specimen, which in turn brought the top plate down. The load was noted from the load indicator for each millimeter displacement of the top plate. Maximum percentage deviation and RMS error for the different stresses are calculated and given in Table A.1 and A.2.

Table A.1 Spring stiffness, percentage deviation, and RMS error for different stresses used for longitudinal creep tests.

True Stress (MPa)	Spring stiffness (N/mm)	Maximum deviation (%)	RMS error (N)
2	1.16	+0.84	0.68
		-1.24	
3	1.78	+1.48	0.98
		-2.02	
4	2.34	+1.68	1.08
		-2.22	
5	2.96	+2.68	2.54
		-3.42	

Table A.2 Spring stiffness, percentage deviation and RMS error for different stresses used for transverse creep tests.

True Stress (MPa)	Spring stiffness (N/mm)	Maximum deviation (%)	RMS error (N)
22	12.76N	+2.28	1.78
		-2.76	
38	18.68N	+2.98	8.24
		-3.88	
58	28.48N	+3.44	14.28
		-4.02	

Technical Specification

a) Load cell:

Items		Load Cell
Capacity		200Kg
Model		SL-
Sensitivity		2.0 ± 10 % mV/V
Non-Linearity		± 0.015% FS
Hysteresis		± 0.02% FS
Creep (20 Min.)		± 0.02% FS
Zero Balance		± 1% FS
Insulation Resistance		≥ 5000 MΩ (@ 50V DC)
Resistance	Input	365 ± 15Ω
	Output	350 ± 3Ω
Temperature Range	Compensated	-10 ~ +55°C
	Operating	-35 ~ +80°C
Temperature Effect	Output (Span)	± 0.02% FS/10°C
	Zero	± 0.02% FS/10°C
Maximum Supply Voltage		12V DC
Recommended Supply Voltage		10V DC
Safe Overload		150% FS
Maximum Overload		200% FS
Finish & Construction		Stainless Steel construction
Hole Size / Pitch		12 mm & 1.75 mm
Environment Protection Class		IP68

b) Digital Indicator:

- Model: T4.
- Wall mounting with 6 digit 7 segment LED display.
- RS 232 compatible output.
- With Tare / Zero facility.
- Battery Back up.

LIST OF PUBLICATIONS

Journals

1 **Saptarshi Dutta**, P.S.Robi, "Analysis of tensile flow and work hardening behavior of Zr-2.5Nb alloy in the framework of Kocks — Mecking approach.", Journal of Mechanical Science and Technology, 35, 3369–3374 (2021).

2 **Saptarshi Dutta**, P.S.Robi, "Experimental Investigation and Modeling of Creep Curve of Zr–2.5Nb Alloy by Machine Learning Techniques.", Metals and Materials International, 28, 2884–2897 (2022).

3 **Saptarshi Dutta**, P.S.Robi, "Experimental investigation and correlation of elevated temperature mechanical behavior of Zr-2.5Nb alloy.", Journal of Materials Science, 57, 22157–22172 (2022).

4 **Saptarshi Dutta**, P.S.Robi, "Analysis of Monkman-Grant relationships and damage tolerance factor for creep of Zr-2.5Nb alloy.", (To be communicated)

5 **Saptarshi Dutta**, P.S.Robi, "Application of Modified Larson–Miller Parameter Technique for Predicting Creep Life of Zr-2.5Nb alloy.", (To be communicated)

Conference

1 **Saptarshi Dutta**, P.S.Robi, P. Majumdar , "High Temperature Tensile Behavior of Zr-2.5 wt % Nb Alloy Pressure Tubes", 4th International Conference on the Science and Engineering of Materials(ICoSEM2019), 26 - 28 August 2019, Malaysia.

2 **Saptarshi Dutta**, P.S.Robi, "Tensile behaviour and microstructural evolution of Zr-2.5%Nb alloy with temperature", 8th Asian Conference on Mechanics of Functional Materials and Structures,(8th ACMFMS-2022), 11th-14th December 2022, IIT Guwahati, Guwahati, India.(Poster)